UNIVERSIDADE FEDERAL DO RIO GRANDE DO SUL

ESCOLA DE ENGENHARIA

DEPARTAMENTO DE ENGENHARIA QUÍMICA

PROGRAMA DE PÓS-GRADUAÇÃO EM ENGENHARIA QUÍMICA

Estratégias no delineamento de fotocatalisadores seletivos via impressão molecular

TESE DE DOUTORADO

Cícero Coelho de Escobar

Porto Alegre

2016

UNIVERSIDADE FEDERAL DO RIO GRANDE DO SUL

ESCOLA DE ENGENHARIA

DEPARTAMENTO DE ENGENHARIA QUÍMICA

PROGRAMA DE PÓS-GRADUAÇÃO EM ENGENHARIA QUÍMICA

Estratégia no delineamento de fotocatalisadores seletivos via impressão molecular

Cícero Coelho de Escobar

Tese de Doutorado apresentada ao Programa de Pós-Graduação Engenharia Química da Universidade Federal do Rio Grande do Sul como parte dos requisitos para obtenção do título de Doutor em Engenharia Química.

Doutorando: Cícero Coelho de Escobar, M. Sc.
Orientador: João Henrique Zimnoch dos Santos, Ph. D.

2016

“There are many hypotheses in science which are wrong. That's perfectly all right; they're the aperture to finding out what's right. Science is a self-correcting process. To be accepted, new ideas must survive the most rigorous standards of evidence and scrutiny.”

(Carl Sagan)

“Existem muitas hipóteses em ciência que estão erradas. Isso é perfeitamente aceitável, eles são a abertura para achar as que estão certas. A ciência é um processo de auto-correção. Para serem aceitas, as novas ideias devem sobreviver aos mais rigorosos padrões de evidências e escrutínio.”

Agradecimentos

O desenvolvimento de uma tese é penoso, porém gratificante. É penoso porque o labor intelectual é constantemente desafiado pelo escrutínio dos pares, uma prática sem a qual o desenvolvimento científico ainda estaria fadado aos métodos amiúdes dogmáticos e obscuros de outrora em nossa humanidade. É gratificante porque, além da possibilidade de contribuir para preencher lacunas do conhecimento atual em uma área de investigação, é um caminho de amadurecimento compartilhado com as pessoas que estiveram presentes ao longo deste período. E poucas coisas são comparadas ao valor intrínseco de uma família amável e de amizades sinceras.

Agradeço ao Prof. Dr^{o}. João Henrique Zimnoch dos Santos pela orientação, compreensão, ensinamentos e dedicação durante a realização deste trabalho que com certeza me fizeram crescer pessoal e profissionalmente.

Ao Programa de Pós-Graduação em Engenharia Química da Universidade Federal do Rio Grande do Sul, pela oportunidade realização deste trabalho. Também à CAPES e ao CNPq, pelo apoio financeiro, sem qual este trabalho não poderia ser realizado. Não fosse pelo apoio financeiro dos órgãos de fomento, dificilmente haveria possibilidade da execução de um estágio sanduíche desenvolvido na Lund University (Suécia). No exterior, tive o prazer de conhecer pessoas estimulantes das quais reservo meus agradecimentos pela recepção e trabalho em conjunto, como o professor Lei Ye e os colegas Tripa Kamra, Ka Zhang, Li Qianjin, Tongchang Zouh, Lingdong Jiang, Héctor Bagán e Hans Johansson.

Aos colegas dos Laboratório de Reatores (LARET), Laboratório de Catálise Ziegler-Natta da UFRGS e de outros departamentos, pela convivência e amizade durante uma significante parte da minha vida. São muitos nomes que eu devo agradecimento, mas não posso deixar de mencionar

alguns dos mais presentes: William da Silva, Tiele Caprioli, Jéssica Theisen, Cristiane dos Santos, Crissiê Zanrosso, Mônica Bagnara, Marla Lansarin, Camila Ribeiro, Luís Brum, Arthur Bernardes, William Feltrin, Larissa Capeletti, Marcéo Milani, Yolice Moreno, César Heck, Marcius Andrei, Eliana Barrera, Grizelda Barrera, Graziela Gheno, Giovani Pavoski, Leandra Campo e Natasha Sievers.

Aos meus amigos pessoais Max Passo, Sérgio Madeira, Júlio Madeira, Guilherme Madeira, Maurício Avila, César Pinheiro, Delilian Fogliatto e Jessika Andras. Em especial, foi a presença dessas pessoas que garantiram meu ânimo nos momentos mais desafortunados e compartilharam meus melhores contentamentos.

Aos meus pais, Elenice Coelho e João Pedro Escobar e irmã Victoria Escobar pela constante presença e apoio. Não há outras pessoas no mundo que tiveram tamanha confiança e dedicação comigo ao longo desses últimos anos. À minha namorada Priscila Rodrigues pelo carinho dedicado e por compartilhar junto a existência, mesmo nos momentos de ausência.

Resumo

A fotocatálise heterogênea é um processo que apresenta baixa seletividade de degradação. Nesse sentido, a síntese de materiais dotados de impressão molecular (IM) deve ajudar a contornar este problema. Os fotocatalisadores dotados de IM foram sintetizados de acordo com duas classes: uma inorgância (via diferentes rotas sol-gel e TEOS como percursor de sílica) e outra orgânica (via impressão não-covalente por precipitação e ácido metacrílico como monômero). No caso da primeira, a impressão molecular foi investigada através do uso de corante (rodamina B) e diferentes fármacos como *template* (substrato molde). No caso da matriz orgânica, o fármaco diclofenaco foi usado como molécula *template*. Os materiais foram caracterizados por análises texturais, estruturais e morfológicas. Com respeito à matriz à base de sílica, os sistemas com maiores valores de área específica foram observados pela rota ácida. Como efeito da rota, foi observado que a rota ácida apresentou um fator de seletividade 47% maior que a rota não-hidrolítica em testes de adsorção seletiva. Os resultados obtidos por análise de isotermas também convergem no sentido de revelarem que a rota ácida apresentou a maior capacidade de adsorção (997,9 mg/g) dentre as diferentes rotas de síntese pelo método sol-gel. Nos ensaios de fotocatálise (rodamina como *template*), foi conseguido um aumento de seletividade e competitividade na fotodegradação da rodamina de até 187% e 290%, respectivamente, comparado ao P25 (amostra comercial de TiO_2). Quanto ao uso de fármacos como *template* em matriz inorgânica, os fotocatalisadores com impressão molecular obtiveram um aumento na adsorção e fotodegradação de até 751 e 427%, respectivamente, em comparação ao P25. Os materiais baseados em matriz orgânica também apresentaram seletividade em comparação ao P25. O valor médio do coeficiente de seletividade (estimado a partir da degradação de moléculas não-alvo, a fluxetina e o paracetamol) foi estimado em 2,8 – portanto sugerindo que a presença de cavidades tridimensionais é um dos principais fatores da seletividade observada. Com o objetivo de explorar o potencial de adsorção das cavidades de impressão molecular, os estudos dos fotocatalisadores seletivos com adição de P25 foram conduzidos de maneira a manter baixa a concentração de TiO_2 (de 7 a 44 mg/L em cada teste fotocatalítico). Estudos de reuso do fotocatalisador (com e sem regeneração) também foram conduzidos. Tanto os materiais de matriz inorgânica como orgânica mantiveram em pelo menos 60% da eficiência fotocatalítica original após vários ciclos.

Palavras-Chaves: Sílica, dióxido de titânio, fotocatálise seletiva, impressão molecular.

Abstract

Heterogeneous photocatalysis is a process that has a low selectivity for degradation. In this sense, the synthesis of materials with molecularly imprinting (MI) should help to overcome this problem. The photocatalyst containing MI was synthesized according to two classes: An inorganic one (via different sol-gel routes and TEOS as silica precursor) and an organic one (via non-covalent imprinting by precipitation having methacrylic acid as monomer). In the first case, MI was investigated by use of the dye (rhodamine B) and several pharmaceutical compounds as template. In case the organic matrix, diclofenac was used as the template molecule. The samples were extensively characterized by textural, structural and morphological analysis. With respect to the silica-based matrix, the systems with larger surface area values were obtained by acid route. As effect of the route, it was observed that the acid route showed a selectivity factor 47% higher than that of the non-hydrolytic route in selective adsorption tests. Among the different synthesis routes prepared by sol-gel method, the isotherms analysis showed that acid route has the highest adsorption capacity (997.9 mg/g). Compared to the P25 (commercial sample of TiO_2), the photocatalysis assays (rhodamine as the template) have shown an increase in selectivity and competitiveness up to 187% and 290%, respectively. Regarding the use of pharmaceutical as template in the inorganic matrix, the imprinted photocatalyst had an increase in adsorption and photodegradation up to 751 and 427%, respectively. The systems based on the organic matrix have also showed selectivity compared to the P25. The mean value of selectivity coefficient for degradation (estimated from the non-target molecules, such as fluoxetine and paracetamol) was estimated to be 2.8 – thus, suggesting that the presence of three-dimensional cavities is a major factor in the observed selectivity. In order to explore the full potential of adsorption from the MI cavities, the photocatalyst containing P25 were prepared with the low concentration of TiO_2 (from 7 to 44 mg/L in each photocatalytic test). The reuse of photocatalysts (with and without regeneration) was also studied. Both inorganic and organic matrix retained at least 60% of the original efficiency after several cycles.

Keywords: Silica, titanium dioxide, selective photocatalysis, molecularly imprinted.

Sumário

Lista de Esquemas

Lista de Tabelas

Lista de Figuas

1. INTRODUÇÃO

Devido ao crescimento das atividades industriais, a legislação e a fiscalização têm se tornado cada vez mais restritivas, sobretudo com respeito à preservação das águas superficiais e subterrâneas (RANADE & BHANDARI, 2014). Dentre os compostos de maior preocupação destacam-se os chamados contaminantes emergentes, e incluem os produtos farmacêuticos e de cuidado pessoal, os esteróides, os surfactantes, os agrotóxicos e os corantes (LUO *et al.*, 2014). No caso dos corantes sintéticos, estima-se que mais de 280.000 toneladas/ano são descartadas no mundo todo (SHAH *et al.*, 2013).

Alguns desses compostos não são regulamentados, pois são candidatos para futuras regulamentações, ou dependem de futuros estudos sobre a sua toxicidade ou ainda são compostos recentemente introduzidos no ambiente. No Brasil, ainda são poucos os estudos que avaliaam a presença de contaminantes emergentes (JARDIM *et al.*, 2012). Entretanto, algumas análises apontam a existência de colesterol, bisfenol A, cafeína (SODRÉ *et al.*, 2010) e hormônios estrogênicos (PESSOA *et al*., 2014) em matrizes aquosas.

Muitos desses contaminantes não são adequadamente removidos pelos processos de tratamento convencionais. Nesse sentido, faz-se necessária sua mineralização, ou seja, é necessário converter a molécula para o seu maior estado de oxidação possível, convertendo-a em água, dióxido de carbono, em ânions inorgânicos oxidados ou em qualquer outra molécula que torne viável a remoção por processos biológicos, nesse caso, qualquer processo que favoreça o aumento da biodegradabilidade. Dessa forma, os processos avançados de oxidação (PAOs) são reconhecidamente métodos de degradação de poluentes devido a sua habilidade de remoção de uma ampla variedade de contaminantes orgânicos (LUO *et al.*, 2014; NITOI *et al*., 2013;

POURAN *et al*., 2014). Dentre esses processos, destaca-se a fotocatálise heterogenêa com o uso de TiO_2. Apesar desse método apresentar evidentes vantagens (como baixo custo e baixa toxicididade do catalisador), a fotocatálise heterogênea não é seletiva na degradação de contaminante (SHARABI & PAZ, 2009; SHAHAM-WALDMANN & PAZ, 2013). Esse aspecto é uma desvantagem à medida que correntes de misturas de efluentes podem conter contaminates perigosos juntos com outros de baixa toxicidade. Em muitos casos, o primeiro está presente em menores concentrações, e o segundo é majoritário (SHARABI & PAZ, 2009; SHAHAM-WALDMANN & PAZ, 2013). Nesses casos, é desejada a degradação preferencial do material mais tóxico (PAZ, 2006).

Uma das alternativas possíveis para contornar a baixa seletividade na fotocatálise é através do uso de suportes. São duas as principais vantagens dessa abordagem: (i) imobilização e dispersão de partículas de TiO_2 no adsorvente e (ii) indução de efeito sinérgico do mecanismo da fotocatálise com a adsorção da molécula orgânica obtida pelo potencial adsorvente (WANG *et al*., 2014). Nesse contexto, alguns estudos têm explorado a técnica de impressão molecuar combinada com a fotocatálise heterogênea.

A impressão molecular pode ser definida como um método de indução de reconhecimento molecular. Este pode ser realizado em uma matriz orgânica ou inorgânica, na presença de uma molécula molde durante a formação tridimensional da matriz (BELTRAN *et al*., 2010). Para o caso de uma matriz inorgânica, a impressão molecular, portanto, pode ser útil como uma rota para preparação de um material, geralmente uma rede de sílica, sintetizada através do método sol-gel, para adsorção de fármacos e/ou corantes. Essa técnica, combinada com a fotocatálise heterogênea, pode visar uma molécula alvo uma vez que esta pode ser adsorvida em domínios inorgânicos localizados nas vizinhanças de sítios ativos seguido por difusão e consequente degradação. Dessa

forma, espera-se encontrar soluções para pelo menos duas desvantagens dos fotocatalisaodres à base de TiO_2: i) a dificuldade de separar o efluente das partículas do fotocatalisador e ii) a baixa seletividade.

A impressão molecular em matriz inorgânica tem recebido atenção devido a algumas vantagens em relação à matriz polimérica, como maior resistência à oxidação e ao envelhecimento (LOFGREEN & OZIN, 2013). Nesse sentido, materais dotados de impressão molecular à base de sílica-gel têm recebido destaque nos últimos anos (LOFGREEN & OZIN, 2013). Por outro lado, recentes trabalhos (LU *et al.*, 2014; LU *et al.*, 2016) têm mostrado que a impressão molecular orgânica é promissora com relação ao aumento de seletividade, sendo a sua vantagem, a versatilidade de uso de *templates* (MAYES & WHITCOMBE, 2005).

Sendo assim, o escopo desse trabalho reside na exploração do conceito de impressão molecular para delineamento de fotocatalisadores seletivos.

2. REVISÃO BIBLIOGRÁFICA E OBJETIVO DA TESE

2.1 **Processos Avançados de Oxidação**

Nas últimas décadas, o crescimento das atividades industriais decorrente do aumento populacional tem causado o agravamento de problemas ambientais, sobretudo com respeito à preservação das águas superficiais e subterrâneas. Em virtude disso, a legislação e a fiscalização têm se tornado cada vez mais restritivas. Assim, tem crescido a preocupação mundial com a qualidade da água, tanto para o reuso industrial, como para o uso residencial (RANADE & BHANDARI, 2014).

Os micropoluentes mais comuns presentes nas águas são majoritariamente de origem antropogênica. Dentre eles destacam-se os produtos farmacêuticos e de cuidado pessoal, os esteróides, os surfactantes, os agrotóxicos e os corantes (LUO *et al.*, 2014). Alguns desses compostos não são regulamentados, ou são candidatos para futuras regulamentações, que dependem de futuros estudos sobre a sua toxicidade. Para esse caso, tem-se utilizado o termo de contaminantes emergentes (GAFFNNEY *et al.*, 2014). Vale salientar que esse termo também pode se referir a compostos recentemente introduzidos no ambiente (como medicamentos recentemente aprovados para o uso doméstico) ou a compostos presentes há algum tempo, mas que só recentemente têm sido detectados (GAFFNNEY *et al.*, 2014). Os contaminates emergentes estão comumente presentes em concentração em nível de traços, na faixa de ngL^{-1} a μgL^{-1}. A baixa concentração e a diversidade desses poluentes geram desafios em desenvolver novos processos de tratamento (LUO *et al.*, 2014).

Compostos de desregulação endócrina (como fármacos e agrotóxicos) estão entre os contaminantes emergentes de maior preocupação, já que são capazes de mimetizar ou bloquear o

sistema hormonal endógeno dos animais. O efeito a longo prazo destes contaminates ainda é desconhecido (MURRAY & ORMECI, 2012). Por outro lado, segundo a literatura, há suspeitas de risco para a saúde humana incluindo desordens reprodutivas, imunológicas e hormonais (YANG *et al*., 2006). Embora haja alguma controvérsia sobre os efeitos nos humanos, o mesmo não acontece acerca do impacto no ecossistema aquático. Nestes ambientes, os organismos estão constantemente sendo expostos a águas contaminadas. As evidências têm mostrado alguns efeitos da presença dos compostos de desregulação endócrina em ambientes aquáticos, como o aumento na proporção de fêmeas relativa aos machos, redução na taxa de produção de espermas e óvulos e diminuição da reprodutividade (YANG *et al.*, 2015; KABIR *et al.*, 2015). Comumente, o tratamento de compostos de águas residuais e/ou de afluentes líquidos industriais divide-se em quatro tipos, a saber: primário, secundário, terciário e avançado. A **Tabela 2.1** apresenta resumidamente esses tipos de tratamentos, bem como o uso sugerido após o processo.

O tratamento primário, baseado, sobretudo em sedimentação, deve ser evitado, porque seus custos excedem os benefícios (LUO *et al.*, 2014). O tratamento secundário garante a remoção significativa de compostos orgânicos, sólidos suspensos e patógenos. Entretanto, esse processo não é indicado para obtenção de água potável, ficando limitado para aplicações como irrigação agrícola, refrigeração e outras aplicações industriais. Além disso, alguns nutrientes como nitrogênio e fósforo, que podem causar a eutrofização, não são adequadamente removidos através do tratamento secundário. Nesse caso, o tratamento terciário pode ser adequado e, dependendo da contaminação, também pode produzir água potável. Entretanto, o critério de potabilidade da água necessita maior atenção.

Tabela 2.1: Tipos de tratamentos de águas residuais e usos sugeridos (Adaptado de US EPA, 2012).

Tratamento	Primário	Secundário	Terciário	Avançado
Tipo de processo	Sedimentação	Oxidação biológica	Coagulação química, remoção biológica de nutrientes químicos, filtração e desinfecção	Adsorção por carvão ativado, osmose inversa, oxidação avançada
Uso sugerido	Não é recomendado.	Irrigação de aplicação limitada; reuso de água para aquífero de água não-potável; processos industriais.	Irrigação; lavagem de veículos; recreação; processos industriais; água potável (dependendo da contaminação).	Água potável, irrigação, reservatório de água para consumo.

Em casos de contaminantes em baixas concentrações, especialmente fármacos, tem-se a preocupação que a longo prazo esses se acumulem no ambiente. Nesse caso, o tratamento terciário pode ser ineficiente. Assim, é necessária a aplicação de tratamentos avançados (GAFFNEY *et al.*, 2014). Dentre os mais comuns estão os processos envolvendo adsorção por carvão ativado, a osmose reversa e os processos avançados de oxidação.

Não são apenas os fármacos que resistem ao tratamento terciário. Outros poluentes, tais como corantes e resíduos industriais aquosos diversos, são de difícil biodegradabilidade, ou seja, apresentam características de compostos recalcitrantes. Esse termo refere-se a qualquer tipo de poluente resistente à degradação microbiológica no solo e na água (POURAN *et al.*, 2014).

Águas contaminadas contendo poluentes emergentes em geral têm uma demanda química de oxigênio (DQO) e baixa demanda biológica de oxigênio (DBO). Essas moléculas, normalmente não-biodegradáveis, entram no ambiente principalmente via atividade industrial (POURAN *et al.*,

2014). Além disso, em geral, os tratamentos convencionais (sobretudo o terciário) conseguem eficientemente a transferência de fase do contaminante, ou seja, da fase líquida para uma fase sólida (adsorvente, ou membrana); contudo, não garantem a completa degradação dos mesmos (NITOI *et al.*, 2013). Para garantir a remoção efetiva dos efluentes recalcitrantes faz-se necessária sua mineralização, isso é, precisa-se converter a molécula para o seu maior estado de oxidação possível, ou seja, convertè-la em água, dióxido de carbono, em ânions inorgânicos oxidados ou em qualquer outra molécula que torne viável a remoção por processos biológicos. Dessa forma, os PAOs são reconhecidamente métodos de degradação de poluentes devido a sua habilidade de remoção de uma ampla variedade de contaminantes orgânicos (LUO *et al.* 2014; NITOI *et al.*, 2013; POURAN *et al.*, 2014). Uma das definições mais usadas para os PAOs foi fornecida por GLAZE e colaboradores (1987), segundo a qual trata-se de processos que envolvem a geração de radicais hidroxilas em quantidades suficientes para a purificação da água, normalmente realizads em condições próximas de temperatura e pressão ambiente.

Os PAOs são divididos em sistemas homogêneos e heterogêneos. A **Tabela 2.2** apresenta os principais sistemas de PAOs. Nos sistemas homogêneos (ausentes de catalisadores sólidos), a degradação do contaminante é efetuada por dois mecanismos: (i) a fotólise direta com ultravioleta (UV); e (ii) a geração de radical hidroxila, sendo que esta pode ocorrer devido à presença de oxidantes fortes, como o ozônio (O_3) e o peróxido de hidrogênio (H_2O_2), combinados ou não com irradiação. Os radicais hidroxilia também podem ser gerados através de radiólise, oxidação eletroquímica, feixe de elétrons, ultrassom (US) e plasma (TEIXEIRA & JARDIM, 2004).

Tabela 2.2: Principais sistemas de PAOs (Adaptado de MACHADO, 2011).

Sistema	Característica
Homogêneo	**Com irradiação**
	Fotólise por UV
	UV/Vácuo
	O_3/UV (ozonação fotocatalítica)
	H_2O_2/UV
	Feixe de elétrons
	Ultrassom
	H_2O_2/Ultrassom
	UV/Ultrassom
	H_2O_2/Fe^{+2} (Fe^{+3})/UV (foto-Fenton)
	Sem irradiação
	O_3/H_2O_2
	O_3/HO^-
	H_2O_2/Fe^{+2} (reagente Fenton)
	H_2O_2/Fe^{+3} (tipo Fenton)
Heterogêneo	**Com irradiação**
	Semicondutor/O_2/UV (fotocatálise heterogênea)
	Semicondutor/H_2O_2/UV
	Foto-elétron-Fentom
	Sem irradiação:
	Eletro-Fenton

De maneira geral, a fotólise direta apresenta uma eficiência baixa, enquanto que a combinação do peróxido de hidrogênio com radiação ultravioleta (H_2O_2/UV) é um processo muito eficiente. Nesse último, o H_2O_2 em solução pode reagir tanto diretamente com os contaminantes como indiretamente, pois quando exposto à luz, H_2O_2 se decompõe formando radicais hidroxila. O processo Fenton é relativamente simples e, especialmente se combinada com radiação UV, apresenta uma elevada eficiência de degradação, o que o torna uma escolha razoável para a mineralização de compostos recalcitrantes (TEIXEIRA & JARDIM, 2004; POURAN *et al.*, 2014).

As aplicações dos PAOs diferem-se da osmose inversa e do uso do carvão ativado porque os poluentes presentes na matriz aquosa são degradados e não concentrados em uma fase diferente. Além disso, os compostos presentes em quantidades traços e que não são adsorvíveis, ou parcialmente adsorvíveis, podem ser alvo de degradação pelo radical hidroxila. Outra vantagem dos PAOs é que operam a temperatura e pressões ambientais. De modo geral, os custos de geração do radical hidroxila podem ser uma desvantagem quanto a escolha dos PAOs. Outras desvantagens são a necessidade de reatores especiais para a iluminação com UV (ozônio/UV), a necessidade de remover o ozônio da saída de gases (ozônio/UV/H_2O_2), a potetencialidade de deterioração da lâmpada UV (peróxido de hidrogênio/luz UV, fotocatálise) e a necessidade de controle de pH (peróxido de hidrogênio/ozônio, reações de Fenton) (METCALF & EDDY, 2016).

Dentre os sistemas heterogêneos destaca-se a fotocatálise. Esse processo é caracterizado pela presença de um catalisador semicondutor que é ativado pela radiação. Neste processo, os semicondutores atuam como aceleradores da reação de fotodegração, sem que haja alteração química dos mesmos (IBHADON & FITZPATRICK, 2013).

A fotocatálise baseia-se na separação de cargas elétricas em materiais semicondutores, a partir da excitação luminosa, o que possibilita reações químicas de oxidação e redução. O fenômeno da excitação eletrônica é possível em semicondutores porque estes materiais possuem uma energia intermediária separando suas bandas eletrônicas, a banda de valência (BV) e banda de condução (BC). Esta propriedade permite que elétrons sejam promovidos a níveis de energia superiores quando o material é submetido a alguma fonte energética suficiente para tal. Em materiais condutores, os elétrons podem se movimentar livremente entre BV e BC e, em isolantes, o acesso de elétrons a BC é bastante restrito.

A fotocatálise ocorre da seguinte forma: se a energia luminosa que incide sobre um semicondutor for igual ou maior que a energia de sua banda proibida (3,0 – 3,2 eV para o TiO_2), os elétrons podem ser excitados da banda de valência para banda de condução (e^-_{BC}), formando vacâncias na banda de valência (h^+_{BV}). Estes pares elétron-vacância, desde que não se recombinem, podem participar de subsequentes reações de oxidação e redução com espécies que se encontrem adsorvidas na superfície do semicondutor, causando a degradação (cisão/oxidação) dos compostos orgânicos presentes no meio reacional (CHATTERJEE & DASGUPTA, 2005; PARK *et al.*, 2013).

O **Esquema 2.1** ilustra as etapas que envolvem a reação fotocatalítica. Primeiramente, a absorção de fótons na superfície (trajeto 1) promove a geração do elétron na BC e vacâncias na BV (trajeto 2) na escala de fentomssegundo, podendo ocorrer a recombinação (trajeto 3) em uma escala de 10-100 ns. Imediatamente, os elétrons fotogerados são capturados por aceptores eletrofílicos (trajeto 4), podendo ser o oxigênio dissolvido, com consequente formação de peróxido de hidrogênio (trajeto 5) e radicais hidroxila (trajeto 6). A água adsorvida reage com a vacância de carga positiva, gerando os radicais hidroxila (trajeto 7), principal agente responsável pela oxidação nos PAOs. A oxidação através desses radicais é chamada de fotocatálise indireta. Alternativamente, o reagente (molécula a ser degradada) pode atuar como doador de elétrons (trajeto 7) e portanto sofrer oxidação diretamente na superfície do catalisador (vacância positiva), processo esse chamado de fotocatálise direta (KISCH & MITORAJ, 2012).

Embora possa haver formação de radicais hidroxilas tanto pela presença do oxigênio dissolvido (trajeto 4-6), como pela oxidação da água adsorvida (trajeto 7), evidências experimentais recentes (KONDRAKOV *et al.*, 2016) têm mostrado que a produção majoritária (95%) desses radicais decorrem devido ao papel deste último fenômeno.

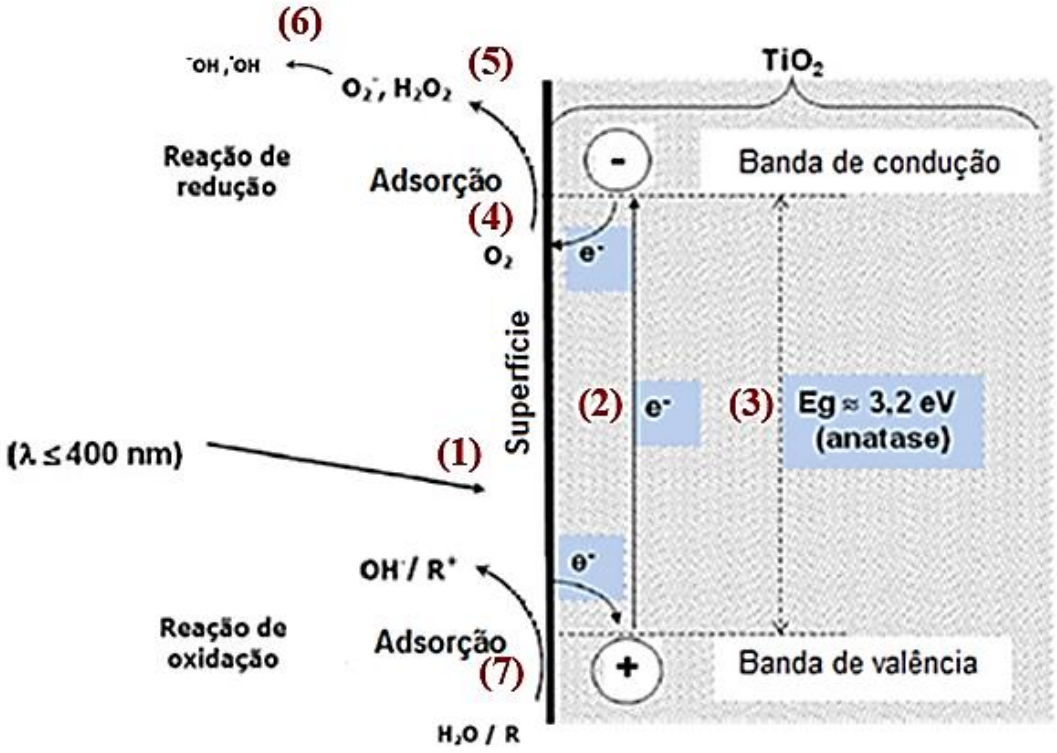

Esquema 2.1: Mecanismo simplificado da fotocatálise (Adaptado de HERRMANN, 2012).

A transferência de elétrons e lacunas ocorre numa taxa mais lenta, sendo aproximadamente 0,33 ms na presença de O_2 como receptor de elétrons (COWAN *et al.*, 2010). Em outras palavras, uma transferência de carga lenta limita a taxa de reação global da reação fotocatalítica. Nesse sentido, modificações na supefície do fotocatalisador podem afetar positivamente a transferência de carga, seja pela introdução de sensitizadores de luz visível ou pela introdução de reservatórios adicionais de cargas (PARK *et al.*, 2013).

Na fotocatálise indireta, a vacância é aprisionada por moléculas de água, levando à formação de radicais $^{\bullet}OH$ e H^+, e os elétrons facilitam a formação de H_2O_2, os quais se decompõem em mais radicais OH através da reação com oxigênio do meio reacional. Assim, os radicais gerados durante o mecanismo são os responsáveis pela oxidação das moléculas orgânicas, que podem ser completamente mineralizadas ou decompostas em produtos intermediários.

No caso da fotocatálise direta, dois mecanismos distintos são propostos na literatura: o de Langmuir-Hinshelwood e o de Eley-Rideal (SERPONE & EMELINE, 2002; MACHADO, 2011). No primeiro caso, a vacância aprisiona uma molécula adsorvida no catalisador formando um radical no estado excitado, e esse pode sofrer neutralização devido à recombinação com um elétron advindo da BV ou sofrer uma reação na qual ocorra um decaimento para produtos mais simples. No segundo tipo de mecanismo, a vacância é aprisionada por defeitos da superfície do catalisador produzindo centros ativos na superfície, e esses reagem com a molécula orgânica (quimissorção) que se decompõem gerando os produtos de fotorreação.

Os catalisadores empregados em fotocatálise, em sua maioria, são semicondutores como o TiO_2, ZnO, CdS, ZnS, CeO_2, WO_3, SnO_2, GaP, Fe_2O_3, entre outros (NOGUEIRA & JARDIM, 1998; GOGATE & PANDIT, 2004). Segundo a literatura (IBHADON & FITZPATRICK, 2013), o dióxido de titânio (TiO_2) é um dos semicondutores mais usados em estudos fotocatalíticos. As vantages ao uso do TiO_2 são seu custo baixo, elevada estabilidade e baixa toxicidade (SHARABI & PAZ, 2010). Por outro lado, o óxido de zinco (ZnO) tem sido apontado como boa alternativa ao dióxido de titânio por apresentar fotoatividade e características semelhantes ao TiO_2.

Apesar das evidentes vantagens do TiO_2, o seu uso como fotocatalisador apresenta sérias dificuldades - algumas delas que o impedem de encontrar aplicação em escalas industriais, a saber: (i) aglomeração das partículas; (ii) dificuldade operacional e/ou elevado custo para separar o efluente das partículas do fotocatalisador; (iii) cinética extensivamente dependente de coeficientes de adsorção, e portanto dificultando a degradação de moléculas na superfície polar do TiO_2 (a maioria dos contaminates emergentes possuem baixa polaridade) e (iv) baixa seletividade de degradação para contaminantes perigosos (PAZ, 2006; SHARABI & PAZ, 2010; CHEN *et al.*, 2011; IBHADON & FITZPATRICK, 2013).

Uma das alternativas possíveis para superar algumas dessas limitações é através do uso de suportes. São duas as principais vantagens dessa abordagem: (i) imobilização e dispersão de partículas de TiO_2 no adsorvente e (ii) indução de efeito sinérgico do mecanismo da fotocatálise com a adsorção da molécula orgânica obtida pelo potencial adsorvente (WANG *et al.*, 2014). Nesse sentido, diversos materiais têm sido explorados como uso de suporte em reações de fotocatálise. A título de ilustração, a **Tabela 2.3** apresenta alguns trabalhos dos últimos anos referentes a essa abordagem.

Tabela 2.3: Exemplos de trabalhos recentes de fotocatalisadores com TiO_2 suportados.

Fonte TiO_2	**TiO_2 em relação ao suporte (% mássica)**	**Suporte**	**Molécula**	**Referência**
Degussa P25	0 a 16	Carvão ativado	Difenil carbazida	ZHANG *et al*, 2012
Degussa P25	1 a 15	Zeólita 5A e 13X	Oxitetraciclina	ZHAO *et al*., 2012
Isopropóxido de titânio	10	Argila (montmorilonita)	Azul de metileno	CHEN *et al.*, 2012
Tetracloreto de titânio	20	Sílica amorfa	Rodamina B	SUN *et al*., 2013
Degussa P25	20 a 80	Alumina	Rodamina B	WANG *et al.*, 2014
Isopropóxido de titânio	10 a 15	Argila (diatomita)	Rodamina B	WANG *et al.*, 2014
Tetracloreto de titânio	25 a 60	Argila (diatomita)	Rodamina B	SUN *et al*., 2014
Etóxido de titânio	25	Argila (bentonita)	Azul de metileno e Remazol	SAHEL *et al*., 2014
Degussa P25	20 a 50	Grafeno	Pentaclorofenol	ZHANG *et al*., 2014
Tetrabutóxido de titânio	10 a 15	Sílica aerogel	Rodamina B	LI *et al.*, 2016
Tetracloreto de titânio	n.d.	Resíduos agroindustriais (casca de arroz, casca de acácia e pó de tabaco)	Rodamina B	SILVA, Da *et al*.., 2016

n.d.: não definido.

Conforme pode ser visto na **Tabela 2.3**, os materiais explorados são os mais diversos, entre eles: carvão ativado, vidro poroso, minerais (como diatomito), alumina, argilas (como diatomita, bentomita, montmorilonita), grafeno, zeólita e sílica (amorfa e aerogel). Nota-se, também, que a fonte de TiO_2 é diversa, contemplando TiO_2 comercial (Degussa P25), oxisulfato de titânio, alcóxidos de titânio e tetracloreto de titânio. A porcentagem mássica de TiO_2 em relação ao suporte varia amplamente, porém tipicamente os estudos relatam valores entre 10 a 50 %.

Considerando que uma das etapas do mecanismo da fotocatálise heterogênea é a adsorção de reagentes na superfície do catalisador (HERRMANN, 2010), trabalhos recentes têm explorado a possibilidade de combinar materiais adsorventes em conjunto com fotocatalisadores (LAZAR & DAOUD, 2013). Dessa forma, espera-se encontrar soluções para pelo menos duas desvantagens dos fotocatalisaodres à base de TiO_2: i) a dificuldade de separar o efluente das partículas do fotocatalisador e ii) a baixa seletividade.

2.2 Estrutura e propriedades do TiO_2

O dióxido de titânio (TiO_2) existe em três diferentes formas: anatase (tetragonal), rutila (tetragonal) e broquita (romboédrica) - embora a rutila seja a forma mais estável, a forma anatase é considerada mais ativa, visto que apresenta uma taxa de formação de HO• maior do que as demais formas (PALAEZ *et al*., 2012). Além disso, a rutila e o bronquito possuem mais dificuldade de absorver o oxigênio, promovendo uma elevada taxa de recombinação dos elétrons com a vacância. A **Figura 2.1** apresenta as estruturas das três geometrias cristalinas do TiO_2.

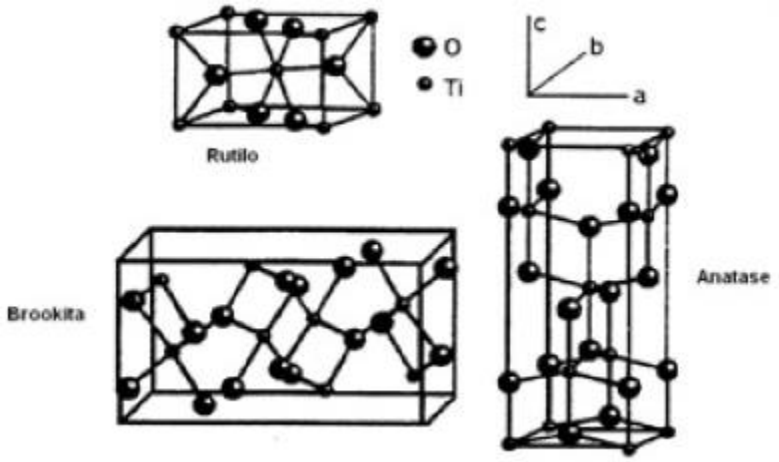

Figura 2.1: Geometrias cristalinas do TiO_2 (Reproduzido de FELTRIN *et al.* 2013).

As três formas podem ser facilmente sintetizadas em laboratório e tipicamente as formas metaestáveis da anatase e broquito são transformadas para a fase rutila que é termodinamicamente estável sob condições de temperatura próximas a 500°C. Nas três formas, os átomos de titânio (Ti^{+4}) estão coordeados com seis átomos de oxigênio (O^{-2}), formando um octaedro de TiO_6 (PALAEZ *et al.*, 2012). O TiO_2 é considerado um semicondutor do tipo n devido a sua deficiência de oxigênio. A **Tabela 2.4** resume algumas das principais propriedades da anatase e rutila (CARP *et al.*, 2004; PALAEZ *et al.*, 2012). Conforme pode ser visto, a absorção da luz para a fase rutila ocorre em valores de comprimento de onda maiores do que a anatase. Como consequência, o valor de *band gap* da anatase é tipicamente superior (3,2 eV) àquele encontrado para a rutila (3,0 eV).

Tabela 2.4: Principais propriedades da anatase e rutila.

Propriedade	Anatase	Rutila
Peso molecular (g/mol)	79,88	78,88
Ponto de fusão (°C)	1825	1825
Absorção de luz (nm)	< 390	< 415
Índice de refração	2,55	2,75
Constante dielétrica	31	114
Estrutura cristalina	Tetragonal	Tetragonal
Comprimento da célula unitária (Å)	a= 3,78; c= 9,52	a= 4,59; c= 2,96
Densidade (g/cm^3)	3,79	4,13
Comprimento da ligação Ti-O (Å)	1,94	1,98

2.3 Dopagem de fotocatalisadores

A dopagem consiste em dissolver quantidades moderadas de um elemento heterovalente em locais da rede de Ti^{4+} para aplicar uma valência induzida. É comum a distinção entre dopagem intersticial e substitucional. Na primeira, os átomos ocupam um sítio na estrutura cristalina em que geralmente não há um átomo, ou dois ou mais átomos compartilhando um ou mais locais de rede em uma configuração em que o número de átomos é maior que o número de locais de rede. No caso da dopagem substitucional, os átomos de diferentes componentes ocupam sítios equivalentes.

O efeito dos dopantes envolve a soma de três fatores (DA SILVA, 2012): (i) a alteração na capacidade de absorver luz solar (indução de absorção da região do espectro visível), (ii) a alteração da superfície do material fotocatalítico com as moléculas do meio (aumentar a adsorção de moléculas poluentes pela superfície) e (iii) alteração na taxa de transferência de carga interfacial.

Os principais métodos de introdução de dopantes descritos na literatura são por impregnação, coprecipitação e via pocesso sol-gel. O estreitamento de *band gap* pode ser

alcançado utilizando-se espécies metálicas e não metálicas. A **Figura 2.2** ilustra estes dois tipos de dopagem em comparação com o TiO_2 não dopado. No caso deste último, o *band gap* é equivalente a $h\upsilon_1$.

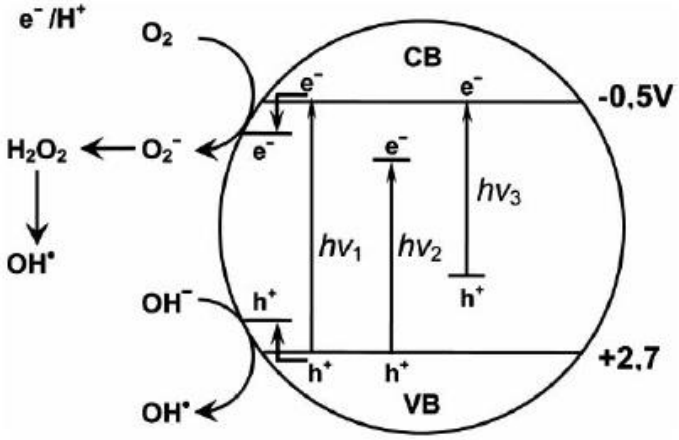

Figura 2.2: Tipos de dopagem no TiO_2. $h\upsilon_1$, $h\upsilon_2$ e $h\upsilon_3$ referem-se ao TiO_2 puro, dopado com metal e dopado com não-metal, respectivamente. (Fonte: ZALESKA, 2008).

A fotoatividade na região visível do material dopado com metal pode ser explicada pela existência de um novo nível de energia produzido no *band gap* do TiO_2 causado pela dispersão de nanopartículas metálicas na matriz do fotocatalisador. Este novo nível de energia, também conhecido como estado de impureza, pode aceitar elétrons da banda de valência ($h\upsilon_2$) ou doar elétrons para a banda de condução ($h\upsilon_3$). Devido a menor energia de separação entre o nível de energia criado pela impureza e a banda de valência ou de condução, a luz visível torna-se energeticamente suficiente para facilitar as transições de elétrons acima mencionadas. No caso da dopagem de metais ($h\upsilon_2$), outra vantagem ocorre devido à melhora de captura de elétrons para

inibir recombinação elétron-lacuna durante a irradiação. Em consequência disso, a fotoatividade pode ser aumentada (ZALESKA, 2008).

A dopagem realizada com não-metais ($h\upsilon_3$) resulta de pelo menos três fenômenos não necessariamente excludentes (ZALESKA, 2008): (i) estreitamento do *band-gap* em virtude do estado híbrido formado em conjunto com o dopante, (ii) formação de impurezas acima da banda de valência e (iii) regiões de vacâncias de átomos de oxigênio formadas pelo dopante que impedem a reoxidação. Por exemplo, a dopagem com nitrogênio têm mostrado que os estados de impureza destes materiais estão perto do limite da banda de valência e os centros de recombinação podem ser minimizados.

2.4 Dopagem com cobre

Conforme já discutido, uma das desvantagens do uso do TiO_2 é sua baixa eficiência na região do espectro visível. Uma maneira promissora de sanar esta desvantagem é combinar o alargado *band-gap* do TiO_2 com outro semicondutor possuindo um *band gap* mais estreito de forma que apresente uma BC menos anódica do que o TiO_2 (ZHANG *et al.*, 2009). Nesse sentido, o uso do óxido cuproso (Cu_2O) tem sido explorado na literatura.

O óxido cuproso é um semicondutor do tipo-p com um *band gap* estreito (1,9-2,17 eV). Tem sido mostrado que a formação de uma junção p-n combinada com o TiO_2 (tipo n) melhora a eficiência deste (LI *et al.* , 2011; WANG *et al.*, 2012; ZHANG *et al.*, 2013). No caso de irradiação com luz visível, os elétrons fotogerados a partir da banda de condução do Cu_2O são transferidos para a banda de condução do TiO_2, enquanto vacâncias permanecem na banda de valência do Cu_2O (ZHANG *et al.*, 2009).

Tabela 2.5: Recentes trabalhos explorando heteroestruturas de Cu_2O/TiO_2.

Material	Fonte de Cobre/método de preparação do compósito de TiO_2 dopado	Molécula de teste	Tipo de teste (UV ou Visível)	% mássica (Cu_2O ou Cu) em relação ao TiO_2	Referência
Heteroestrutura Cu_2O/TiO_2	$Cu_2(OAc)_4(H_2O)_2$/ Co-precipitação	Alaranjado II	UV e Visível	2-70 de Cu_2O	HUANG *et al.*, 2009
Dopagem de TiO_2 preparado por método sol-gel	$Cu(NO_3)_2$/Dissolução em solução de isopropóxido de tiânio	Fenol	UV	0,5 de Cu	COLÓN *et al.*, 2006
Compósito com polímero inorgânico (aluminosisilicato)	$Cu_2(OAc)_4(H_2O)_2$/ Co-precipitação	Azul de metileno	UV	50 de Cu_2O	FALAH *et al.*, 2015
Heterojunção *core-shell*	CuCl/Química *soft*	4-nitrofenol	Visível	n.d.	CHU *et al.*, 2011
Heteroestrutura Cu_2O/TiO_2	Cu_2SO_4/Precipitação química sem uso de surfactante	Alaranjado de metila	Visível	2-70 de Cu_2O	ZHANG *et al*, 2013
Compósito suportado em sílica mesoporosa (SBA-15)	$Cu_2(OAc)_4$/Dissolução em solução de isopropóxido de titânio	Paraquat (Herbicida)	UV e Visível	2 de Cu	SOROLLA *et al.*, 2012
Heteroestrutura Cu_2O/TiO_2	$Cu(NO_3)_2.3H_2O$/ Dissolução em butóxido de titânio IV	Azul de metileno e Alaranjado de metila	Visível	0,3 de Cu	KERKEZ-KUYUMCU *et al.*, 2015

A **Tabela 2.5** apresenta alguns recentes trabalhos explorando heteroestruturas de Cu_2O/TiO_2.De maneira geral, nota-se que os métodos envolvendo precipitação e dissolução (em soluções de alcoóxidos) de percursores de cobre estão entre os mais empregados. A investigação da eficiência fotocatalítica tem sido feita tanto na região do UV, como na região do visível. Por exemplo, o estudo realizado por HUANG e colaboradores (2009) mostrou que a heteroestrutura investigada - preparada via precipitação química em solução alcoólica -, apresentou melhor eficiência, em comparação ao TiO_2, nos dois tipos de espectros de luz. Do ponto de vista qualitativo, resultados semelhantes foram encontrados por SOROLLA e colaboradores (2012).

Outra tendência observada na **Tabela 2.5** é que a porcentagem mássica (Cu_2O em relação ao TiO_2) estudada varia amplamente: entre 2 a 70%. Entretanto, o estudo de HUANG e colaboradores (2009) mostrou que, no espectro de luz UV, os melhores resultados de degradação foram alcançados com o material contendo 30% de Cu_2O, enquanto que no espectro da luz visível o material com 70% de Cu_2O apresentou a melhor eficiência fotocatalítica. Além disso, o material puro de Cu_2O apresentou piores resultados nas duas regiões do espectro. Segundo os autores, esses resultados sugerem que a heteroestrutura formada por Cu_2O/TiO_2 restringe a recombinação do par-elétron lacuna, com consequente melhora na eficiência na degradação. Em recente estudo (KERKEZ-KUYUMCU *et al.*, 2015), foi realizada uma comparação entre diferentes dopantes metálicos, tais como o Cu, Ni, Co, Fe, Mn e Cr. Os autores alegam que dentre os catalisadores estudados o material Cu/TiO_2 exibiu a maior eficiência fotocatalítica sob radiação visível para a degradação de corantes.

Embora o dopante desloque a banda de absorção, e portanto torne o fotocatalisador mais eficiente na região do espectro visível, o processo de dopagem não supera a dificiência em termos de seletividade. Nesse sentido, a combinação com a técnica de impressão molecular pode auxiliar a sanar essa dificuldade.

2.5 Impressão molecular

A impressão molecular (IM) pode ser definida como um método de indução de propriedades de reconhecimento molecular, em uma matriz polimérica, devido à presença de um *template* (molécula molde) durante a formação da estrutura tridimensional do polímero. As posições dos monômeros são fixadas numa posição que é “congelada” por copolimerização com agente de reticulação (*cross-linker*), que também tem a função de garantir estabilidade mecânica,

sendo que um dos mais utilizados é dimetacrilato de etilenoglicol (BELTRAN *et al.*, 2010). A geração de uma cavidade específica ocorre após a remoção da molécula *template* do interior do polímero (CHEONG *et al.*, 2013). Assim, a geração de IM pode ser entendida como uma ligação preferencial da molécula a um receptor, esse possuindo elevada seletividade em relação a análogos estruturais (DÍAZ-GARCIA & LAÍÑO, 2005). O princípio geral da IM é mostrado no **Esquema 2.2**.

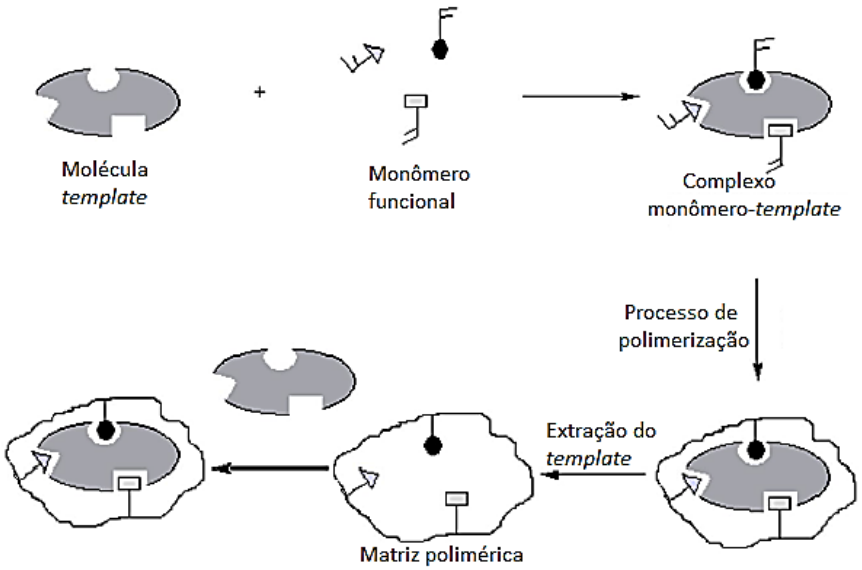

Esquema 2.2: Princípio geral da Impressão Molecular (Adaptado de VASOPOLLO *et al.*, 2011).

Inicialmente, os monômeros funcionais são ligados ao *template*. Esse processo pode ocorrer através da formação de ligações covalentes entre os monômeros e o *template* (impressão covalente) ou por interações não-covalente (impressão não-covalente). A seguir, ocorre a polimerização das moléculas monoméricas, formando a matriz polimérica com o *template*, que é, então, revomido por um processo de extração líquida, tratamento químico ou térmico. O material resultante é um polímero poroso constituído de sítios de impressão com forma e tamanho da molécula molde. Esses sítios estão disponíveis para interação ou ligação com as moléculas

idênticas ao do *template* ou estruturalmente análogas, presentes em uma solução (DÍAZ-GARCIA & LAÍÑO, 2005).

A tecnologia baseada em impressão molecular oferece um método simultâneo de pré-concentração e extração. Esta é uma vantagem sobre as tecnologias inespecíficas como o carvão ativado, já que nestes pode haver uma uma remoção elevada de contaminantes não-traços – assim exaurindo os sítios ativos de adsorção e podendo comprometer a eficácia de remoção de um poluente alvo encontrado em baixa concentração (MURRAY & OMERCI, 2012).

As limitações e desvantagens da IM em polímeros orgânicos incluem a produção de sítios não-específicos, interações fracas entre o *template* e as unidades funcionais do polímero, heterogeneidade de sítios receptores, grupos funcionais distantes dos sítios de impressão e a lixiviação do *template* (MAYES & WHITCOMBE, 2005). Além disso, moléculas que são solúveis somente em matrizes aquosas são incapazes de impressão molecular em polímeros orgânicos (MAYES & WHITCOMBE, 2005; MORAIS, 2011). Sendo assim, o desenvolvimento de novos materiais com impressão molecular que possam ser utilizados para aplicações de adsorção em sistemas aquosos, e também passíveis de aplicação nas áreas de química biológica e ambiental, têm sido incentivados na comunidade científica (MAYES & WHITCOMBE, 2005; LOFGREEN & OZIN, 2014).

A impressão molecular em matriz inorgânica tem recebido atenção devido a algumas vantagens em relação à matriz polimérica, como maior resistência à oxidação e envelhecimento (LOFGREEN & OZIN, 2013). Nesse contexto, os materiais híbridos inorgânico-orgânicos dotados de impressão molecular, preparados através do método sol-gel, têm recebido crescente atenção (WALCARIUS & COLLINSON, 2009; LOFGREEN & OZIN, 2014; CONCU *et al.*, 2015; LEVI, 2015).

2.6 Fotocatálise Seletiva com Materiais Dotados com Impressão Molecular

A fotocatálise seletiva pode ser dividida em duas categorias, (i) formação seletiva: quando é desejado um produto específico, preferecialmente obtido com elevado rendimento a partir do(s) reagente(s) e (ii) degradação seletiva: quando um ou mais componentes devem ser mineralizados preferencialmente em detrimento de outros (LAZAR & DAOUD, 2013). Segundo PAZ (2006), outra possível categoria é a transformação química de compostos inorgânicos de elevada toxicidade em outros menos perigosos ou a separação seletiva de diversos íons contaminantes (p. ex., Cr(VI) do Hg(II) -- ambos possuem potential redox similares). O **Esquema 2.3** ilustra os principais tipos de seletividade encontrados na literatura.

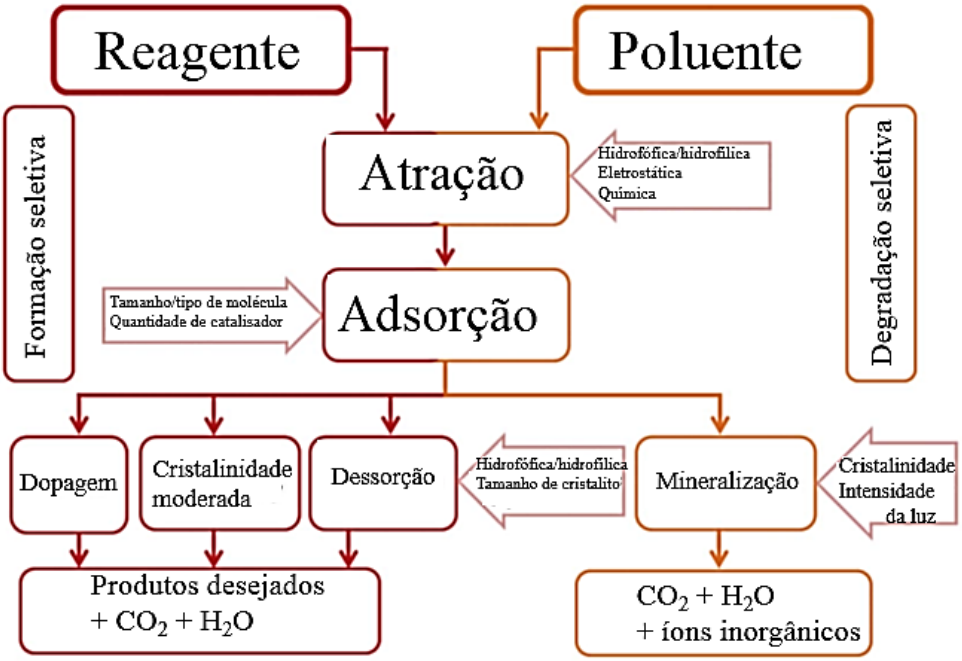

Esquema 2.3: Formação e degradação seletiva (Fonte: LAZAR & DAOUD, 2013).

As principais abordagens de estudo de fotocatálise seletiva envolvem alterações nos parâmetros de processo (temperatura, tempo de residência, pH, presença de íons, tipo de solvente

e concentração do catalisador) e parâmetros do fotocatalisador (fontes distintas de TiO_2, dopagem, revestimento, adsorção em domínios orgânicos e inorgânicos inertes localizados nas vizinhanças de sítios ativos seguido por difusão) (PAZ, 2006).

Os estudos de fotocatálise seletiva podem envolver apenas um componente ou vários componentes (mistura). No primeiro caso, os testes são realizados invidualmente para cada molécula (seletividade), e no segundo, há uma mistura de dois ou mais compontes (competitividade). A maioria dos estudos tem focado nos testes envolvendo seletividade, e apenas nos últimos anos têm sido dada mais atenção aos testes de competitividade (PAZ, 2006; LAZAR & DAOUD, 2013). Segundo PAZ (2006), os testes de seletividade (um componente de cada vez) - que simula uma condição limitada -, ainda é valiosa, sobretudo do ponto de vista qualitativo dos novos materiais desenvolvidos. Embora os testes de competitividade possam ser entendidos como preditivos, os valores de taxa de degradação, obtidos através dos testes seletividade, não devem variar amplamente na presença de outros contaminantes para o caso das moléculas que adsorvem fortemente no adsorbato.

A título de ilustração, a **Tabela 2.6** resume alguns dos principais trabalhos encontrados na literatura referentes à fotocatálise seletiva baseada em impressão molecular. Por exemplo, estruturas do tipo *core-shell* foram investigadas (XIAO *et al.***,** 2015). Neste estudo, a impressão molecular foi feita na superfície de quitosana (*core*) e portanto favorecendo o enriquecimento molecular ao passo que o fotocalisador (shell) induziu a degradação. Importante ressaltar que a maioria dos trabalhos tem explorado a degradação seletiva de contaminantes baseado em materiais com impressão molecular em polímeros orgânicos. Embora esse tipo de abordagem tenha apresentado seletividade relativa nos testes de fotodegradação, o potencial de seletividade desses

materiais pode apresentar queda de eficiência seletiva ao longo da reação devido ao contato com a radiação UV que pode comprometer a estrutura do material (DENG *et al.*, 2014).

Tabela 2.6: Principais trabalhos encontrados na literatura referentes à fotocatálise seletiva combinada com impressão molecular.

Material	Fonte TiO_2	Tipo de teste	Molécula *template*	Molécula competidora	Referência
Fotocatalisador baseado em xerogel de $Ti(OH)_4$ dopado com íons Co^{+2}	TTBT	Seletividade	Ciprofloxacina	Tetraciclina	LU *et al.*, 2015
Impressão molecular via compósito de quitonasa-TiO_2 em estrutura *core-shell*	Degussa-P25	Competitividade	Alaranjado de metila	Amarelo crepúsculo, Rodamina B	XIAO *et al*, 2015
Impressão molecular polimérica assistida por microondas (Metil metacrilato como monômero)	TTBT	Competitividade	Enrofloxacina	Tetraciclina	LU et al., 2014
Fotocatalisador com propriedades magnéticas (TiO_2/Fe_3O_4/nanotubo de carbono)	TTBT	Seletividade	Metil-imidazol	Florfenicol	LUO *et al.*, 2014
Impressão molecular à base de sílica (TEOS como precursor)	TTBT	Seletividade Competitividade	4-Nitrofenol	2-Nitrofenol	DENG *et al.*, 2014
TiO_2/Impressão polimérica orgânica (oFEN como monômero)	Degussa P25	Seletividade Competitividade	4-Nitrofenol	2-Nitrofenol	SHEN *et al.*, 2014
Fotocatalisador dopado com enxofre em rede polimérica orgânica	$TiCl_4$	Nenhum	Ácido salicílico	Nenhum	WANG *et al.*, 2014
Fotocatalisador dopado com cloro em rede polimérica orgânica (pFEN como monômero)	Degussa P25	Seletividade	Ciprofloxacina	Tetraciclina	LIU *et al.*, 2014
TiO_2/Impresão polimérica orgânica (oFEN como monômero)	Degussa P25	Seletividade Competitividade	2,4-Dinitrofenol	Fenol 4-Clorofenol	HUANG *et al.*, 2013

Continuação da **Tabela 2.6**

Compósito orgânico (oFEN como monômero) com co-produto da combustão de carvão	TTBT	Competitividade	Tetraciclina	Oxytetraciclina Ciprofloxacina	LU *et al.*, 2013
Membrana à base de alginato de cálcio	Degussa P25	Competitividade	Alaranjado de metila	Vermelho de metila	ZHAO *et al.*, 2014
Filme	NH_4TiF_6	Nenhum	Tetraciclina	Nenhum	WANG *et al.*, 2012
Membrana à base de alginato de cálcio	Degussa P25	Competitividade	Alaranjado de metila	Vermelho de metila	ZHAO *et al.*, 2014
Filme	NH_4TiF_6	Nenhum	Tetraciclina	Nenhum	WANG *et al.*, 2012

pFEN: *p*-Fenilenodiamina; oFEN: *o*-Fenilenodiamina; TTBT: Tetrabutilortotitanato; Nenhum: Significa que apenas a molécula *template* foi avaliada.

Algumas dessas abordagens requerem mais de uma etapa de síntese, em que geralmente é preparado o fotocatalisador e posteriormente é feito o processo de IM (LIU *et al.*, 2014; WANG *et al.*, 2014). Materiais dotados de IM à base de filmes também têm sido estudados (WANG *et al.*, 2012), e ainda são poucos os estudos que investigam a potencialidade de IM à base de sílica.

Considerando esta bibliografia recente, a impressão molecular a partir do método sol-gel é uma rota de síntese promissora e ainda pouco explorada no contexto da fotocatálise.

2.7 Impressão Molecular a partir do Processo Sol-Gel

O processo sol-gel consiste em qualquer rota de síntese de materiais na qual, a um determinado momento, ocorre a transição de um sistema sol para um sistema gel. Sol é definido como partículas de 1 a 1000 nm dispersas de uma suspensão de partículas coloidais estáveis em um fluido, enquanto que um sistema gel pode ser entendido como um sistema formado pela estrutura rígida de partículas coloidais ou de cadeiais poliméricas (BRINKER & SCHERER, 1990). A reação de polimerização sol-gel pode ser dividida em duas etapas: i) a hidrólise do grupo alcóxido levando à formação de grupos reativos do tipo silanol e ii) a condensação do grupo silanol, levando, posteriormente, à formação do gel. O **Esquema 2.4** ilustra essas etapas de reação.

Hidrólise:

$$Si(OR)_4 + nH_2O \leftrightarrows Si(OR)_{4-n}(OH)_n + nROH$$

Condensação:

$$\equiv Si{-}OH + HO{-}Si\equiv \leftrightarrows \equiv Si{-}O{-}Si\equiv + H_2O$$

$$\equiv Si{-}OR + HO{-}Si\equiv \leftrightarrows \equiv Si{-}O{-}Si\equiv + ROH$$

Esquema 2.4: Reações de hidrólise e condensação envolvidas na síntese de sílicas pelo método sol-gel (adaptado de BRINKER & SCHERER, 1990).

No caso do **Esquema 2.4**, R é um grupo alquil. Os percursores inicialmente formam a solução coloidal (sol) e em seguida a rede amorfa de sílica (gel). As reações sol-gel podem ser conduzidas com catalisadores ácidos ou com catalisadores básicos. O processo sol-gel pode ser conduzido a temperaturas baixas, geralmente entre 0 e 100 °C, e em condições químicas brandas,

ou seja, o pH e a quantidade de água são facilmente ajustáveis (LOFGREEN & OZIN, 2014). O **Esquema 2.5** representa o mecanismo geral da reação sol-gel catalisada em meio ácido e básico.

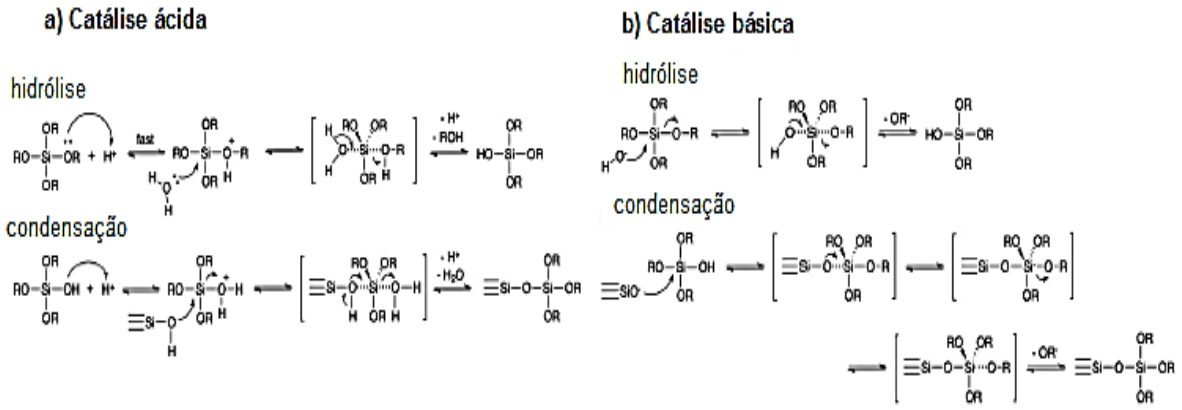

Esquema 2.5: Mecanismo geral da (a) catálise ácida e (b) catálise básica (Adaptado de LOFGREEN & OZIN, 2014).

Nas reações de hidrólise, ocorre a substituição do grupo alcóxido (OR) do alcoxisilano, pelo grupo OH da molécula de água formando o grupo silanol (Si-OH) e um álcool. Nas reações de condensação, ocorre o ataque nucleofílico do grupo silanol do alcoxisilano hidrolisado ao átomo de silício do alcoxisilano, liberando álcool, ou o ataque nucleofílico do grupo silanol ao átomo de Si de outro grupo silanol, liberando água. Essas reações podem acontecer simultaneamente durante todo o processo de formação do sol, do gel e mesmo durante o envelhecimento da sílica.

Existe uma ampla variedade de precursores de sílica no mercado. Dentre os mais comuns destacam-se o metiltrimetoxisilano (MTES), aminopropiletoxisilano (APTES), tetrametoxisilano (TMOS) e tetraetoxisilano (TEOS). Assim, dependendo do objetivo da aplicação ou do tipo de interação nos materiais com impressão molecular (covalente ou não-covalente), diferentes precursores podem ser utilizados (LOFGREEN & OZIN, 2014).

Outra possibilidade de síntese de sílica pelo método sol-gel é através da rota não-hidrolítica. Nessa rota, é utilizado um precursor cloreto e ocorre a eliminação de um haleto alquílico. A condensação ocorre entre o alcóxido e o cloreto metálico, formando uma rede de óxido. A reação envolve a clivagem nucleofílica de ligações O-R. No caso de metais de transição, a condensação ocorre na faixa entre 80 a 100 °C. Entretanto, deve-se levar em consideração que o silício é menos reativo - assim, são necessários catalisadores à base de ácidos de Lewis, como cloretos de ferro ou alumínio, para catalisar a reação (BOURGET *et al.*, 1998). O mecanismo proposto para essa rota é apresentado no **Esquema 2.6**.

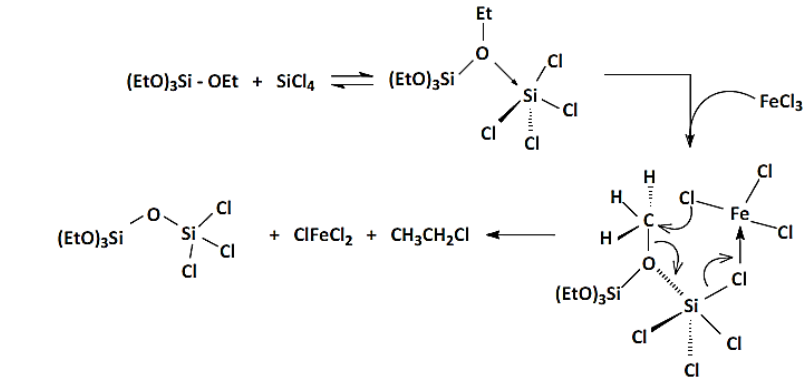

Esquema 2.6: Mecanismo proposto para a rota não-hidrolítica (Adaptado de BOURGET *et al.*, 1998).

Vários fatores influenciam a estrutura dos materiais obtidos pelo método sol-gel, a saber: a razão molar grupo alcóxido/água, o tipo de precursor, a taxa relativa entre as reações de hidrólise e condensação, o tipo de catalisador, o tipo de solvente, a temperatura e as concentrações dos componentes em misturas de precursores. O **Esquema 2.7** ilustra o desenvolvimento estrutural de uma sílica-gel em função das condições do meio.

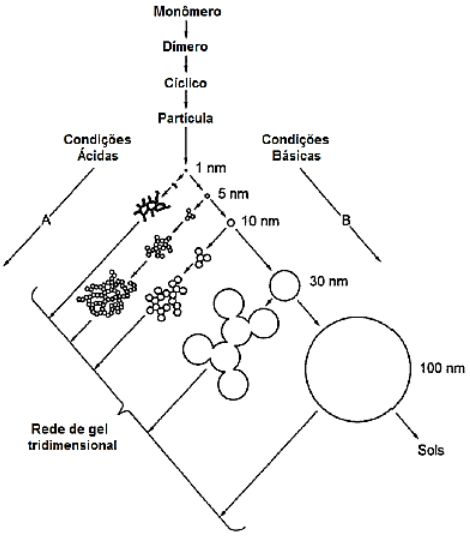

Esquema 2.7: Desenvolvimento estrutural de uma sílica-gel em função das condições do meio (Adaptado de SCHUBERT & HÜSING, 2005).

Conforme observado no **Esquema 2.7**, o pH do meio é um parâmetro decisivo para as taxas relativas de hidrólise e condensação dos tetraalcoxisilanos. Em condições ácidas (pH < 5,0), a hidrólise é favorecida e a condensação é a etapa limitante, ou seja, há a formação de um grande número de monômeros ou pequenos oligômeros com grupos Si-OH reativos. Por outro lado, em condições básicas (pH > 5,0), a hidrólise é a etapa limitante, de forma que as espécies hidrolisadas são imediatamente consumidas em virtude da condensação ocorrer rapidamente. Esse fenômeno pode levar à precipitação das partículas ao invés da gelificação (SCHUBERT & HÜSING, 2005).

Há diversas razões para optar pela síntese de impressão molecular baseada em sílicas obtidas por sol-gel. Sílicas exibem inchamento mínimo na presença de solventes e mostram excelente estabilidade térmica. Esses atributos facilitam a manutenção da forma e tamanho das cavidades formadas (LOFGREEN & OZIN, 2014). Também são notavelmente compatíveis com

sistemas aquosos e biológicos, sendo possível encapsular com sucesso enzimas e anticorpos sem prejudicar sua atividade (DOODY *et al.*, 2000; AVNIR, 1995).

Em geral, o material obtido por processo sol-gel é estável em contato com ácidos e bases fortes e oxidantes (COLLINSON, 2010). Essa característica torna a sílica aplicável a uma variedade de finalidades e adaptável a diversos ambientes químicos. A estrutura rígida, altamente reticulada, da estrutura da sílica xerogel permite a criação de cavidades com maior flexibilidade e com potencial para um elevado grau de seletividade em relação aos polímeros orgânicos (LOFGREEN & OZIN, 2014). Comparando com esses últimos, a sílica é mais resistente à oxidação e ao envelhecimento, o que é geralmente um dos maiores desafios dos materiais de impressão molecular baseados em polímeros orgânicos. Além disso, a fidelidade ao *template* é provavelmente uma contribuição importante para o sucesso de sílica como fonte de cavidades de impressão molecular. Durante a fase sol, é possível controlar com maior precisão a forma com que a cavidade será formada (LOFGREEN & OZIN, 2014).

Apesar das vantagens, alguns desafios podem dificultar a aplicação dessas sílicas. Embora o processo sol-gel possa oferecer materiais altamente porosos, a porosidade obtida é normalmente desordenada e, portanto, a difusão das moléculas pode ser dificultada. Em comparação aos polímeros orgânicos, a distância entre as reticulações presentes nas sílicas são muito menores, fazendo com que o inchamento na sílica seja quase desprezível na maior parte dos casos. Isso significa que é necessário atentar para o fato da necessidade de exercer um controle sobre a difusão nesses materiais. Isto pode ser feito através da incorporação de agentes porogênicos para controlar a porosidade (LOFGREEN & OZIN, 2014).

2.8 Impressão Molecular em Matriz Orgânica

No caso de uma matriz orgânica, a impressão molecular polimérica (IMP) é obtida por uma combinação de interações covalentes e não-covalentes entre uma molécula de impressão desejada e o(s) monômero(s) funcional(ais) complementar(es). Dependendo do tipo de interação, diferentes métodos são empregados (**Esquema 2.8**). Na primeira etapa, o complexo monômero-funcional (CMF) dotado de impressão molecular é formado através das interações adequadas, dependendo do método escolhido. Um monômero de reticulação (*cross-linker*) compatível é então utilizado para formar a matriz do polímero. Dependendo do método de impressão, a formação do complexo ocorre antes da adição de agente de ligação cruzada ou *in situ* durante a polimerização da matriz. A remoção da molécula *template* se dá através da ruptura da interação entre o monômero funcional e a molécula-alvo, formando dessa forma uma cavidade de impressão de forma e tamanho definido Esta cavidade tem os grupos funcionais orgânicos residuais do(s) monômero(s) funcional(ais) ligado(s) numa configuração precisa, a qual pode, então, interagir preferencialmente com uma molécula-alvo de um tamanho, forma ou estrutura química adequada. A seguir, serão discutidos os tipos mais importantes de impressão molecular polimérica, a saber: não-covalente, covalente, semi-covalente e eletrostática.

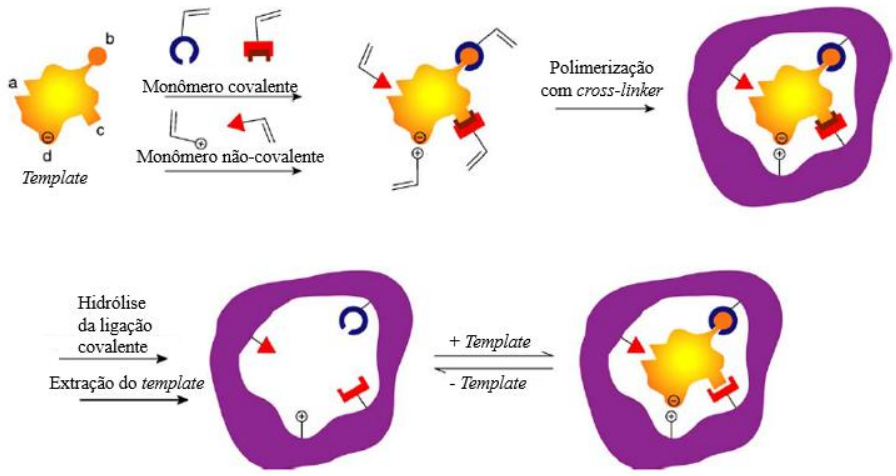

Esquema 2.8: Principais tipos de impressão molecular polimérica orgânica: (a) não-covalente; (b) covalente; (c) semi-covalente; (d) eletrostática. (Adaptado de MAYES & WHITCOMBE, 2005).

2.8.1 Impressão Não-Covalente

Este tipo de impressão pode ser realizado através de interações iônicas ou não-iônicas (interação (a) no **Esquema 2.8**). Comumente, a interação dominante é por ponte de hidrogênio, ocorrendo, por exemplo, entre o ácido metacrílico e aminas primárias em solventes não-polares (RAMSTROM *et al.*, 1994). A principal vantagem desse método é a ausência de barreiras cinéticas para a formação do CMF; ao invés disso, o fator limitante é a difusão, a qual pode ser facilmente mitigada pela escolha dos parâmetros reacionais do sistema. Entretanto, essas interações fracas requerem o uso de um excesso de monômero funcional devido ao fato que o sistema não favorece a formação do CMF. No caso do uso de solventes polares, as interações iônicas (como a formação de pares iônicos) são suficientemente fortes para garantirem a formação estequiométrica do CMF

(TOMINAGA *et al.*, 2009). Dessa forma, as ocorrências de regiões de ligações não-específicas são reduzidas no material dotado de IMP.

Embora simples, a impressão não-covalente é sensível a interferências que prejudiquem as interações que mantém conservada o CMF (por exemplo, a presença de água), sendo assim um método pouco robusto. Adicionalmente, caso um excesso de monômero funcional estiver presente, a existência de regiões de ligações não específicas pode comprometer a seletividade do material. O material final pode ser tratado após a polimerização com a finalidade de reduzir esse problema (McNIVEN *et al.*, 1997), mas isso deve ser feito com precaução e controle, uma vez que as cavidades de interesse podem sofrer danos (LOFGREEN & OZIN, 2014).

2.8.2 Impressão Covalente

O uso de ligações covalentes reversíveis tem a vantagem de garantir elevada especificidade para uma molécula alvo (interação (b) no **Esquema 2.8**). Usualmente, reações de condensações são empregadas, como a formação de éster boronato (WULFF, 1977), acetais (SHEA & DOUGHERTY, 1986) e bases de Schiff (WULFF, 1984). A impressão covalente, sendo estequiométrica, garante que a formação de monômeros funcionais exista somente nas cavidades de impressão, portanto reduzindo as interações não-específicas. Por outro lado, tanto a necessidade de uma síntese distinta para a geração do CMF, tanto quanto a necessidade de quebra da ligação para remover a molécula *template* incrementam a complexidade deste método. Além disso, a barreira cinética da ligação covalente pode resultar em ligações lentas com a molécula-alvo. Outra

desvantagem do método é sua limitada oferta de monômeros funcionais, o que torna sua aplicação menos versátil (ALEXANDER, 2006).

2.8.3 Impressão Semi-Covalente

Nessa estratégia, ligações covalentes são usadas para a formação do CMF durante a polimerização, enquanto que interações não-covalentes são usadas para a religação com a molécula-alvo (interação (c) no **Esquema 2.8**). Esta abordagem tem como objetivo combinar a durabilidade dos sítios de impressão do método covalente com a rápida adsorção obtida pelo método não-covalente. Apesar da adição de etapas, a religação da molécula-alvo ocorre rapidamente via interações não-covalentes. Sendo assim, este método combina a precisão advinda da impressão covalente com a velocidade da interação com a molécula-alvo.

2.8.4 Impressão Eletrostática

Íons metálicos (interação (d) no **Esquema 2.8**) podem participar na impressão de duas maneiras: (i) fazendo parte do complexo que é covalentemente ligado a uma cavidade e participando no reconhecimento através de uma ligante metálico via interações (no qual o alvo é o ligante para o íon metálico em questão) ou (ii) podem atuar como impressores verdadeiros quando o objetivo é a adsorção seletiva do íon metálico. Esse método permite uma variedade de escolhas de metais e seus ligantes, o que garante fácil aplicação para necessidades específicas. Um dos critérios é que a troca entre o ligante marcador (não mostrado) e a molécula de impressão

(futuramente a molécula-alvo) ocorra em condições compatíveis com o sistema em questão (FUJII *et al.*, 1985). Alternativamente, um íon metálico pode atuar como a espécie de impressão para criar uma cavidade que deverá interagir com um metal-alvo apropriado. O tipo de seletividade que é possível obter nesse tipo de impressão é governada menos pelo tamanho da cavidade criada e mais pela (parcial) carga existente na cavidade bem como a força de interação entre os íons metálicos alvo e os ligantes em sua cavidade (BURLEIGH *et al.*, 2001).

Embora cada um dos métodos anteriormente discutidos possa ser utilizado sozinhos, combinações de diferentes tipos são úteis. Por exemplo, uma combinação de íons com interações de hidrogênio pode melhorar a eficácia global de um sistema dotado de impressão não-covalente (ALIZADEH, 2008). A escolha da combinação depende da molécula-alvo, da matriz, das condições de síntese e da aplicação pretendida para a IMP.

Os tipos de impressão molecular são categorizados de acordo com a interação funcional presentes entre o monômero e a molécula-alvo. Contudo, a escolha do agente de ligação-cruzada, o método de polimerização, a adição de porogênicos e solvente(s) também influenciam o desempenho dos materiais. Explorar as interações de ligação não-específica entre moléculas-alvo e a matriz, por exemplo, pode servir para melhorar a retenção do alvo. Por outro lado, estas interações podem ter consequências prejudiciais no que diz respeito sobre a seletividade do sistema. Este tipo de otimização requer levar em conta uma grande variedade de fatores que vão muito além do tipo de impressão selecionado.

2.8.5 Impressão Não-Covalente

Conforme já discutido anteriormente, a característica principal desta abordagem se dá pelas interações não-covalentes entre o monômero funcional e a molécula *template*. Independentemente do método empregado, o protocolo de síntese requer a escolha de um monômero funcional, um iniciador, um agente de ligante transversal (*cross-linker*) e o *template* desejado. A remoção do *template* pode ser feita por diferentes formas, sendo a mais usual uma lavagem repetitiva com uma mistura de ácido acético e metanol. A **Figura 2.3** ilustra algumas das moléculas tipicamente usadas como monômeros, ligantes transversais e iniciadores.

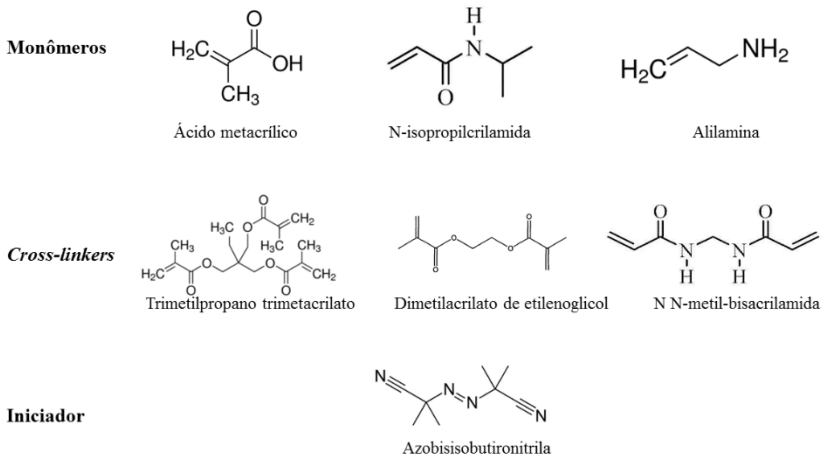

Figura 2.3: Moléculas tipicamente usadas como monômeros, ligantes transversais e iniciadores.

Os métodos de impressão molecular não-covalente podem ser divididos em três tipos: precipitação, *core-shell* e radicalar controlada/viva.

2.8.5.1 Polimerização por Precipitação

Um dos métodos mais convencionais de produção de IMP é por polimerização *bulk*. O material resultante é macerado e peneirado para futuras aplicações. Embora simples e barato, o método normalmente produz partículas de forma e tamanho irregulares. Além disso, o processo de moagem pode eventualmente destruir os sítios de reconhecimento, reduzindo assim a capacidade de religação (POMA *et al.*, 2010). Para determinadas aplicações, sobretudo as analíticas, é necessário um controle maior da geometria e tamanho das partículas. Nesse sentido, a polimerização por precipitação tem a vantagem de ser capaz de produzir partículas esféricas muitas vezes na faixa de tamanho de nanômetros (YE *et al.*, 1999; YE *et al.*, 2000).

Na polimerização por precipitação, a mistura de monômeros é a mesma utilizada na polimerização *bulk*, com exceção que se faz uso de um excesso de solvente. Dessa forma, a cadeia polimérica cresce continuamente até que sofra precipitação no momento em que o tamanho do polímero torna-se grande o suficiente e não é mais capaz de manter-se solúvel no solvente. Não é necessário o uso de reagentes como surfactantes ou estabilizadores, o que garante ao método mais flexibilidade na escolha de *templates*.

Uma desvantagem desse método é a necessidade da molécula *template* possuir elevada solubilidade na mistura monomérica, caso contrário, poderá ser perdida no solvente da reação. Dessa forma, o solvente tem um papel importante na produção da IMP no sentido de estabilizar todos os reagentes em uma fase de polimerização para a criação de poros. Em outras palavras, o solvente - atuando como agente porogênico -, governa a força das interações não covalentes bem como influencia na morfologia do polímero. De maneira geral, quanto mais polar for o solvente, pior será o efeito de reconhecimento molecular. Segundo a literatura (SELLERGREN, 2001;

RAMSTRÖM, 1996), os melhores solventes são aqueles que atenuam os efeitos da polaridade do solvente. Sendo assim, são mais adequados solventes menos polares (com pequenos valores de constante dielétrica (ε), tais como o tolueno (ε = 2,4) e o diclorometano (ε = 8,9). O uso de solventes mais polares, como a água (ε = 80), inevitavelmente enfraquece as forças de interações entre a molécula-alvo e o monômero funcional, resultando em baixa capacidade de reconhecimento molecular. Por outro lado, a influência do solvente na estrutura do polímero pode ser compensada pelo aumento da área específica e do diâmetro de poro. Assim, a acetonitrila (ε = 36) - relativamente mais polar que o tolueno e o diclorometano - conduz a polímeros mais macroporosos do que solventes menos polares como o clorofórmio (ε = 5). Importante ressaltar que uma menor área específica e uma menor macroporosidade podem levar à diminuição da propriedade de reconhecimento molecular, devido à baixa acessibilidade de moléculas aos sítios específicos de adsorção.

Nos testes de reconhecimento molecular, preocupações similares ocorrem. Geralmente, solventes não polares resultam em melhores desempenhos de reconhecimento. Quando aplicado a solventes gradualmente mais polares, a habilidade de reconhecimento dos polímeros é diminuída. A morfologia também pode ser afetada, uma vez que o efeito de inchaço é mais pronunciado em solventes clorados, como o clorofórmio e o diclorometano. Eventualmente, esse efeito pode induzir a mudanças na configuração tridimensional resultante dos poros gerados, e assim prejudicrm a capacidade de religação de moléculas-alvo. Como regra geral, a escolha do melhor solvente para os testes de reconhecimento molecular deve ser o mais semelhante possível daquele usado na preparação do polímero. Dessa forma, efeitos de inchaço são minimizados. Entretanto, mostrou-se que para o caso do uso de água, o efeito do comprometimento no reconhecimento

molecular não será necessariamente pior do que o uso de outros solventes orgânicos como a acetonitrila (BJÖRJE, 2001; RAMSTRÖM, 1996).

2.8.5.2 Partículas com Estrutura *Core-Shell*

Uma possível rota para obter este tipo de estrutura é fazendo uso de polimerização em emulsão com sementes. Primeiramente, partículas que compõe o cerne (*core*) são sintetizadas. Essas servem como sementes, que podem ser constituídas de estireno ou metacrilato como monômeros. As partículas dessas sementes são normalmente monodispersas podendo variar de alguns nm a vários μm de diâmetro. Em uma segunda etapa, essas partículas são misturadas com outro conjunto de monômeros para que a polimerização ao redor do *core* possa ocorrer. Seguindo este protocolo, é possível obter partículas com tamanhos e formas controladas. Recentes estudos usando esta metodologia podem ser encontrados na literatura (HAJIZADEH *et al.*, 2013; KAMRA *et al.*, 2015; KAMRA *et al.*, 2015).

2.8.5.3 Polimerização Radicalar Controlada/Viva

A polimerização por radical livre é um dos métodos mais comuns na IMP. A reação pode ser conduzida sob condições suaves de temperatura e pressão, além de ser tolerante a diferentes grupos funcionais. Estas razões fazem com que este método seja um dos mais convenientes na síntese de IMP. A polimerização radicalar pode ser iniciada por calor, foto-irradiação, ou reações redox, e consiste em três estágios: (i) iniciação, (ii) propagação e (iii) terminação. Tipicamente,

em todas as polimerizações radicalares, o estágio (ii) (crescimento de cadeia) é muito mais rápido do que o estágio (i). Isso resulta em um crescimento da cadeia polimérica com um elevado peso molecular em um curto espaço de tempo. Como consequência, nesta abordagem é difícil controlar o tamanho e a arquitetura do polímero resultante (ZETTERLUND *et al.*, 2008).

Com o objetivo de superar estas limitações, e obter estruturas bem definidas, tem emergido nos últimos anos a abordagem da polimerização radicalar controlada/viva (PRC). A PRC combina a rápida etapa de iniciação radicalar com a lenta, mas simultânea, propagação de cadeia, resultando em um material com estrutura mais organizada e uma distribuição de peso molecular menor. O que garante o controle dessas reações é o fato de exibirem características de uma polimerização viva, ou seja, as reações de terminação e outras reações secundárias, que ocasionam a morte da espécie propagadora, são mantidas em níveis reduzidos. O termo "vivo" é usado para descrever mecanismos em que cadeias poliméricas podem ter seu tamanho estendido quando mais monômero for adicionado ao meio reacional. Nessas reações, a etapa de terminação não é completamente suprimida e o centro ativo não é constituído por um íon, mas por um radical livre. Os métodos mais conhecidos de PRC são os de polimerização mediada por nitróxido (*Nitroxide Mediated Polymerization*, NMP), polimerização radicalar por transferência de átomos (*Atom Transfer Radical Polymerization*, ATRP) a transferência reversível de cadeia por adição-fragmentação (*Reversible Addition-Fragmentation Chain Transfer*, RAFT). O método RAFT tem sido um dos mais explorados na literatura (ZETTERLUND *et al.*, 2008; OLIVEIRA *et al.*, 2013). Em alguns casos, as reações PRC procedem normalmente conforme o protocolo de uma polimerização não-covalente. A diferença está na adição de outros reagentes. Por exemplo, no método RAFT é adicionado uma certa quantidade de agente RAFT (compostos químicos que possuam uma função tiocarbonila ligada a outros dois grupos distintos) a uma reação de

polimerização convencional. De maneira geral, os reagentes químicos (monômero, iniciador e solvente) e as condições operacionais do sistema (temperatura, pressão e pH) são idênticas àquelas usadas nas reações de polimerização não-covalente (OLIVEIRA *et al.*, 2013).

2.9 Problemática e Objetivos da Tese

Conforme discutido anteriormente, há dois mecanismos principais que ocorrem na fotocatálise heterogênea. A grande maioria da degradação de moléculas orgânicas acontece através do mecanismo envolvendo a fotocatálise indireta (MACHADO, 2011). Considerando que esse mecanismo é governado por radicais livres, é esperado que o processo fotocatalítico dificilmente não diferencie os contaminantes. Uma consequência disso é a baixa seletividade apresentada pelo processo fotocatalítico (SHARABI & PAZ, 2009; SHAHAM-WALDMANN & PAZ, 2013). De fato, há relatos em que - no caso de moléculas que apresentam adsorções comparáveis -, a taxa de degradação apresentou pouca diferença (MATTHEWS, 1986). À primeira vista, a ausência de seletividade pode ser entendida como vantajosa. Todavia, essa aparente abrangência pode ser prejudicial considerado-se o seguinte cenário: correntes de misturas de efluentes podem conter contaminates perigosos juntos com outros de baixa toxicidade, ou podem também estar em contato com outros compostos que possam funcionar como nutrientes no ecossistema, que acabam sendo também degradados. Em muitos casos, os contaminates mais perigosos estão presentes em menores concentrações, e os de menor toxicidade são majoritário (SHARABI & PAZ, 2009; SHAHAM-WALDMANN & PAZ, 2013). Nesses casos, é desejada a degradação preferencial do material mais tóxico (PAZ, 2006). Em outras palavras, baixa seletividade implica que o fotocatalisador não seja capaz de diferenciar adequadamente os contaminantes perigosos dos

contaminantes de baixa toxicidade. Essa deficiência é ainda agravada pelo fato de que, ao contrário dos contaminantes de baixa toxicidade, muitos dos compostos mais perigosos não são biodegradáveis (SHARABI & PAZ, 2009; SHAHAM-WALDMANN & PAZ, 2013).

Levando em conta o aspecto da baixa seletividade e a potencialidade do uso de impressão molecular para adsorção seletiva surgiram-nos alguns questionamentos: (i) será que a cavidade gerada pela impressão molecular de um dado fármaco e/ou corante promoveria um aumento na atividade fotocatalítica de sua decomposição? (ii) O conceito de impressão molecular no desenvolvimento de fotocatalisadores heterogêneos acarretaria uma seletividade na degradação? (iii) A rota sol-gel de síntese (rotas hidrolíticas geradas por catalisadores ácidos, por catalisadores básicos, rotas não-hidrolíticas, catalisadas por ácidos de Lewis) afetaria as propriedades texturais, estruturais e morfológicas desses catalisadores, que por sua vez acarretariam em atividades fotocatalíticas diferenciadas? (iv) É possível gerar espécies de titânia *in situ* nesses suportes com atividade comparável a de catalisadores comerciais (P25)? (v) É possível combinar a impressão molecular em matriz orgânica com o processo de fotocatálise, sob ação da luz ultravioleta, sem comprometimento da seletividade? É possível combinar fotocatalisadores dopados sem comprometer a seletividade? (vi) Os catalisadores gerados seriam suficientemente robustos a fim de garantir uma reutilização em vários ciclos?

Tendo em vista a problemática exposta acima, a presente tese tem a seguinte hipótese científica: a geração de fotocatalisadores heterogêneos, suportados em adsorventes à base de sílica-gel, ou à base de polímero orgânico, dotados de impressão molecular de uma dada molécula-alvo (corantes e fármacos), deve incrementar a selevidade catalítica na fotodegradação dessa molécula-alvo.

Sendo assim, o objetivo geral é investigar as potencialidades e limitações no desenvolvimento de fotocatalisadores heterogêneos dotados de impressão molecular na fotodecomposição seletiva de corantes e fármacos a partir de matrizes inorgânicas (sílica) e orgânica (a partir do monômero ácido metacrílico).

O projeto tem os seguintes objetivos específicos:

- Avaliar o efeito da rota de síntese sol-gel nas características texturais, estruturais e morfológicas dos materiais adsorventes e dos fotocatalisadores;

- Correlacionar a potencialidade dos materiais adsorventes na remoção seletiva de contaminantes com a natureza da rota de síntese;

- Avaliar o efeito da rota de síntese na seletividade dos fotocatalisadores na fotodegradação do composto-alvo em sistemas de teste de seletividade e competitividade;

- Estudar o desempenho de impressão molecular polimérica combinada com fotocatalisadores em presença;

- Avaliar a seletividade em materiais dopados com cobre;

- Avaliar a capacidade de reutilização permitida pelos fotocatalisadores sem perda da atividade fotocatalítica aceitável.

3. Metodologia Experimental

Neste capítulo, serão apresentados os materiais, bem como as metodologias e caracterizações usados no presente estudo.

3.1 Materiais

Salvo algumas exceções, os materiais foram utilizados na forma em que foram recebidos.

- Tetraetoxisilano (TEOS) (Sigma-Aldrich, 99%);

- NH_4OH (Sigma-Aldrich, 28% NH_3);

- HCl (Merck, 23%)

- $FeCl_3$ (Sigma-Aldrich, 97%)

- $SiCl_4$ (Sigma-Aldrich, 99%)

- $TiCl_4$ (Merck, 97%)

- Rodamina B (Vetec, ponto de fusão = 210°C)

- Rodamina 6G (Sigma-Aldrich)

- Azul de metileno (Vetec)

- Água purificada - destilada e deionizada

- Metanol (Nuclear)

- TiO_2 (P25, Degussa)

- Acetonitrila (Burdick & Jackson, 99%)

- Ácido metacrílico (Sigma-Aldrich, 99%)

- Trimetilpropano trimetacrilato (Sigma-Aldrich, 99%)

- Azobis*iso*butironitrila (Sigma-Aldrich, 99%)

- Ácido acético (Sigma-Aldrich, 99,7 %)

- Etanol (Sigma-Aldrich, 99,7 %)

- Atorvastatina (Lipton)

- Diclofenaco de sódio (Multilab)

- Iboprufeno (Multilab)

- Tioconazol (Multilab)

- Valsartana (Multilab)

- Cetoconazol (Multilab)

- Gentamicina (IQ Soluções & Química SA)

- Paracetamol (Multilab)

- Fluoxetina (Multilab)

- Acetato de cobre (II) hidratado (Janssen Chimica)

- Glicose (Merck)

3.2 Preparação de materiais com impressão molecular a partir da rota sol-gel

Cinco diferentes rotas foram empregadas para o preparo de amostras baseadas em sílica através do processo sol-gel utilizando TEOS como material de partida, a saber: rota hidrolítica Ácida 1 (A1), rota hidrolítica Ácida 2 (A2), rota hidrolítica Básica (B), rota hidrolítica *Two-Steps* (TS) e rota Não-Hidrolítica (NH). A rota A1 foi catalisada por 0,2 M de HCl mantendo a razão volumétrica de 1:2 (HCl:TEOS). A rota A2 foi procedida de maneira similar, porém as amostras foram preparadas sem adição de HCl (ou seja, tendo o $TiCl_4$ como potencial catalisador de ácido de Lewis). A rota B foi catalisada por 0,2 M de NH_4OH mantendo a razão volumétrica de 1:2 (NH_4OH:TEOS). A rota TS foi catalisada primeiramente por 0,2 M de HCl seguido da adição de NH_4OH após 30 min. e, em ambos os casos, a razão volumétrica utilizada foi a mesma das rotas supracitadas. Na rota NH foram utilizados TEOS e $SiCl_4$ catalisados por $FeCl_3$ (0,5% da massa do produto final). Para todas as rotas, a quantidade de corante Rodamina B (RhB) adicionada foi de 150 mg.

As amostras (em pó) obtidas através das rotas hidrolíticas foram preparadas como segue: primeiro, RhB foi adicionada em uma solução de TEOS, seguido de $TiCl_4$ e do catalisador (HCl ou NH_4OH), sendo que este último esteve ausente no caso da rota A2. A solução resultante foi mantida sob agitação em temperatura ambiente até o estágio da gelificação, que depende de cada rota. A rota NH foi sintetizada sob atmosfera inerte (Argônio). Inicialmente, foi adicionado RhB e o catalisador ($FeCl_3$), seguido por TEOS, $SiCl_4$, e $TiCl_4$. A solução final foi mantida sob agitação a 80°C até a gelificação.

Para a remoção da RhB, as sílicas foram submetidas a cinco diferentes métodos de extração, a saber: (i) Térmica, no qual o material foi introduzido em um tubo de quartzo, aquecido

isotermicamente a 190°C por cerca de 16 h (5°C/min); (ii) Soxhlet com solvente metanol por aproximadamente 24 h; (iii) Lavagem utilizando água deionizada; (iv) Ultrassom de ponteira (Branson-Sonifer ®, Model 250), em que a sílica foi suspensa em água, por aproximadamente 10 min, intercalados por intervalos de 20 s.; e (v) Ultrassom de ponteira, de maneira similar ao (iv), porém utilizando metanol como solvente.

As amostras resultantes foram nomeadas de acordo com a rota sol-gel empregada, considerando a presença ou ausência do corante (RhB) e $TiCl_4$ (Ti). Por exemplo, a rota não-hidrolítica (NH) com a presença de $TiCl_4$ e RhB encapsulada é representada pela nomenclatura NHTiRhB. No caso de amostras ausentes de RhB, convencionou-se usar a nomenclatura NHTi. As amostras extraídas receberam a letra E. Nesse caso, a nomenclatura é ENHTiRhB. Quando necessário, as amostras calcinadas serão indicadas pela letra C, referindo-se tanto para as amostras nas quais a RhB foi adicionada na síntese (CNHTiRhB) quanto às amostras com ausência de RhB $TiCl_4$ (CNHTi). O **Esquema 3.1** apresenta um fluxograma descrevendo as rotas utilizadas e a **Tabela 3.2** ilustra todas as possibilidades de sistemas para o caso da rota NH, bem como a especificação de aplicabilidade.

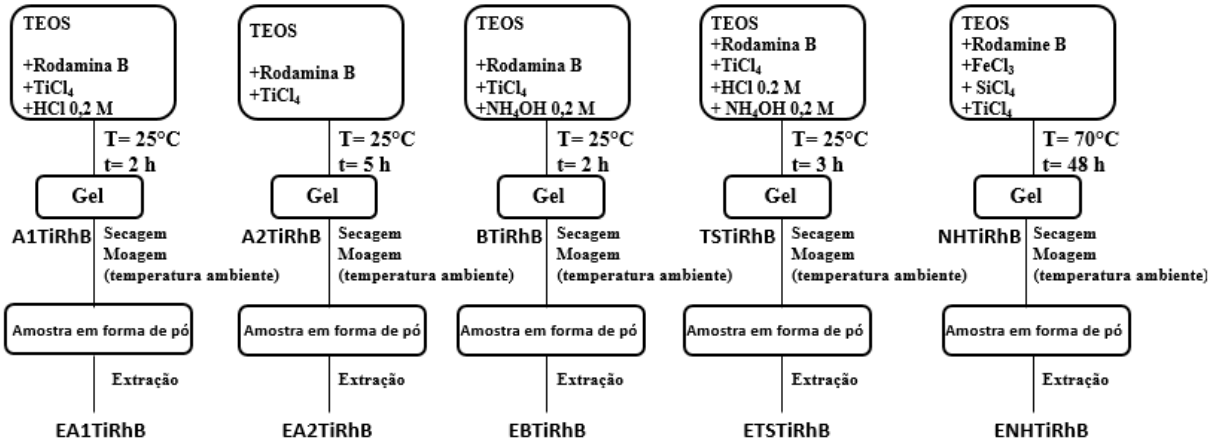

Esquema 3.1: Fluxograma descrevendo as rotas utilizadas via método sol-gel.

Tabela 3.1: Sistemas para preparados pela rota não-hidrolítica (método sol-gel).

Sigla	Descrição	Avaliação
NH	Sílica	Testes de adsorção ("branco")
NHTi	Adição de $TiCl_4$	n.d.[(1)]
NHTiRhB	Adição de $TiCl_4$ e RhB	n.d.[(1)]
ENHTiRhB	Adição de $TiCl_4$ e RhB, e posterior extração do corante	Testes de adsorção
CNHTi	Amostra com adição de $TiCl_4$ e posterior calcinação	Testes de fotocatálise ("branco")
CNHTiRhB	Amostra com adição de $TiCl_4$ e RhB e posterior calcinação (após extração)	Testes de fotocatálise

(1) Embora sem aplicação (testes de adsorção ou fotocatálise), esses sistemas servem como etapas intermediárias para a síntese das amostras extraídas e calcinadas ou para estudos de caracterização.

3.2.1 Preparação dos fotocatalisadores pelo método sol-gel

Os fotocatalisadores foram obtidos por um processo de calcinação do material com o corante extraído (p. ex., NHTiRhB) ou a partir do material no qual foi adicionado apenas $TiCl_4$ (por exemplo, NHTi). A calcinação ocorreu em um forno mufla a 450 °C por 4 h a uma taxa de 5°C/min. Em alguns casos, a calcinação ocorreu lentamente (com rampas de aquecimento e patamares), mantida a temperatura constante por 1 h a cada 100°C com uma taxa de aquecimento de 1°C/min.

3.3 Preparação de fotocatalisadores contendo impressão molecular a partir de precipitação por polimerização orgânica

Os materiais dotados de impressão molecular à base de polímero orgânico foram sintetizados via precipitação por polimerização. A **Tabela 3.3** apresenta as quantidades e a descrição de cada reagente necessário para a síntese.

Tabela 3.2: Materiais utilizados na síntese de polímeros orgânicos.

Reagente	Quantidade (mmol)	Descrição
Acetonitrila	765,0	Solvente
Ácido metacrílico (MAA)	1,31	Monômero funcional
Trimetilpropano trimetacrilato (TRIM)	2,20	Agente de ligação cruzada
Azobisisobutironitrila (AIBN)	0,17	Iniciador radicalar
Diclofenaco	0,40	Molécula *template*
P25	0,25	Fotocatalisador

Inicialmente, o monômero funcional, agente de ligação cruzada e a molécula *template* foram adicionados em um frasco (tubo horizontal de borosilicato) contendo o solvente. Em seguida, foi feita a adição do iniciador (em pó) e do fotocatalisador (P25). Para garantir uma boa homogeneização, a mistura foi mantida em um banho de ultrassom por cerca de 10 minutos. Na sequência, a mistura foi submetida a uma corrente de nitrogênio gasoso por cerca de 5 minutos. Após esse procedimento, o frasco foi selado e inserido em um forno com grades rotatórias (Greensboro, NC, USA) de maneira a manter a mistura sob agitação e temperatura constante de 60 °C por 24 h. Após a reação coletou-se o sólido formado por centrifugação (4.500 rpm, 15 min).

A remoção do *template* foi feita por ciclos de banhos de ultrassom com uma solução de metanol contento 10% de ácido acético (V/V) até que o *template* não fosse mais detectado (via espectroscopia UV) no líquido de lavagem (após centrifugação). Finalmente, o polímero foi lavado com metanol (para remoção de ácido acético remanescente) e seco em uma câmara de vácuo. Para fins comparativos, também foram sintetizados materias com ausência de *template* (sem impressão molecular), nos quais a síntese ocorreu de maneira similar ao descrito acima.

3.3.1 Preparação de fotocatalisadores dopados contendo impressão molecular a partir de precipitação por polimerização orgânica

Os fotocatalisadores dopados dotados de impressão molecular à base de polímero orgânico foram preparados de maneira similar ao protocolo descrito na secção 3.3. A única diferença foi a adição de TiO_2 dopado com cobre ao invés do TiO_2 não dopado (mantida a mesma quantidade).

Previamente, a dopagem do TiO_2 foi feita a partir de um método de co-precipitação química em solução alcoólica (HUANG *et al.,* 2009) como descrito a seguir. Uma quantidade calculada de acetado de cobre (II) foi dissolvida por 30 min em 100 mL de etanol com consequente formação de uma solução de coloração verde. A esta solução foi adicionada uma quantidade de TiO_2 de forma que a porcentagem mássica fosse fixada em 50/50 CuO_2:TiO_2. A solução foi sonicada (Branson 3200) para que uma suspensão uniforme fosse obtida. Em seguida, 100 mL de uma solução aquosa de glicose (0,2 M) foram adicionadas gota a gota enquanto que a solução era mantida a 60°C. Na sequencia, 120 mL de NaOH (0,3 M) dissolvido em 70 mL de etanol e 50 mL de água foi adicionado gota a gota, produzindo um precipitado amarelado. O precipitado foi

separado da suspensão por centrifugação (3.500 rmp) (Awel MF 48R) por 20 min, e depois lavado 3 vezes com etanol e água para remoção residual de acetato, glicose e base. O produto final foi secado a vácuo por 12 h.

3.4 Caracterização

Os materiais sintetizados foram caracterizados por um conjunto de técnicas espectroscópicas, microscópicas e volumétrias, visando à caracterização elementar, estrutural, textural e morfológica dos materiais.

3.4.1 Análise Textural

3.4.1.1 Adsorção de Nitrogênio

A área específica foi calculada pelo método BET a partir dos dados obtidos por experimentos de adsorção de nitrogênio a -196°C. O equipamento utilizado foi um Gemini 2375 (Micrometrics, Norcross, GA, USA). As pressões relativas de nitrogênio (P/P_0) compreenderam o intervalo de 0,2 a 0,9. As amostras (cerca de 150 mg) foram previamente tratadas por cerca de 12 h a 110°C e 10^{-2} mbar. O procedimento também permitiu a determinação da porosidade através da aplicação do método BJH.

3.4.1.2 Potencial Zeta

Utilizou-se o equipamento da marca Malvern-Zetasizer® modelo nanoZS com células capilares fechadas (DTS 1060) para medir os valores do potencial Zeta das amostras sintetizadas. Prepararam-se as amostras do seguinte modo: a) utilizou-se cerca de 1,0 g da amostra em pó para ser dispersado em água deionizada; b) retirou-se uma amostra do sobrenadante e c) adicionou-se na célula de leitura do analisador de potencial zeta, obtendo-se assim os valores do potencial zeta da amostra expressos em mV (milivolts), registrados a cada medida.

3.4.1.3 Espalhamento de Raios X em Baixo Ângulo (SAXS)

Os experimentos de SAXS foram realizados nas linhas D2A e D11A no Laboratório Nacional de Luz Síncrotron (LNLS, Campinas, Brasil) usando um comprimento de onda igual a 1,488 nm. O feixe de raios X foi monocromatizado por um monocromador de silício e colimado por um conjunto de fendas definindo uma geometria do tipo *pin-hole*[1]. O feixe incidente foi detectado em duas diferentes distâncias amostra-detector (1549,8 e 2245,7 nm) aumentando, assim, a faixa do vetor de espalhamento ($q = (4\pi/\lambda)\sin\Theta$; 2Θ= ângulo de espalhamento) coletada. Amostras secas foram dispostas entre duas fitas Kapton® e o feixe de raios X colimado foi passado através de uma câmara contendo o porta-amostra de aço inoxidável. Todas as medidas foram executadas à temperatura ambiente e um pó de behenato de prata foi utilizado como padrão de calibração para a distância amostra-detector, para a inclinação e também posição do feixe direto.

[1] *Pin-hole* - Designação do inglês "buraco de agulha" relacionado à geometria de colimação do feixe eletromagnético na linha de SAXS.

A transmissão e correção da radiação de fundo e para as fitas Kapton® foram realizadas na imagem 2D antes do processamento seguinte de dados. A média dos padrões de espalhamento isotrópicos foi feita radialmente.

A análise de dados de SAXS foi realizada através da avaliação de rotina Irena (ILAVSKY, 2009) implementada no software Pro Igor (WaveMetrics, Portland, EUA) (KLINE, 2006). Um ajuste multi-nível unificado foi utilizado para descrever um ou dois níveis de organização estrutural evidente nos dados de espalhamento (BEAUCAGE, 1995; BEAUCAGE, 1996). Utilizando esse método, o espalhamento apresentado por cada nível estrutural é a soma de uma forma de Guinier exponencial e uma cauda descrita pela Lei das Potências estruturalmente limitada.

Uma equação equação generalizada, representando qualquer número de níveis, está apresentada na Equação 3.1.

$$I(q) = \sum_{i=1}^{n} G_i \exp\left(\frac{-q^2 R_{gi}^2}{3}\right) + B_i \exp\left(\frac{-q^2 R_{g(i+1)}^2}{3}\right)\left[\frac{(\mathrm{erf}(qR_{gi}/\sqrt{6}))^3}{q}\right]^{Pi} \quad (3.1)$$

em que n é o número de níveis estruturais observados, G é pré-fator de Guinier, Rg é o raio de giro e B é um pré-fator específico para o espalhamento correspondente à lei de Potências, o qual é especificado como o decaimento exponencial de P.

É possível estudar a estrutura multi-escala de partículas fractais através da técnica de Espalhamento de Raios X em Baixo Ângulo (SAXS) (GREEN *et al.*, 2003), que investiga as diferenças nas densidades eletrônicas do material através do perfil de intensidade de espalhamento de raios x. A intensidade de espalhamento é medida experimentalmente como um vetor espalhamento *q*, cujo módulo é dado pela Equação 3.2.

$$q = (4\pi / \lambda) sen\Theta \qquad (3.2)$$

onde λ é o comprimento de onda da radição incidente e Θ é a metade do ângulo de espalhamento, formado entre as direções do feixe espalhado e transmitido.

O gráfico I(q) × q de uma amostra apresenta duas regiões de interesse: as regiões de Guinier e a região da leis de potência. A primeira região é dada por uma função gaussiana, que permite determinar o tamanho da particula espalhadora, considerando o sistema tomado como composto por N partículas idênticas. Em função do raio de giro (Rg), a lei de Guinier é expressa pela Equação 3.4 (BALE & SCHIMIDT, 1984).

$$I(q) = I_0 \exp[-q^2 Rg^{2/3}] \qquad (3.4)$$

em que I_0 é a intensidade em q = 0, e é proporcional ao número de partículas espalhadoras em um dado volume N (RO & CHUNG, 1991). A lei de Guinier é válida somente para altos valores de q, de forma que Rg × q < 1. A região que pode ser analisada pela lei de potências localiza-se a valores de q inferiores e obedece à Equação 3.5 (BALE & SCHMIDT, 1984; SHAEFER & KAEEFER, 1984).

$$I(q) = I_0 q^{-P} \qquad (3.5)$$

em que o expoente P pode assumir valores não inteiros entre 1 e 4 e está relacionado à dimensão fractal da partícula (GREEN *et al.*, 2003). Para sistemas complexos e randômicos, o conceito de fractal pode ser aplicado na interpretação de seus perfis de espalhamento (SCHMIDT, 1991; SCHMIDT, 1995; SCHAEFER *et al.*, 1995). A dimensão fractal D é quantificada como a massa M em um fractal mássico, ou a área A em um fractal de superfície, que mudam com a escala de

comprimento que identifica o material (L). No caso de fractais mássicos, esses podem ser descritos como estruturas poliméricas, abertas e de baixa densidade. A massa M segue a Esquação 3.6.

$$M \propto L^{-Dm} \tag{3.6}$$

em que Dm é a dimensão fractal mássica da partícula (1 < P < 2 – estrutura caulhe-folha). Nesse caso, Dm= P. No caso de fractais de superfície, esses são descritos como núcleos densos e com superfícies rugosas de área A, de acordo com a Equação 3.7 (SCHMIDT, 1991; SCHAEFER *et al.*, 1995):

$$A \propto L^{-Ds} \tag{3.7}$$

em que Ds é a dimensão do fractal de superfície (2 < P < 4 – estrutura rugosa). Nesse caso, P = 6-Ds. Uma superfície perfeitamente uniforme apresenta Ds = 2 e P = 4 (estrutura de Porod).

3.4.2 Análise Morfológica

3.4.2.1 Microscopia Eletrônica de Varredura (MEV)

As imagens de MEV foram obtidas em um microscópio Zeiss (modelo EVO 50) equipado com detector Everhart-Thornley operado com voltagem de 10,0 kV. As amostras foram previamente metalizadas com ouro, com 24 h de antecedência.

3.4.2.2 Microscopia Confocal

A microscopia confocal foi conduzida em um microscópio de zoom, modelo V16, da Carl Zeiss Inc. equipado com sistema de fluorescência (HXP 200), objetivas PlanNeoFluor com magnificação de 1,0 e 2,3 × e uma faixa de magnificação de 0,75-9,0 ×. A aquisição de imagens foi feita com uma Axioxam MRc.

3.5.3 Análise Estrutural

3.5.3.1 Espectroscopia de Transmissão no Infravermelho com Transformada de Fourier (FT-IR)

As vibrações ν_{as}(Si-O-)Si e ν_{s}(Si-O-)Si compreendendo as regiões espectrais entre 900 e 1300 cm^{-1} contêm quatro contribuições (modo óptico longitudinal, LO, e modo óptico transversal, TO, distribuídas em componentes de anéis de quatro e seis membros do grupo siloxano: LO_6, LO_4, TO_6 e TO_4) para a primeira e duas para a segunda (estiramento da ligação Si-O nos grupos Si-OH e $Si-O^-$) (FIDALGO, 2001). Para uma análise estrutural detalhada, a região espectral entre 900 e 1300 cm^{-1} foi deconvoluída em componentes Gaussianas utilizando um ajuste não-linear por mínimos-quadrados (FIDALGO, 2001). A porcentagem de anéis de seis membros (%(SiO_6)) foi estimada a partir da razão entre as áreas obtidas através da deconvolução, segundo a equação a seguir:

$$\%(SiO)_6 = 100 \times [A(LO_6) + A(TO_6)/A(LO_6) + A(LO_4) + A(TO_4) + A(TO_6)] \quad (3.9)$$

3.5.3.2 Espectroscopia Raman

As medidas de espectroscopia Raman foram executadas em temperatura ambiente usando um sistema microscópio Via Renishaw equipado com distância de lente longa (50×), um diodo de laser para infravermelho próximo (785 nm) e detector de carga acoplado. Os espectros foram medidos com potência de laser de 300 mW em um tempo de aquisição de 20 s. Para a aquisição e análise de dados foi utilizado o software WiRETM.

3.5.3.3 Espectroscopia de refletância difusa no ultravioleta-visível (UV-DRS)

As amostras foram analisadas por espectroscopia molecular no ultravioleta-vísivel em estado sólido, onde uma pequena quantidade de amostra (cerca de 0,05 g) foi dispersa sobre uma célula com janela de quartzo confeccionada para análise de DRS. Estas amostras foram analisadas em espectrofotômetro Varian (Cary 100) com acessório DRA-CA-301 (Labsphere) acoplado para a análise em modo de refletância difusa. Os espectros foram obtidos a temperatura ambiente, sendo utilizado o sal $BaSO_4$ como referência e a faixa espectral estudada foi de 200 a 800 nm e as amostras não sofreram nenhum pré-tratamento.

3.5.3.4 Espectroscopia Fotoeletrônica de Raios X (XPS)

As análises de XPS foram realizadas em um equipamento Omicron-SPHERA, usando radiação de Mg/Kalpha (1253,6 eV) no Laboratório de Superfícies e Interfaces Sólidas (LACIM) da UFRGS. O ânodo foi operado a 225 W (15 kV, 15 mA). Os espectros foram registrados com energia de passagem de 50 eV. As regiões específicas de interesse - N(1s), O(1s) e Si(2p) - foram registradas com uma resolução maior (energia de passagem de 10 eV). O ângulo de detecção dos fotoelétrons em relação à amostra foi fixado a 0° para todas as medidas. O sinal de carbono adventício C(1s) em 285 eV foi usado como referência interna para correção da energia. Todos os espectros foram ajustados assumindo uma linha de base Shirley. As linhas foram ajustadas através das funções Gaussinas e Lorentziana, com valores selecionados na largura a meia altura de cada linha.

3.5.3.5 Medidas de Fluorescência

As medidas de emissão de fluorescência foram obtidas em um equipamento Shimadzu RF-5301 a temperatura ambiente. O comprimento de onda de emissão foi fixado em 545 nm. Cerca de 30 mg de amostra foi colocada no porta-amostra sem necessidade de tratamento prévio.

3.5.3.6 Espectroscopia de Massas por inserção direta (DI-MS)

A espectrometria de massa foi realizada em um equipamento Shimadzu modelo GCMS-QP2010S com um dispositivo de entrada de inserção direta. As amostras foram preparadas por adição de aproximadamente 2 mL de acetona em uma amostra de 5 mg de pó, resultando em um material em suspensão. Em seguida, cerca de 10 µL desta foi transferida para um microtubo (capacidade de 25 µL) utilizando um capilar. O solvente foi seco à temperatura e pressão ambiente. Em seguida, o microtubo foi colocado em uma sonda de inserção e introduzido à porta de injecção através da entrada de inserção. A temperatura foi programada para atingir inicialmente 70 ºC a 80 ºC/min. Manteve-se a amostra a 70 ºC durante 1 min, e depois foi elevada para 320 ºC a 40 ºC/ min, e, finalmente, aquecida até 350 ºC a 20 ºC /min e assim mantida durante 10 min. O tempo total de análise foi de 21 min. A fonte de íon e a interface foram mantidas a 260 e 250 ºC, respectivamente. Aquisição foi realizada em modo SCAN entre 50 (*m/z*) a 1090 (*m/z*).

3.5.3.7 Difração de raios X (DRX)

As análises de difração de raios X foram realizadas em um difratômetro Rigaku DMAX 2200 equipado com tubo de Cu e monocromador secundário, sendo o dector de cintilação [NaI(Tl)].

3.6 Experimentos de Adsorção dos Materiais à Base de Sílica Dotados de Impressão Molecular

Em um experimento típico, 10 mg de sílica com impressão molecular foi inserido em um tubo de ensaio. Em seguida, adicionou-se 5 mL de solução de diferentes concentrações de RhB, que permaneceram em contato com a sílica por 1 hora, sob agitação. A solução sobrenadante foi diluída apropriadamente para posterior análise por espectroscopia molecular de absorção UV-visível no comprimento de onda de 553 nm. Experimentos similares foram conduzidos com as amostras sem impressão molecular. A porcentagem de remoção por adsorção foi calculado segundo a Equação 3.9:

$$\text{Remoção}(\%) = \frac{Concentração_{inicial} - Concentração_{final}}{Concentração_{inicial}} \times 100\% \qquad (3.9)$$

Para determinar o efeito relativo dos pares de amostras com impressão molecular (IM) e sem impressão molecular (SIM) foi utilizado o parâmetro fator *imprinting* (FI), definido como a razão entre as concentrações finais desses dois tipos de sistemas, representado na Equação 3.10:

$$FI = \frac{Concentração_{final}^{IM}}{Concentração_{final}^{SIM}} \qquad (3.10)$$

Também foram realizados testes de seletividade e competitividade. O primeiro refere-se a testes de adsorção com outra molécula diferente da RhB, e o segundo refere-se aos testes com misturas de dois corantes em um mesmo ensaio. A molécula de estudo para esses ensaios foram a Rodamina 6G (Rh6G) e o Azul de Metileno (AM). Para os testes de seletividade, a solução ssobrenadante foi analisada por

espectroscopia molecular de absorção UV-visível no comprimento de onda de 530 nm (RhB) e 663 nm (AM). No caso dos testes de competitividade, a concentração final foi calculada através de uma metodologia na qual leva-se em consideração a lei de Lambert-Beer estendida para misturas (CONNORS & EBOKA, 1979).

Para avaliar a extensão de degradação de um componente em detrimento de outro, definiu-se o fator seletividade (FS) e fator competitividade (FC) como sendo a razão da concentração final entre a RhB e Rh6G para um mesmo sistema, em que FS refere-se aos testes com um único componente e FC para reações com misturas. As Equações 3.11 e 3.12 apresentam matematicamente esses fatores:

$$FS = \frac{\text{Concentração da RhB}}{\text{Concentração da Rh 6G (ou AM)}} (\text{testes com corantes separados}) \quad (3.11)$$

$$FC = \frac{\text{Concentração da RhB}}{\text{Concentração da Rh 6G (ou AM)}} (\text{testes com corantes misturados}) \quad (3.12)$$

Todos os experimentos foram realizados em duplicatas. Assim, o cálculo dos fatores leva em consideração a média dos valores de concentração.

3.7 Isotermas de Adsorção dos Materiais à base de Sílica Dotados de Impressão Molecular

A estimativa dos parâmetros das isotermas Freundlich e Langmuir foram realizadas utilizando o quadrado mínimo não-linear restrito (NLLS), que foi implementado em Matlab, usando a função *fmincon* (LINDFIEL & PENNY, 1995) e analisada a partir do invervalo de confiança do parâmetro (I), matriz de correlação do parâmetro (C) e variância experimental (v_{exp}).

O intervalo de confiança e a matriz de correlação foram calculados considerando a distribuição *t*-Student, para um intervalo de confiança de 95%, de acordo com as Equações 3.14-3.22:

$$I = p \pm t_{\alpha,(n-n_p)}\sigma_p(i) \tag{3.14}$$

$$\sigma_p = \sqrt{diag(v_p^2)} \tag{3.15}$$

$$\alpha = \frac{1+0,95}{2} \tag{3.16}$$

$$v_p^2 = v_{\exp}^2 (M^T M)^{-1} \tag{3.17}$$

$$v_{\exp}^2 = \frac{\varepsilon^T \varepsilon}{(n-n_p)} \tag{3.18}$$

$$\varepsilon = \left[q_e\right]_{\text{estimado}} - \left[q_e\right]_{\text{experimental}} \tag{3.19}$$

$$M(q_e, p) = \left[\frac{\partial q_e}{\partial p}\right] \tag{3.20}$$

$$C_{ij} = \frac{(v_p)_{ij}}{\sqrt{(v_p)_{ii}(v_p)_{jj}}}; \quad \text{for i} \neq \text{j} \tag{3.21}$$

$$C_{ij} = 1; \quad \text{for i} = \text{j} \tag{3.22}$$

Em que:

I é o intervalo de confiança do parâmetro

p é o parâmetro estimado;

σ_p é o desvio-padrão do parâmetro

v_p é a matriz de covariância do parâmetro;

v_{exp} é a variância experimental;

M é a derivada da matriz;

C é a matriz de correlação;

D_{iag} é a matriz de covariância (diagonal);

ε é o desvio previsto;

q_e é a quantidade adsorvida;

n é o número de pontos experimentais;

n_p é o número de pontos ajustáveis.

A isoterma de Freundlich é mostrada na Equação 3.23. Muitas estimativas de correlação k_f e 1/n podem ser obtidas a partir dessa equação (Himmelblau, 1967).

$$q_e = k_f C_e^{\frac{1}{n}} \tag{3.23}$$

A fim de se obter parâmetros de baixa correlação, a Equação 3.23 foi redefinida considerando uma nova variável, $C_e^* = KC_e$, conforme as Equações 3.24 e 3.35, utilizada no ajuste de dados. Dessa forma, parâmetros de baixa correlação podem ser estimados a partir de estabelecimento adequado de K, que permite a matriz $M^T M$ não ser singular (HIMMELBLAU, 1967).

$$q_e = \alpha(C_e *)^{\beta} \tag{3.24}$$

$$q_e = \alpha K^{\beta}(C_e)^{\beta} \tag{3.25}$$

em que: $K_f = \alpha K^{\beta}$ e $1/n = \beta$.

Infelizmente, uma modificação singular não é facilmente obtida para a isoterma de adsorção original de Langmuir, de acordo com a Equação 3.26.

$$q_e = \frac{q_m k_a C_e}{1 + k_a C_e} \tag{3.26}$$

Considerando a isoterma de Freundlich, *K* é o parâmetro que corresponde aos sítios de adsorção e o valor de 1/n representa a capacidade de adsorção. Para a isoterma de Langmuir, q_m é o parâmetro relacionado com o preenchimento de poros do adsorvente em uma monocamada, e K_a é o parâmetro relacionado com a energia de adsorção e fornece um indicativo de afinidade entre o adsorbato com a superfície do adsorvente. O valor de *K* foi obtido através de um ajuste por tentativa e erro. A extensão de ajuste entre os dados experimentais com os valores estimados foram avaliadas por determinação do coeficiente de determinação (r^2).

Em nossos estudos, também utilizamos a isoterma BET-modificada para adsorção sólido-líquido, segundo a Equação 3.47 (EBAI *et al*., 2009):

$$q_e = \frac{y_1 y_2 C_e}{\text{abs}(y_3 - C_e)\left(1 + (y_2 - 1)\frac{C_e}{y_3}\right)} \tag{3.27}$$

em que:

abs(x) é o valor absoluto do argumento x;

y_1 é o equivalente ao q_m;

y_2 é a razão entre a constante de equilíbrio para a primeira camada e a constante de equilíbrio de adsorção de camadas superiores (KS/KL);

y_3 é a solubilidade do soluto.

A isoterma de BET-modificada não é uma função contínua. Quando $C_e = y_3$, a função tende ao infinito. Assim, foi necessário dividí-la em duas regiões, ou seja, $C_e < y_3$ e $C_e > y_3$.

4. RESULTADOS E DISCUSSÃO

No início do desenvolvimento da presente tese, apenas um trabalho tinha sido encontrado explorando a combinação de matriz de sílica com TiO_2 (SHEN *et al.*, 2009). Neste estudo, os autores relataram a síntese e caracterização de um material visando à degradação seletiva do éster ftalato. O catalisador foi preparado pelo método de Stöber (TEOS como precursor da rede inorgânica em rota básica usando $NH_3.H_2O$ como catalisador da reação sol-gel) e utilizando P25 como fonte de TiO_2. Recentemente (DENG *et al*., 2014), um compósito SiO_2/TiO_2 foi sintetizado a partir de um método hidrotermal (aquecimento em autoclave) usando ácido acético como catalisador da reação sol-gel (TEOS como precursor de sílica). Neste estudo, um alcóoxido de titânio foi escolhido como fonte de TiO_2.

Apesar destes estudos encontrados, antes do desenvolvimento da presente tese, inexistiam na literatura relatos comparativos das diferentes rotas de síntese (ácida, básica, *two-steps* e não-hidrolítica) na atividade fotocatalítica. Além disso, o uso de P25 é dominante, e não havia sido encontrado estudos referentes ao uso de $TiCl_4$ como fonte de TiO_2. Segundo YAO e colaboradores (2011), na síntese de sílica-gel contendo derivados de alcóxido de titânio, a taxa de hidrólise deste último é geralmente maior do que os alcóxidos de sílica. Esse aspecto acaba induzindo a precipitação do TiO_2, prejudicando a eficiência fotocatalítica. Nesse sentido, a introdução de titânio a partir de fontes inorgânicas (como o $TiCl_4$) pode evitar esse problema (YAO *et al.*, 2001). Também é importante ressaltar que nenhum estudo visando a degradação de fármacos no contexto de fotocatálise seletiva em matriz inorgânica havia sido encontrado antes do desenvolvimento da presente tese.

Os resultados desta tese estão apresentados no formato de integração por artigos. Os resultados do trabalho estão dispostos em duas grandes classes de materiais dotados com impressão molecular, distintas pela natureza da matriz (inorgânica e orgânica). O **Esquema 4.1** ilustra em qual dessas classes cada artigo está inserido, bem como uma breve descrição dos objetivos de cada um deles.

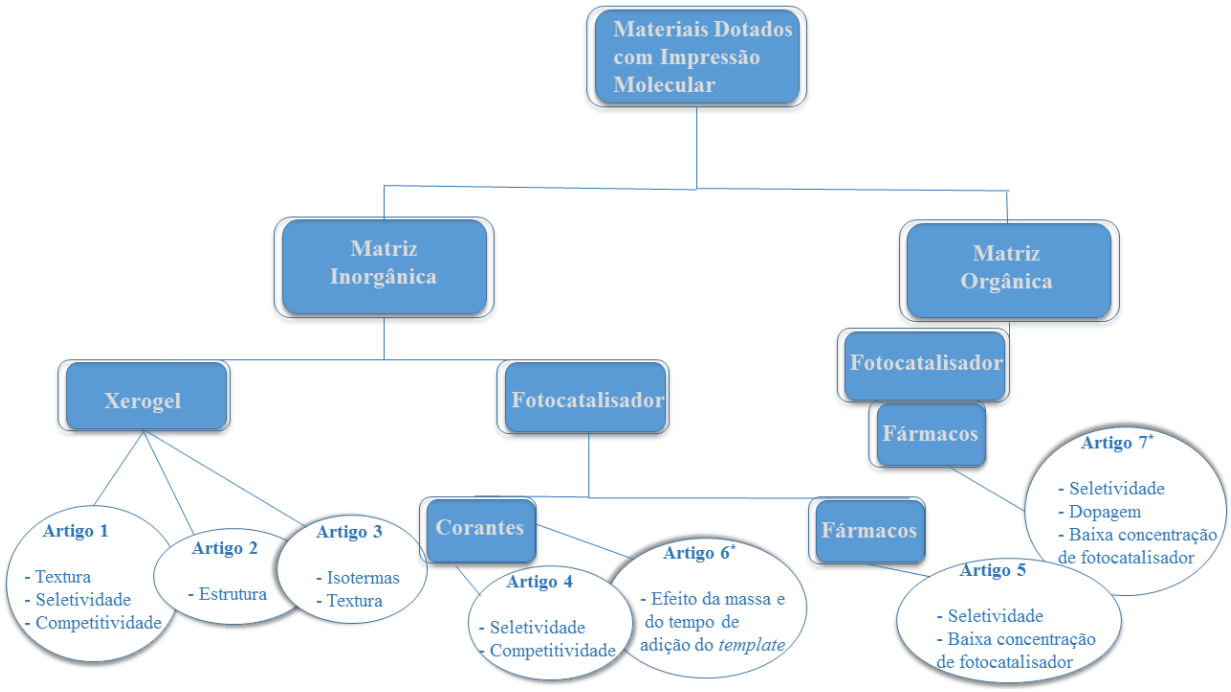

Esquema 4.1: Artigos publicados e não submetidos (*) a partir de diferentes matrizes dos materias.

4.1 Artigo 1

Publicado no *Journal of Separation Science*, v. 37, p. 868-875, 2014.

Cícero de Coelho Escobar[1]
João Henrique Zimnoch dos Santos[2]

[1]Departamento de Engenharia Química—Universidade Federal do Rio Grande do Sul Rua Eng. Luis Englert s/n, Porto Alegre -RS, Brazil
[2]Instituto de Química, Universidade Federal do Rio Grande do Sul, Porto Alegre, CEP, Brazil

Received October 21, 2013
Revised January 16, 2014
Accepted January 18, 2014

Research Article

Effect of the sol–gel route on the textural characteristics of silica imprinted with Rhodamine B

A series of silica xerogels that support Rhodamine B as a template were synthesized using distinct sol–gel routes, namely, acid-catalyzed routes, a base-catalyzed route, acid-catalyzed with base-catalyzed (two steps) hydrolytic routes, and a $FeCl_3$-catalyzed nonhydrolytic route. The extraction methods (thermal, Soxhlet, water washing, and ultrasound) were also evaluated. The resulting xerogels were characterized through porosimetry using nitrogen adsorption/desorption. The samples were further analyzed through small-angle X-ray scattering, Fourier transform infrared spectroscopy, and SEM. The preparation route affected the materials' textural properties. Extraction was optimized using acid and two-step routes. The acid route from Rhodamine B to Rhodamine 6G generated the highest selectivity factor (2.5). The nonhydrolytic route produced the best imprinting factor. Competitive adsorption was also used, from which the approximate imprinting factor was 2. The cavity shape generated during the production of the imprinted silica dictates the adsorption behavior, not the magnitude of the surface area.

Keywords: Molecular imprinting / Silica / Small-angle X-ray scattering / Sol–gel
DOI 10.1002/jssc.201301143

Additional supporting information may be found in the online version of this article at the publisher's web-site

Introduction

Research on molecularly imprinted (MI) materials has received considerable attention in recent years. Because such materials represent a valid alternative to molecular recognition systems, they demonstrate high affinity and selectivity for the molecules employed as templates for their synthesis [1,2]. An MI system's molecular recognition ability facilitates use of such materials in processes such as drug delivery [3], catalysis [4], adsorption [5], chemical sensing [6], preconcentration [7], biological antibodies, and receptor systems [8].

In addition, such materials may yield low-to-moderate template recovery and heterogeneity of the receptor sites generated [9]. A promising approach for overcoming such inconveniences is to use inorganic matrices, such as silica-based materials.

In developing such MI materials as sorbents for removal processes, most studies have reported using organic polymeric phases. Certain drawbacks are associated with polymeric materials, such as functional chemical groups outside the printing sites, which produce nonspecific and weak interactions between the template and polymer functional units.

One potential approach for producing silica-based imprinted materials is the sol–gel process. In this strategy, the template reacts with the precursor (e.g., tetraethylorthosilicate [TEOS]), which produces a silica network with the encapsulated molecule. Specific adsorptive sites are created after removing the template from the silica network, which produces materials with imprinted sites. As shown in the literature [10,11], matrices prepared by the sol–gel method offer certain advantages compared with conventional organic polymerization methods, such as rigidity, thermal stability, tailored porosity, and flexibility in processing conditions. Most

studies discuss silica materials that are adsorbent in solid-phase drug extraction [5], such as for ibuprofen [12], methylxanthines [13], and diethylstilbestrol [14].

Because the silica xerogel composition is tunable, the synthesis route may affect the silica xerogels' texture and morphological characteristics. Several approaches for developing silica-based materials using the sol–gel process have been reported. Such materials can be classified into two large families: (i) silicate-based materials, for which xerogel is formed using a silicate precursor, and (ii) silica–alkoxide materials, which facilitate solid material synthesis through gelation via a liquid reaction medium with molecular precursors used to create an oxide network through progressive polycondensation [15]. For silica–alkoxide xerogels, several parameters affect the final materials, such as the pH, hydrolysis rate, nature of the precursor, molar ratio between H_2O and precursor, and aging time [16]. In hydrolytic routes, the gelling process may be accelerated using acid or base catalysts, which affect hydrolysis and condensation reactions differently and, thus, generate materials with different morphologies and textures. In the nonhydrolytic sol–gel route (i.e. without water in the medium), a metal halide reacts with an alkoxysilane, which is catalyzed by a Lewis acid and forms a tridimensional oxide net [17, 18].

The literature includes examples of silica-imprinted materials that have been developed using alkoxide-based silica materials. For instance, the acid route has been applied to synthesize molecular imprinted xerogels for use as a sorbent in capillary microextraction with atrazine as the template and 3-(propylmethacrylate)trimethoxysilane as the precursor [19]. The acid route has also been employed to develop a sensor that detects trace olaquindox in chicken feed [20] and to prepare an imprinted xerogel that specifically uptakes creatinine using tetraethoxysilane as the monomer precursor [21]. Acid and base routes were used to investigate glycylglycine-imprinted silica synthesis for a potential application in selective chromatographic separation using

tetramethoxysilane as the precursor [22]. Similarly, the base route has been examined for applications such as removing cadmium(II) ions using $CdCl_2$ as the molecule template and tetraethoxysilane as the precursor [23]. Nonhydrolytic materials with molecular imprinting were explored to recognize sulfonylurea herbicides using methacryloxypropyltrimethoxysilane as the precursor [24]. In addition, silicate-based materials have been applied for Au(III) adsorption using a sodium silicate solution as the precursor and Au(III) as the template [25].

For the target molecule, a few studies have developed imprinted materials using Rhodamine B (RhB) as the template. For instance, sulfonated polysulfone, which is a functional polymer, was prepared and subsequently blended with cellulose diacetate as the matrix polymer to prepare molecular- imprinted polymer membranes [26]. The authors imprinted porous membrane surfaces with relatively high permeability. Using similar MI polymer-blend membranes, the potential for reusing membranes for SPE in recovering RhB was also addressed [27]. Xu et al. prepared a surface with MI fiber for RhB by bonding polyethylenimine onto polypropylene for selective adsorption [28].

The interaction capacity of organic molecules with titanium dioxide surfaces has been demonstrated in the literature [29]. Combined with molecular imprinting, selective adsorption may be improved. In this manuscript, we detail preparation of silica-based materials using TiCl4 as the Ti source and different sol–gel processes, namely, hydrolytic (base and acid catalyzed), two-step (base catalysts with acid catalysts), and nonhydrolytic routes.

To investigate the sol–gel route's effects on the resulting xerogel textural properties, RhB was used as the template molecule. The extraction methods (thermal, Soxhlet, washing, and ultrasound) were also evaluated. The sol–gel route's effects on imprinted silica-based materials' textural properties have not been comparatively described in the literature. Therefore, we

compared the imprinted sol–gel silica materials using RhB as the template for synthesis and the textural properties.

2 Materials and methods

2.1 Materials

RhB (Vetec), Rhodamine 6G (Rh6G; Sigma-Aldrich), tetraethoxysilane ($Si(OCH_2CH_3)_4$, TEOS, Merck, >98%), titanium tetrachloride (Merck, >99%) and silicon tetrachloride ($SiCl_4$, Sigma-Aldrich, 99%) were used as received. Hydrochloric acid (HCl, Nuclear, 38%), ammonium hydroxide (NH_4OH, Nuclear, 29%), and $FeCl_3$ (98%, Merck) were employed as catalysts.

2.2 Preparation of the sol–gel materials

Five different routes were employed to prepare the samples using the sol–gel process and TEOS as the raw material. The routes were labeled as follows: the acid-catalyzed route 1 (A1), acid-catalyzed route 2 (A2), base-catalyzed route (B), two-step route (TS), and nonhydrolytic route (NH). The acid-catalyzed route 1 was catalyzed using 0.2 M of hydrochloric acid at a 1:2 HCl/TEOS ratio. The acid-catalyzed route 2 was similar to acid-catalyzed route 1, but the samples were prepared without hydrochloric acid (i.e. $TiCl_4$ acted as a potential Lewis acid catalyst). The base-catalyzed route was catalyzed using 0.2 M of ammonium hydroxide at a 1:2 NH_4OH/TEOS ratio. The two-step route was catalyzed using 0.2 M of hydrochloric acid at a 1:2 HCl/TEOS ratio; after 30 min, 0.2 M of ammonium hydroxide was added at a 1:2 NH_4OH/TEOS ratio. The non-hydrolytic route employed TEOS and $SiCl_4$ and was catalyzed using $FeCl_3$ (0.5 wt% of the final product weight). For each sample, the RhB was fixed at 5 wt% of the final xerogel weight.

The samples (powder) from the acid-catalyzed, base-catalyzed, and two-step routes were prepared as follows. RhB was added to a solution of TEOS followed by $TiCl_4$ addition, and finally, the catalyst was added. During this process, the solution was constantly stirred at room temperature. The solution was stirred until gelation or precipitation, which depends on the route. For the nonhydrolytic route, the procedures were executed under an inert atmosphere (Ar). TEOS, $SiCl_4$ and $TiCl_4$ were added after adding the catalysts and RhB. The resulting solution was stirred at 80°C until gelation. The solids were dried at room temperature and milled.

The following four extraction methods were evaluated for template removal: thermal, Soxhlet, solvent washing, and ultrasound. Thermal extraction was performed under Ar flow from room temperature to 190°C at the heating rate 5°C /min. Soxhlet extraction was employed in a suitable device for 24 h using methanol as the solvent. Methanol and water were employed as the solvents for ultrasound-assisted extraction. The process was conducted by altering pulse-on (20 s) and pulse-off (5 s) modes for 5 min. Extraction was employed using water as the washing solvent. The solid was filtered and dried at room temperature.

The resulting samples were labeled based on the sol– gel route. For example, NH denoted the nonhydrolytic route. $TiCl_4$ and encapsulated RhB use were indicated by Ti and RhB, respectively. When necessary, E denoted systems with extraction. Therefore, ENHTiRhB refers to a xerogel prepared through the nonhydrolytic route using $TiCl_4$ during synthesis and involving RhB extraction. For comparison, bare silica was also synthesized under the same conditions without a template. Thus, NH refers to a xerogel prepared through the non- hydrolytic route without $TiCl_4$ and RhB. In this manuscript, the system without $TiCl_4$ was considered as nonimprinted (NI) material. Scheme 1 depicts the sol–gel routes used and the corresponding materials produced.

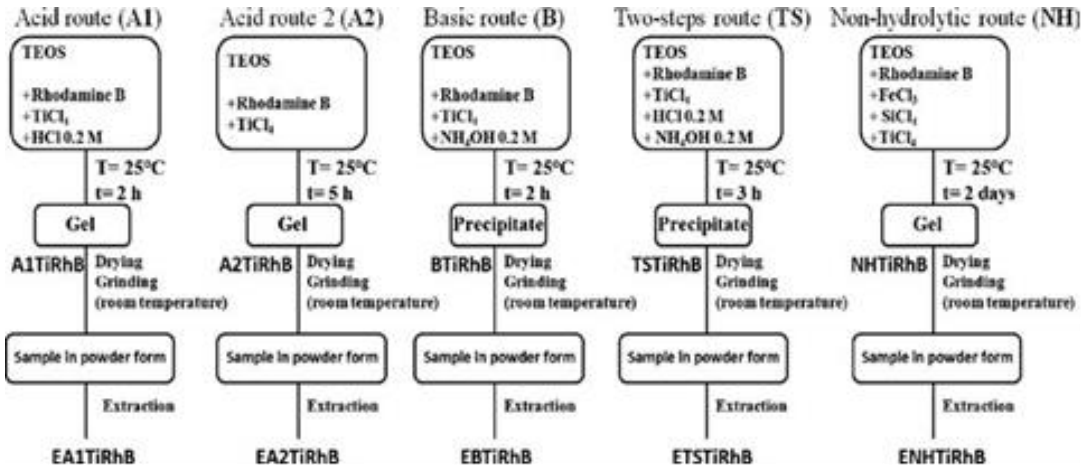

Scheme 1. The different sol– gel routes employed for xerogel synthesis.

2.3 Xerogel characterization

The specific surface area was determined by the Brunauer–Emmett–Teller (BET) method at −196°C within the partial pressure range $0.2 < P/P_0 < 0.9$. Prior to each measurement, the samples were preheated at 110°C for 14 h under a vacuum. The total pore volume was determining from single-point desorption at $P/P_0 = 0.967$. The pore diameter was determined using the Barret–Joyner–Halenda (BJH) method.

FTIR measurements were recorded using a Bomem MB-102 spectrometer by adding 36 scans with a 4 cm^{-1} resolution. Small-angle X-ray scattering (SAXS) experiments were performed on the D11A beamline at the Brazilian Synchrotron Light Laboratory (LNLS, Brazil) at 1.488 nm. The incident beam was detected at two different sample-to-detector distances (1549.8 mm and 2245.7 mm) to increase the scattering vector q range ($q = (4\pi/\lambda)\sin\theta$; 2θ= scattering angle). The dried samples were placed between two Kapton foils, and the collimated X-ray beam passed through a chamber with the stainless steel sample holder. Silver behenate powder was employed as the standard to calibrate the sample-to-detector distance, detector tilt, and direct beam position. The isotropic scattering patterns were radially averaged. SAXS data analysis was performed using

the Irena evaluation routine [30], which was implemented using Igor Pro Software (WaveMetrics, Portland, USA) [31].

SEM was further used to examine the morphologies of the as-synthesized silica xerogel particles. The samples were previously deposited on a carbon tape and then sputtered with a thin layer of conductive gold. The SEM images were obtained on a SEM instrument (Zeiss, model EVO 50) that was equipped with an Everhart–Thornley Detector (secondary electrons) and a tungsten filament. SEM imaging was operated at acceleration voltages of 10.0 kV.

2.4 Adsorption experiments

In a typical experiment, 10 mg of RhB-imprinted silica (extracted by ultrasound/methanol) was introduced into a cartridge, through which 5 mL of RhB solution was percolated over 1 h. Similar experiments were conducted using NI silica. The eluate was analyzed using UV-visible spectrometry at 553 nm. The adsorption (%) was calculated as $(C_{final} - C_{initial})/C_{initial} \times 100\%$. To determine the relative performance of the MI/NI pairs, the imprinting factor was defined as the MI/NI concentration ratio after the experiment.

To study the imprinted materials' selectivity and competitiveness, similar experiments were performed using an Rh6G solution. In this case, the eluate was analyzed through UV/Vis spectrometry at 525 nm. The selectivity factor was defined as the ratio between the RhB and Rh6G adsorptions. For the competition experiments, the final concentration was calculated using an alternate methodology [32]. Each experiment was performed in duplicate.

3 Results and discussion

As shown in Scheme 1, the nonhydrolytic route required 2 days for gelification, whereas the hydrolytic routes required between 2 and 5 h for gelification. Notably, in the systems without RhB (bare silica), the gelification process was more rapid (between 1 and 2 h) for each system, which indicates that the dye interfered with silica network formation. The higher yield was generated using the base route, whereas the lowest yield was generated using the acid route 2.

3.1 Characterization of the xerogels

The A1TiRhB and EA1TiRhB N_2 adsorption/desorption isotherms and pore-size distributions (ultrasound in methanol) are shown in Supporting Information Fig. S1. According to Sing et al. [33], this profile is typical for a type IV isotherm; the quantity adsorbed approaches a finite value that corresponds to complete capillary filling. Considering that the desorption curve runs parallel to the adsorption curve, this system exhibits type H2 hysteresis (bottle-shaped pores), which indicates that the solid desorbs lower adsorbed gas quantities for an equivalent relative pressure [34]. Recently, Morais et al. [35] showed similar results for sol–gel imprinted silicas prepared using the acid route and with fluoxetine, gentamicin, lidocaine, morphine, nifedipine, paracetamol, and tetracycline as the template. The resulting imprinted material's textural properties likely depend on the sol–gel route.

Considering the pore diameters (Table 1), we conclude that the resulting xerogels are mesoporous. Both samples clearly have narrow pore-size distributions (Supporting Information Fig. S1), which suggests that the extraction process did not affect this system's textural properties.

Compared with A1TiRhB, the isotherm and pore-size distribution patterns were similar for TSTiRhB and NHTiRhB. Isotherm type I represents A2TiRhB and BTiRhB, which indicates that microporous materials with type H4 are present (slit-shaped pores). For certain routes, the textural properties clearly changed after extraction. For instance, EBTiRhB exhibited typical characteristics of isotherm type IV with H2 hysteresis. These results suggest that the preparation route affected the materials' textural properties.

Table 1. Textural characteristics of the xerogels obtained from nitrogen adsorption and SAXS analyses.

Route	S_{BET} (m^2/g)	V[a] (cm^3/g)	Dp[b] (Å)	Rg[c] (nm)	p[d]	Rp[e] (Å)
A1	408	0.2	26.2	0.47	3.9	6
A1TiRhB	639	0.5	30.4	2.51	3.8	32.4
EA1TiRhB (Extraction method)						
(Thermal)	649	0.4	26.0	n.d.	n.d.	n.d.
(Soxhlet metanol)	854	0.04	27.0	n.d.	n.d.	n.d.
(Washing)	794	0.4	24.0	n.d.	n.d.	n.d.
(Ultrasound water)	786	0.5	26.0	n.d.	n.d.	n.d.
(Ultrasound methanol)	831	0.5	26.8	3.60	3.47	4.3
A2TiRhB	11	0.005	34.0	0.22	3.70	2.8
EA2TiRhB (Ultrasound methanol)	17	0.009	153.0	0.74	3.80	9.5
B	269	0.5	61.0	0.64	3.40	8.3
BTiRhB	511	0.3	26.0	6.30	3.50	81
EBTiRhB (Ultrasound methanol)	482	0.3	27.5	0.70	3.60	9
TS	373	0.18	23.0	1.46	4.0	18.8
TSTiRhB	568	0.5	29.0	1.80	3.70	23.3
ETSTiRhB (Ultrasound methanol)	350	0.13	30.0	0.95	3.90	12.4
NH	10	0.02	115.0	0.30	4.00	2.8
NHTiRhB	3	0.004	48.0	3.30	3.70	43.2
ENHTiRhB (Ultrasound methanol)	31	0.014	28.0	0.74	3.70	9.5

a) Single point desorption total pore volume of pores at $P/P_0 = 0.967$; b) Determined by BJH method; c) Radius of gyration (Rg) extracted from high-q region (SAXS); d) Power-law decay (P) extracted from low-q region (SAXS); e) Data calculated from spherical mode.

Table 1 shows the samples with encapsulated materials compared with samples without Rhodamine (e.g. A1 and A1TiRhB), which demonstrates a surface area increase after encapsulation. Excepting the nonhydrolytic route, all the other ones have shown an increasing of surface area in more than 50% after the addition of RhB. This finding indicates that the dye

perturbs the system and occludes the pores, as previously reported in the literature [36]. On the other hand, such results differ from results using films, where the surface area decreased [37].

The acid route (A1TiRhB) generated the highest S_{BET} values, which corresponds to the literature [38, 39]. Five extractions were employed for this system. Considering the BET surface area from the initial xerogel (639 $m^2 g^{-1}$), the extraction steps increased the surface area, which indicates that the dye was removed from the silica matrix. The surface area increased after extraction because the silica pores, which were previously occupied by dye molecules, became free and facilitated nitrogen adsorption. Therefore, the increased surface area after the extraction process can be attributed to cavity formation, which produces an imprinted material. The thermal extraction yielded a small surface area increase. As discussed by Limpo et al. [40], this result suggests that the thermal treatment collapsed the silica structure. Conversely, ultrasound extraction (methanol) yielded the highest surface area increase, which was estimated at 854 $m^2 g^{-1}$. The pore diameter decrease also suggests that the dye molecules were removed from inside the silica network. Therefore, extractions for the remaining samples were performed using ultrasound with methanol.

The pore diameters did not change for the xerogel before and after extraction using A2TiRhB. Although the surface area varied slightly, the pore volume after extraction was half the volume of the initial xerogel. An analysis of the infrared spectra of this system before and after extracion further supported extraction (Supporting Information Fig. S2). Three primary absorption bands related to RhB for system A2TiRhB are 1589, 1340, and 1180 cm^{-1}, which correspond to the benzene ring C=C stretch vibrational mode, the C–N-linked benzene ring vibration and (C–O)–C asymmetric stretching vibration, respectively, [41]. These bands were absent after extraction (EA2TiRhB).

For both BTiRhB and TSTiRhB, extraction reduced the surface area but did not change the pore diameter (see Table 1). Compared with the basic route, which did not change the pore volume, the two-step route yielded an approximately four-fold pore volume decrease. Notably, NH_4OH was employed as the catalyst in both routes. Based on the literture [16], sol–gel processes using a basic pH yield material with a compact morphology. Thus, the silica network with the dye may have been morphologically altered during extraction.

For the nonhydrolytic route, a greater than ten-fold increase in the specific area after extraction was observed. In addition, the pore volume increased after extraction, whereas the pore diameter decreased 1.7 fold. Thus, these results demonstrate efficient extraction of the dye molecules from within the silica network. Compared with other systems, NH exhibited the largest pore diameter. It is reasonable to assume that this peculiarity may have facilitated the dye extraction from the silica network.

The differences of the extraction effects on the pore volume and surface area are consequences of the employed sol–gel route. It is well known that under conditions in which hydrolysis rate is rapid compared to condensation (acid-catalyzed conditions), more extensively cross-linked polymeric clusters are formed [16]. Thus, a higher value of surface area is expected for acid route in which HCl was used as the catalysts (A1TRhB) [38, 39]. The effect of the absence of HCl on the resulting surface area and the pore volume is clearly seen in A2TiRhB (Table 1). In such a system, both surface area and pore volume are very low, which may explain the compact and flat observed morphology. Conversely to the reports concerning the morphology obtained by basic-catalyzed routes [16], that is, production of spherical particles, in the present case, both in basic-catalyzed and two steps routes, flat surface, and granular particles were obtained. One cannot neglect that the presence of both $TiCl_4$ and of RhB may also impinge such alteration.

The xerogels were analyzed using SAXS. We observed a distinct power-law decay (green line) for the q values in the SAXS curve analyses where the acid route was used (Supporting Information Fig. S3), which indicates the fractal dimension of such particles or clusters and provides information about their surfaces. The unified SAXS dataset shows that the materials were arranged in a structure with two levels of organization.

By adjusting level 1, which is located in the q region > 0.03 $Å^{-1}$, the primary particles' gyration radii (Rg) can be determined. Level 2, which is located in the q region < 0.01 $Å^{-1}$, provides information on these particles' organization (i.e. on the fractal clusters' structures [secondary particles] generated through primary particle aggregation). The primary particle cluster structures can be determined by analyzing the power-law exponent. An exponent between 1.0 and 3.0 indicates that the secondary particles have a mass fractal structure [42], whereas an exponent between 3.0 and 4.0 indicates that the secondary particles have a fractal surface. When the exponent is 4.0, the secondary particles have a dense core and uniform surface. In this study, the SAXS curve systems showed two distinct levels of organization (see Table 1). The samples did not include a Guinier region in the low-q region, which indicates that the material formed was considerably long using particles or clusters >100 nm [43].

As shown in Table 1, analysis of the SAXS data shows that most of the systems had minimal or no P coefficient variation. The acid-catalyzed and two-step routes were significantly affected by the dye, as demonstrated by the greater variation between A1TiRhB with EA1RhB and TSTiRhB with ETSTiRhB. This result indicates that the dye increases the material roughness and that neither the extraction nor synthesis route altered the silica network fractal dimension at this level of organization. As discussed in the literature [43], the small P values among the routes

at this level of organization are due to the dried gel surface similarities, not the internal structure of the material.

The effect of the route on the Rg after extraction is evident; Table 1 shows that each system's Rg increased compared with bare silica. For instance, A1TiRhB (with encapsulated RhB) showed an Rg value five times higher than A1 (bare silica). This result demonstrates dye encapsulation within the silica network and corresponds to a surface area increase, as previously described.

After extraction, the EA1TiRhB and EA2TiRhB systems' Rg values increased, whereas EBTiRhB, ETSTiRhB and ENHTiRhB exhibited a lower Rg. These results suggest that extraction influences the final pore size. A total pore size increase is the logical result from removing dye molecules from the silica network. Although the Rg did not increase in each system, the Rg results are consistent with the surface about their surfaces area values. For the same system, lower S_{BET} values correlated with lower Rg values (base-catalyzed and two-step routes) after extraction. However, this trend was not observed for the nonhydrolytic route, from which the Rg decrease was evident, even though the extraction process contributed to a surface area increase.

The Rg can be converted into a diameter if a spherical mode is assumed. The diameters calculated from the SAXS data were compared with the diameters acquired using the BJH method. As discussed by Morais et al. [35], the findings support the hypothesis that the Rg observed in the high-q region corresponds to pore size. Notably, the observed deviations are likely due the lack of spherical pores in the synthesized materials. Under this interpretation, the power-law decay describes the silica-pore interface [35].

3.2 Adsorption experiments

Selective RhB and Rh6G adsorption experiments were performed. Figure 1 shows the effect of the different sol–gel routes on the imprinted materials' selectively. Generally, the imprinted materials were capable of selectively removing RhB but not Rh6G. As shown in Table 2, the highest selectivity factor (SF) was generated by the ETSTiRhB system (SF = 4), and the lowest SF was generated by the ENHTiRhB system (SF = 1.7). These results suggest that the capacity of silica for selective adsorption may be due to shape selectivity, which depends on the xerogel preparation route. These results indicate that the pores (e.g. in the ENHTiRhB system) not only generate higher removal values but also a removal specificity 1.7 times greater for RhB compared with Rh6G.

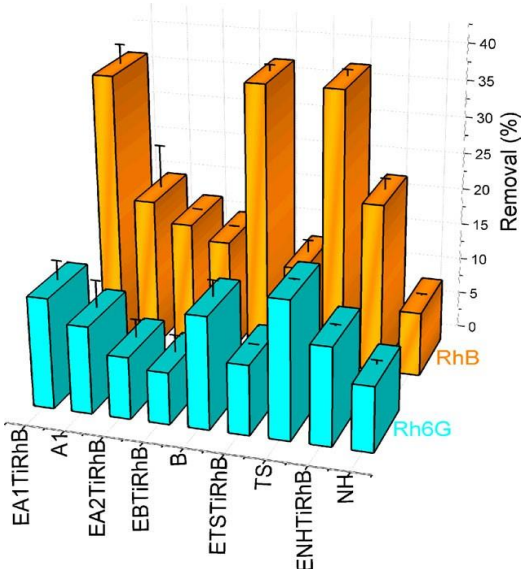

Figure 1. The influence of the sol–gel route on adsorption removal: selectivity experiments (C_0 = 400 ppm and adsorption time = 1 h).

Table 2. Imprinting factor and selectivity factor of imprinted-silica.

System	Maximum removal RhB (%)	Maximum removal R6G (%)	Imprinting fator	Selectivity factor
EA1TiRhB	36.9	14.8	1.8	2.5
EA2TiRhB	17.53	8.4	n.d.	2.1
EBTiRhB	15.6	7.0	0.4	2.2
ETSTiRhB	37.6	9.4	1.3	4.0
ENHTiRhB	22.9	13.2	2.6	1.7

Scheme 2 shows the pore shapes before and after the extraction process, as well as the morphology of the encapsulated systems. According to Scheme 2, only the basic route did not afford alteration of pores shape after the extraction of RhB. SEM analysis suggests, as a general trend, that the particles showed a rough surface and very fine structure, which indicate the presence of nanopores. Similar behavior has already been reported in literature [36]. Moreover, formation of lamellae can be observed both in the acid 1 and acid 2 routes. A relationship between textural characteristics and imprinting properties can be noted if one compares the pore shape with extraction capacity of RhB (see Supporting Information Table S1). Except for the basic route, bottle-shaped pores of the extracted systems seem to be correlated with a good extraction capacity of RhB. This result suggests that textural properties may affect the maximum extraction capacity of the template. A correlation between surface area and RhB extraction capacity was also found: an increasing of S_{BET} is resulting from the RhB extraction capacity, except for the basic catalyzed material (see Supporting Information Fig. S4).

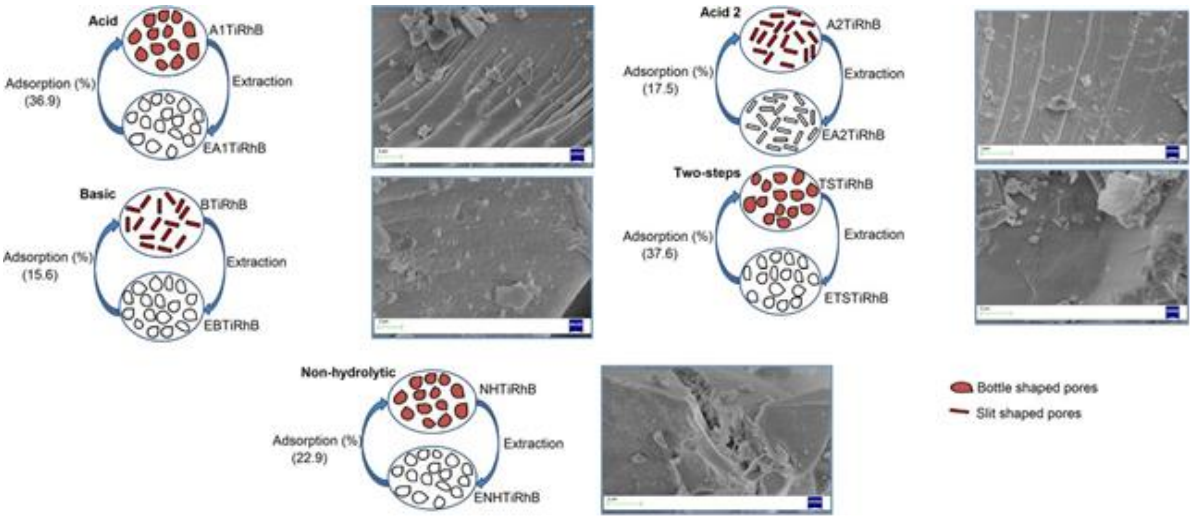

Scheme 2. Pore shapes before and after the extraction process and scanning electron microscopy of encapsulated systems.

As shown in Table 2, the imprinted xerogel yielded the highest adsorption capacity compared with the NI xerogel (bare silica). The systems EA1TiRhB and ENHTiRhB showed the highest imprinting factor (Table 2), which demonstrates that imprinted xerogels include specific RhB binding sites. The exception was the EBTiRhB system, which exhibited lower RhB removal and a 0.4 imprinting factor. One reason for this result may be that the RhB was leached from the silica network interior during the adsorption, which seems to be in agreement with the above discussion about textural properties. As discussed previously, this finding corresponds with a lower area compared with BTiRhB (Table 1). The extraction process was ineffective or the silica network was affected by the ultrasound process. Similar behavior was observed for ETSTiRhB; although the imprinting factor was 1.3.

The nonhydrolytic route showed the lowest value of surface area (Table 1). On the other hand, this system afforded the highest increasing in surface area after RhB extraction

(Supporting Information Table S1). Despite this, the system ENHTiRhB presented the lowest value of selectivity factor (Table 2). This result indicates that, although higher values of surface area could be related to dye extraction, the selectivity in RhB extraction seems not be determined by the surface area magnitude. This is clearly observed if one compares ETSTiRhB with EA1TiRhB, in which the former showed a surface area value 2.37 times lower than the latter but achieved high selectivity factor.

Competitive RhB adsorption by the imprinted sol–gel was also investigated using a Rh6G mixture for the EA1TiRhB and A1 systems. Figure 2 shows that the EA1TiRhB system removed 1.7 fold more RhB (27.2%) than Rh6G (15.8%). Similar to the selectivity experiments, these results suggest that imprinting was successful within the silica network. In addition, the imprinting factor was approximately 2, which also indicates that the imprinted sol–gel (EA1TiRhB) had better binding capacity.

It is worth mentioning that experiments were conducted considering NI samples containing $TiCl_4$ in its constitution. Nevertheless, no clear difference could be observed in comparable to systems synthesized in the absence of $TiCl_4$ (as used in the present manuscript). The aim of such approach is to produce MI materials bearing titania moieties within the matrix network, which may potentially act as photocatalyst centers. Thus, in an attempt to avoid false-positive results, we decided to compare adsorption experiments results with bare silica.

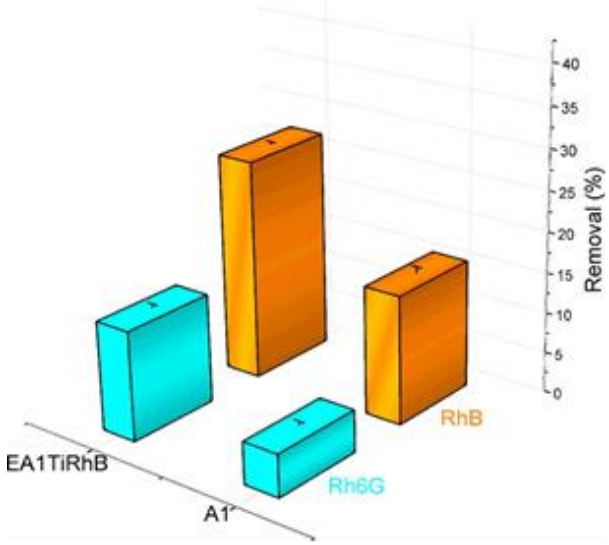

Figure 2. The sol–gel route influence on adsorption removal: competitive experiments (C_0 = 4 ppm and adsorption time = 1 h).

4 Conclusions

This study demonstrates that the sol–gel route employed during synthesis of the imprinting materials can affect the resulting xerogels' textural characteristics, which may affect the selective adsorption capacity. The preparation route affected the materials' textural properties, as demonstrated by the different nitrogen adsorption isotherm patterns, which depended on the route and surface area; the highest surface area systems were generated through the acid-catalyzed routes (acid-catalyzed and two-step routes).

Among the systems investigated, the nonhydrolytic route showed the greatest area increase after extraction, which was over tenfold greater compared with the encapsulated system (NHTiRhB). This result explains the higher imprinting factor achieved by this system (2.6). On the other hand, this route presented the lowest value of selectivity factor (1.74), which indicates that the selective extraction of RhB may be related to the generated silica network

shape rather to its surface area. Greater surface areas (EA1TiRhB and ETSTiRhB) influenced the maximum RhB removal. This trend is related to additional factors because the EBTiRhB system also produced an elevated surface area; although, it yielded the lowest RhB removal maximum.

This project was partially financed by the CNPq. C. Escobar is grateful for the grant provided by the CAPES. The authors also thank the LNLS (Project D11A-SAXS1-8691) for the SAXS beamline measurements.

5 References

[1] Chen, L., Xu, S., Li, J., Chem. Soc. Rev. 2011, 40, 2922– 2942.

[2] Cheong, W. J., Yang, S. H., Ali, F., J. Sep. Sci. 2013, 36, 609–628.

[3] Cunliffe, D., Kirby, A., Alexander, C., Adv. Drug Deliv. Rev. 2005, 57, 1836–1853.

[4] Liu, X., Lv, P., Yao, G., Ma, C., Huo, P., Yan, Y., Chem. Eng. J. 2013, 217, 398–406.

[5] Morais, E. C., Correa, G. G., Brambilla, R., dos Santos, J. H. Z., Fisch, A. G., J. Sep. Sci. 2013, 36, 636–643.

[6] Santos, W. d. J. R., Santhiago, M., Yoshida, I. V. P., Kubota, L. T., Sens. Actuators B Chem. 2012, 167, 739–745.

[7] Dai, C.-m., Geissen, S.-U., Zhang, Y.-l., Zhang, Y.-j., Zhou, X.-f., Environ. Pollut. 2011, 159, 1660–1666.

[8] Longo, L., Scorrano, S., Vasapollo, G., J. Polym. Res. 2010, 17, 683–687.

[9] Mayes, A. G., Whitcombe, M. J., Adv. Drug Deliv. Rev. 2005, 57, 1742–1778.

[10] Dıaz-Garcıa, M. E., Laınn˜ o, R. B., Microchim. Acta 2005, 149, 19–36.

[11] Walcarius, A., Collinson, M. M., Annu. Ver. Anal Chem. 2009, 2, 121–143.

[12] Farrington, K., Regan, F., Talanta 2009, 78, 653–659.

[13] da Costa Silva, R. G., Augusto, F., J. Chromatogr. A 2006, 1114, 216–223.

[14] Jiang, X., Zhao, C., Jiang, N., Zhang, H., Liu, M., Food Chem. 2008, 108, 1061–1067.

[15] Schubert, U., Hu¨ sing, N., Synthesis of Inorganic Materials, 2nd ed., Wiley-VCH, Weinheim 2004.

[16] Brinker, C. J., Scherer, G. W., Sol–gel Science: The Physics and Chemistry of Sol–gel Processing, Academic Press, New York 1990.

[17] Bourget, L., Corriu, R. J. P., Leclercq, D., Mutin, P. H., Vioux, A., J. Non. Cryst. Solids 1998, 242, 81–91.

[18] Hay, J., Raval, H., J. Solgel Sci. Technol. 1998, 13, 109–112.

[19] Bagheri, H., Piri-Moghadam, H., Anal. Bioanal. Chem. 2012, 404, 1597– 602.

[20] Xu, Z., Song, J., Li, L., Qiao, X., Chen, H., J. Sci. Food Agric. 2012, 92, 2696–2702.

[21] Tsai, H.-A., Syu, M.-J., Chem. Eng. J. 2011, 168, 1369–1376.

[22] Ornelas, M., Loureiro, D., Araújo, M. J., Marques, E., Dias-Cabral, C., Azenha, M., Silva, F., J. Chromaogr. A 2013, 1297, 138–145.

[23] Wu, J. B., Yi, Y. L., Korean J. Chem. Eng. 2013, 30, 1111–1118.

[24] Si, B., Zhou, J., Chin. J. Chem. 2011, 29, 2487–2494.

[25] Sakti, S. C. W., Siswanta, D., Nuryono, N., Pure Appl. Chem. 2013, 5, 211–223.

[26] Ramamoorthy, M., Ulbricht, M., J. Memb. Sci. 2003, 217, 207–214.

[27] Malaisamy, R., Ulbricht, M., Sep. Purif. Technol. 2004, 39, 211–219.

[28] Xu, X., Chen, S., Wu, Q., J. Colloid Interface Sci. 2012, 385, 193–201.

[29] Thomas, A. G., Syres, K. L., Chem. Soc. Rev. 2012, 41, 4207–4217.

[30] Ilavsky, J., Jemian, P. R., J. Appl. Crystallogr. 2009, 42, 347–353.

[31] Kline, S., J. Appl. Crystallogr. 2006, 39, 895–900.

[32] Connors, K. A. Eboka, C. J., Anal. Chem. 1979, 51, 1262–1266.

[33] Sing, K. S. W., Pure Appl. Chem. 1982, 54, 2201–2218.

[34] Rouquerol, J., Avnir, D., Fairbridge, C. W., Everett, D. H., Haynes, J. H., Pernicone, N., Ramsy, J. D. F., Sing, K. S.W., Unger, K. K., Pure Appl. Chem. 1994, 66, 1739–1758.

[35] Morais, E., Correa, G., Brambilla, R., Livotto, P., dos Santos, J., Cardoso, M., J. Solgel Sci. Technol. 2012, 64, 324–334.

[36] Munusamy, P., Seleem, M. N., Alqublan, H., Tyler Jr, R., Sriranganathan, N., Pickrell, G., Mater. Sci. Eng. C Mater. Biol. Appl. 2009, 29, 2313–2318.

[37] Dhanya, S., Joy, J., Rao, T. P., Sens. Actuators B Chem. 2012, 173, 510–516.

[38] Iler, R. K., The Chemistry of Silica: Solubility, Polymerization, Colloid and Surface Properties, and Biochemistry, Wiley, New York 1979.

[39] Curran, M. D., Stiegman, A. E., J. Non. Cryst. Solids 1999, 249, 62–68.

[40] Limpo, J., Bautista, M. C., Rubio, J., Oteo, J. L., Stud. Surf. Sci. Catal. 1994, 87, 429–437.

[41] Liu, X., Cui, D., Wang, Q., Xu, H., Li, M., J. Mater. Sci. 2005, 40, 1111–1114.

[42] Schmidt, P. W., The Fractal Approach to Heterogeneous Chemistry: Surface, Colloids, Polymers, Wiley, London 1989.

[43] Capeletti, L. B., Bertotto, F. L., Dos Santos, J. H. Z., Moncada, E., Cardoso, M. B., Sens. Actuators B Chem. 2010, 151, 169–176.

Supporting Information

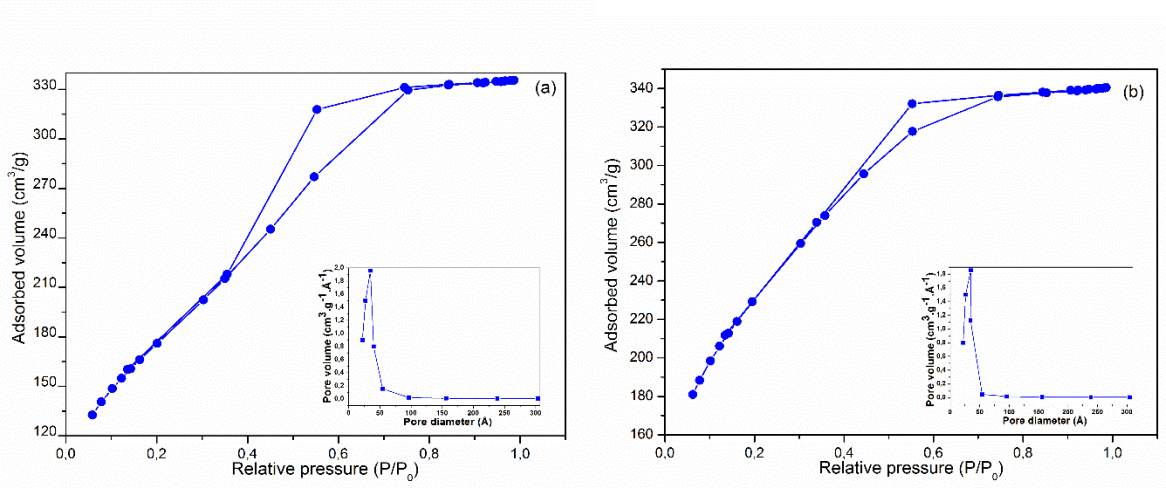

Figure S1: N_2 adsorption/desorption isotherms and pore-size distributions for (a) A1TiRhB and (b) EA1TiRhB

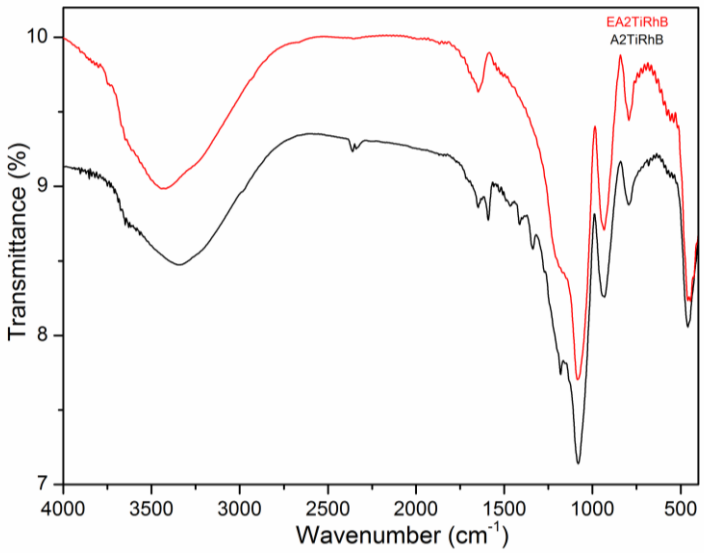

Figure S2: FT-IR for acid route 2 encapsulated (A2TiRhB) and extracted (EA2TiRhB).

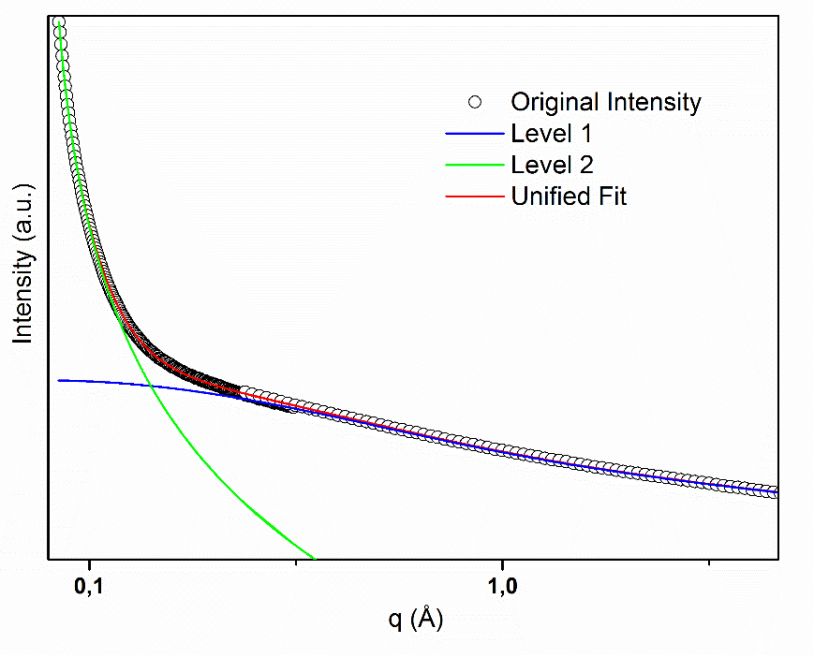

Figure S3: SAXS curve for acid route (A1TiRhB).

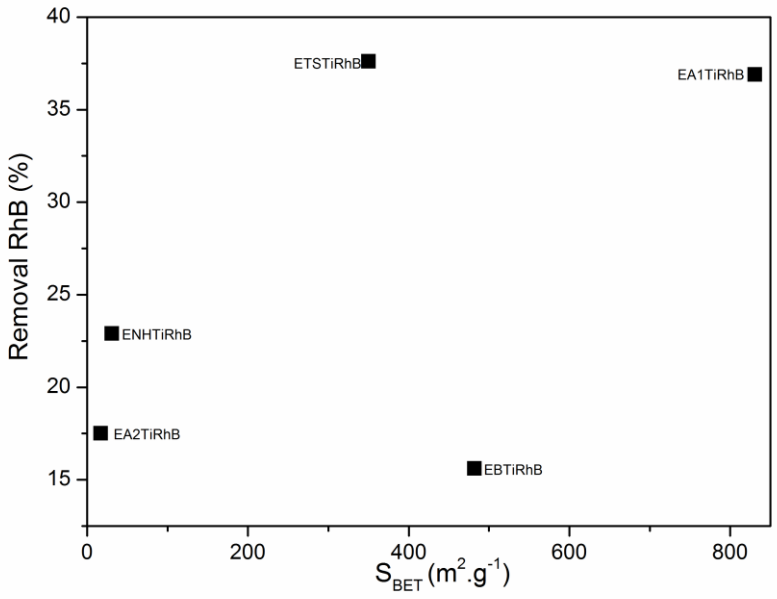

Figure S4: S_{BET} vs Removal of RhB for extracted systems.

Supplementary Table 1: Effect of the increase on S_{BET} after addition and extraction of RhB and influence of pore shape on RhB extraction capacity.

[a]

Route	Acid	Acid 2	Basic	Two Steps	Non-Hydrolytic
Increasing of S_{BET} after RhB addition (%) [a]	56	n.d.[(d)]	89	52	n.d. [(e)]
Increasing of of S_{BET} after RhB extraction (%) [b]	30	54	n.d. [(e)]	n.d. [(e)]	933
Pore shape of the extracted system [c]	bottle	slit	bottle	bottle	bottle
RhB extraction (%)	36.9	17.5	15.6	37.6	22.9

[a]Calculated considering the bare and encapsulated systems; [b] Calculated considering encapsulated and extracted systems; [c] Obtained from adsorption-desorption isotherms; [d] There is no bare silica for this system; [e] A decrease was obtained.

4.2 Artigo 2

Publicado no *Journal of Sol-Gel Science and Thecnology*, v. 72, p. 260-272, 2014.

J Sol-Gel Sci Technol
DOI 10.1007/s10971-014-3376-7

ORIGINAL PAPER

The role of the sol–gel route on the interaction between rhodamine B and a silica matrix

Cícero Coelho de Escobar · Mauro Henrique Dartora · Leandra Franciscato Campo · Claudio Radtke · Julia M. Bayne · Ian S. Butler · Rafael M. Lattuada · João Henrique Zimnoch dos Santos

Received: 18 November 2013 / Accepted: 22 April 2014

Abstract A series of silica xerogels having rhodamine B (RhB) as a template and Ti centers were synthesized by distinct sol–gel routes, namely, acid-catalyzed, base-catalyzed, acid-catalyzed with base-catalyzed (two steps) hydrolytic routes and a $FeCl_3$-catalyzed non-hydrolytic route. The interaction of RhB with the prepared silica matrix was investigated by Fourier transform infrared spectroscopy, attenuated total reflectance, diffuse reflectance spectroscopy in the ultraviolet–visible region, Raman spectroscopy, mass spectrometry, X-ray photoelectron spectroscopy (XPS), photoluminescence (PL) and confocal microscopy. Raman spectroscopy suggested the presence of Ti–O and Si–O–Ti moieties within the silica matrix. Infrared band shifts provided insight into potential interaction sites. Taking into account the results from ART, XPS, PL and confocal microscopy, encapsulation of RhB preferentially occurs inside the silica network for acid 1, basic and two-steps routes, and the presence of Ti occurs on the surface of the silica occurs for acid 2, basic and two-steps routes. Also, we have shown that although the structural characteristics of the encapsulated and extracted systems are affected by the route, the molecular structure is conserved during and after the encapsulation process.

Keywords Hydrolytic sol–gel · Non-hydrolytic sol–gel · Rhodamine · Encapsulation

Introduction

The sol-gel process is a potential tool for encapsulating labile organic molecules, enzymes and cells within inorganic oxide matrices at mild conditions (low temperature and pressure) [1, 2]. The interaction between the encapsulated molecule and matrix network determines the degree to which the molecule retains its native properties [3]. Several efforts have been made to provide optimized (bio)materials suitable for a variety of applications, including selective coatings for optical and electrochemical biosensors [4, 5], catalysts [6], and drug delivery systems [7, 8], to name a few.

Evaluating the interaction between encapsulated molecules and a matrix such as silica is not an easy task. In some cases, even sensitive techniques such as Raman spectroscopy can only provide information about the xerogel structure [9]. Depending on the nature of the encapsulated molecules, the interaction can sometimes be estimated using X-ray photoelectron spectroscopy [10], FT-IR [11,12], solid-state ^{29}Si MAS NMR [7], UV-Vis spectroscopy [10, 13], Raman spectroscopy [14], SAXS [15], X-ray diffraction techniques [16], and cyclic (CV) or differential pulse voltammetry [9].

Information about the nature of these interactions will inform the development of hybrid materials, particularly how to tune the strength of the interactions depending on the intended final material application [10].

In this study, we investigated the effect of different sol-gel routes on the final material structure. A series of silica-based materials with Ti centers for potential adsorption/interaction sites were prepared by different sol-gel processes, namely, hydrolytic (base- and acid-catalyzed), two-step (base catalysts with acid catalysts) and non-hydrolytic routes. We also investigated the interaction between the template (Rhodamine B) and the silica network. To our knowledge, the

effect of the sol-gel route both during and after encapsulation on the structure of the silica matrix has not been comparatively investigated in the literature. Such information is very relevant to the development of adsorption/preconcentration phases for solid phase extraction methodologies or to the development of materials for selective photocatalysis. To investigate the interaction of Rhodamine B with prepared silica matrixes, transmission and attenuated total reflectance (ATR) Fourier transform infrared (FT-IR) spectroscopy, Raman spectroscopy, ultraviolet-visible diffuse reflectance spectroscopy (UV-Vis DRS) and mass spectroscopy (MS), X-ray Photoelectron Spectroscopy (XPS), photoluminescence (PL) and confocal microscopy were employed.

Materials and methods

Rhodamine B (Vetec), tetraethoxysilane ($Si(OCH_2CH_3)_4$, TEOS, Merck, >98%), titanium tetrachloride (Merck, >99%) and silicon tetrachloride ($SiCl_4$, Sigma–Aldrich, 99%) were used as received. Hydrochloric acid (HCl, Nuclear, 38%), ammonium hydroxide (NH_4OH, Nuclear, 29%) and $FeCl_3$ (98%, Merck) were employed as catalysts.

Preparation of sol-gel materials

Samples were prepared by five different sol-gel routes with TEOS as the raw material. These routes were labeled as follows: acid-catalyzed route 1 (A1), acid-catalyzed route 2 (A2), base-catalyzed route (B), two-step route (TS) and non-hydrolytic route (NH). Acid-catalyzed route 1 was catalyzed by 0.2 M hydrochloric acid in a 1:2 (HCl:TEOS) ratio. Acid-catalyzed route 2 was similar to acid-catalyzed route 1, but without the hydrochloric acid (i.e., $TiCl_4$ alone acted as a potential Lewis acid catalyst). The base-catalyzed route was catalyzed by 0.2 M ammonium hydroxide in a 1:2 (NH_4OH:TEOS) ratio. The two-step route was catalyzed by 0.2 M hydrochloric

acid in a 1:2 (HCl:TEOS) ratio; then, after 30 min., 0.2 M ammonium hydroxide was added in a 1:2 (NH_4OH:TEOS) ratio. The non-hydrolytic route employed TEOS and $SiCl_4$ and was catalyzed by $FeCl_3$ (0.5 wt.% of final product weight). For all samples, the total amount of Rhodamine B (RhB) was fixed at 5 wt.% of the final xerogel weight.

The samples (powder) obtained by the acid-catalyzed, base-catalyzed and two-step routes were prepared as follows: first, Rhodamine B (0.313 mmol) was added to a solution of TEOS (51.5 mmol), followed by $TiCl_4$ (3.16 mmol), and then, finally, the catalyst (5.5 mL) was introduced. The solution was constantly stirred at room temperature throughout this process until gelation or precipitation. The time of aging was different for each route (Scheme 1). For the non-hydrolytic route, all procedures were carried out in an inert atmosphere (Ar). TEOS (8.95 mmol), $SiCl_4$ (8.32 mmol) and $TiCl_4$ (2.1 mmol) were added after the catalysts; Rhodamine B was the last added reagent. The resulting solution was stirred at 80°C until gelation. All solids were dried at room temperature and milled. For template removal, ultrasound-assisted extraction was employed with methanol as the solvent. The process consisted of a pulsed cycle (20 s on, 5 s off) lasting five min. The solids were filtered and dried at room temperature.

The resulting samples were labeled according to the sol-gel route; for example, NH denotes the non-hydrolytic route. The use of $TiCl_4$ and the presence of encapsulated Rhodamine B were represented by the labels Ti and RhB, respectively. Where necessary, E denotes systems after template extraction. Therefore, ENHTiRhB refers to a xerogel prepared through the non-hydrolytic route that employed $TiCl_4$ during synthesis and had Rhodamine B extracted. For comparison, bare silica samples were also synthesized under equivalent conditions without a template. Thus, NH refers to a xerogel prepared through the non-hydrolytic route without the addition of $TiCl_4$ and Rhodamine B. Scheme 1 depicts the sol-gel routes studied and the materials they produced.

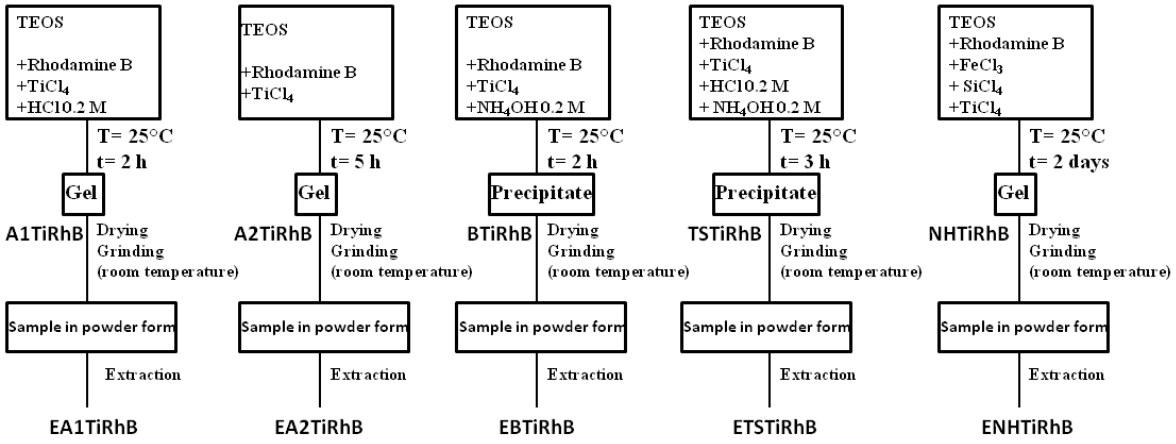

Scheme 1: All of the employed sol–gel routes.

Xerogel Characterization

The specific surface area was determined by the Brunauer-Emmett-Teller (BET) method at -196 °C, in the partial pressure range of $0.2 < P/P_0 < 0.9$. Prior to each measurement, samples were preheated at 110°C for 14 h under vacuum.

FT-IR spectroscopic measurements were recorded at room temperature on a Bomem MB-102 Spectrometer by co-adding 36 scans with a resolution of 4 cm^{-1}. Samples were diluted in dried KBr and measured as pellets. ATR measurements were carried out under the same conditions using the same tool in a different operating mode.The υ_{as}(Si-O-)Si and the υ_{s}(Si-O-)Si spectral regions (900-1300 cm^{-1}) contain four contributions to the υ_{as}(Si-O-)Si (the longitudinal, LO, and transverse optical, TO, components of the six and four-member siloxane rings, LO_6, LO_4, TO_6 and TO_4), and two components in the υ_{s}(Si-O-)Si band (the stretching of Si-O bond, both in Si-OH and in $Si-O^-$ groups) [17]. For a detailed structural analysis, the spectral regions between 900 and 1300 cm^{-1} were independently deconvoluted into Gaussian components using a nonlinear least-squares fitting

method [1717]. The percentage of six-membered rings, $\%(SiO)_6$, was estimated as described by Cappeletti et al. [18].

The percentage of six-member rings ($\%(SiO)_6$) was estimated as the following ratio of fitted areas:

$$\%(SiO)_6 = 100 \times [A(LO_6) + A(TO_6)/A(LO_6) + A(LO_4) + A(TO_4) + A(TO_6)] \quad (1)$$

Raman measurements were performed at room temperature using an inVia Renishaw Raman microscope system with a long-working distance lens (50×) equipped with a near-infrared diode laser (785 nm), a charge-coupled detector and a 1200 lines mm^{-1} diffraction grating. The spectra were recorded at a laser power of 300 mW with a 20 s acquisition time. Data acquisition and analyses were accomplished with WiRETM software.

Samples were analyzed in a UV–Vis region (DRS) accessory equipped with a round sampling cup covered by a quartz window. The spectra were recorded at room temperature on a Varian Cary 100 UV–Vis spectrophotometer by co-adding 32 scans in the 200–800 nm range. Spectra were measured before solvent extraction.

The X-ray Photoelectron Spectroscopy (XPS) measurements were performed on a machine-Omicron SPHERA employing radiation Al / Kα (1,486.6 eV) and the anode was operated at 225 W (15 kV, 15 mA). Investigative spectrum was obtained with an energy of 50 eV step. Specific regions of interest were recorded at a higher resolution (pass energy of 20 eV). The detection angle of photoelectrons with respect to the sample was fixed at 0° for all measurements. All spectra were fitted assuming a Shirley background. The signal from adventitious carbon C (1s) at 285 eV was used as an internal reference to correct the energy. The lines were fitted by a

combination of Gaussian and Lorentzian functions, setting a value width at half height for each line. A numerical analysis of the peaks was performed using Multipack program provided by the manufacturer, which assesses the peak area and uses tables with sensitivity factors for quantitative analysis. Spectra were taken before solvent extraction.

Mass spectrometry was carried out on a SHIMADZU, model GCMS-QP2010S, with a direct sample inlet device. The samples were prepared by adding ca. 2 mL of acetone to ca. 5 mg of powder, resulting in a slurry material. Then, ca. 10 μL of this slurry was transferred into a microvial (capacity of 25 μL) using a capillary. The solvent was then dried at room temperature and pressure. Next, the microvial was put in an insertion probe and introduced into the injection port via the insertion inlet. The temperature was programmed to initially reach 70°C at 80°C/min, hold there for 1 min, climb to 320°C at 40°C/min, and then finally climb to 350°C at 20°C/min and hold there for 10 min. The total analysis time was 21 min. The ion source and the interface were kept at 260 and 250°C, respectively. Acquisition was performed with SCAN at 50 (m/z) to 1090 (m/z).

Fluorescence emission spectra were obtained on a Shimadzu RF-5301PC spectrofluorometer at room temperature. The emission wavelength was fixed at 545 nm for all samples.

Confocal microscopy were conducted on a zoom microscope, model V16 from Carl Zeiss Inc., equiped with fluorescence system (HXP 200), objectives PlanNeoFluoar with 1.0 and 2.3× of magnification, eyepiece of 10×/ 23 mm and body with magnification range of 0.75 - 8.0× (motorized - extended focus), with Axiocam MRc for image acquisition.

Results and Discussion

Table 1 shows the surface area (S_{BET}) values for encapsulated and extracted systems. The acid route (A1TiRhB) generated the highest S_{BET} values, which is in agreement with materials prepared by this route, reported in the literature [19; 20]. Considering S_{BET} from the initial xerogel (639 m^2g^{-1}), the extraction step increased the surface area (ca. 35 % after the extraction), indicating that the dye was removed from the silica matrix. Thus, the increased surface area after the extraction process can be attributed to cavity formation [21, 22]. An increase in S_{BET} after RhB extraction is also seen for A2 (54 %) and NH routes (933 %). The basic-catalyzed and two-steps routes did not show an increase in surface area after the extraction process. One should note that NH_4OH was employed as the catalyst in both routes. As discussed in our previously work [22], sol-gel processes using a basic pH yield materials with a compact morphology [23]. Thus, the silica network with the dye should be texturally altered during extraction [22].

Table 1: Effect of the increase on S_{BET} after extraction of RhB.

Route	S_{BET} (m^2/g)	Increasing of of S_{BET} after RhB extraction (%)[a]
A1TiRhB	639	30
EA1TiRhB	831	
A2TiRhB	11	54
EA2TiRhB	17	
BTiRhB	511	n.d.[b]
EBTiRhB	482	
TSTiRhB	568	n.d.[b]
ETSTiRhB	350	
NHTiRhB	10	933
ENHTiRhB	31	

[a] Calculated considering encapsulated and extracted systems; [b] A decrease was obtained.

Fig. 1 shows the FT-IR spectra of acid and non-hydrolytic routes for encapsulated (A1TiRhB and NHTiRhB) and extracted (EA1TiRhB and ENHTiRhB) systems. The broad band at ca. 3,450 cm^{-1} is assigned to the OH stretching of silanol groups (interacting through hydrogen bonds) and residual adsorbed water, which can be confirmed by the deformation band present at 1,640 cm^{-1}. The strong absorption bands at 790 and 1,080 cm^{-1} correspond to asymmetrical and symmetrical Si-O stretching of the Si-O-Si network, respectively [24, 25]. The stretching vibration of Si-OH occurs at 950 cm^{-1} [26].

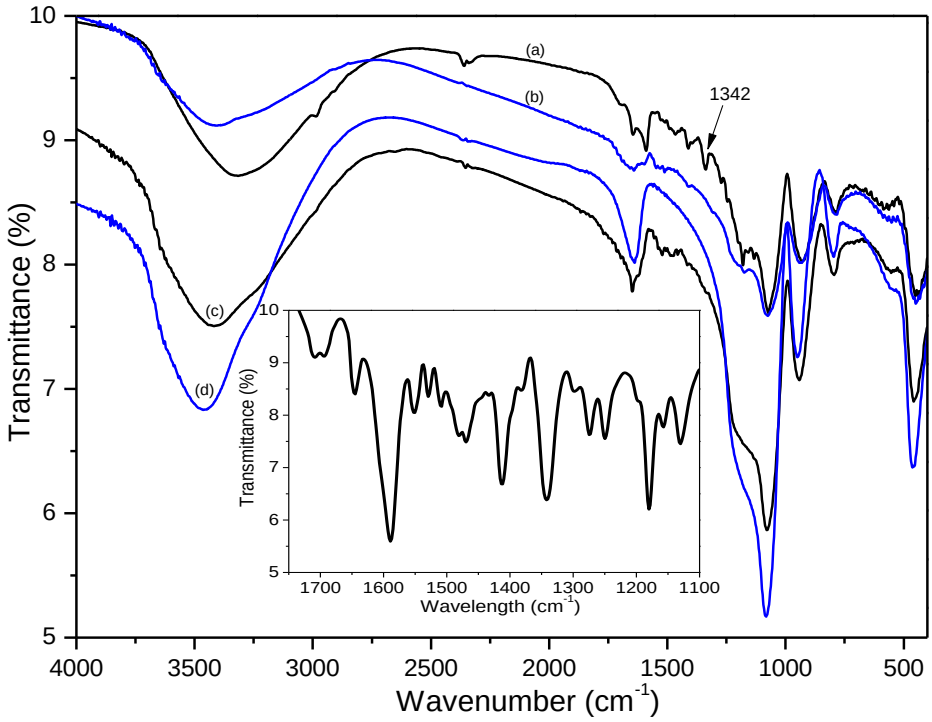

Fig. 1: FT-IR spectra for encapsulated (black line) and extracted (blue line) samples. (a) NHTiRhB, (b) ENHTiRhB, (c) A1TiRhB, (d) EA1TiRhB. Insert: FT-IR spectrum of Rhodamine between 1100 and 1550 cm^{-1}.

The main bands detected in the FT-IR spectra of encapsulated systems (Fig. 1 (a) and (c)) can be associated with Rhodamine B (Fig. 1 - Insert). It is worth noting that some bands present in NHTiRhB are absent in A1TiRhB. For instance, as observed in Fig. 1, the 1,342 cm^{-1} band, assigned to asymmetric stretching of C-N-linked benzene ring and C-O-C [27] for NHTiRhB (spectrum a), is absent after extraction in system ENHTiRhB (spectrum b). Some of the main bands of Rhodamine B showed wavenumber shifts. Table 2 summarizes the band shifts for all Rhodamine encapsulated systems. Excepting for the basic-catalyzed route (BTiRhB), all other systems exhibited wavenumber shifts consistent with the spectrum of free Rhodamine, suggesting an interaction between some dye structure groups and the silica network.

Table 2: Main bands of Rhodamine and their post-encapsulation band shift in the silica matrix.

Neat Rhodamine		Encapsulated – Δν (cm^{-1})				
Wavenumber (cm^{-1})	Assignment	A1TiRhB	A2TiRhB	BTiRhB	TSTiRhB	NHTiRhB
1,708	C=O stretching [28]	+6	+8		+8	-6
1,180	Asymmetric stretch of (C-O)-C [27]					+1
1,249	Stretch of C–N in $–N(C_2H_5)_2$ group [27]					-6
1,342	Asymmetric stretch of C-N-linked benzene ring and of C-O-C [27]		-6			+1
1,412	Bending of CH_2 in $–N^+(C_2H_5)_2$ [27]		-1		-10	+1
1,529	Stretching modes of aromatic groups [29]	-8	-2			
1,589	Stretch mode of C=C in benzene rings [27]		+1			+1
2,870	Symmetric streching of CH_3 [30]					-16
2,930	Antisymmetrical stretches of CH_2 [28]					+5
2,979	Asymmetric stretches of CH_3 [31]					+2

The band shifts suffered by the organic chemical groups toward higher wavenumbers may result from a strong rearrangement of such chemical functions. The functional groups whose absorption bands were shifted toward lower wavenumbers (hypsochromic shift) may result from an increase in tension from the rotational conformation of the molecule [32]. This tension increase may occur because encapsulation may make the vibrational movements of the functional groups difficult and therefore demand more energy [10].

For the system A1TiRhB, the most evident band shift is attributed to the asymmetric stretching of C-N-linked benzene ring, which indicates an interaction between surface silanol and the π-electron system of the aromatic ring present in RhB. Similar results have been reported elsewhere [33, 34]. The systems A2TiRhB and TSTiRhB showed shifts in the bands related to the N-containing groups. As discussed by Morais et al [10], this result indicates the possibility of a hydrogen bonding interaction between the dye and the silica via electron donation of these groups to the silica network. Additionally, considering the incorporation of Ti within the silica matrix (discussed later in the text), the band shift showed by these systems may represent an indication of interaction with Ti atoms. The system NHTiRhB showed a significant band shift attributed to symmetric stretching of methyl groups. According to the literature, methyl groups may facilitate the retention of the molecule in the silica network [35], which may have cause the higher band shift observed in this system. In addition, such systems showed a band shift involving nitrogen moieties most likely to the Lewis acid center, namely, the Ti atoms. Finally, except for RBTiRhB, all other systems showed a band shift related to the carbonyl centered at 1708 cm^{-1} [28]. Additionally, a reduction in band intensity was observed, which suggests an interaction with the silica through this chemical group [10]. By taking into account the results of wavenumber shifts

for each route, it is possible to propose a model that summarizes all the potential interactions of the rhodamine with the silica network, as depicted in Scheme 2.

FT-IR analysis is also a powerful technique for interpreting the silica structure resulting from the presence of encapsulated Rhodamine. Because the Si-O-Si bands provide a fingerprint for silica [36], information on the primary cyclic arrangement of structural SiO_4 units in xerogels can be extrapolated. Thus, it is possible to relate this information to crystallinity and hydrophilicity/lipophilicity [37].

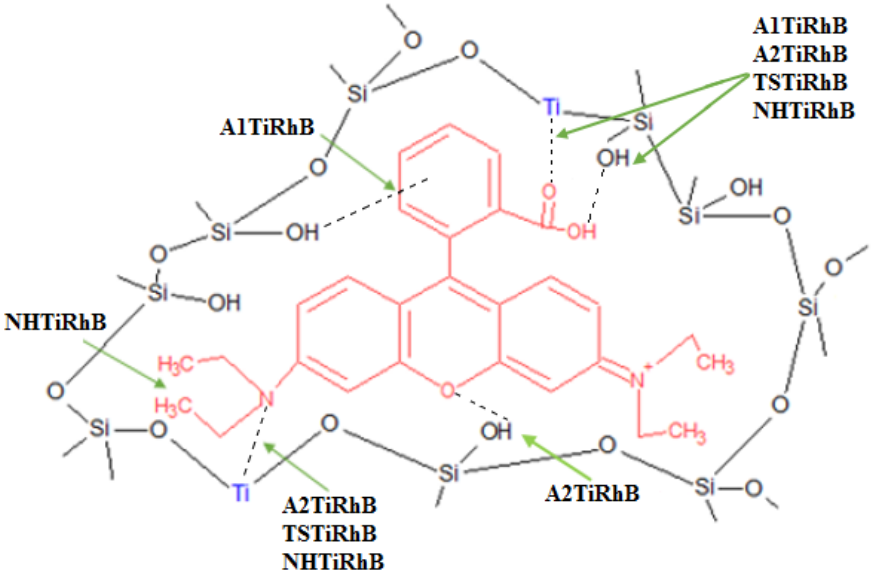

Scheme 2. Proposed interaction between Rhodamine and the silica network.

Fig. 2 shows the bare silica fingerprint region obtained from the acid 1 route (A1). Asymmetric stretching of sequential Si-O-Si groups in the transversal optic (TO) mode appears most intensively at 1,084 cm^{-1}. The shoulder at approximately 1,190 cm^{-1} is related to the

longitudinal optic (LO) element of the same vibration [38]. The bands at 564 and 944 cm^{-1} are due to TO and LO optic modes, respectively. The latter corresponds to Si-O- group stretching, the former to the rocking mode. Rocking vibrations (the oxygen of Si-O moves out of the plane of Si-O-Si) and bending vibrations (O atom vibration occurs along the plane and the angle bisector formed by Si-O-Si) both relate to the LO mode and were observed at 455 and 794 cm^{-1}, respectively [36].

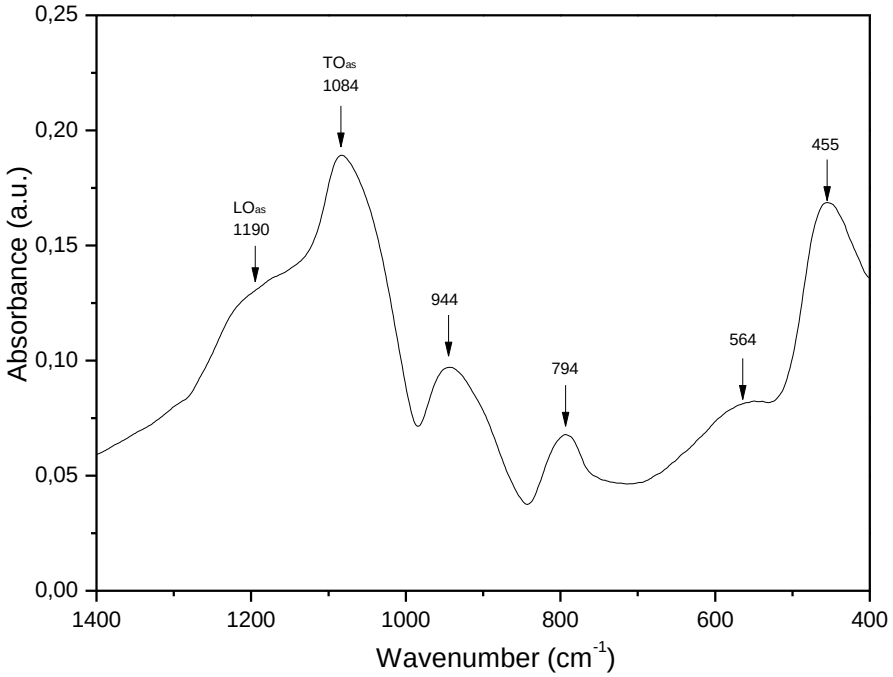

Fig. 2: Characteristic band of Si-O-Si vibrations in bare silica obtained for the acid route (A1).

Table 3 compares the stretching frequencies (ν_{Si-O}) of silanol groups in bare silica (obtained from the different sol-gel routes) with the corresponding encapsulated systems (943 – 964 cm^{-1}). No band shift was observed for the acid 1 and two-step routes. In the basic and non-hydrolytic

routes, however, the band shifted to a lower wavenumber. This behavior suggests interactions with the xerogel through electron displacement.

The interval of bands shown in Table 3 (943 – 964 cm^{-1}) is widely accepted as the characteristic set of vibrations of Ti-O-Si formation [39] and thus indicates this formation in systems where $TiCl_4$ was added during synthesis. The exact band position depends on the chemical composition of the sample as well as the calibration and resolution of the instrument. To investigate the contribution of Ti to the silica network, the area ratio between the Si-O-Si, ca. 1,200 cm^{-1} (obtained from deconvolution), and Ti-O-Si, ca. 940 cm^{-1}, vibration peaks was estimated for A1 and A1Ti; the calculated values were 0.57 and 0.65, respectively. This finding suggests that in the A1Ti system, the presence of Ti indeed affected the silica network.

Table 3: Stretching frequencies (ν_{Si-O}) of silanol groups in bare silica and encapsulated systems.

System	Frequency (cm^{-1})
A1	943
A1TiRhB	944
A2TiRhB	943
B	964
BTiRhB	943
TS	943
TSTiRhB	942
NH	954
NHTiRhB	943

The bands from 1,300 to 1,000 cm^{-1}, corresponding to Si-O-Si moieties, were deconvolved using Gaussian curves for evaluation in terms of LO and TO modes for four and six-membered rings [37]. A typical FT-IR spectrum of the deconvolved bands is shown in Fig. 3. As discussed in the literature [6], changes in the $\nu_{as}(Si-O)_{Si-O-Si}$ band could be related to the

concentration of $(SiO)_6$ (especially TO_6) and $(SiO)_4$ (especially LO_4) components. The presence of rhodamine may reduce long-range Coulomb interactions; thus, the LO/TO ratio could be affected. The $(SiO)_6$ content was calculated according to Eq. 1.

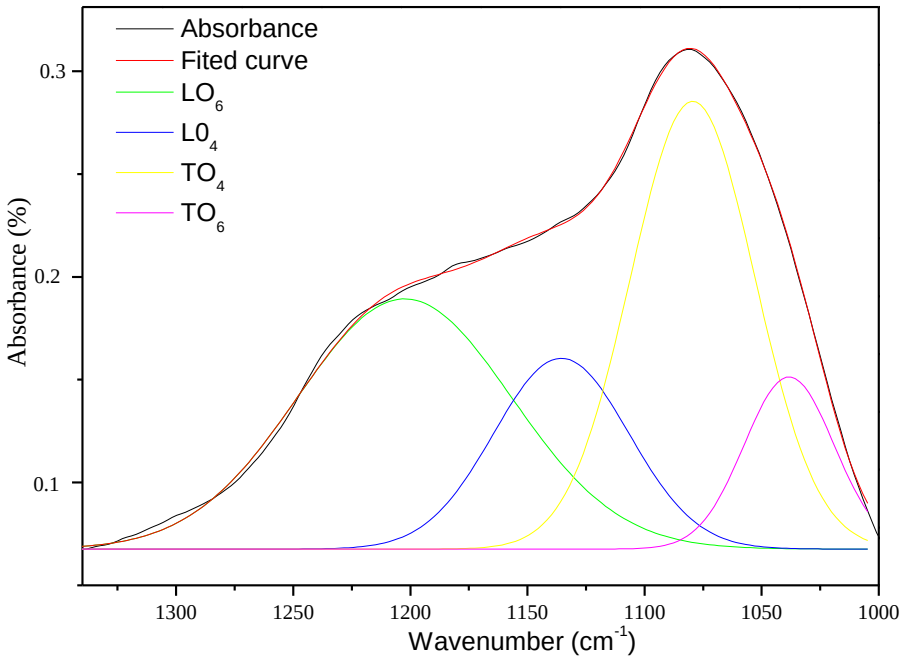

Fig. 3: Band deconvolution of asymmetric stretching of the as(Si-O(-Si)) bond in the A1TiRhB FT-IR spectrum.

All other samples were also deconvolved, and the $\%(SiO)_6$ was calculated. The results are shown in Table 4, together with the maximum peak center wavenumber and relative area. For comparison, bare silica was also investigated. As observed in Table 4, the $\%(SiO)_6$ ranged from 45 to 70 %. The presence of rhodamine in the sol-gel syntheses of silica-based hybrid materials caused different network structures depending on the synthesis protocol. In the case of the basic route (BTiRhB), there was an increase in $(SiO)_6$ rings compared to the bare system (B). In contrast, all other routes showed a decrease in $(SiO)_6$ percentage after encapsulation. This result suggests

that the addition of rhodamine in the synthesis of BTiRhB produced a denser, more compact network compared to the other systems. The increase in six-membered rings in BTiRhB most likely occurs because this structure has less tension and thus could accommodate the organic species in the tridimensional network with greater ease. This outcome is in agreement with previous description of sol-gel reaction under basic-catalyzed conditions, in which the condensation rate is rapid compared to that under hydrolysis conditions. Therefore, a more compact xerogel is typically formed [23]. However, one may note that the two-steps route, which also includes a basic-catalyzed step, did not show an increase in $(SiO)_6$ percentage after encapsulation. This behavior can be explained by the nature of protocol synthesis, in which both HCl and $TiCl_4$ were simultaneously added, followed by the addition of NH_4OH after 30 minutes. Thus, the structure of the silica could be dramatically influenced during the first 30 minutes of the the acid step, which in turn could affect the final xerogel and, therefore, affect the $(SiO)_6$ percentage in a similar way that was found in the acid 1 and acid 2 routes.

After extraction, the percentage of $(SiO)_6$ in the acid, two-step and non-hydrolytic routes increased. This result indicates that the Si-O-Si bonding arrangements in these systems experienced less stress.

Table 4: Areas of contribution, obtained using the deconvolution of the band between 1300 and 1,000 cm^{-1} and the $(SiO)_6$ percentage for each system.

Sample	LO_6	LO_4	TO_4	TO_6	r^2	$\%SiO_6$
	Band center (cm^{-1}); area (a.u)					
A1	1,186; 9.16	1,142; 0.78	1,081; 7.48	1,032; 2.92	0.9930	59.40
A1TiRhB	1,202; 19.93	1,135; 4.71	1,079; 14.51	1,038; 4.02	0.9998	45.83
EA1TiRhB	1,196; 20.51	1,125; 9.10	1,075; 16.54	1,038; 4.05	0.9989	48.92
A2TiRhB	1,180; 19.05	1,130; 0.252	1,080; 12.15	1,033; 4.25	0.9994	65.26
EA2TiRhB	1,180; 18.45	1,144; 0.382	1,078; 12.65	1,031; 3.72	0.9989	62.97
B	1,192; 17.5	1,161; 0.688	1,103; 16.76	1,053; 5.95	0.9989	57.33
BTiRhB	1,201; 22.00	1,127; 6.34	1,087; 6.72	1,048; 12.00	0.9992	72.24
EBTiRhB	1,206; 15.42	1,141; 4.15	1,080; 15.07	1,036; 4.05	0.9991	50.32
TS	1,187; 28.40	1,136; 2.12	1,076; 16.65	1,033; 4.51	0.9988	63.68
TSTiRhB	1,213; 8.95	1,147; 5.80	1,079; 13.8	1,035; 2.20	0.9981	36.26
ETSTiRhB	1,186; 48.57	1,138; 3.27	1,075; 32.00	1,030; 9.46	0.9986	62.20
NH	1,180; 40.94	1,115; 6.07	1,071; 23.72	1,033; 6.72	0.9978	61.53
TSTiRhB	1,341; 1.07	1,170; 30.08	1,072; 11.94	1,027; 2.79	0.9934	8.41
ENHTiRhB	1,228; 0.33	1,170; 9.26	1,075; 6.30	1,028; 2.47	0.9993	15.24

Fig. 4 shows the ATR results for encapsulated systems (A1TiRhB and NHTiRhB). The non-hydrolytic route showed rhodamine-more related bands than the acid 1 route. Thus, it is reasonable to assume that encapsulation preferentially occurs on the silica surface in the non-hydrolytic route. Similar behavior was observed for A2TiRhB and TSTiRhB. Interestingly, the absence of HCl in the acid route (A2TiRhB) changed the dye distribution in the silica network.

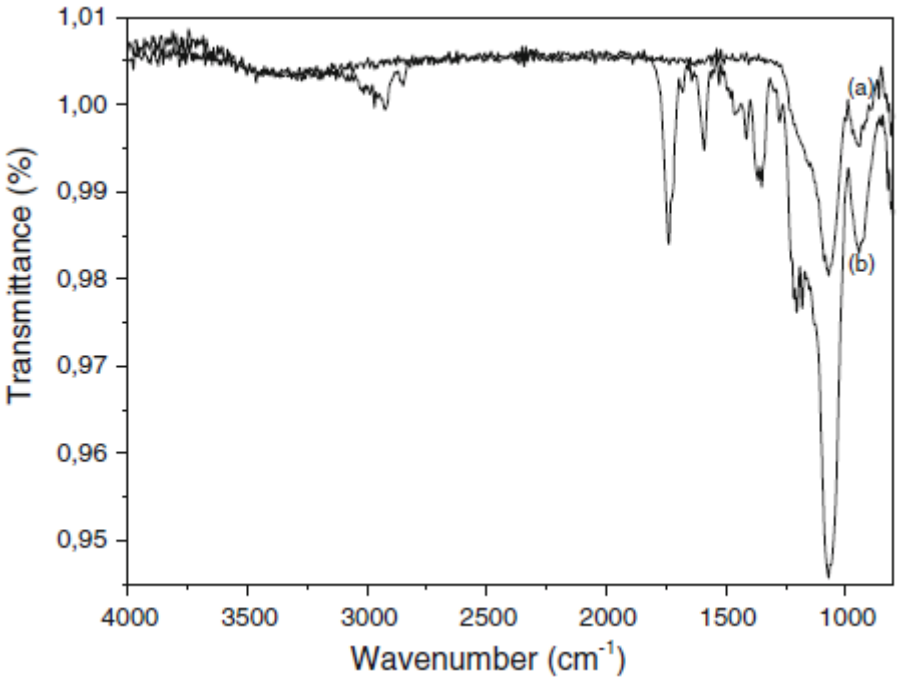

Fig. 4: ATR spectra for encapsulated samples. (a) A1TiRhB, (b) NHTiRhB.

Attempts to investigate the presence of Ti-O(-Si) moieties were carried out using Raman spectroscopy. Fig. 5 compares typical Raman spectra for different samples produced using the acid 1 route: A1TiRhB (encapsulated), A1Ti (bare silica with $TiCl_4$ during the synthesis) and A1 (bare silica). Four bands, at 583, 618, 927 and 1,089 cm^{-1}, were observed in A1TiRhB and A1Ti; the first two are assigned to asymmetric stretching of Ti-O [40], and the last two are assigned to Si-O-Ti bonds [39, 41, 42]. These bands are absent in the A1 system, as expected. Moreover, the band near at 920 cm^{-1} related to the Si-O-Ti only appeared in the system A1TiRhB. Similarly, the band at 1,089 cm^{-1} related to the Si-O-Ti only appeared in the A1Ti system. It is possible that confinement within the silica network (depending on the sol-gel route) altered the molecular symmetry of the dye, which migh have affected the active bands in the Raman spectrum. Similar bands were found in other routes, although these four peaks were not always evident. Table 5

summarizes the band attribution related to Ti-O-Si moieties for samples that employed $TiCl_4$ during synthesis.

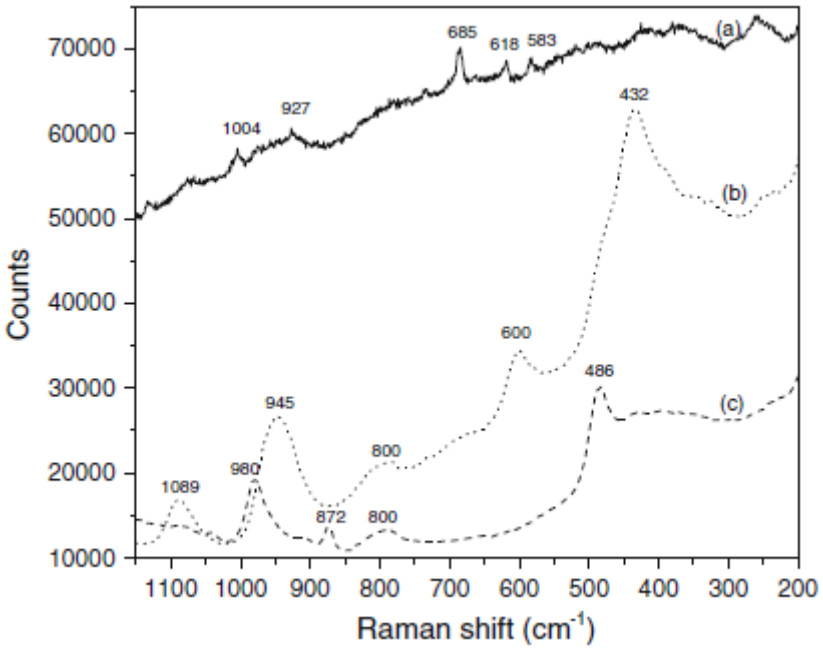

Fig. 5: Raman spectra. (a) A1TiRhB, (b) A1Ti, (c) A1.

Table 5: Band attribution of Raman spectra related to Ti-O-Ti bonds and Ti-O stretching for each system.

System	Attribution (cm^{-1})				
	Ti-O-Ti Bond [40]	Asymmetric stretching of Ti-O [40]	Asymmetric stretching of Ti-O [40]	Si-O-Ti bond [39, 41, 42]	Si-O-Ti bond [39, 41, 42]
A1TiRhB		583	618	927	
A1Ti					1,089
A2TiRhB			618		1,076
A2Ti					1,089
RBTiRhB			618		
Bti					1,089
TSTiRhB		583	618	926	1,072
TSTi					1,089
NHTiRhB			616		1,035
NHTi	330	589		920	

As observed in Table 5, most of the systems showed the band associated with Si-O- near 1,090 cm^{-1}. Furthermore, the 618 cm^{-1} band associated with Ti-O stretching appeared in all encapsulated systems. Interestingly, the NH system contained the only peak associated with Ti-O-Ti to exhibit a lower Raman shift. Thus, the results presented in Table 5 evidence an interaction between Ti and the silica network.

Raman spectra can also be used to investigate silica structures, as illustrated in Fig. 5. The bands at 432 cm^{-1} (A1Ti) and at 486 cm^{-1} (A1) are associated with a network of Si-O-Si bond bending vibrations, and the band at 800 cm^{-1} is assigned to (Si-O)-Si network symmetric bond

stretching vibrations [39]. Comparing the system without Ti (A1) to the system with Ti (A1Ti), the latter showed a new band assigned to the Si-O-Ti bondings [15, 17]. Additionally, it is possible to note the presence of a shoulder near 600 cm^{-1} for the system A1Ti that arises mainly from network defects in the gel structure [43, 44]. Such defects, formed by breaking Si–O bridging bonds, cause bending of the oxygen bonds participating in the 'defective' structures, which appear as a band centered at 685 cm^{-1} for system A1TiRhB [45]. Considering that the mainly differences between these systems are the addition of $TiCl_4$ and RhB, one cannot neglect the influence of both during the formation of the silica network. Finally, the bands located at 980-945 and 1,004 cm^{-1} can be associated with Si-O(H) stretching [43,46]. As discussed by Gao et al [42], the Raman band at 940-960 cm^{-1}, present in A1Ti and absent in A1, may be associated with Si-OH groups perturbed by nearby Ti cations, which result from the hydrolysis of Ti-O-Si bonds.

The effect of the sol–gel route was further investigated by diffuse reflectance spectroscopy in the UV–Vis region (UV-DRS), as shown in Fig. 6. The spectrum of neat rhodamine was also included for comparison.

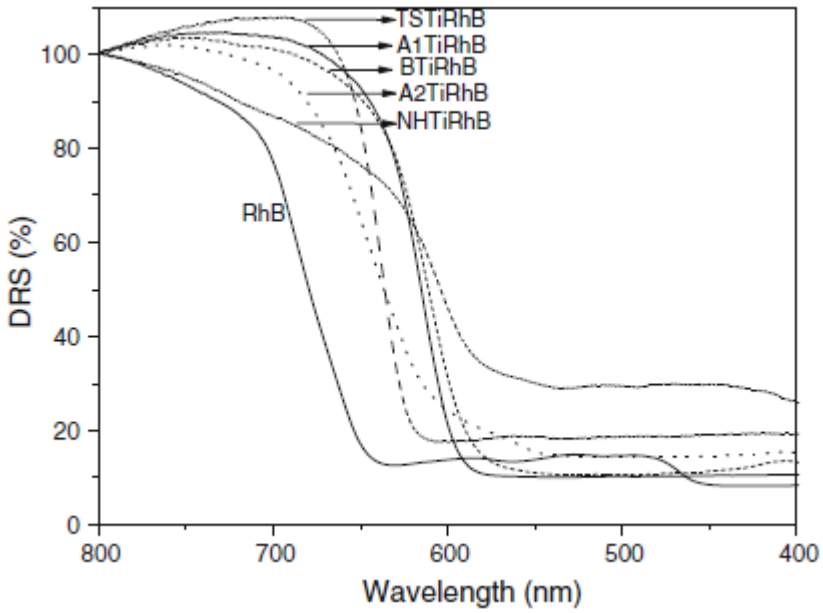

Fig. 6: DRS for encapsulated systems.

The maximum band position can be affected by several factors, such as polarity of the medium, steric effects, hydrogen bonding and surface acidity [47]. As noted in Fig. 6, in all routes, the encapsulation process shifted the absorption maximum to a lower wavenumber compared to the neat compound, constituting a hypsochromic shift (blue shift). The polarity could be increased due to the interaction with the silanol groups on the silica surface. Furthermore, this phenomenon may also occur due to loss of conjugation [48]. Based on these results, it is reasonable to assume that the encapsulated system medium is more polarized than the neat dye. Increased electron flow between the molecule (donor) and the silica (receptor) could cause this polarity. Thus, the n → pi* transitions undergo hypsochromic shift as the polarity increases.

The DRS results suggest an interaction between the dye and the silica network. Nevertheless, because it does not account for the structure of the molecules inside the silica, the samples were further analyzed by GC-MS. Fig. 7 compares a typical mass spectrogram of

A1TiRhB to that of rhodamine. We found the main peaks of rhodamine B (m/z = 326 and 397) to always be present, independent of encapsulation. This result suggests that the molecular structure is preserved during and after the encapsulation process. However, it should be noted that further investigations are necessary to more definitively demonstrate conservation of the molecular structure.

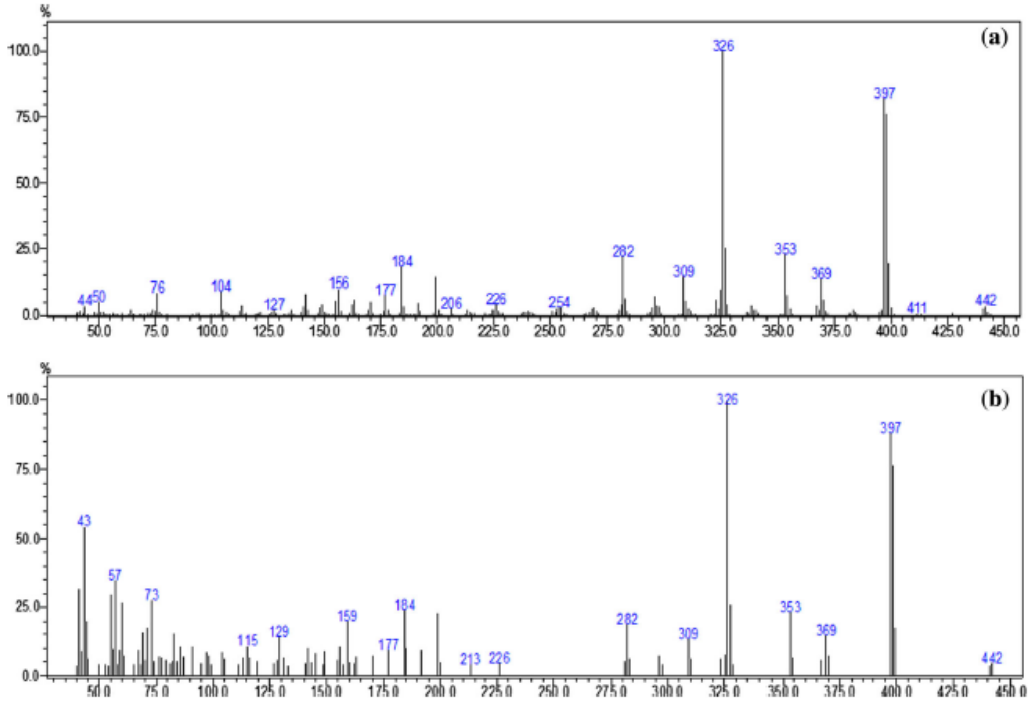

Fig. 7: Mass spectrograms: (a) Rhodamine B; (b) A1TiRhB.

An attempt to estimate the amount of encapsulated RhB on the outermost external surface of the grain was made by X-ray photoelectron spectroscopy (XPS). According the XPS spectra, N 1*s* was found only in the systems NHTiRhB and A2TiRhB. Except for TSTiRhB, this finding is in agreement with ART results, which also indicates that for NH and A2 routes the encapsulation preferentially occurs on the silica surface. In addition, the effect of route on the encapsulation of the different sol-gel matrices is clearly observed if one compares the two acid routes; the absence

of HCl in acid 2 route results in a xerogel that contains dye molecules distributed primarily on the silica surface.

From our results, it was possible to find a peak centered at 397.72 and 398.92 eV (N 1*s*) for A2TiRhB and NHTiRhB, respectively, while neat RhB showed a peak centered at 399.33 eV. This finding suggests that at least one of the interactions might occur via the nitrogen; such interaction could generate species with higher electron density, resulting from the donation of pi electron density from the oxygen to the conjugated system, which undergoes a $\pi \rightarrow \pi*$ transition into the silica.

The surface analysis can be expressed as N/Si, where the amount of nitrogen is assigned to RhB, while that of Si 2*p* contents is assigned to silica. The calculated ratios were 0.278 and 0.123 for acid 2 and non-hydrolytic route, respectively. This suggests that A2TiRhB material bears a higher RhB concentration on its surface.

Table 6 provides the surface analysis results, expressed as Ti/Si measured by XPS. For systems A1TiRhB and NHTiRhB, Ti 2*p* was not detectable by XPS analysis. The system A2TiRhB showed the highest Ti content on its outtermost external surface, followed by the systems TSTiRhB and BTiRhB. Thus, for these systems, unlike in the A1 and NH routes, the Si-Ti moieties most likely occurred on the silica surface. Similar to the analysis of N 1*s*, one can note that, in comparison to A1TiRhB, the absence of HCl during the synthesis of this system (A2TiRhB) results in the presence of Ti preferably on the silica surface. Additionally, this results did not guarantee the absence of Ti deepper inside the silica network, but strongly suggests at this route leads to a higher content of Ti on the surface of the silica.

Table 6: Ti/Si ratio measured by XPS and Rg obtained by SAXS

System	Ti/Si	Rg(*)
A1TiRhB	n.d.	2.5
A2TiRhB	1.42	0.22
BTiRhB	0.11	6.3
TSTiRhB	0.15	1.8
NHTiRhB	n.d.	3.4

(*) Radius of gyration (Rg) extracted from high-q region (SAXS). For more details see ref.22.

XPS indicates that the Ti was incorporated into the silica network in a different manner depending on the route. Therefore, the presence of Ti mostly on the surface in A2TiRhB is mostly like due to the higher hydrolysis constant of the $TiCl_4$ compared with the condensation of the silica precursor. Thus, while the silica network was forming, $TiCl_4$ condensed much more rapidly, resulting in Ti-based domains mostly on the surface. However, the opposite behavior may have occurred in the system in which Ti appeared deep inside the silica network. Compared to the A1TiRhB, the absence of HCl in the A2TiRhB system resulted in the presence of Ti on the silica surface.

XPS is a surface technique. XPS measurable region is estimated roughly as 5 nm in depth. Therefore, XPS is more sensitive to the outermost surface composition. The low concentration or absence of counts for N 1*s* on the high resolution spectrum indicates that rhodamine is located deeper within the grain particle. The varying distribution of rhodamine along the depth profile may have been caused by the different ratios of hydrolysis and condensation reactions among the specific reagents in each route (acid or basic catalyst; Lewis acid catalyst in the NH route), which could cause segregation of the dye deeper or closer to the surface of the final particle. Furthermore, the size of the primary particle may also affect these results. SAXS allowed the Rg (radius of

gyration) of the primary particle to be estimated. According to our previous work [22], the system A2TiRhB exhibits the lowest Rg value. Perhaps this lower Rg value allowed the X-ray to reach further into the grain, sampling a larger area and therefore accusing a higher N/Si ratio.

Owing to the fluorescence properties of RhB and its several potential applications such as measuring quantum yield of semiconductor materials [49], the PL properties of the encapsulated system were also measured (Fig. 8). For comparison, the PF of bare silica (SILA1) and RhB (dissolved in ethanol) are also shown. The system SILA1 presented a maximum emission centered at 570 nm, attributed to the silica matrix [50]; RhB had a maximum emission centered at 575 nm. Compared to both SILA1 and RhB, all encapsulated materials had a maximum emission shifted to higher wavelength.

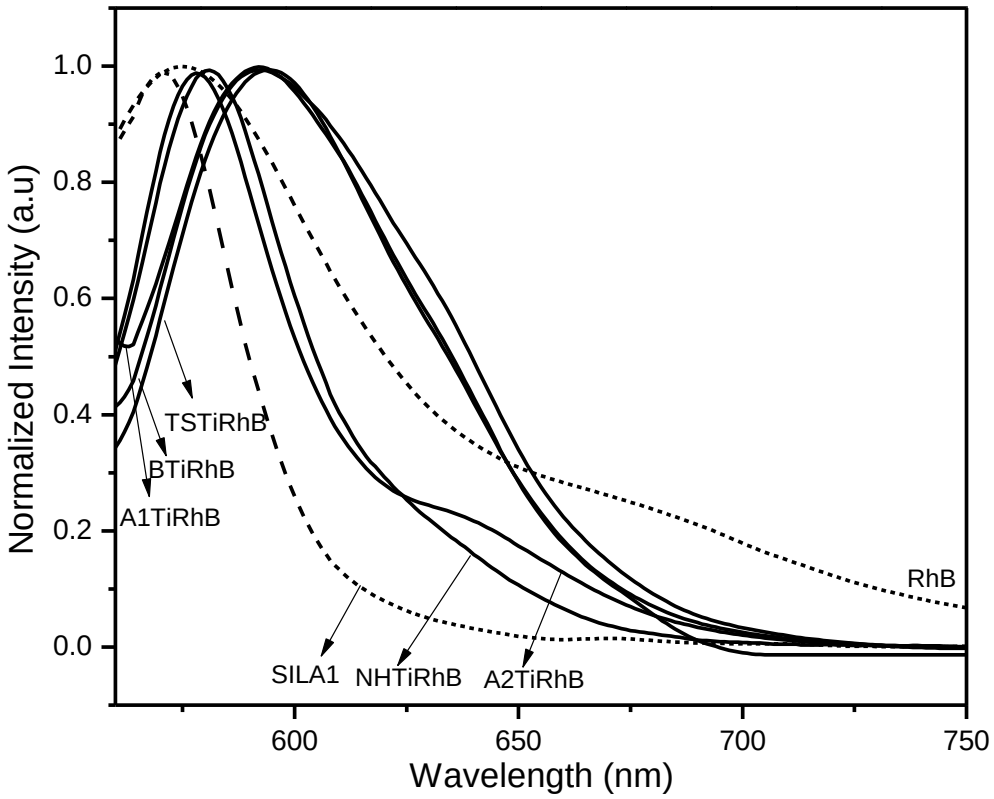

Fig. 8: Photoluminescence of encapsulated systems, bare silica (SILA1) and RhB.

The maximum emission wavelengths observed in the systems A2TiRhB and NHTiRhB, at 578 and 581 nm, respectively, are similar to that was reported by Nishiguchi et al [51] by Si-Ti binary oxide matrices synthetized via an acid (HCl) route (577 nm). Because the fluorescence maximum of RhB in solution (EtOH) is around 575 nm, the authors attributed the red shift due the transition from zwitterion to cationic form of RhB. Additionally, such behavior suggests that carboxyl acid dissociated during the sol-gel synthesis [52]. The system A2TiRhB showed a shoulder near at 640 nm, which is attributed to the dimer of RhB [53].

The systems A1TiRhB, BTiRhB and TSTiRhB showed a red shift compared with the two others encapsulated systems. As discussed by Shao et al. [54], this finding can be attributed to the confinement effect. When RhB are incorporated into the silica network, the HOMO and LUMO energy levels all increase due the confinement effect, but the HOMO energy increases more than that of LUMO energy. In other words, these systems seemed to produce much more confined molecules, while in the acid 2 and non-hydrolytic routes, RhB was preferentially on the surface of the silica. This is also corroborated by the lower PL intensity found for NHTiRhB and A1TiRhB (not shown), which again suggests a higher aggregation within the silica network, while other systems appear to display better dispersion of RhB [55, 56].

Confocal microscopy was conducted in an attempt to further analyze the effect of the route on the encapsulation of RhB. According to Scheme 3, the acid and basic route seem to show less intense fluorescence. The opposite was found for acid 2 and non-hydrolytyc routes, while the two steps route displayed intermediate fluorescence emission.

The results of XPS, ATR, PL and confocal microscopy, revealed several interesting observations. As discussed above, the systems A1TiRhB, BTiRhB and TSTiRhB showed red shift in the PL spectra compared to the other systems. The literature suggests that such behavior can be

attributed to the interaction with RhB with acidic TiOH sites on the gel surface [51]. Interestingly, with exception of A1TiRhB, this finding is in agreement with the results showed by XPS regarding the presence of Ti on the surface of the silica. In this sense, it is expected that A2TiRhB (with a higher Ti/Si ratio) would also display a red shift in the PL spectra. Thus, although the Ti is most likely concentrated on the surface of the silica, the interaction between RhB and TiOH is lower due to steric effects.

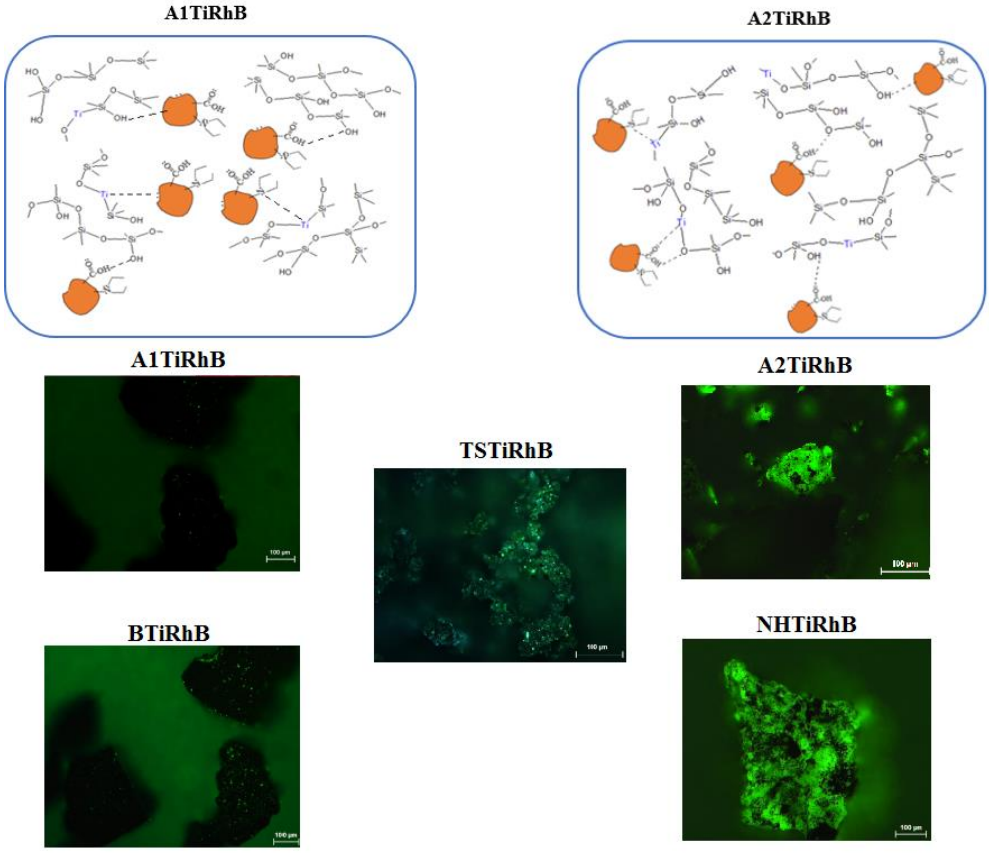

Scheme 3. Confocal microscopy and effect of the synthesis route on the encapsulated systems.

Except for TSTiRhB, the results of N 1*s* from XPS are in agreement with those of ATR, which also indicates that for NH and A2 routes, the encapsulation of RhB preferentially occurs on

the silica surface. In addition, XPS and PL measurement results corroborated the results of confocal microscopy regarding the effect of the route on the encapsulation of RhB.

The effect on the encapsulation of the different sol-gel matrices can be clearly observed by comparing the two acid routes. Considering the lower confinement effect, as indicated by PL measurement, the presence RhB bands ascribed to RhB (ATR), and the higher N/Si ratio shown by XPS, the system A2TiRhB is likely a xerogel that contains dye molecules distributed primarily on the surface of the silica. Similar observations can be made for all other encapsulated systems. Confocal microscopy also corroborated the results found by ATR, XPS and PL.

Generally speaking, the effect of the sol-gel route on RhB encapsulations and on Ti moieties can be described as follow: the encapsulation of RhB preferentially occurs inside the silica network in the systems A1TiRhB, BTiRhB and TSTiRhB; and the presence of Ti preferentially present on the surface of the silica in the systems A2TiRhB, BTiRhB and TSTiRhB. Scheme 3 depicts the effect of the synthesis route on the encapsulated systems, taking into account the XPS, ATR, PL and confocal microscopy results.

Conclusions

We studied rhodamine encapsulation within a silica network. Although our results were not conclusive, we found evidence that the RhB molecular structure is conserved during and after the encapsulation process, independent of the sol–gel route.

This study demonstrates that the structural characteristics of the encapsulated system are affected by the route. Deconvolution analysis of infrared absorption bands showed that the addition of rhodamine to the basic route produced a denser, more compact network compared to the other

systems. Shifts in the dye's main FT-IR spectral bands suggest electron interactions between the molecule and the silica. This interaction is also evidenced by increased electron flow between the molecule (donor) and the silica (receptor).

Imprinted xerogels were also affected by the sol–gel route, as observed by the increased $(SiO)_6$ percentage for the acid, two-step and non-hydrolytic routes. Raman spectroscopy detected evidence of Ti–O and Si–O–Ti in the xerogels.

XPS, ATR, PL and confocal microscopy provided evidence about the effect of the sol–gel route on the distribution of RhB within the silica network; the encapsulation of RhB was observed to occur preferentially inside the silica network in the systems A1TiRhB, BTiRhB and STiRhB. According to XPS, the presence of Ti on the surface of the silica occurs preferentially in the systems A2TiRhB, BTiRhB and TSTiRhB.

The results presented in this study indicate potential applications for these materials as adsorption/preconcentration and selective photocatalysis materials because a recognition site can be formed within the silica network.

Acknowledgments

This project was partially financed by the CNPq and FAPERGS. C. Escobar is grateful for the grant provided by CAPES.

References

1. Matsui K (2005) In: Sakka S, Kozuka H (ed) Entrapment of Organic Molecules, 1st edn. Kluwer Academic Publishers, New York

2. Ciriminna R, Fidalgo A, Pandarus V, Béland F, Ilharco LM, Pagliaro M (2013) The Sol–Gel Route to Advanced Silica-Based Materials and Recent Applications. Chemical Reviews 113:6592-6620

3. Jin W, Brennan JD (2002) Properties and applications of proteins encapsulated within sol–gel derived materials. Anal Chim Acta 461:1-36

4. Gupta R, Chaudhury NK (2007) Entrapment of biomolecules in sol–gel matrix for applications in biosensors: Problems and future prospects. Biosens Bioelectron 22:2387-2399

5. Xu G, Zhang H, Zhong M, Zhang T, Lu X, Kan X (2014) Imprinted sol–gel electrochemical sensor for melamine direct recognition and detection. J Electroanal Chem 713:112-118.

6. Fisch AG, Cardozo NSM, Secchi AR, Stedile FC, Silveira NPd, Santos JHZd (2008) Investigation of silica particle structure containing metallocene immobilized by a sol–gel method. Journal of Non-Crystalline Solids 354:3973-3979

7. Parambadath S, Rana VK, Zhao D, Ha C-S (2011) N,N′-diureylenepiperazine-bridged periodic mesoporous organosilica for controlled drug delivery. Microporous and Mesoporous Materials 141:94-101

8. Perumal S, Ramadass Sk, Madhan B (2014) Sol–gel processed mupirocin silica microspheres loaded collagen scaffold: A synergistic bio-composite for wound healing. European Journal of Pharmaceutical Sciences 52:26-33

9. Capeletti LB, Dos Santos JHZ, Moncada E, Da Rocha ZN, Pepe IM (2013) Encapsulated alizarin red species: The role of the sol–gel route on the interaction with silica matrix. Powder Technol 237:117-124

10. Morais EC, Correa GG, Brambilla R, Radtke C, Baibich IM, Santos JHZd (2013) The interaction of encapsulated pharmaceutical drugs with a silica matrix. Colloid Surface B 103:422-429

11. Farrington K, Regan F (2009) Molecularly imprinted sol gel for ibuprofen: An analytical study of the factors influencing selectivity. Talanta 78:653-659

12. Gupta R, Kumar A (2011) Synthesis and characterization of sol–gel-derived molecular imprinted polymeric materials for cholesterol recognition. J Sol-Gel Sci 58:182-194

13. Lee SM, Lee BS, Byun TG, Song KC (2010) Preparation and antibacterial activity of silver-doped organic–inorganic hybrid coatings on glass substrates. Colloid Surf A 355:167-171

14. Juszczak LJ, Friedman JM (1999) UV Resonance Raman Spectra of Ligand Binding Intermediates of Sol-Gel Encapsulated Hemoglobin. J Biol Chem 274:30357-30360

15. Martínez-Zapata O, Méndez-Vivar J, Bosch P, Lara VH (2011) Synthesis and characterization of amorphous aluminosilicates prepared by sol–gel to encapsulate organic dyes. J Non-Crystall Solids 357:3480-3485.

16. Albarran L, López T, Quintana P, Chagoya V (2011) Controlled release of IFC-305 encapsulated in silica nanoparticles for liver cancer synthesized by sol–gel. Colloids and Surface A 384:131-136

17. Fidalgo A, Ilharco L (2001) The defect structure of sol-gel derived silica/polytetrahydrofuran hybrid films by FTIR. J Non-Crystall Solids 283:144-154.

18. Cappeletti LB, Moncada E, Poisson J, Butler IS, Dos Santos JHZ (2013) Determination of the Network Structure of Sensor Materials Prepared by Three Different Sol-Gel Routes Using Fourier Transform Infrared Spectroscopy (FT-IR). Appl Spectroscopy 67 (4):441-447

19. Iler RK (1979) The chemistry of silica: solubility, polymerization, colloid and surface properties, and biochemistry. Wiley, New York

20. Curran MD, Stiegman AE (1999) Morphology and pore structure of silica xerogels made at low pH. J Non-Crystall Solids 249:62-68

21. A Morais E, Correa G, Brambilla R, Livotto P, dos Santos J, Cardoso M (2012) Silica imprinted materials containing pharmaceuticals as a template: textural aspects. J Sol-Gel Sci Tech 64:324-334

22. Escobar CC, dos Santos JHZ (2014) Effect of the Sol-Gel Route on the Textural Characteristics of Silica Imprinted With Rhodamine B. J Sep Sci doi:10.1002/jssc.201301143

23. Brinker CJ, Scherer GW (1990) Sol-Gel Science: The Physics and Chemistry of Sol-Gel Processing. Academic Press, New York 1990.

24. Krol DM, van Lierop JG (1984) The densification of monolithic gels. J Non-Cryst Solids 63:131-144

25. Gonzalez-Oliver CJR, James PF, Rawson H (1982) Silica and silica-titania glasses prepared by the sol-gel process. J Non-Cryst Solids 48 129-152

26. Li X, King TA (1996) Spectroscopic studies of sol-gel-derived organically modified silicates. J Non-Cryst Solids 204:235-242

27. Liu X, Cui D, Wang Q, Xu H, Li M (2005) Photoluminescence enhancement of ZrO_2/Rhodamine B nanocomposites. J Mater Sci 40:1111-1114

28. Ereshchenko AG, Stepantsova NP, Geller, BÉ (1971) Infrared spectroscopic study of the action of inorganic peroxides and gamma radiation on the arymethane dye rhodaminde S. J Appl Spectros 15:1203-1206

29. Kerr JL, Baldwin DS, Tobin MJ, Puskar L, Kappen P, Rees GN, Silvester E (2013) High Spatial Resolution Infrared Micro-Spectroscopy Reveals the Mechanism of Leaf Lignin Decomposition by Aquatic Fungi. PloS ONE 8: e60857

30. Wainipee W, Weiss DJ, Sephton MA, Coles BJ, Unsworth C, Court R (2010) The effect of crude oil on arsenate adsorption on goethite. Water Res 44:5673-5683

31. Wang J-H, Lin MC (2005) Reactions of Trimethylindium on TiO_2 Nanoparticles: Experimental and Computational Study. J Phys Chem 109:20858-20867

32. Dzherayan TG, Bykov IV, Kostitsyna MV, Shipulo EV, Petrukhin OM, Dunaeva AA, Vladimirova EV (2010) Study of a gentamicin-selective membrane polymer matrix by infrared spectroscopy. J Anal Chem 65:726-731

33. Low MJD, Cusumano JA (1969) Dual interaction of anisole with surface hydroxyls. Can J Chem 47:3906-3909

34. Hoffman P, Knozinger EE (1987) Novel Aspects of IR Fourier Spectroscopy. Surf Sci 188:181

35. Kowada Y, Ozeki T, Minami T (2005) Preparation of Silica-Gel Film with pH Indicators by the Sol–Gel Method. Journal of Sol-Gel Science and Technology 33:175-185

36. Montero I, Galán L, Najmi O, Albella JM (1994) Disorder-induced vibration-mode coupling in SiO films observed under normal-incidence infrared radiation. Phys Rev A 50:4881-4884

37. Fidalgo A, Ciriminna R, Ilharco LM, Pagliaro M (2005) Role of the Alkyl−Alkoxide Precursor on the Structure and Catalytic Properties of Hybrid Sol−Gel Catalysts. Chem Mater 17:6686-6694

38. Almeida RM, Guiton TA, Pantano CG (1990) Characterization of silica gels by infrared reflection spectroscopy. J Non-Cryst Solids 121:193-197

39. Gao X, Wachs IE (1999) Titania–silica as catalysts: molecular structural characteristics and physic-chemical properties. Catal Today 51:233-254

40. Moran PD, Bowmaker GA, Cooney RP, Finnie KS, Bartlett JR, Woolfrey JL (1998) Vibrational Spectra and Molecular Association of Titanium Tetraisopropoxide. Inorg Chem 37:2741-2748

41. Strunk J, Vining WC, Bell AT (2010) A Study of Oxygen Vacancy Formation and Annihilation in Submonolayer Coverages of TiO_2 Dispersed on MCM-48. J Phys Chem C 114:16937-16945

42. Gao X, Bare SR, Fierro JLG, Banares MA, Wachs IE (1998) Preparation and in-Situ Spectroscopic Characterization of Molecularly Dispersed Titanium Oxide on Silica. J Phys Chem B 102:5653-5666

43. Bertoluzza A, Fagnano C, Antonietta Morelli M, Gottardi V, Guglielmi M (1982) Raman and infrared spectra on silica gel evolving toward glass. . J Non-Cryst Solids 48:117-128

44. Morrow BA, Molapo DT (2005) In: Bergna HE, Roberts WO (ed) Colloidal Silica: Fundamentals and Applications, CRC Press, Boca Raton

45. Gautam C, Yadav A, Mishra V, Vikram K (2012) Synthesis, IR and Raman Spectroscopic Studies of (Ba,Sr)TiO_3 Borosilicate Glasses with Addition of La_2O_3. Open J Inorg Non-metallic Mater 2:47-54

46. Cappeletti LB, Moncada E, Poisson J, Butler IS, Dos Santos JHZ (2013) Determination of the Network Structure of Sensor Materials Prepared by Three Different Sol-Gel Routes Using Fourier Transform Infrared Spectroscopy (FT-IR). Appl Spectrosc 67:441-447

47. Rao CNR (1975) Ultraviolet and Visible Spectroscopy. Butter-worth, London.

48. Williamns DH, Fleming I (1966) Spectroscopic Methods in Organic Chemistry. McGraw-Hill Publishing, London.

49. Bertino MF, Gadipalli RR, Martin LA, Rich LE, Yamilov A, Heckman BR, Laventis N, Guha S, Katsoudas J, Divan R, Mancini DC (2007) Quantum dots by ultraviolet and x-ray lithography. Nanotechnology 18:1-6.

50. Zhao Y, Hou S, Liang X, Fang L, Sheng G, Xu F (2010) Si Ion Implantation-Induced Defect Photoluminescence in Silica Films. Adv Mater Res 160-162:1450-1457

51. Nishiguchi H, Zhang JL, Anpo M (2001) Characteristics of the Phosphorescence Spectra of Benzophenone Adsorbed on Ti−Al Binary Oxides. Langmuir 17:3958-3963

52. Drexhage (1976) Fluorescence Efficiency of Laser Dyes. J Res NBS A: Phys and Chem 80A:421-428

53. Bockstette M, Wöhrle D, Braun I, Schulz-Ekloff G (1998) Conventional and microwave-assisted crystallization inclusion of substituted Rhodamine derivatives in $AlPO_4$-5. Micro Meso Mat 23:83-96

54. Shao Y, Wang L, Zhang J, Anpo M (2006) The photoluminescence of rhodamine B encapsulated in mesoporous Si-MCM-48, Ce-MCM-48, Fe-MCM-48 and Cr-MCM-48 molecular sieves. J Photochem Photobiol A: Chem 180:59–64

55. Yamashita H, Tanaka A, Nishimura M, Koyano K, Tatsumi T, Anpo M (1998) Photochemical properties of Rhodamine-B dye molecules included within mesoporous molecular sieves, Stud Surf Sci Catal 117:551-558

56. Gong JR, Wan LJ, Lei SB, Bai CL, Zhang XH, Lee ST (2005) Direct evidence of molecular aggregation and degradation mechanism of organic light-emitting diodes under joule heating: An STM and photoluminescence study. J Phys Chem B 109:1675-1682

4.3 Artigo 3

Publicado no *Industrial & Enginnering Chemistry Research*, v. 54, p. 254-262, 2015.

Graphical Abstract

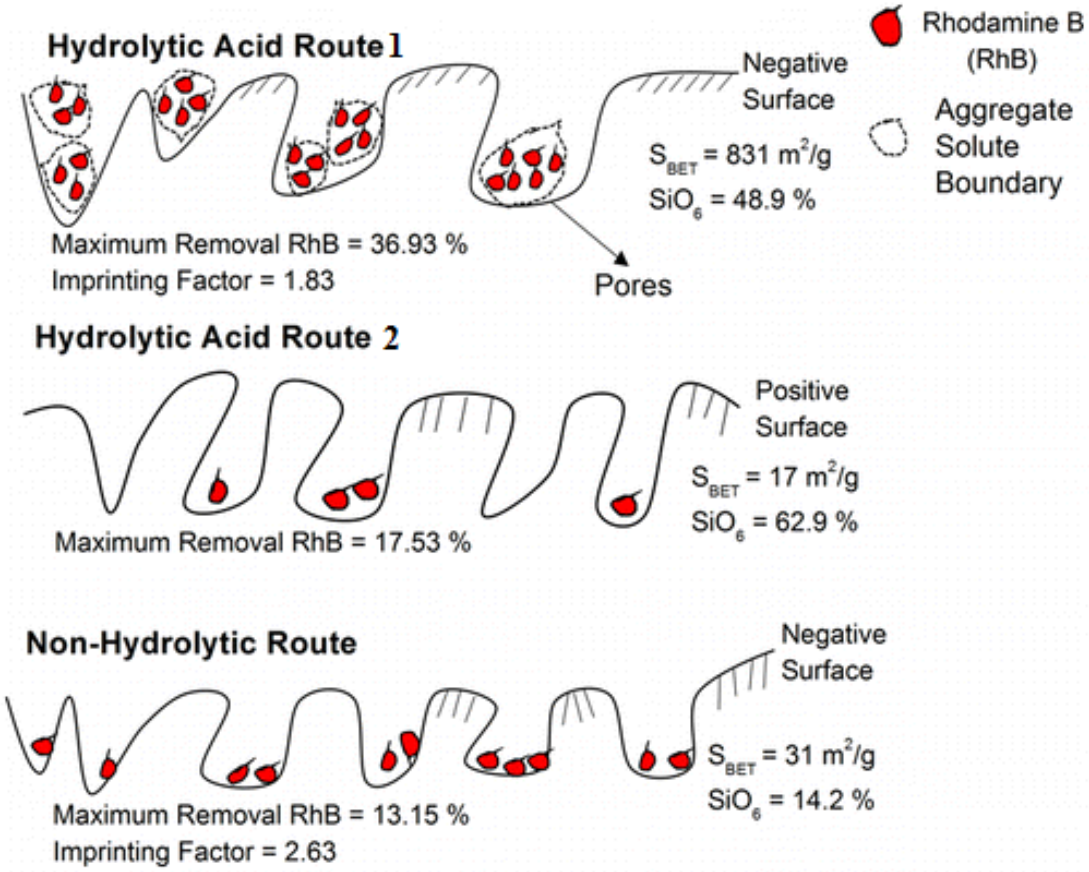

I&EC research
Industrial & Engineering Chemistry Research

Article

pubs.acs.org/IECR

Effect of a Sol–Gel Route on the Preparation of Silica-Based Sorbent Materials Synthesized by Molecular Imprinting for the Adsorption of Dyes

Cícero Coelho de Escobar,[†] Adriano Fisch,[‡] and João Henrique Zimnoch dos Santos*[,§]

[†]Departamento de Engenharia Química, Universidade Federal do Rio Grande do Sul Rua Eng. Luis Englert s/n, Porto Alegre, CEP 90040-040, Brazil

[‡]Departamento de Engenharia Química, Universidade Luterana do Brasil Avenida Farroupilha, 8001, Canoas, CEP 96501-595, Brazil

[§]Instituto de Química, Universidade Federal do Rio Grande do Sul, Avenida Bento Gonçalves 9500, Porto Alegre, CEP 91500-000, Brazil

S *Supporting Information*

ABSTRACT: A series of imprinted silica xerogels that support rhodamine B as the template were synthesized by distinct sol–gel routes. The adsorption capacity was discussed in terms of isotherm adsorption evaluated in terms of Langmuir, Freundlich, and modified Brunauer–Emmett–Teller (BET) models. Although only one acid-catalyzed route could be fit with the Langmuir and Freundlich models, yielding a q_m value of 998.3 mg/g, the BET-modified model showed a good fit for all systems studied. The effect of the sol–gel route chosen to prepare silica-based sorbent materials that are imprinted to adsorb dyes on their characteristics can be understood by taking into consideration the fact that statistical analysis suggests that other properties (namely, ζ potential, radius of gyration, and percentage of six-membered rings) seem to be relevant to the selective adsorption of dye rather than being indicated by S_{BET} uniquely. On the basis of the similarity of S-type isotherms observed, we propose that the mechanism of adsorption may be roughly the same for the basic, two-step, nonhydrolytic and the second of two reported acidic routes. This means that, except in the case of the first acid-catalyzed route, there is a tendency for large adsorbed molecules to associate rather than to remain as isolated units.

Introduction

Synthetic dyes are extensively used in the plastic, textile, dye, paper, printing, cosmetic and pharmaceutical industries [1]. Since 1856, over 10^5 different dyes have been produced worldwide with an annual production of over 7×10^5 metric tons [2]. In addition, the traditional textile finishing industry consumes approximately 100 L of water to process approximately 1 kg of textile materials [3]. It is estimated that 280,000 tons of textile dyes are discharged in industrial textile effluent every year worldwide [4]. Discharged dyes color the water systems they enter, hindering sunlight penetration to the lower layers of the water body and hence affecting aquatic life [1]

Different methods are available for the remediation of dye wastewaters, including sedimentation, filtration, chemical treatment, oxidation, advanced oxidation processing, biological treatment, adsorption and ion exchange [5].

For some dyes, degradation using oxidizing agent is difficult because complex aromatic structures are rendered ineffective in the presence of heat, light and microorganisms [1]. Studies have shown that the efficiency of advanced oxidation processes (AOPs) based on heterogeneous photocatalysis strongly depends on the basic molecular structure of the dye and the nature of auxiliary groups attached to the aromatic nuclei of the dyes [6].

Recently, many studies have used rhodamine B (RhB) as a molecular probe for adsorption experiments. Several adsorbents have been studied, such as rice rusk [7], activated carbon [7, 8], tannery-derived residual biomass [9], AlMCM-41 [10] Fe_3O_4 nanoparticles [11, 12], sodium montmorillonite [13], Kaolinite [14] and cation-exchange resins [15]. Although some of these materials possessed good adsorption capacity, little is known about their selectivity. Selectivity is an important issue because hazardous materials may be present in the environment in the presence of other organics of low of no toxicity. While many low-toxicity contaminants can be degraded by biological means, the same process can be much more difficult for highly hazardous substances [16].

From the adsorption point of view, the development of selective sorbent materials has become an important issue in environmental chemical analysis for the detection of pollutants present in aqueous matrices at minute concentrations. In this sense, molecular imprinting materials have received much attention in the last years [17, 18]. Considering that such materials are made with pore sizes and shapes tailored to the target molecule, these materials potentially bear high affinity and selectivity for the molecule employed as the template in their synthesis [19, 20].

The majority of the studies concerning the development of molecular imprinted materials as sorbents for removal processes are based on organic polymeric phases. As discussed in the literature, some drawbacks are associated with polymeric materials such as the potential presence of functional groups outside the printing sites, resulting in non-specific, weak interactions between the template and polymer functional units, which in turn results in the leaching of the template during the early stages of polymerization. Moreover, one cannot neglect the possibility of low-to-moderate template recovery and heterogeneity of the produced receptor sites [21]. In this context, the use of inorganic matrices, such as silica-based materials, is a promising way to overcome some of these inconveniences.

Silica-based materials can be produced by the sol-gel process. Briefly, this strategy consists of reacting the template with a silica precursor (e.g., tetraethylorthosilicate – TEOS), resulting in a silica network containing encapsulated template molecules. Specific adsorptive sites are created after the removal of the template from the silica network, resulting in materials with imprinted sites. Matrices prepared by the sol-gel method have some advantages in comparison with conventional organic polymerization methods, such as rigidity, tailored porosity, thermal stability, and flexibility in processing conditions as well as in the choice of monomers used [22, 23].

Several works have explored the development of imprinted materials made using RhB as the template. For example, Xu et al. [24] prepared a fiber with a surface molecularly imprinted with RhB by bonding polyethylenimine onto polypropylene for selective adsorption. In another case, a functional polymer, sulfonated polysulfone, was prepared and then blended with cellulose diacetate as the matrix polymer for the preparation of molecularly imprinted polymer membranes [25]. The authors related that relatively high permeability was achieved by imprinting the surfaces of porous membranes. Using similar molecularly imprinted polymer blend membranes, the

possibility of reusing the membranes for the recovery of RhB by solid phase extraction was also addressed [26].

In a previous study, we investigated the effect of a series of silica xerogels on the synthesis of imprinted materials made from them, as well the effect of preparation route on the selective adsorption of RhB. We found that the preparation route affected the textural properties of the materials. Particularly, the highest selectivity factor (2.5) and competitiveness factor (1.7) was found for the sorbent produced by the acid route when used to select between RhB and rhodamine 6G (Rh6G). Furthermore, we presented evidence that selectivity was dictated by the imprinted shape generated by the encapsulation and extraction of the template rather than the magnitude of the surface area [27]. Through our analysis, we have shown that although the structural characteristics of the encapsulated and extracted systems are affected by the processing route taken, the structure of molecule is conserved during and after the encapsulation process [28].

As an extension of these studies, the present paper reports the results of isotherm adsorption evaluated in terms of Langmuir, Freundlich and modified BET models. We also investigated the correlation between textural (nitrogen adsorption, small-angle X-ray scattering), structural (Fourier transform infrared) and electronic aspects (ζ potential) in an attempt to gather some understanding of the role of route on adsorption capacity.

EXPERIMENTAL SECTION

Materials and methods

Rhodamine B (Vetec), rhodamine 6G (Sigma–Aldrich), tetraethoxysilane ($Si(OCH_2CH_3)_4$, TEOS, Merck, >98%), titanium tetrachloride (Merck, >99%) and silicon tetrachloride ($SiCl_4$, Sigma–Aldrich, 99%) were used as received. Hydrochloric acid (HCl, Nuclear, 38%), ammonium

hydroxide (NH_4OH, Nuclear, 29%) and $FeCl_3$ (98%, Merck) were employed as catalysts, depending on the sol-gel route.

Preparation of sol-gel materials

Five different routes were employed to prepare the samples by the sol-gel process and with TEOS as the silica precursor. The five routes are as follows: acid-catalyzed route 1 (A1), acid-catalyzed route 2 (A2), a base-catalyzed route (B), a two-step route (TS) and a non-hydrolytic route (NH). Route A1 was catalyzed using 0.2 M of hydrochloric acid at a 1:2 (HCl:TEOS) ratio. Route A2 was similar to A1, but the samples were prepared without HCl; instead, $TiCl_4$ acted as a Lewis acid catalyst. The base-catalyzed route was catalyzed using 0.2 M of NH_4OH at a 1:2 (NH_4OH:TEOS) ratio. Route TS was catalyzed using 0.2 M of HCl at a 1:2 (HCl:TEOS) ratio, and after 30 min, 0.2 M of NH_4OH was added at a 1:2 (NH_4OH:TEOS) ratio. Route NH employed TEOS as well as $SiCl_4$ and was catalyzed using $FeCl_3$ at 0.5 wt.% of the final product weight. For each sample, the RhB concentration was fixed at 5 wt.% of the final xerogel weight.

The powder-form imprinted samples prepared by the acid-catalyzed, base-catalyzed and two-step routes were made as follows. RhB was added to a solution of TEOS, followed by $TiCl_4$, and finally the catalyst. During this process, the solution was stirred constantly at room temperature. Stirring was continued until gelation or precipitation occurred, depending on the route. The non-hydrolytic route was executed under an inert atmosphere (Ar). In this case, TEOS, $SiCl_4$ and $TiCl_4$ were added after adding the catalysts and RhB. The resulting solution was stirred at 80 °C until gelation. The solids were dried at room temperature and milled. Further details are reported elsewhere [27].

For template removal, ultrasound-assisted extraction was employed using methanol as the solvent. The process was conducted by alternating between pulse-on (20 s) and pulse-off (5 s) modes for 5 min. The solid was then filtered and dried at room temperature.

Xerogel Characterization

The specific surface areas of the xerogels were determined by the Brunauer-Emmett-Teller (BET) method at -196 °C, in the partial pressure range of $0.2 < P/P_0 < 0.9$. Prior to each measurement, samples were preheated at 110 °C for 14 h under vacuum.

Fourier-transform infrared spectroscopy (FTIR) measurements were recorded at room temperature on a Bomem MB-102 spectrometer by co-adding 36 scans with a resolution of 4 cm^{-1}. For a detailed structural analysis, the υ_{as}(Si-O)-Si and the υ_{s}(Si-O)-Si spectral regions (900-1300 cm^{-1}) were independently deconvoluted into Gaussian components, using a nonlinear least-squares fitting method as described by the literature [29]. Therefore, the band is composed of four basic elements namely: the longitudinal components to six-membered rings (LO6) and to four-membered rings (LO4) and the transversal components to these same six-membered rings (TO6) and to four-membered one (TO4). The percentage of six-member rings ($\%(SiO)_6$) was estimated as the following ratio of fitted areas (A) according equation 1:

$$\%(SiO)_6 = 100 \times [(A(LO_6) + A(TO_6))/(A(LO_6) + A(LO_4) + A(TO_4) + A(TO_6))] \quad (1)$$

SAXS experiments were performed on the D11A beamline at the Brazilian Synchrotron Light Laboratory (LNLS, Campinas, Brazil) using a wavelength of 1.488 nm. The incident beam was detected at two different sample-to-detector distances (1549.8 mm and 2245.7 mm) to increase the range of the scattering vector q ($q = (4\pi/\lambda) \sin\theta$; 2θ = scattering angle). The dried samples were placed between two Kapton® foils and the collimated X-ray beam was passed through a chamber

containing the stainless steel sample holder. All measurements were performed at room temperature. Silver behenate powder was employed as a standard for calibrating the sample-to-detector distance, the detector tilt and the direct beam position. Transmission, dark current and Kapton® foil corrections were performed on the 2D image prior to additional data processing.

The isotropic scattering patterns were radially averaged. SAXS data analysis was performed using the Irena evaluation routine [30], which was implemented using Igor Pro Software [31] (WaveMetrics, Portland, USA). A multilevel unified fit was used to describe the two levels of structural organization that was evident in the scattering data. In this method, the scattering provided by each structural level is the sum of a Guinier exponential form and a structurally limited power-law tail. A generalized equation that represents various levels can be written as

$$I(q) = \sum_{i=1}^{n} G_i \exp\left(\frac{-q^2 R_{gi}^2}{3}\right) + B_i \exp\left(\frac{-q^2 R_{g(i+1)}^2}{3}\right)\left[\frac{(\mathrm{erf}(qR_{gi}/\sqrt{6}))^3}{q}\right]^{Pi} \qquad (1)$$

where n is the number of observed structural levels, G is the Guinier prefactor, R_g is the radius of gyration and B is a prefactor specific to the power-law scattering, which is specified as the decay of the exponent P [32, 33].

Statistical Analysis

The SPSS Statistical System (SPSS for Windows, version 19, IBM®) was used to analyze the relationships among the data. All statistical tests were performed at the $P < 0.05$ level of significance. Cluster analysis was performed on experimental data standardized through a z-scale transformation to avoid misclassification due to wide differences in data dimensionality. Standardization eliminates the influence of different units of measurement and renders the data

dimensionless. The distances between samples were calculated using square Euclidean distances. The dendrogram similarity scales that were generated by the SPSS program range from 0 (greater similarity) to 25 (lower similarity).

Adsorption isotherm acquisition procedure

Adsorption experiments

In a typical experiment, 10 mg of RhB-imprinted silica (extracted by ultrasound/methanol) were introduced into a cartridge, through which 5 mL of RhB solution was percolated over 1 h. The selectivity of imprinted materials was studied under similar experiment conditions using an Rh6G solution.

Eluent was analyzed by UV-visible spectrometry at 553 nm for RhB B and 525 nm for RhB 6G. Similar experiments were conducted using non-imprinted (NI) silica. The percentage of adsorption was calculated by the equation $(C_{final} - C_{initial})/C_{initial} \times 100\%$. To determine the relative performance of the molecular-imprinted (MI)/non-imprinted (NI) pairs, the imprinting factor (IF) was defined as the MI/NI ratio of the concentration after the experiment.

Parameter estimation

Parameter estimation of both isotherms was carried out using restricted non-linear least-square (NLLS) analysis, which was implemented in Matlab by using *fmincon* function [34].

The quality of parameter estimation was analyzed by the parameter confidence interval (*I*), parameter correlation matrix (*C*), experimental variance (ν^2_{exp}), determination coefficient (r^2), and by visually evaluating the goodness-of-fit (predicted vs. experimental data).

Confidence intervals and correlation matrices were calculated using a *t*-student distribution for 95% confidence as given in Equations 2-9. The complete algorithm is presented in Equation 2-9.

$$I = p \pm t_{\alpha,(n-n_p)}\sigma_p(i) \tag{2}$$

$$\sigma_p = \sqrt{diag(v_p^2)} \tag{3}$$

$$\alpha = \frac{1+0.95}{2} \tag{4}$$

$$v_p^2 = v_{\exp}^2 (M^T M)^{-1} \tag{5}$$

$$v_{\exp}^2 = \frac{\varepsilon^T \varepsilon}{(n-n_p)} \tag{6}$$

$$\varepsilon = [q_e]_{\text{estimated}} - [q_e]_{\text{experimental}} \tag{7}$$

$$M(q_e, p) = \left[\frac{\partial q_e}{\partial p}\right] \tag{8}$$

$$C_{ij} = \frac{(v_p)_{ij}}{\sqrt{(v_p)_{ii}(v_p)_{jj}}};\ \text{for i} \neq \text{j}$$
$$C_{ij} = 1;\ \text{for i} = \text{j} \tag{9}$$

where p is the estimated parameter; σ_p is the standard deviation of the parameter vector; v_p^2 is the covariance matrix of the parameters; $v_{\exp}^2$ is the experimental variance; M is the derivative matrix; C is the correlation matrix; *diag* is the diagonal covariance matrix; ε is the predicted deviation; q_e

is the adsorbed amount of compound; *n* is the number of experimental points; and n_p is the number of adjustable parameters.

Freundlich and Langmuir adsorption isotherms

The Freundlich adsorption isotherm is given in Equation 10. However, using Equation 10 in estimations leads to highly correlated values of k_f and $1/n$ [35].

$$q_e = k_f C_e^{\frac{1}{n}} \quad (10)$$

To obtain weakly correlated parameters, Equation 10 was redefined using the new variable $C_e* = KC_e$. Equations 11-12 could be used in the data fitting from a proper substitution of C_e* in Equation 10. In this sense, weakly correlated parameters could be estimated with an adequate set up of *K*, preventing the M^TM matrix in Equation 5 from being singular [36].

$$q_e = \alpha(C_e*)^{\beta} \quad (11)$$

$$q_e = \alpha K^{\beta}(C_e)^{\beta} \quad (12)$$

where: $k_f = \alpha K^{\beta}$ and $1/n = \beta$.

Unfortunately, a similar modification is not easily applied to the original Langmuir adsorption isotherm (Equation 13).

$$q_e = \frac{q_m k_a C_e}{1 + k_a C_e} \tag{13}$$

BET isotherm modified for solid-liquid adsorption

$$q_e = \frac{y_1 y_2 C_e}{\mathrm{abs}\left(y_3 - C_e\right)\left(1 + \left(y_2 - 1\right)\frac{C_e}{y_3}\right)} \tag{14}$$

where *abs(x)* is the absolute value of the argument *x*, y_1 is equivalent to q_m, y_2 is a ratio between the equilibrium constant of adsorption for the first layer and the equilibrium constant of adsorption for upper layers and y_3 is the solubility of the solute [36]. The BET-modified isotherm is not a continuous function. When $C_e = y_3$ the function is infinite. Thus, it was necessary to derive in two regions, i.e., $C_e < y_3$ and $C_e > y_3$.

Results and Discussion

The systems were evaluated in terms of textural characteristics by performing nitrogen adsorption before and after the extraction process. Table 1 shows the resulting surface areas. With the exception of the B and TS routes, all other systems showed an increase of area after RhB extraction, ranging from 30 (A1) to 933% (NH). It was worth noting that NH_4OH was employed as a catalyst in both of the exceptional routes. According to the literature, sol–gel processes conducted at basic pH yield materials with a compact morphology [37]. Thus, the extraction process may cause morphological and textural alteration in such systems. For all other systems, the increase in area observed after extraction suggests that solvent removal did not cause a collapse

of the silica network. The values of S_{BET} found are in agreement with other studies in which acid-catalyzed routes were investigated for the encapsulation of organic molecules [38].

Table 1: Parameters of extracted samples.

Route	S_{BET} (m^2/g) Before solvent extraction	S_{BET} (m^2/g) MIP xerogel	Rg[a)]	P[b)]	Max. removal RhB (%)	Max. removal R6G (%)	IF[c)]	SF[d)]	SiO_6 (%)	ζ (mV)
A1TiRhB	639	831	3.35	3.80	36.93 (±2.6)	14.75 (±2.7)	1.83	2.5	48.92 (±3.6)	-11.9 (± 1.3)
A2TiRhB	11	17	0.74	3.80	17.53 (±0.9)	8.36 (±2.4)	n.d.	2.1	62.97 (±5.5)	13.1 (±3.6)
BTiRhB	511	482	0.70	3.60	15.6 (±0.17)	7 (±2.3)	0.42	2.2	50.32 (±1.6)	-12.6 (±2.1)
TSTiRhB	568	350	0.95	3.90	37.61 (±1.38)	9.4 (± 0.6)	1.31	4.0	62.2 (±4.7)	-8.99 (±1.9)
NHTiRhB	10	31	0.74	3.70	22.92 (±1.52)	13.15 (±0.33)	2.63	1.7	14.24 (±3.4)	-14.9 (± 2.6)

[a)]Estimated from q region> 0.03 $Å^{-1}$; [b)]Estimated from q region < 0.01 $Å^{-1}$; [c)] Imprinting Factor - Defined as MI/NI concentration ratio after the adsorption experiment; [d)] Selectivity Factor - Defined as: Concentration of RhB/Concentration Rh6G.

The values of ζ potential also help explain the values of maximum removal achieved by the systems. As shown in Table 1, the ζ potentials for the systems that exhibit the highest adsorption rates are negative. According the literature [39], RhB has a positive charge below pH 6.0 (experiments were carried out under a pH of around 5.0). Therefore, the systems with negative zeta potential may interact better with the dye. This is clearly evident for system A2, which showed positive zeta potential and removed approximately two times less RhB and Rh6G than the A1 system. However, system B also exhibited a negative zeta potential but had a maximum removal level similar to that of A2. This behavior may occur for several reasons: (i) the leaching of RhB molecules from the interior of the silica network; (ii) the smaller surface area of B after the

extraction process and (iii) ineffective generation of specific sites for the recognition of RhB within the B matrix.

As Figure 1 shows, it is possible for a system to experience a decrease in zeta potential as the surface area increases. Interestingly, the NH system showed a value of surface area twice as large as that of system A2, while its value of zeta potential was negative. This finding also suggests the role of charge interactions in extraction and thus that the extraction process appeared be dictated by the shape of the imprint generated rather than the magnitude of the surface area.

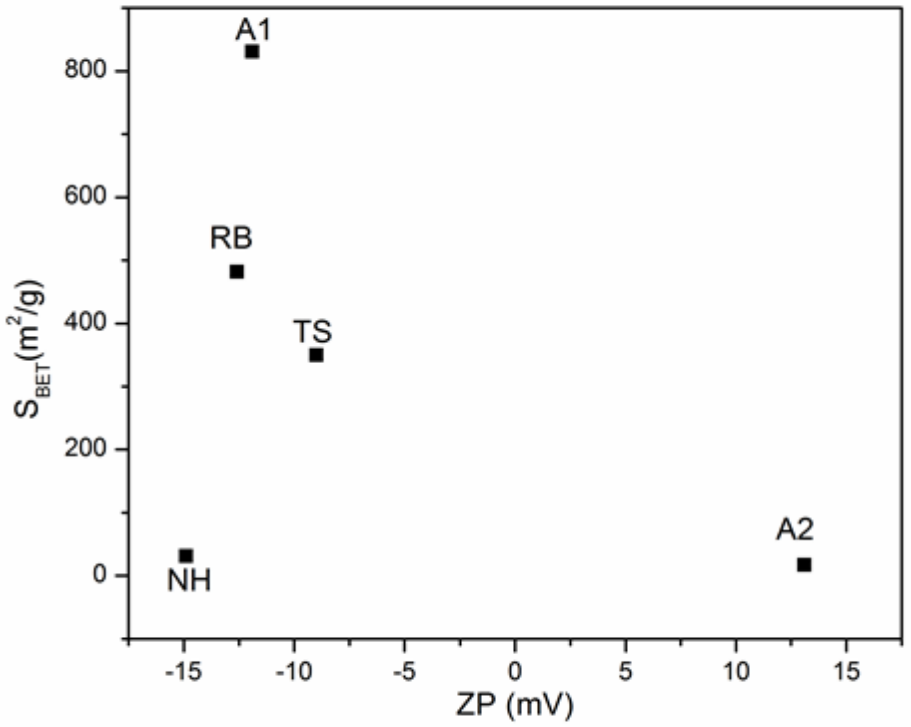

Figure 1: Influence of zeta potential on S_{BET} for extracted samples.

Taking into account the results shown in Table 1, strong direct Spearman correlations could be observed between (i) the radius of gyration (Rg) and the maximum removal of RhB (r_{Sp} > 0.872); (ii) P2 (degree of roughness) and the maximum removal of RhB (r_{Sp} > 0.821); the ζ

potential and the percentage of six-member rings (%SiO_6) (r_{Sp} > 0.900); the %SiO_6 and imprinting factor (IF) (r_{Sp} > -0.900); and IF and maximum removal of Rh6G (r_{Sp} > 0.800).

Some remarks can be made regarding these correlations. First, the higher the radius of gyration (*Rg*) of the primary particles, the higher the maximum removal of RhB, but the correlation seems to be limited at *Rg* = 1.0 nm, above which further increase in *Rg* does not affect RhB removal. Regarding the organization of primary particles in terms of *P* (level 2), it is worth noting that systems with less roughness (higher *P2*) seem to achieve better RhB removal. Silicas with higher %SiO_6 values (less tension) tend to be more hydrophilic. Thus, it is interesting to observe that higher IFs are obtained by systems with less % SiO_6. However, one cannot neglect that higher IFs could also increase the maximum removal of Rh6G. In other words, while lower values of % SiO_6, which can be achieved by altering the extraction process, increase the IF, higher values of IF may increase the removal of Rh6G, which is not desirable for selective removal. This seems to explain the behavior of the NH system. According to Table 1, this system showed the lowest % SiO_6 and the highest IF but also one of the highest removal levels of Rh6G and was most likely not higher than A1 because of the lower S_{BET} value. In addition, the systems with higher ζ potential tend to form more hydrophilic materials (higher % SiO_6 content). However, no correlation was found between ζ potential and maximum removal of the RhB or with maximum removal of Rh6G. Also, the value of area and selectivity factor (SF) was not statistically correlated with the variables studied herein (Table 1). Taking into account the above results, one can suggest that textural characteristics, other than solely S_{BET}, seem to be relevant in defining the degree of selective adsorption of these dyes.

Figure 2 shows a dendrogram obtained by taking into account the spectroscopic data, textural characteristics and adsorption capacities of the extracted systems. Three main groups

could be identified: (i) B and TS, (ii) A2 and NH and (iii) A1. The textural characteristics appear to be relevant to this outcome. This is evident if one considers that group ii embraces two different routes (hydrolytic and non-hydrolytic) for which some of the textural parameters are quite similar, as the *Rg* and S_{BET} values indicate (see Table 1). Similarly, the A1 group (group iii) showed the highest values of both Rg and S_{BET}. One cannot neglect that the size of the cavity produced in the imprinted material in the A1 material would be sufficient to allow for selective adsorption [40]. In this sense, the superior removal accomplished with the A1 material could also explain the distance observed in the dendrogram.

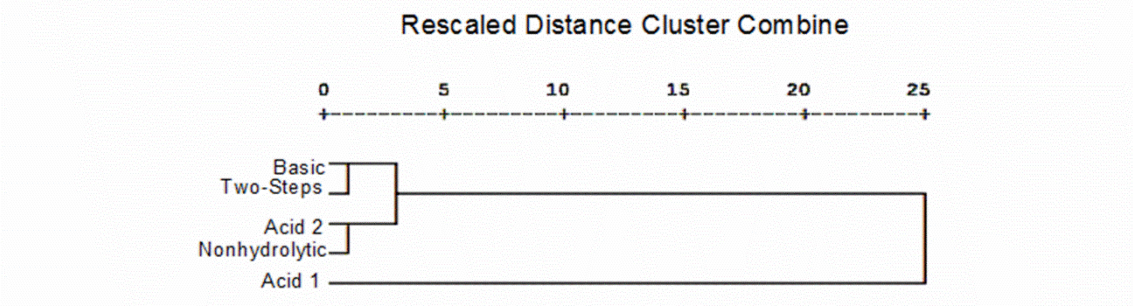

Figure 2: Dendrogram of the extracted samples.

Freundlich and Langmuir isotherms were used to estimate parameters using the experimental data obtained from A1. The values of the estimated parameters are presented in Supporting Information (Table S1). In the Freundlich isotherm, *K* is a parameter that corresponds to the adsorption site affinity, K_F is the Freundlich parameter, which refers to the distribution of active sites, and *(1/n)* is the adsorption capacity. For the Langmuir isotherm, q_m is the parameter related to the coverage of the adsorbent from solute in a monolayer, and K_L is the Langmuir isotherm parameter, which is related to the adsorption energy and corresponds to the affinity between the adsorbate and the adsorbent surface. The parameters shown in Supporting Information Table S1 were obtained by setting the parameter *K* by trial and error for the Freundlich isotherms.

The degree of fit between the estimated and experimental values was assessed by the determination coefficient (r^2) and the plot of the provided data versus experimental data. According to Fig. 3, the estimated parameters allowed for a suitable fit of both Freundlich and Langmuir adsorption isotherm with the experimental data. The goodness-of-fit, which was evaluated by r^2, was adequate as one can see by comparing the estimated adsorbed amount (q_e) of the compound to experimental values, as illustrated in Fig. 3. The experimental variance (ν_{exp}^2) obtained using the Langmuir isotherm is lower than that obtained using the Freundlich isotherm.

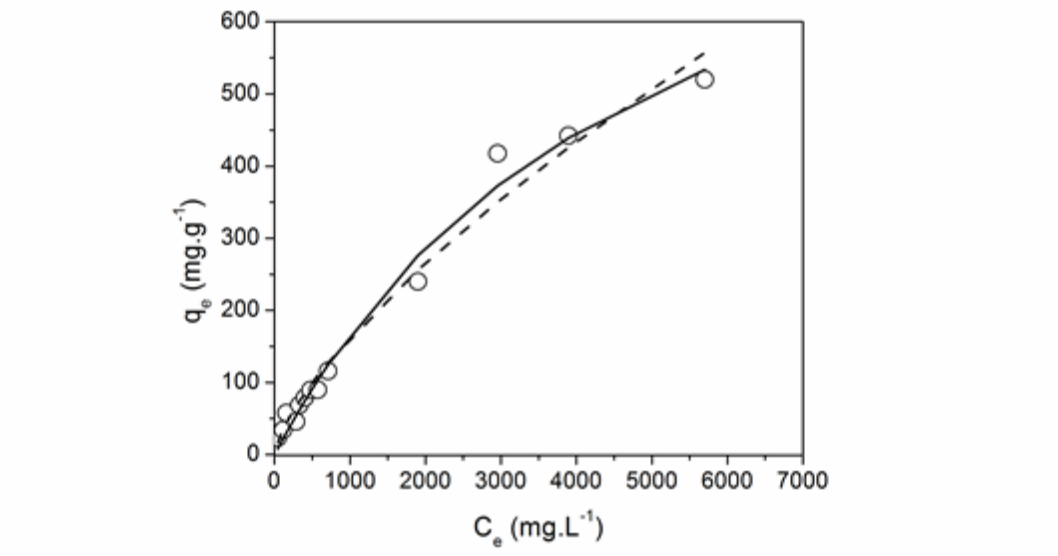

Figure 3: Fitting of the Freundlich (line) and Langmuir (dashed line) isotherm to the experimental data for acid route 1. Experimental data circles.

Recently, several works have been published regarding the adsorption of RhB. Table 2 shows a comparison of q_m and *1/n* for different materials found in the literature. Using the Langmuir isotherm, the value of q_m ranged from 5.2 to 529.1 mg/g. Our imprinted silica prepared by route A1 achieved a q_m value more than 1.8 times higher than the highest one found in recent work [12]. This finding highlights the good adsorption capacity of this adsorbent. It is possible

that this material is the best of the extracted systems tested because it has the highest surface area and because the sites on it that result from the printing process exhibit a strong affinity for RhB.

Table 2: Recent reported values of q_m and 1/n for some materials.

Adsorbent	q_m (mg/g)[(a)]	1/n[(b)]	T (°C)	Reference
Silica Imprinted (EA1TiRhB)	998.3 (±267.4)	0.709 (±0.097)	25	Present Work
Titania-silica	59.69	0.617	25	41
Zeolite MCM-22	48.8	0.089	30	42
Cellulose-based wastes	20.60	0.472	30	43
Sodium montmorillonite	42.19	0.310	30	13
Fe_3O_4 nanoparticles	161.8	---	20	11
Molecular imprinting on polypropylene fibers	19.00	---	25	44
Activated carbon	25.5	5.587	40	8
Surface modified tannery waste	212.77	0.286	30	9
AlMCM-41	57	---	25	10
Activated carbon	277.7	0.218	25	8
Iron-pillared bentonite	98.2	0.485	25	45
Duolite C-20 resin	28.571	0.249	30	15
Fe_3O_4 magnetic nanoparticles	529.1	0.246	25	12
Kaolinite	46.08	1.449	30	46
Exhausted coffee ground	5.255	0.485	25	47

a) Obtained from Langmuir isotherm; b) Obtained from Freundlich isotherm

Higher *1/n* values obtained from the Freundlich isotherm suggest a better adsorbent capacity of the material tested. It is worth noting that our system exhibited a value much lower than that obtained for activated carbon but higher than the value for Zeolite MCM-22 [42] and comparable to one for titania-silica [41]. This last material may be structurally similar to the present imprinted materials due the fact that it contains both silica and titania moieties.

The *1/n* value of our system is similar to those found by Morais et al. [48], in which silicas were synthesized by the molecular imprinting (MI) technique using an acid-catalyzed sol-gel process that employed drugs (fluoxetine, gentamicin, lidocaine, morphine, nifedipine, paracetamol, and tetracycline) as templates. Moreover, in the present study, the value of *K* found was 3450 mM^{-1} (see Table S1), which suggests a great affinity of the RhB for the resulting site of molecular imprinting and which supports the conclusions obtained from Langmuir isotherm regarding the value of q_m.

For all others routes, an attempt to adjust the experimental data to the Freundlich and Langmuir isotherms did not result in a good fit. Thus, the BET-modified isotherm was used for fitting the experimental data for all systems (see Figure S1). The estimated parameters are shown in Table 3. All systems showed a good value of r^2, ranging from 0.9232 to 0.9861. According to Table 1, A1 exhibited the highest *y1* value (997.91 mg/g). Considering that this parameter is equivalent to the q_m, this finding corroborates the results found for Langmuir isotherm (998.3 mg/g). All other systems had *y1* values ranging from 46.63 (NH) to 87.31 mg/g (TS).

Table 3: Estimated parameters BET-modified isotherms.

Parameter	A1	A2	B	TS	NH
y_1 (mg/g)	997.91 ($\pm 2.2\times10^3$)	61.3256 ($\pm$14.7259)	54.3612 ($\pm$24.0210)	87.3104 ($\pm$53.0054)	46.6336 ($\pm$22.9211)
y_2 (---)	3.49×10^5 ($\pm 8.1\times10^{10}$)	0.5709 ($\pm$0.1737)	27.8838 ($\pm$68.2230)	0.5921 ($\pm$0.0687)	71.2169 ($\pm$288.2332)
y_3 (mg/L)	1.73×10^9 ($\pm 4.0\times10^{14}$)	3.1962×10^3 ($\pm$50.9351)	3.6243×10^3 ($\pm$292.0801)	3.2085×10^3 ($\pm$275.6640)	3.6827×10^3 ($\pm$303.7411)
r^2	0.9861	0.9918	0.9232	0.9599	0.9560
ν^2_{exp}	505.91	1.2543×10^3	1.2219×10^3	1.8680×10^3	776.25
C	$\begin{bmatrix} 1 & & \\ 0.9945 & 1 & \\ 0.9945 & 1 & 1 \end{bmatrix}$	$\begin{bmatrix} 1 & & \\ 0.3640 & 1 & \\ 0.9606 & 0.2347 & 1 \end{bmatrix}$	$\begin{bmatrix} 1 & & \\ -0.6244 & 1 & \\ 0.9639 & -0.5932 & 1 \end{bmatrix}$	$\begin{bmatrix} 1 & & \\ 0.8678 & 1 & \\ 0.9732 & 0.7955 & 1 \end{bmatrix}$	$\begin{bmatrix} 1 & & \\ -0.6244 & 1 & \\ 0.9639 & -0.5932 & 1 \end{bmatrix}$

Because of the nature of the fractal system usually observed in silica [49], it was worth investigating the relationship between the SAXS parameters and the y_1 value. As shown by Figure 4, the systems with lower *Rg* values presented the lowest y_1 values, whereas higher *Rg* value were found for systems with the highest y_1 values ($r_{Sp} > 0.82$). This finding suggest that fractal clusters` structure, formed by the aggregation of primary particles, could improve the adsorption capacity to extent that it increases the value of *Rg*. This finding appears to corroborate the Spearman's correlation discussed before between *Rg* and maximum removal of RhB. However, from the point of view of selectivity, because systems bearing lower *Rg* values (TS) showed higher IFs (see Table S1), other influences besides the *Rg* value seem to dictate the adsorption process.

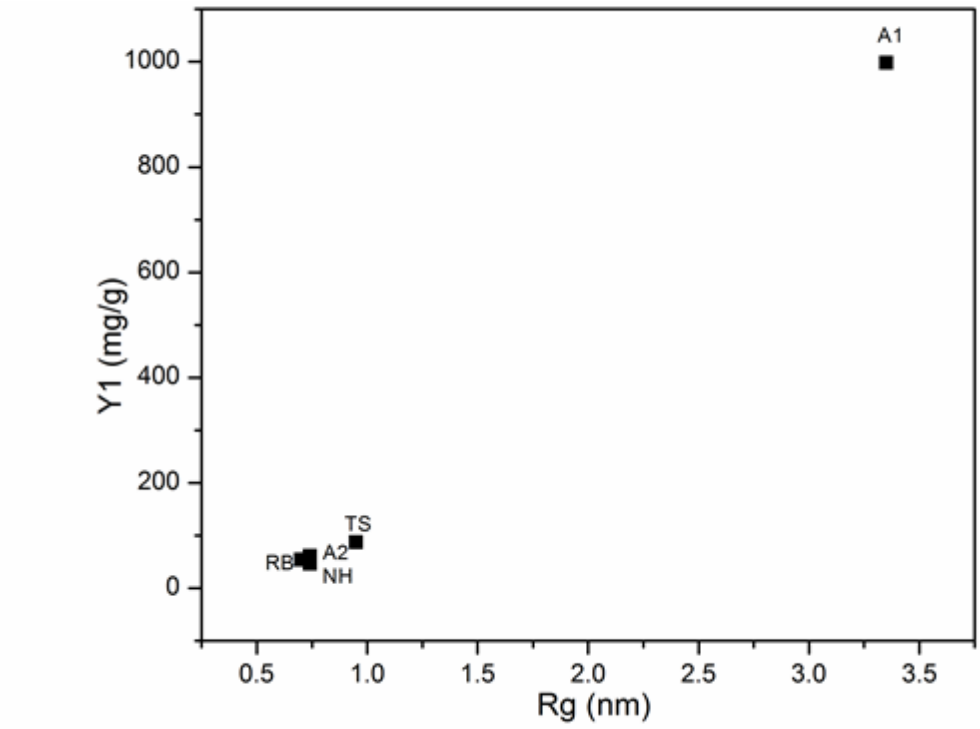

Figure 4: Influence of gyration radii on y1.

Remarkably, a strong correlation was found between *y1* and SF (r_{SP} = 0.8). Thus, this finding suggests that the sol-gel route chosen to prepare molecularly imprinted materials can be designed for high adsorption capacity without compromise the selectivity.

Comparing only the hydrolytic sol-gel systems allows for additional remarks to be made. Except for acid route, the basic route yielded the lowest *y1* value while the two-step route had the highest one. This behavior highlights the effect of the synthesis route on adsorption capacity. The TS route follows a synthesis protocol that combines both acidic and basic catalysts, which, considering that A1 had the highest *y1* value, may explain the reason of the value found for TS. While the ratio of surface area of the materials produced by TS and A2 was 20.5, the ratio of *y1* between these two systems is 1.42. Although A2 possessed the lowest S_{BET}, the *y1* value is not so different from the TS. In other words, a lower S_{BET} does not necessarily result in low adsorption capacities. Similarly, although B had an S_{BET} area almost 1.37 higher than TS, the *y1* value for TS is 1.6 higher than that of B. Similarly, although B had S_{BET} almost 1.37 higher than that of TS, the *y1* value for TS was 1.6 higher than that of B. However, in the case of B, it is important to recall that despite the high S_{BET} value, this system may be suffering from leaching or infective generation of specific sites for recognition of RhB.

The BET-modified isotherms can be classified according to their initial slope and sub-grouped into classes based on the shapes of the upper parts of the curves. The initial slope depends on the rate of change of site availability as the amount of adsorbed solute increases. According to the classification of Giles et al. [50] we identified two main groups of isotherms: Type L and S curves. For the L curves and the later stages of the S curves, there is less of a chance that a solute molecule will find a site to adsorb to the extent that a measurable increase in the uptake of solute occurs. Additionally, for L curves, the sites are few and widely separated and adsorption occurs

by either a monodisperse or an aggregated solute [51]. Conversely, the initial part of an S curve represents different behavior such that when more solute is adsorbed, it becomes easier for additional amounts to adsorb. As discussed by Giles et al. [50], this enhancement of adsorption to the surface is due to a side-by-side association between adjacent adsorbed molecules. On the basis of the above descriptions, it was possible to classify the BET-modified isotherm for A1 as L curve, and all of the rest as S curves. It is important to note that the curves of A2, B and TS shared a commonality in that they had at least one maximum in the value of q_e following a decrease, whereas the q_e tends to a constant value for NH. The similarity found between B and TS is also in agreement the dendrogram analysis presented in the above discussion. Such an analysis is also in agreement with the very fact that all systems, except A1, presented S-type isotherms.

The identification of all of the systems except for A1 as S curves indicates that, for these systems, the solute molecule (i) experiences moderate intermolecular attraction, (ii) meets strong competition for substrate sites from molecules of the solvent or of any another adsorbed species and (iii) is monofunctional; i.e., the solute molecule has a fairly large hydrophobic residue (> C5) and that it is adsorbed as a single unit and not in the form of a micelle.

In addition, the presence of S type curves is typical for systems in polar solvents such as water. The results of the isotherm analysis may also indicate a remarkable difference between the other systems and the A1 system, in that there is a tendency for large adsorbed molecules to associate to their surfaces rather than to remain as isolated units as they adsorb [50]. S-curves may also indicate "cooperative adsorption", in the sense that solute molecules tend to adsorb in packed rows or clusters [51]. Such is the case when molecules tend to be adsorbed as ionic micelles, or when their intermolecular attraction is very high. In contrast, for L type isotherms, there is no strong competition with the solvent.

Among the types of curves described in the literature, there is also a type C curve which occurs when the availability of sites remains constant at all concentrations up to saturation [50]. One feature of systems that exhibit such curves is that the solute has a higher affinity for the substrate than the solvent has. Considering that no such curves were observed for our systems, one cannot neglect the possibility that the solvent may compete with the solute for substrate sites (which is one of characteristic of S type curves). Nevertheless, the high value of estimated adsorbent capacity for the A1 system, which is even greater than others found in literature [8, 9, 12], suggests that adsorption indeed occurs due to the presence of the imprinted sites available on the surface of silica rather than due to interaction with the solvent. Furthermore, in terms of selectivity, this is in agreement with the better results achieved for the adsorption of RhB over Rh6G as observed in the selectivity and competitive experiments discussed previously [27].

We propose that the mechanism of adsorption may be roughly the same for B, TS, A2 and NH based on the similarities of their isotherm shapes. Taking into account the above findings, Scheme 1 depicts the main differences between the A1, A2 and NH systems. A1 uniquely exhibited an L-type isotherm, as well as the highest S_{BET} and *Rg* values, which, to some extent, could contribute to an improvement in the removal of the dye. Considering the parameters herein studied, A1 produced material with the least similarity to those produced by other routes. Remarkably, a comparison of A2 and NH shows that, although prepared by different routes (in the sense that one was prepared by a hydrolytic route and the other by a nonhydrolytic process), both showed statistical similarity – even though the latter proved better at selectively removing dye. To some extent, this improvement may be explained by the negative ζ potential values measured for NH.

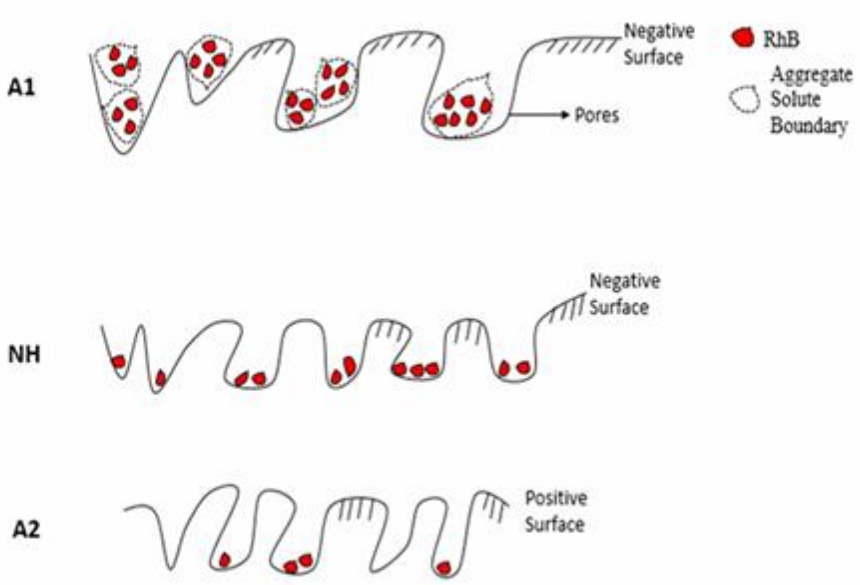

Scheme 1: Simplified proposal model of adsorption for A1, NH and A2.

Conclusion

The employed methodologies, based on sol-gel processes catalyzed by various species, were shown to be efficient for the production of molecularly imprinted materials. The effect of the sol-gel route employed in the preparation of imprinted silica for the adsorption of dyes significantly alters both its structure and dye adsorption properties. The synthesis route was found to alter other characteristics of the silica surface and structure, including ζ potential, radius of gyration and percentage of six-membered rings, which, in turn, seem to influence the selective adsorption properties of these dyes. Thus, although S_{BET} value is an important indicator of adsorption capacity (as observed for A1), the present systems have shown that the role of interaction of surface charges and the extraction process need to be considered to design new molecularly imprinted materials by sol-gel methods aiming at optimizing selective adsorption. In this sense, the sol-gel route chosen to prepare molecularly imprinted materials can be tuned for a specific probe molecule.

Although different in their nature, dendrogram analysis showed that the extracted systems obtained by hydrolytic (A2) and non-hydrolytic (NH) synthesis routes are similar in their textural characteristics; even so, they exhibit markedly different adsorption capacities.

The Langmuir model was a good fit for the experimental data gathered for material produced by the A1 route, and the value of q_m achieved was comparable to and even higher than that reported in other studies, which suggest it possesses very good adsorption capacities for RhB removal.

A BET-modified isotherm was used to fit the experimental data for all of the systems. The observed nature of the adsorption isotherms for all of the routes except the A1 route indicated that there is a tendency for large adsorbed molecules to associate to these surfaces rather than to remain as isolated units during adsorption. In addition, the present results suggest that molecularly imprinted materials can be designed for high adsorption capacity without compromise the selectivity.

Acknowledgments

This project was partially financed by the CNPq. C. Escobar is grateful for the grant provided by the CAPES. The authors also thank the LNLS (Project D11A-SAXS1-8691) for SAXS beamline measurements.

References

(1) Bharathi, K. S. Ramesh, S. T. Removal of dyes using agricultural waste as low-cost adsorbents: a review. *Appl. Water Sci.* **2013**, 3, 773-790.

(2) Gupta, V. K.; Jain, R.; Nayak, A.; Agarwal, S. Shrivastava, M. Removal of the hazardous dye - Tartrazine by photodegradation on titanium dioxide surface. *Mater. Sci. Eng. C* **2011**, 31, 1062-1067.

(3) Saratale, R. G.; Saratale, G. D.; Chang, J. S.; Govindwar, S. P. Bacterial decolorization and degradation of azo dyes: A review. *J. Taiwan Inst. Chem. Eng.* **2011**, 42, 138-157.

(4) Shah, M. P.; Patel, K. A.; Nair, S. S.; Darji, A. M. Microbial Decolorization of Methyl Orange Dye by *Pseudomonas spp. Int. J. Env. Bio. Bio.* **2013**, 1, 54-59.

(5) Gupta, V. K.; Suhas, J. Application of low-cost adsorbents for dye removal – A review. *J. Env. Manag.* **2009**, 90, 2313-2342.

(6) Khataee, A. R.; Kasiri, M. B. Photocatalytic degradation of organic dyes in the presence of nanostructured titanium dioxide: Influence of the chemical structure of dyes. *J. Mol. Catal. A Chem.* **2010**, 328, 8-26.

(7) Jain, R.; Mathur, M.; Sikarwar, S.; Mittal, A. Removal of the hazardous dye rhodamine B through photocatalytic and adsorption treatments. *J. Env. Manag.* **2007**, 85, 956-964.

(8) Li, L.; Liu, S.; Zhu, T. Application of activated carbon derived from scrap tires for adsorption of rhodamine B. *J. Env. Sci. Sci.* **2010**, 22, 1273-1280.

(9) Anandkumar, J.; Mandal, B. Adsorption of chromium (VI) and rhodamine B by surface modified tannery waste: Kinetic, mechanistic and thermodynamic studies. *J. Hazard. Mat.* **2011**, 186, 1088-1096.

(10) Eftekhari, S.; Habibi-Yangjeh, A.; Sohrabnezhad, S. Application of AlMCM-41 for competitive adsorption of methylene blue and rhodamine B: Thermodynamic and kinetic studies. *J. Hazard. Mat.* **2010**, 178, 349-355.

(11) Peng, L.; Qin, P.; Lei, M.; Zeng, Q.; Song, H.; Yang, J.; Shao, J.; Liao, B.; Gu, J. Modifying Fe_3O_4 nanoparticles with humic acid for removal of Rhodamine B in water. *J. Hazard. Mat.* **2012**, 209–210, 193-198.

(12) Mittal, H.; Mishra, S. B. Gum ghatti and Fe_3O_4 magnetic nanoparticles based nanocomposites for the effective adsorption of rhodamine B. *Carbo. Pol.* **2014**, 101, 1255-1264.

(13) Selvam, P. P.; Preethi, S.; Basakaralingam, P.; N.Thinakaran; Sivasamy, A.; Sivanesan, S. Removal of rhodamine B from aqueous solution by adsorption onto sodium montmorillonite. *J. Hazard. Mat.* **2008**, 155, 39-44.

(14) Khan, T. A.; Dahiya, S.; Ali, I. Use of kaolinite as adsorbent: Equilibrium, dynamics and thermodynamic studies on the adsorption of Rhodamine B from aqueous solution. *Appl. Clay Sci.* **2012**, 69, 58-66.

(15) Al-Rashed, S. M.; Al-Gaid, A. A. Kinetic and thermodynamic studies on the adsorption behavior of Rhodamine B dye on Duolite C-20 resin. *J. of Saudi Chem. Soc.* **2012**, 16, 209-215.

(16) Paz, Y. Preferential photodegradation – why and how? *Compt. Rend. Chim.* **2006**, 9, 774-787.

(17) Cheong, W. J.; Yang, S. H.; Ali, F. Molecular imprinted polymers for separation science: A review of reviews. *J. Sep. Sci.* **2013**, 36, 609-628.

(18) Lofgreen, J. E.; Ozin, G. A. Controlling morphology and porosity to improve performance of molecularly imprinted sol-gel silica. *Chem. Soc. Rev.* **2014**, 43, 911-933.

(19) Chen, L.; Xu, S.; Li, J. Recent advances in molecular imprinting technology: current status, challenges and highlighted applications. *Chem. Soc. Rev.* **2011**, 40, 2922-2942.

(20) Cheong, W. J.; Yang, S. H.; Ali, F. Molecular imprinted polymers for separation science: A review of reviews. *J. Sep. Sci.* **2013**, 36, 609-628.

(21) Mayes, A. G.; Whitcombe, M. J. Synthetic strategies for the generation of molecularly imprinted organic polymers. *Adv. Drug Del. Rev.* **2005**, 57, 1742-1778.

(22) Díaz-García, M. E.; Laínño, R. B. Molecular Imprinting in Sol-Gel Materials: Recent Developments and Applications. *Microchim. Acta* **2005**, 149, 19-36.

(23) Walcarius, A.; Collinson, M. M. Analytical chemistry with silica sol-gels:

traditional routes to new materials for chemical analysis. *Annu. Rev. Anal. Chem.* **2009**, 2, 121-43.

(24) Xu, X.; Chen, S.; Wu, Q. Surface molecular imprinting on polypropylene fibers for rhodamine B selective adsorption. *J. Sci. Food Agric.* **2012**, 385, 193-201.

(25) Ramamoorthy, M.; Ulbricht, M. Molecular imprinting of cellulose acetate-sulfonated polysulfone blend membranes for rhodamine B by phase inversion technique. *J. Memb. Sci.* **2003**, 217, 207-214.

(26) Malaisamy, R.; Ulbricht, M. Evaluation of molecularly imprinted polymer blend filtration membranes under solid phase extraction conditions. *Sep. Purif. Technol.* **2004**, 39, 211-219.

(27) de Coelho Escobar, C.; dos Santos, J. H. Z. Effect of the sol–gel route on the textural characteristics of silica imprinted with rhodamine B. *J. Sep. Sci.* **2014**, 37, 868-875.

(28) de Escobar, C., Dartora, M., Campo, L., Radtke, C., Bayne, J.M., Butler, I.S., Latuada, R.M, dos Santos, J.H.Z. The role of the sol-gel route on the interaction between rhodaminhe B and a silica matrix. *J.Solgel Sci. Tech.* **2014**, 1-13.

(29) Fidalgo, A.; Ilharco, L. M. The defect structure of sol–gel-derived silica/polytetrahydrofuran hybrid films by FTIR. *J. Non-Cryst Solids* **2001**, 283, 144-154.

(30) Ilavsky, J., Jemian, P. R. Irena: tool suite for modeling and analysis of small-angle scattering. *J. Appl. Crystallogr.* **2009**, *42*, 347-353.

(31) Kline, S. Reduction and analysis of SANS and USANS data using IGOR Pro. J. *Appl. Crystallogr.* **2006**, *39*, 895-900.

(32) Beaucage, G. Small-angle scattering from polymeric mass fractals of arbitrary mass-fractal dimension. *J. Appl. Crystallogr.* **1996**, 29, 134-146.

(33) Beaucage, G. Approximations leading to a unified exponential/power-law approach to small-angle scattering. *J. Appl. Crystallogr.* **1995**, 28, 717-728.

(34) Lindfiel, G., Penny, J. *Numerical Method using Matlab. Numerical Methods Using Matlab*; Ellis Horwood, London, **1995**.

(35) Himmelblau, D. M. *Process Analysis by Statistical Methods*; Prentice-Hall, Upper Saddle River, **1967**.

(36) Ebadi, A.; Soltan Mohammadzadeh, J.; Khudiev, A. What is the correct form of BET isotherm for modeling liquid phase adsorption? *Adsorption* **2009**, 15, 65-73.

(37) Brinker, C. J., Scherer, G. W. *Sol-Gel Science: The Physics and Chemistry of Sol-Gel Processing*; Academic Press, New York, **1990**.

(38) Capeletti, L. B.; Bertotto, F. L.; Dos Santos, J. H. Z.; Moncada, E. Cardoso, M. B. The effect of the sol–gel route on the characteristics of acid–base sensors. *Sens. Actuators B Chem.* **2010**, 151, 169-176.

(39) Garcia, A. L.; Ista, L. K.; Petsev, D. N.; O'Brien, M. J.; Bisong, P.; Mammoli, A. A.; Brueck, S. R. J.; Lopez, G. P. Electrokinetic molecular separation in nanoscale fluidic channels. *Lab. Chip* **2005**, 5, 1271-1276.

(40) Morais, E.; Correa, G.; Brambilla, R.; Livotto, P.; dos Santos, J.; Cardoso, M. Silica imprinted materials containing pharmaceuticals as a template: textural aspects. *J. Solgel Sci. Tech.* **2012**, 64, 324-334.

(41) Messina, P. V.; Schulz, P. C. Adsorption of reactive dyes on titania–silica mesoporous materials. *J. Colloid Interface Sci.* **2006**, 299, 305-320.

(42) Wang, S.; Li, H.; Xu, L. Application of zeolite MCM-22 for basic dye removal from wastewater. *J. Colloid Interface Sci.* **2006**, 295, 71-78.

(43) Annadurai, G.; Juang, R.-S.; Lee, D.-J. Use of cellulose-based wastes for adsorption of dyes from aqueous solutions. *J. Hazard. Mat.* **2002**, 92, 263-274.

(44) Xu, X., Chen, S., Wu, Q. Surface molecular imprinting on polypropylene fibers for rhodamine B selective adsorption. *J. Colloid Interface Sci.* **2012**, 385, 193-201.

(45) Hou, M.-F.; Ma, C.-X.; Zhang, W.-D.; Tang, X.-Y.; Fan, Y.-N.; Wan, H.-F. Removal of rhodamine B using iron-pillared bentonite. *J. Hazard. Mat.* **2011**, 186, 1118-

1123.

(46) Khan, T. A.; Dahiya, S.; Ali, I. Use of kaolinite as adsorbent: Equilibrium, dynamics and thermodynamic studies on the adsorption of rhodamine B from aqueous solution. *Appl. Clay Sci.* **2012**, 69, 58-66.

(47) Shen, K., Gondal, M. A., J. Removal of hazardous Rhodamine dye from water by adsorption onto exhausted coffee ground *Saudi Chem. Soc*., **2013**, doi: 10.1016/j.jscs.2013.11.005.

(48) Morais, E. C.; Correa, G. G.; Brambilla, R.; dos Santos, J. H. Z.; Fisch, A. G. Selective silica-based sorbent materials synthesized by molecular imprinting for adsorption of pharmaceuticals in aqueous matrices. *J. Sep. Sci.* **2013**, 36, 636-643.

(49) Avnir, D. *The Fractal Approach to Heterogeneous Chemistry*, J. Wiley and Sons, New York, **1990**.

(50) Giles, C. H.; MacEwan, T. H.; Nakhwa, S. N.; Smith, D. Studies in adsorption. Part XI. A system of classification of solution adsorption isotherms, and its use in diagnosis of adsorption mechanisms and in measurement of specific surface areas of solids. *J. Chem. Soc.* **1960**, 3973-3993.

(51) Giles, C. H.; Smith, D.; Huitson, A. A general treatment and classification of the solute adsorption isotherm. I. Theoretical. *J. Colloid Interface Sci.* **1974**, 47, 755-765.

Supporting Information

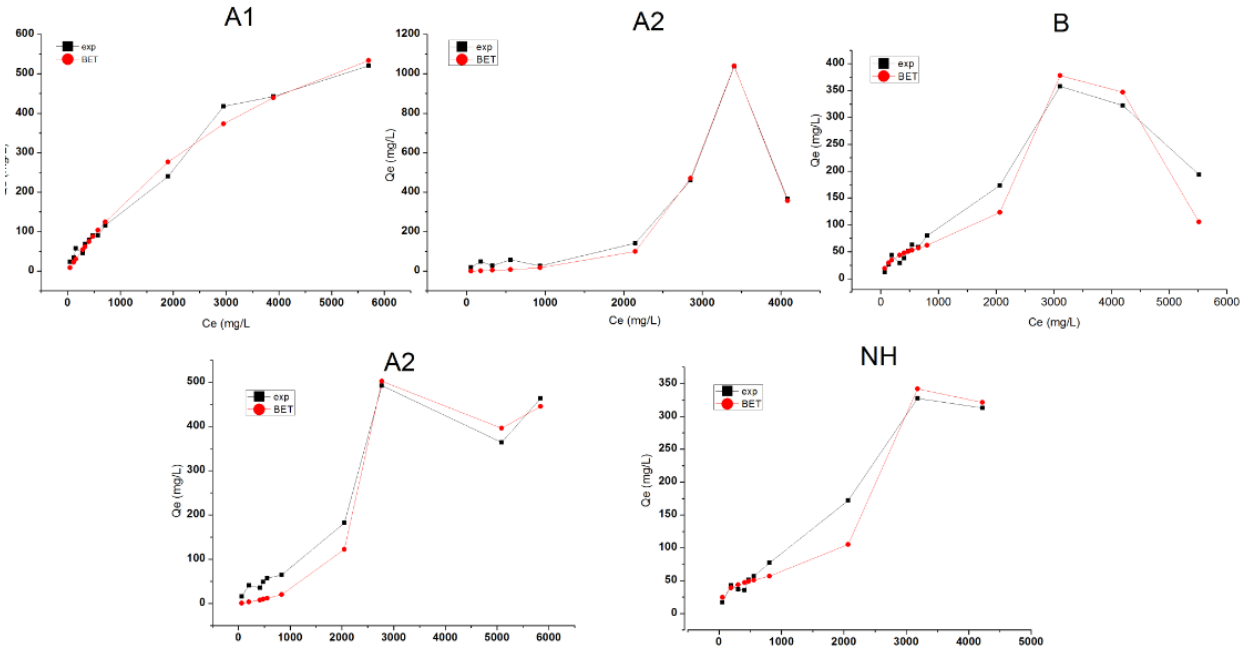

Supporting Information Figure S1 - Predicted and estimated BET isotherms.

Supporting Information Table S1: Parameters of Freundlich and Langmuir

	Parameter	Value
Freundlich	K (mM^{-1})	3450
	k_f (mg/g)(L/g)^n	1.2236 (±0.0834)
	(1/*n*)	0.7078 (±0.0968)
	r^2	0.9787
	V^2_{exp}	707.53
	C	$\begin{bmatrix} 1 & 0.0061 \\ 0.0061 & 1 \end{bmatrix}$
Langmuir	q_m (mg/g)	998.3032 (±267.4843)
	k_a (L/mg)	0.0002 (±0.0001)
	r^2	0.9861
	V^2_{exp}	459.9224
	C=	$\begin{bmatrix} 1 & -0.9788 \\ -0.9788 & 1 \end{bmatrix}$

4.4 Artigo 4

Publicado no *Colloids and Surfaces A: Physicochemical and Engineering Aspects*, v. 486, p. 96-105.

Colloids and Surfaces A: Physicochem. Eng. Aspects 486 (2015) 96–105

Contents lists available at ScienceDirect

Colloids and Surfaces A: Physicochemical and Engineering Aspects

journal homepage: www.elsevier.com/locate/colsurfa

The sol–gel route effect on the preparation of molecularly imprinted silica-based materials for selective and competitive photocatalysis

Cícero Coelho de Escobar [a], Alexsandro Dallegrave [b], Marla Azário Lasarin [a], João Henrique Zimnoch dos Santos [b,*]

[a] Departamento de Engenharia Química – Universidade Federal do Rio Grande do Sul, Rua Eng. Luis Englert s/n, 90040-040 Porto Alegre, RS, Brazil
[b] Instituto de Química, Universidade Federal do Rio Grande do Sul, Av. Bento Gonçalves, 9500, Porto Alegre CEP 91500-000, Brazil

HIGHLIGHTS

- A series of molecularly imprinted photocatalysts were prepared by sol–gel routes.
- Photocatalytic tests were conducted to evaluate the selectivity and competitiveness.
- Adsorption occurs on the domains of silica imprinted.
- An increase in selectivity was obtained (up to 2.8-fold) compared to the P25.
- An increase in competitiveness was obtained (up to 55%) compared to the P25.

GRAPHICAL ABSTRACT

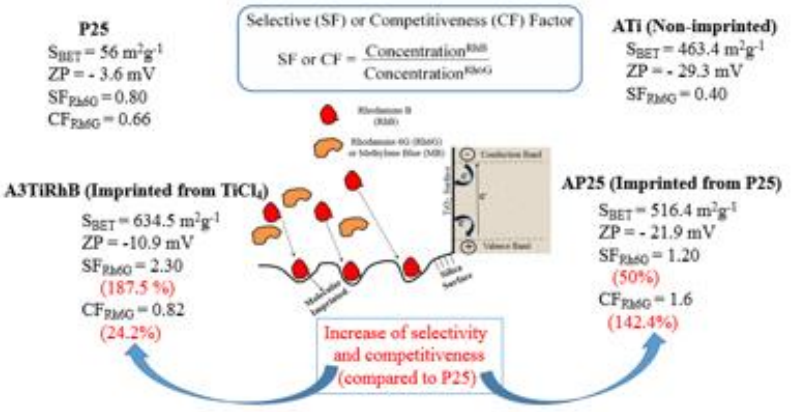

ARTICLE INFO

Article history:
Received 2 July 2015
Received in revised form 26 August 2015
Accepted 11 September 2015
Available online 14 September 2015

Keywords:
Sol–gel
Imprinted materials
Selective photocatalysis
Silica
Titania

ABSTRACT

A series of molecularly imprinted photocatalysts containing rhodamine B (RhB) as a template were prepared from four different routes, namely acid, basic-catalyzed, two-steps and non-hydrolytic sol–gel routes, using $TiCl_4$ as a TiO_2 source. Variations in acid route synthesis (rate of heat on calcination, absence of HCl and replacement of $TiCl_4$ for commercial P25) were also evaluated. For comparison, non-imprinted samples were also synthesized. Photocatalytic tests were conducted to evaluate the selectivity (RhB, rhodamine 6G (Rh6G) and methylene blue (MB)), competitiveness (RhB versus Rh6G and RhB versus MB) and regeneration of catalysts in terms of initial adsorption and degradation. The effects of the solid photocatalyst texture and structure (surface area, zeta potential, radius of gyration and fractal geometry) on the degree of RhB degradation were also examined. From the results of the photocatalysis tests and statistical analysis, we have shown that dye adsorption occurs on the silica domains that are imprinted in the vicinity of the photocatalyst due to photocatalytic degradation. Compared to the commercial photocatalyst (P25), an increase in selectivity (up to 180%) and competitiveness (up to 290%) were obtained. Regarding the acid route, the absence of HCl during the catalyst synthesis resulted in a loss of degradation compared to P25 and a 3-fold lower factor of competitiveness compared to the system in which HCl was used. In the regeneration tests, degradation was maintained at 80% of that of initial tests for up to three cycles.

* Corresponding author. Fax: +55 51 3316 7304.
E-mail address: jhzds@iq.ufrgs.br (J.H. Zimnoch dos Santos).

INTRODUCTION

Advanced oxidation processes (AOPs) are known methods of pollutant degradation that involve mineralization of a wide variety of organic contaminants. Among the compounds of concern, there are emerging contaminants, that include pharmaceutical and personal care products, steroids, surfactants, pesticides and dyes [1]. In the case of synthetic dyes, it is estimated that more than 280,000 tons are discarded worldwide [2]. Many of these contaminants are not adequately removed in conventional treatment processes. In these cases, mineralization, or the conversion of the molecules to their highest possible oxidation state and then into water, carbon dioxide, oxidized inorganic anions and/or other molecules that can be removed by biological processes, is required for full removal.

Among the AOPs, heterogeneous photocatalysis using TiO_2 is one of the most promising for use with emerging contaminants. Although this method shows clear advantages, such as low cost, low toxicity and chemical stability [3], heterogeneous photocatalysis lacks selectivity for the

most hazardous contaminants [4, 5]. This characteristic is a disadvantage, as mixtures derived from effluent streams may contain hazardous contaminants and low toxicity contaminants. In many cases, the former is present in lower concentrations, and the latter is the majority [4, 5], but it is desirable to preferentially degrade the most toxic materials.

The commercial use of TiO_2 is also difficult due the cost of separating the treated effluent and the photoactive micro-particles. One possible method to overcome this challenge is to the use of supports [6], which provides other advantages, including immobilization of the active catalyst, increases in the catalytic material surface area, and improvements in thermal and chemical stability [7]. Thus, several studies have explored different uses of supports, such as activated carbon [8], clay [9], graphene [10] and zeolites [11].

Although extensively studied, the use of supports in heterogeneous photocatalysis does not necessarily address the problem of selectivity. Therefore, a new approach has been investigated here that combines the technique of molecular imprinting (MI) with heterogeneous photocatalysis. MI is a promising technique for creating a template of specific molecular recognition [12]. This technique can be carried out in an organic or inorganic matrix due to the presence of a template molecule during the formation of the three-dimensional polymer [13, 14]. The majority of MI applications in inorganic matrix materials are based on a silica network that is synthesized by the sol-gel method. Recent studies have shown the feasibility of this approach for selective adsorption and pre-concentration of compounds such as drugs and dyes [15; 16].

The imprinting approach combined with photocatalysis is very promising due to its simplicity. However, among the studies that have been conducted on this approach [5], the majority of them have utilized an organic matrix. Thus, the effect of MI in inorganic matrices on selective photocatalysis is not well understood. We have previously investigated the effect of the

sol-gel route in molecularly imprinted materials in terms of textural and structural properties. We have shown the potential of silica imprinted materials for use in selective adsorption, and we have demonstrated that Ti moieties (using $TiCl_4$ as a source of TiO_2) can be incorporated into the silica network [16, 17]. We also have discussed adsorption capacity (q_m) for RhB in terms of isotherm adsorption for different sol-gel routes [18]. We have shown that acid-catalyzed route yielded a q_m value of 998.3 $mg.g^{-1}$ (Langmuir model), which is comparable or even higher than the recent reports. Taking into consideration, we were motivated to explore different methodologies (comparing $TiCl_4$ and P25 as precursor to TiO_2) to prepare photocatalysis based on acid-route. As an extension of these studies, the present work reports the effect of the sol-gel route on preparation of photocatalysts for selective and competitive photocatalysis. The effects of textural characteristics (surface area, zeta potential, radius of gyration and fractal geometry) on RhB degradation are also discussed. To the best of our knowledge, the current work is the first report on the influence of material sol-gel routes on heterogeneous selective and competitive photocatalysis.

EXPERIMENTAL SECTION

Materials and methods

Rhodamine B (RhB) (Vetec), rhodamine 6G (Rh6B) (Sigma–Aldrich), methylene blue (MB) (Vetec), tetraethoxysilane ($Si(OCH_2CH_3)_4$, TEOS, Merck, >98%), titanium tetrachloride (Merck, >99%), silicon tetrachloride ($SiCl_4$, Sigma–Aldrich, 99%) and titanium dioxide (TiO_2, P25-Degussa) were used as received. Hydrochloric acid (HCl, Nuclear, 38%), ammonium hydroxide (NH_4OH, Nuclear, 29%) and $FeCl_3$ (98%, Merck) were employed as catalysts.

Preparation of the photocatalysts

Five different routes were employed to prepare the samples using the sol-gel process and TEOS as the raw material. The routes were labeled as follows: acid-catalyzed route 1 (A1), acid-catalyzed route 2 (A2), base-catalyzed route (B), two-step route (TS) and non-hydrolytic route (NH). Acid-catalyzed route 1 utilized 0.2 M hydrochloric acid at a 1:2 (HCl:TEOS) ratio. Acid-catalyzed route 2 was similar to acid-catalyzed route 1, but the samples were prepared without hydrochloric acid (i.e., $TiCl_4$ acted as a potential Lewis acid catalyst). The base-catalyzed route utilized 0.2 M ammonium hydroxide at a 1:2 (NH_4OH:TEOS) ratio. The two-step route utilized 0.2 M hydrochloric acid at a 1:2 (HCl:TEOS) ratio; then, after 30 min., 0.2 M ammonium hydroxide was added at a 1:2 (NH_4OH:TEOS) ratio. The non-hydrolytic route employed TEOS and $SiCl_4$ and was catalyzed with $FeCl_3$ (0.5 wt.% of the final product weight). For each sample, RhB was fixed at 150 mg.

Samples (powder) from the acid-catalyzed, base-catalyzed and two-step routes were prepared as follows. RhB was added to a solution of TEOS followed by addition of $TiCl_4$, and then the catalyst was added. During this process, the solution was continuously stirred at room temperature until gelation or precipitation occurred, depending on the route. For the non-hydrolytic route, the procedures were executed under inert atmosphere (Ar). TEOS, $SiCl_4$ and $TiCl_4$ were added after adding the catalysts and RhB. The resulting solution was stirred at 80°C until gelation. The solids were dried at room temperature and milled.

For template removal, ultrasound-assisted (Branson-Sonifer®, Model 250) extraction was employed using methanol as the solvent (approximately 70 mL) The process was conducted by altering modes of pulse-on (20 s) and pulse-off (5 s) for five minutes. The solid was filtered and dried at room temperature. These samples were labeled molecularly imprinted (MI). For all of the

routes, equivalent synthesized samples were prepared without the addition of RhB, i.e., non-imprinted (NI) systems.

MI and NI systems were submitted to a calcination process. This process was carried out in a muffle furnace at 450 °C for 4 hours at a rate of 5 °C/min. For acid route 1, the effect of heating rate was also evaluated. In this case, the system was labeled as acid route 3 (A3), in which calcination occurred slowly by keeping the temperature constant for 1 hour at each increment of 100 °C and by utilizing a heating rate of 1 °C/min. This procedure was continued until the temperature reached 450 °C, and then the material was held at this temperature for 4 h.

In order to combine the concept of molecular imprinting with photocatyst impregnation, acid route was also evaluated by replacing $TiCl_4$ with P25 (Degussa). In this case, P25 was added 2 ½ hours after the beginning of the synthesis reaction (AP25). For comparison, the same material was synthesized without P25 (AWP25). There was no need for calcination in these systems.

The resulting photocatalysts were named according to the employed sol-gel route, considering the presence or absence of dye (RhB). For example, the MI system based on the non-hydrolytic route with RhB is represented by NHTiRhB. For NI systems, the label used was NHTi. Scheme 1 shows a flowchart of the MI system routes.

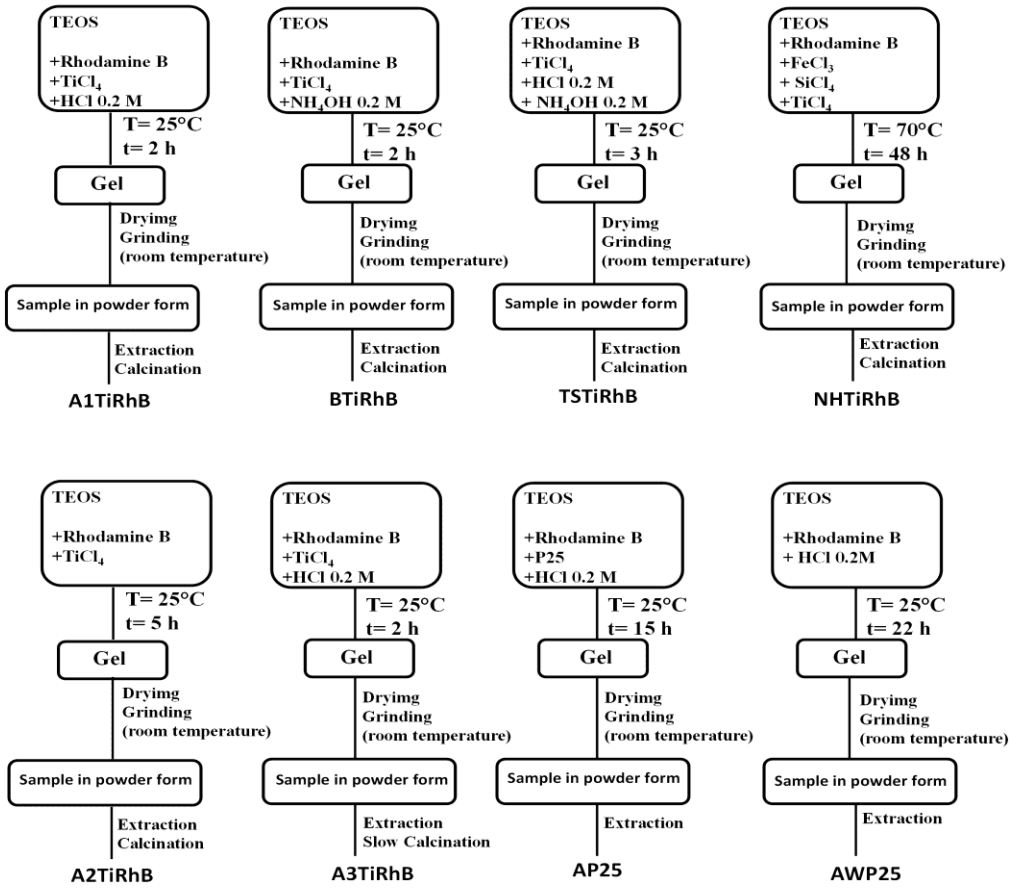

Scheme 1: Different sol–gel routes employed for photocatalyst synthesis.

Photocatalyst tests

Selective Tests

All photocatalytic tests were designed so that the theoretical mass of TiO_2 present was 2.75 mg. In all tests, the solution volume was 60 mL.

Selective photocatalysis was conducted with RhB, Rh6G or MB in separate tests. For systems with $TiCl_4$ as the precursor, the dye and catalyst concentrations were 20 ppm and 550 mg/L, respectively, and the photocatalyst mass was 33 mg. For the system with the addition of P25 as the support, the catalyst mass was 100 mg. For comparison, the commercial photocatalyst (Degussa P25) was tested from a 46 mg/L solution prepared in a solution of 20 ppm of each dye.

The results of the photocatalytic tests were assessed at two stages: (i) one hour with the lamp off (initial adsorption) and (ii) one hour with the lighted bulb (degradation). An ultraviolet lamp was used (125 W Hg vapor lamp) (General Electric), and the radiation was adjusted to 30 $W \cdot m^{-2}$ (Radiometer Series 9811, Cole-Parmer Instruments). A circulating water jacket was utilized to maintain the reaction vessel temperature at 30 ºC.

Samples were collected with a syringe, stored in Eppendorf tubes and protected from light. For the catalyst separation, samples were centrifuged for 20 minutes at 5000 rpm (Cientec CT-5000R). The final concentration was determined by UV-vis molecular absorption spectroscopy in a Varian Cary 100 spectrophotometer at wavelengths of 553, 530 and 663 nm for RhB, Rh6G and MB, respectively. Adsorption and degradation were estimated from the calibration curves of each dye shown in Equations 1, 2 and 3 (A is the absorbance value and C is the concentration, mg/L, of each species). Equation 4 was utilized to calculate adsorption and degradation.

$$A_{RhB} = 0.21.C_{RhB} + 0.03, N = 7, R^2 = 0.996 \quad (1)$$

$$A_{Rh6G} = 0.18.C_{Rh6G} - 0.04, N = 7, R^2 = 0.994 \quad (2)$$

$$A_{MB} = 0.16.C_{MB} - 0.02, N = 7, R^2 = 0.995 \quad (3)$$

$$\text{Adsorption or Concentration (\%)} = \frac{Ci\text{-}Cf}{Ci} \times 100\% \quad (4)$$

Photolysis tests were also performed to determine the percentage of dye degradation due to UV light exposure without the presence of a photocatalyst.

To assess the relative effect of the sample pairs with molecular imprinting (MI) and non-imprinting (NI), the imprinting factor (IF), defined as the ratio between the final concentrations of these two system types, as shown in Equation 5, was used. The IF parameter was calculated for the adsorption (IF_{ads}) and degradation steps (IF_{degr}).

$$IF = \frac{Concentration^{MI}}{Concentration^{NI}} \quad (5)$$

To assess the extent of degradation of one component relative to another, we defined the selectivity factor (SF) as the ratio of degradation (or adsorption) between RhB and Rh6G (or methylene blue) achieved in a given system (Equation 6).

$$SF = \frac{Concentration^{RhB}}{Concentration^{Rh6G/MB}} \quad (6)$$

All tests were performed in duplicate with an error below 5 %, and these parameters utilize mean concentration values.

Competitive Tests

Photocatalytic tests were performed with mixtures of RhB with Rh6G and RhB with MB. For each case, the initial dye concentration was 10 ppm in 30 mL. The initial catalyst mass was 33 mg for the systems containing $TiCl_4$ and 100 mg for the P25-based systems. The commercial photocatalyst was also evaluated with all reaction parameters of reactions (dark stage, light stage, lamp, time and temperature of reaction) maintained.

The mixture of RhB and Rh6G was analyzed by high performance liquid chromatography using an Ultimate Dionex 3000 liquid chromatography system equipped with an auto-injector, an UV-vis detector, and the Chromeleon data processing system. Separation was performed on an Acclaim RSLCl C-18 column (50 mm long × 3 mm i.d.; 2.2 µm particle size). The mobile phase was water and methanol (35:65) in isocratic mode. The oven temperature was maintained at 35 °C, the flow rate was 0.9 mL min^{-1}, the injection volume was 20 µL, and the UV-vis reading was taken at 525 nm. The analysis time was 7 minutes. Calibration curves obtained for the two dyes are shown in Equations 7 and 8, in which A is the chromatogram area and R is the total removal (including the initial adsorption of the first 60 minutes and the final degradation of the photocatalytic test).

$$A_{RhB} = 1.01.R_{RhB} - 0.86,\ N = 8,\ R^2 = 0.995 \quad (7)$$

$$A_{Rh6G} = 0.33.R_{Rh6G} - 0.23,\ N = 8,\ R^2 = 0.997 \quad (8)$$

For the mixture with MB, the concentration was analyzed by UV-vis spectrometry following methodology described elsewhere [19] that utilizes the Beer Lambert law for mixtures.

The results were evaluated by the parameter competitiveness factor (CF), as described by Equation 9.

$$CF = \frac{\text{Concentration}^{RhB}}{\text{Concentration}^{Rh6G/MB}} \quad (9)$$

To assess the relative effect of selectivity or competitiveness factor of the systems with commercial sample, the P25 factor (F_{P25}) was used (Equation 10).

$$F_{P25} = \frac{\text{SF or CF}^{ads/degr}}{\text{SF or CF}^{P25}} \quad (10)$$

Regeneration and stability tests

The AP25 system was assessed to five cycles of regeneration. At the end of each cycle, vacuum filtration was performed using deionized water. The procedure consisted of adding 20 mL aliquots to a total of approximately 460 mL. Then, the resulting material was maintained at 80 °C until all water was evaporated, after which the photocatalyst was used again in the next test cycle. The initial RhB concentration was 20 ppm, and the initial catalyst mass was 100 mg. The solution volume in each cycle was 60 ml.

Catalyst Characterization

The specific surface area was determined by the Brunauer-Emmett-Teller (BET) method at -196 °C, in the partial pressure range of $0.2 < P/P_0 < 0.9$. Prior to each measurement, samples were preheated at 110°C for 14 h under vacuum. The total pore volume was obtained from single-point desorption at $P/P_0 = 0.967$. The pore diameter was determined by the Barret-Joyner-Halenda (BJH) method.

Zeta potential measurements were carried out in a Zeta PALS Analyzer (Brookhaven Instruments). Zeta Potential Analyser version 3.18 (Brookhaven Instruments) software was utilized to collect the data. For these studies, 50 mg of sample were diluted in 20 mL of MilliQ water and filtered through a VertiPure NYLON syringe filter (13 mm, 0.45 μm, 100/pk). Thereafter, 1.5 mL of filtrate was introduced into polystyrene cuvettes (square, 10 mm, 4.5 mL, four sided clear). The instrument automatically calculated the zeta potential from electrophoretic mobility using the Smoluchowski equation.

Fourier-transform infrared spectroscopy (FT-IR) measurements were recorded at room temperature on a Bomem MB-102 Spectrometer by co-adding 36 scans with a resolution of 4 cm^{-1}.

Transmittance tests were conducted using a Varian Cary 100 spectrophotometer at wavelength of 553 nm and deionized water as used to set 100% of transmittance. All samples were prepared at the same concentration used in the photocatalytic tests.

Scanning electron microscopy (SEM) was further used to examine the morphologies of the as-synthesized silica xerogel particles. The samples were previously deposited on a carbon tape and then sputtered with a thin layer of conductive gold. The SEM images were obtained on a SEM instrument (Zeiss Inc., model EVO 50) that was equipped with an Everhart-Thornley Detector (secondary electrons) and a tungsten filament. SEM imaging was operated at acceleration voltages of 10.0 kV.

SAXS experiments were performed on a D11A beamline at the Brazilian Synchrotron Light Laboratory (LNLS, Campinas, Brazil) using a wavelength of 1.488 nm. The incident beam was detected at two different sample-to-detector distances (1549.8 mm and 2245.7 mm) to increase the range of the scattering vector q ($q = (4\pi/\lambda) \cdot \sin\theta$; 2θ = scattering angle). The dried samples were placed between two Kapton® foils, and the collimated X-ray beam was passed through a chamber containing the stainless steel sample holder. All measurements were performed at room temperature. Silver behenate powder was employed as a standard for calibrating the sample-to-detector distance, detector tilt and direct beam position. Transmission, dark current and Kapton® foil corrections were performed on the 2D image prior to additional data processing.

The isotropic scattering patterns were radially averaged. SAXS data analysis was performed using the Irena evaluation routine [20], which was implemented using Igor Pro Software [21] (WaveMetrics, Portland, USA). A multilevel unified fit was utilized to describe the two levels of structural organization that were evident in the scattering data. In this method, the scattering provided by each structural level is the sum of a Guinier exponential form and a

structurally limited power-law tail. A generalized equation that represents the various levels can be written as:

$$I(q) = \sum_{i=1}^{n} G_i \exp\left(\frac{-q^2 R_{gi}^2}{3}\right) + B_i \exp\left(\frac{-q^2 R_{g(i+1)}^2}{3}\right)\left[\frac{(\mathrm{erf}(qR_{gi}/\sqrt{6}))^3}{q}\right]^{Pi} \qquad (11)$$

where n is the number of observed structural levels, G is the Guinier prefactor, R_g is the radius of gyration and B is a prefactor specific to power-law scattering, which is specified as the decay of the exponent P [22; 23].

Statistical Analysis

The SPSS Statistical System (SPSS for Windows, version 19, IBM®) was utilized to analyze the relationships (Spearman) among data. All statistical tests were performed at the $P < 0.05$ level of significance.

RESULTS AND DISCUSSION

Catalyst Characterization

In a previous work [16, 17], we have performed textural, morphological and structural characterizations of the molecularly imprinted silica-based materials. We have shown that RhB was incorporated within the silica network and we also provided evidences that imprinted sites were achieved by different sol-gel routes.

Transmittance tests revealed that the solution of commercial TiO_2 showed 65% of transmittance. All MI systems showed transmittance between 88 and 95%, while NI systems lain between 80 to 93%. These results suggest that the light absorption of TiO_2 is less influenced by

silica network if compared to commercial titania. Transmittance decrease in the present systems may be due to scattering phenomena.

Considering that such photocatalyst are based on silica, we carried out FT-IR analyses to investigate the presence of stretching vibration of Si-OH at 950 cm^{-1}. **Supporting Information Figure 1** shows typical FT-IR spectra from 850 to 1450 cm^{-1}. In order to investigate the contribution of the stretching vibration of Si-OH on the prepared photocatalysts, the area between this vibration and the symmetrical Si-O stretching of the Si-O-Si network (ca. 1,080 cm^{-1}) was estimated from the value of calculated area (A) of these peaks ($R = A_{Si\text{-}OH}/A_{Si\text{-}O}$). All MI systems showed R less than 0.18, which suggest that eventual hydroxyls on the silica surface are not present in great quantity to provoke non-specific adsorption, which in turn could lead to decreasing in selectivity and competitiveness.

According to the SEM analysis (Supporting Information Figure 2), the prepared MI systems are irregularly shaped and agglomerated. Similar morphologies for samples prepared via sol-gel can be found elsewhere [16, 25].

All the other investigated properties are shown in Table 1. As a general trend, MI systems tend to show lower values (module) of potential zeta than the NI ones. One possible reason for this behavior is the presence of residual RhB in the case of MI systems. The presence of the dye, being positively charged, could induce zeta potential values tending to positive values.

Table 1: Textural characteristics of the photocatalysts.

	System	S_{BET} (m^2g^{-1})	Pore volume ($mL.g^{-1}$)	Pore diameter (Å)	Rg[a)] (nm)	P[b)]	Zeta Potential (mV)
Molecular Imprinted (MI)	**A1TiRhB**	634.5	0.55	30.9	9.8	3.4	-22.9
	A2TiRhB	10.5	0.0034	44.7	4.6	3.7	-24.5
	A3TiRhB	750.6	0.6	42.3	9.8	3.6	-10.9
	BTiRhB	350.2	0.3	33.3	6.5	3.6	-10.8
	TSTiRhB	197.0	0.011	28.1	4.7	3.7	+0.17
	NHTiRhB	2.0	0.017	72	0.8	3.4	-6.7
	AP25	516.4	0.05	25.6	7.5	3.3	-21.9
	AWP25	837.8	0.25	23.4	1.0	3.7	-10.6
Non - Imprinted (NI)	**A1Ti**	463.4	0.29	28.9	4.3[c)]	3.3[d)]	-29.3
	A2Ti	1.5	0.0017	41.2	6.3	3.7	-20.1
	BTi	436.0	0.3	28	8.9	3.6	-28.6
	TSTi	496.6	0.20	26.0	6.2	3.6	+0.18
	NHTi	5.2	0.017	293	2.9	3.7	-26.4
	P25	56.0	0.07	48	1.4	4	-3.6

a) Extracted from high-q region (SAXS); b) Power-law decay (P) extracted from low-q region (SAXS); c, d) This systems showed a structure that consists of two organizational levels.

The effect of the synthesis route on surface area is shown in **Table 1**. Among the acid route systems with MI, the highest surface areas were achieved with A1TiRhB and A3TiRhB. The A2TiRhB system had a surface area of more than 60 times lower than that of A1TiRhB. It should be noted that the slower calcination rate of system A3TiRhB resulted in an 18% area relative to that of A1TiRhB.

In comparing the other MI systems, the highest area value was achieved with AWP25. Additionally, the system in which P25 was added (AP25) demonstrated a decrease in area by a factor of approximately 1.6, which is likely due to incorporation of P25 in the silica network during material synthesis. The NHTiRhB system showed the lowest surface area value.

When comparing the MI with NI systems of each route, it can be seen that only the acid-catalyzed routes resulted in greater area for the MI systems. These results suggest that both the method of preparation and the calcination steps affect the photocatalyst surface.

As a general trend, MI systems showed the highest values of both pore volume and pore diameter if compared with NI systems and P25. Pore enhancement if compared to the commercial sample was also reported in a recent work [26], and suggests the presence of cavities on MI systems.

The samples were further analyzed by SAXS, which provides information about sample geometry and fractal nature by utilizing the structure formed by the organizational levels composed of a Guinier region and a Potency Law. The former provides an estimation of the Guinier radius of gyration (Rg), while the latter provides details about the system organization. The formation of pores in silica based materials is related to the aggregation of primary particles. A typical SAXS curve from these systems is shown in **Supporting Information Figure 3**.

With the exception of A1Ti, all of the investigated systems showed a structure with three organizational levels. By adjusting Level 1, which is located in the q region above 1 nm, one can determine the primary particle Rg, and through adjusting Level 2, located in the q region below 1 nm, one can determine the Rg of the primary particle aggregate. Level 3, which is located in the q region below 0.1 nm, provides information on the particle organization, i.e., the structure of fractal clusters generated through secondary particle aggregation. The cluster structures can be determined by analyzing the power-law exponent ($I \alpha q^{-P}$). An exponent between 1.0 and 3.0 indicates that the final particle aggregation has a mass fractal structure [27], whereas an exponent between 3.0 and 4.0 indicates a fractal surface. When the exponent is 4.0, the particles have a dense core and uniform surface.

As shown in **Table 1**, all systems (MI and NI) showed a fractal surface. Comparing the MI systems to the NI systems, samples that contain RhB (MI systems) tend to show higher P values. This result indicates that the presence of the dye during synthesis increases the material roughness. The influence of the dye on the Rg is also evident, as all MI systems had lower Rg values than their corollary NI systems (the A1 system is not considered here, as A1Ti showed only two organizational levels). In addition, the lowest Rg was found in the NH routes (MI and NI systems).

Photocatalysis of Rhodamine B

As shown in Table 2, among the investigated MI systems, A1TiRhB exhibited the highest adsorption capacity, which in turn is reflected on the values of both adsorption and degradation stages during the photocatalysis test. The system AP25 demonstrated the best initial adsorption. Furthermore, with the exception of the A2TiRhB and NHTiRhB systems, higher initial adsorption values were observed compared to that of P25. The A1TiRhB and A3TiRhB systems had the next highest initial adsorptions, with the initial adsorption of A3TiRhB 31% higher than that of A1TiRhB. This finding can be explained by the calcination process in which the A3TiRhB system was submitted and suggests that is possible to maintain a greater number of sites for molecular imprinting by subjecting the system to slow heating during calcination.

Table 2: Photocatalysis results and adsorption capacity of RhB.

	System	Adsorption capacity ($mg.g^{-1}$)[a]	Adsorption (%)	Degradation (%)	IF_{ads}[(b)]	IF_{degr}[(c)]
(MI)	**A1TiRhB**	997.91	19.6	32.2	1.9	2.5
	A2TiRhB	61.35	1.9	10.9	0.2	1.0
	A3TiRhB	n.d.	25.7	37.8	2.5	3.0
	BTiRhB	54.36	16.5	26.7	3.9	1.4
	TSTiRhB	87.31	16.2	14.0	2.4	1.8
	NHTiRhB	46.63	3.0	18.9	0.5	1.6
	AP25	n.d	40.5	50.9	3.9	4.0
	AWP25	n.d	13.5	20.0	1.3	1.5
(NI)	**A1Ti**	n.d.	10.3	12.7	n.d.	n.d.
	A2Ti	n.d	8.3	10.7	n.d.	n.d.
	BTi	n.d.	4.2	19.5	n.d.	n.d.
	TSTi	n.d.	6.7	7.7	n.d.	n.d.
	NHTi		5.6	12.1	n.d.	n.d.
	P25	n.d.	8.6	44.3	n.d.	n.d.
	PHOTO	n.d.	n.d.	5.5	n.d.	n.d.

n.d. – not defined

a) Details are reported elsewhere [18]

b, c) Values of systems A3TiRhB, AP25 and AWP25 were estimated from system A1Ti.

Although there were no observable trends between surface area and initial adsorption, only A2TiRhB and NHTiRhB systems had IF_{ads} values less than the unity. For these systems, it is possible that there are a lower number of sites for molecular recognition within the silica network, thus hindering the RhB molecule adsorption in the initial period before the photocatalytic process. On the other hand, the observance of IF_{ads} values greater than unity in other systems suggests the existence of imprinted sites.

With respect to the photocatalytic tests, all systems showed activity superior to that of photolysis. The highest values were observed by the systems A1TiRhB, A3TiRhB and AP25.

The A2 system had the lowest initial adsorption and was the only system that did not demonstrate greater degradation than the NI pair (IF_{degr} = 1.0). As discussed in our previous work [17], the encapsulation of RhB occurred preferentially in the silica surface routes A2TiRhB and NHTiRhB. It is possible that compared with other systems, the lowest IF, adsorption and degradation values (see **Table 2**) of these systems are a consequence of the low number of molecular imprinting sites in the silica network. Thus, the adsorption of RhB molecules during the initial period before the photocatalytic process was limited, which affected degradation of the molecule.

Considering the values of **Table 2**, a strong direct Spearman correlation (r_{Sp}> 0.700) was found between the following variable pairs of the MI systems: initial adsorption with IF_{degr} (r_{Sp} = 0.830), initial adsorption with IF_{ads} (r_{Sp} = 0.850), initial adsorption with degradation (r_{Sp} = 0.930) and pore volume with degradation (r_{Sp} = 0.762). It is worth noting that no strong similar correlation has been found in the case of these two last relationships.

Figure 1 shows the correlation between initial adsorption and degradation. As can be seen, there is a clear correlation between increased initial adsorption and increased degradation. This result, together with the IF values higher than the unity already discussed, provides evidence for the presence of sites for selective removal of RhB at the domains of specific cavities, which is corroborated by other correlation results: higher initial adsorption induces higher RhB adsorption and degradation compared to the NI pairs (i.e., higher values of IF_{ads} and IF_{degr}). In addition, among the NI system variables (**Table 1**), the only strong Spearman correlation was between degradation and zeta potential (r_{sp} > - 0.730). Considering that this correlation was not observed for the MI

systems, this finding suggests that charge plays an important role in the photodegradation of materials without molecular imprinting. For MI systems, other characteristics, such as the presence of cavities, may have been more influential on the observed degradation results.

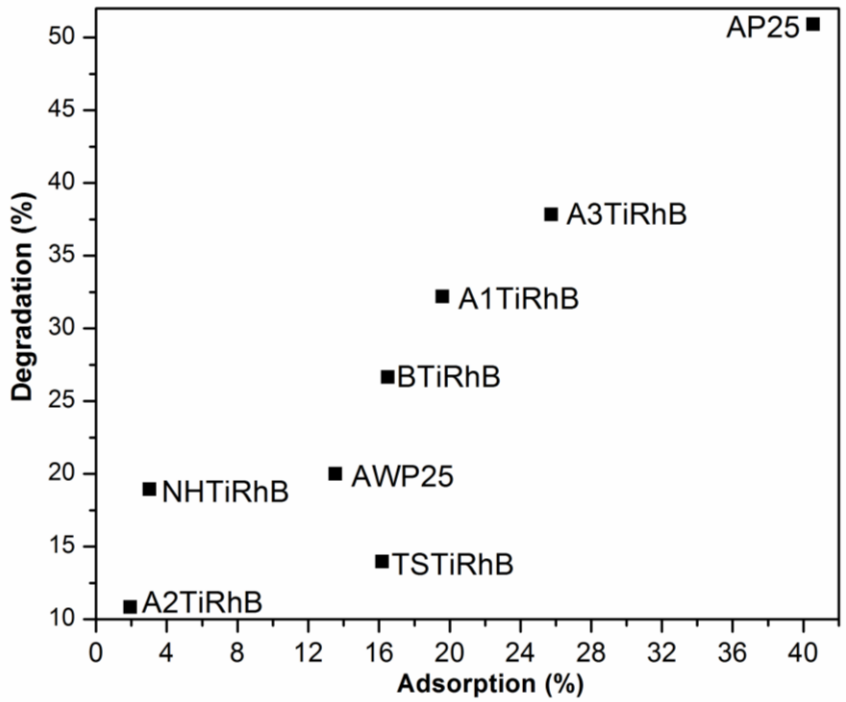

Figura 1: Effect of route on adsorption versus degradation.

Although a strong Spearman correlation could not be found between S_{BET} and IF_{degr}, it is evident that higher values of the former result in higher values of the latter (Supporting Information Figure 4). Taking this observation together with the other correlations, these results indirectly indicate that higher surface areas provide more sites for imprinting. An exception to this trend is observed in the BTiRhB system. In our previous work [16], the effects of material surface characteristics on RhB adsorption were evaluated with molecularly imprinted silica. One of the findings was that MI prepared in a basic route (not calcinated) demonstrated lower efficiency compared to the NI system. Some possible reasons for this result have been discussed that seem to

correlate with the photocatalysis tests; namely, leaching of RhB inside the silica network, decreases in specific area after RhB extraction, and ineffective extraction.

Comparing the MI and NI systems (see **Table 2**), the basic and two-step routes resulted in IF (for both adsorption and degradation) above the unity, despite the fact that NI systems for these routes presented S_{BET} values of approximately 1.2 and 2.5 higher than the corresponding MI systems, respectively (see **Table 1**). These results suggest that surface area cannot solely explain the observed IF values, and RhB adsorption and degradation primarily occur due the presence of molecularly imprinted sites.

Considering the findings already discussed about SAXS parameters, a Spearman correlation was conducted to better understand the influence of these findings on the results obtained from the photocatalytic reactions.

For the MI systems, Rg strongly correlated with adsorption and degradation, with Spearman correlations of 0.850 and 0.730, respectively. These findings suggest that the presence of molecular recognition sites can be linked to higher Rg values, which is corroborated by a lack of correlation for the NI systems. Furthermore, degradation negatively correlated with P (r_{Sp} = -0.700), as expected, as a higher degree of roughness (i.e., lower P values) may enhance degradation due the presence of rough silica domains in which pores are generated.

Considering that the most desirable photocatalytic activity results were generated by the acid routes, these systems were submitted to selectivity tests using Rh6G and MB.

Selective Photocatalysis of Rh6G and MB

The Rh6G photocatalysis results are shown in **Table 3**. The Rh6G adsorption was between 3.0 and 17.0 %. The AP25 system showed an initial adsorption that was nearly 6 times higher than the equivalent system without P25 (AWP25), which indicates the effect of imprinted sites on the former. It should also be noted that this result agrees with the behavior presented by the commercial photocatalyst, i.e., the presence of the P25 in the AP25 system promoted an increase in the initial adsorption that was likely due to the dye affinity of the photocatalyst surface.

Table 3: Selective photocatalysis of Rh6G.

System	Adsorption (%)	Degradation (%)	SF_{ads}	SF_{degr}	F_{P25ads}	$F_{P25degr}$
A3TiRhB	15.7	15.9	1.6	2.3	16	2.8
A1Ti	11.9	27.4	0.8	0.4	8	0.5
AP25	17.0	35.9	2.3	1.2	23	1.5
AWP25	3.0	12.2	4.4	1.6	44	2
P25	48.4	53.0	0.1	0.8	1.0	1.0
PHOTO	n.d.	9.9	n.d.	0.5	n.d.	0.6

As can be seen in **Table 3**, all systems with MI (A3TiRhB, AP25 and AWP25) were more selective for RhB in both adsorption and degradation (SF_{ads} and $SF_{degr} > 1.0$), with the maximum SF_{degr} value found for A3 (2.3).

All MI systems showed selectivity towards the target molecule, which can be seen by the values of F_{P25} higher than unity (**Table 3**), ranging from 16 (2-fold higher than NI system) to 44 and from 1.5 to 2.8, for adsorption and degradation, respectively. Taking into consideration that the commercial sample (P25) is more selective for Rh6G than RhB both for adsorption (10 ×) and degradation (1.25 ×), the fact that the adsorption and degradation were favorable for the MI systems suggests selective degradation of RhB over Rh6G that is primarily due to the presence of

RhB molecular imprinting sites. Moreover, the lack of selectivity in favor of RhB degradation in the AlTi system (SF_{degr} = 0.4 and $F_{P25degr}$ = 0.5, both similar to the photolysis) suggests that photodegradation occurs primarily by the affinity of TiO_2 for Rh6G, because this system does not have any sites for molecular imprinting. This also explain the results obtained for P25.

The lowest degradation value achieved was with the AWP25 system, which is attributed to the absence of the photocatalyst, as degradation occurs by photolysis. When comparing the values for this system with those achieved by photolysis, only a small increase (1.2-fold) is obtained by the AWP25 system. This difference is due to the presence of sites that, although not designed to accommodate Rh6G molecules, could increase dye adsorption to some extent and thereby should facilitate degradation of a larger number of molecules compared to photolysis.

It should be noted that Rhodamine dyes often form H- and J-dimers on solid surfaces, which should affect the imprinting and photocatalytic processes. Also, photocatalytic Rhodamine decomposition involves partial decomposition by demethylation, formation of intermediate compound and full mineralization. In this sense - although we did not intend to fully address these issues -, it was possible to observe that despite complete mineralization was not achieved for the prepared samples, all systems showed a decrease in absorbance without evidence of formation of intermediate. A typical result obtained from acid-route for both RhB and Rh6B are presented at Supporting Information Figure 5. If compared with initial and final stages (t=0 min and t= 60 min), the general shape of RhB and Rh6G spectrum does not vary during its reaction. Since there are no additional peaks appearing in the UV–vis spectra in the course of the experiment, it is possible to suggests that the dyes are being degraded and not only photobleached.

The results of MB photocatalysis are shown in Table 4. While the system A3TiRhB showed an adsorption that is favorable to MB, the value of SF_{ads} (0.6) is twice higher than that of P25. In

addition, this system presented the highest SF_{degr} value (1.95), almost twice that of P25. Although system AP25 showed $F_{P25degr}$ lower than the unity, the value of F_{P25ads} obtained was 3.3. The AWP25 system also demonstrated SF_{ads} and SF_{degr} values that are almost 7- and 2-fold higher if compared to those of P25, respectively. On the other hand, non-imprinted systems (A1Ti) showed both F_{P25ads} and $F_{P25degr}$ lower than the unity, indicating that no gain in selectivity was obtained if compared to the commercial samples. In other words, selectivity was achieved by MI system ranging from 100 to 600% and from 70 to 90% to adsorption and degradation, respectively.

While the system AP25 does not efficiently differentiate between RhB and MB during the adsorption stage (SF_{ads} = 1.05), its corresponding system deployed without P25 (AWP25) adsorbed 2.1 times more RhB than MB. Moreover, the latter demonstrated selective degradation in favor of RhB, which was not observed for the AP25 system. It is hypothesized that the mass of P25 is large enough to induce strong interactions with MB molecules, as the MB molecules were adsorbed on the surface of the commercial photocatalyst at a level that was 3.3 times higher than that of RhB molecules (see **Table 4**).

Table 4: Selective photocatalysis of MB.

System	Adsorption (%)	Degradation (%)	SF_{ads}	SF_{degr}	F_{P25ads}	$F_{P25degr}$
A3TiRhB	41.8	19.4	0.6	1.9	2.0	1.9
A1Ti	51.5	29.4	0.2	0.4	0.6	0.4
AP25	38.6	74.5	1.0	0.6	3.3	0.6
AWP25	6.4	11.4	2.1	1.8	7.0	1.8
P25	29.0	44.81	0.3	1.0	1.0	1.0
PHOTO	n.d	2.62	n.d.	2.1	n.d	2.1

The SF`s values found for our system are comparable to other materials recently reported in the literature, as MI-coated photocalaysts prepared via organic polymerization (SF ranging from 1.59 to 3.29) using 2, 4 - Dinitrophenol as target molecule [28].

Competitive Photocatalysis of Rh6G and RhB

Competition between RhB and Rh6G was evaluated for all MI systems, and the results are shown in **Table 5**. Only the AP25 and AWP25 systems demonstrated competitive performance in favor of RhB, wherein the former achieved the highest CF value (1.6). In addition, the effect of the presence of molecular imprinting sites is clearly evident when comparing both systems. While there is no appreciable difference in removal of Rh6G between the systems (approximately 57%), RhB removal increased (compared to Rh6G removal) by 1.27-fold and 1.6-fold for AWP25 and AP25, respectively.

Table 5: Competitive photocatalysis of RhB and Rh6G.

System	Rh6G	RhB	CF_{degr}	F_{P25}
	Removal (%)	**Removal (%)**		
A1TiRhB	78.2	62.3	0.80	1.21
A2TiRhB	44.2	10.9	0.25	0.38
A3TiRhB	80.5	66.2	0.82	1.24
BTiRhB	57.5	41.4	0.72	1.09
TSTiRhB	75.5	50.1	0.66	1.00
NHTiRhB	79.8	61.7	0.77	1.17
AP25	57.2	91.3	1.60	2.42
AWP25	58.8	74.8	1.27	1.92
P25	25.8	17.0	0.66	1.00
PHOTO	22.3	9.9	0.44	0.67

Although the CF value was lower than 1.0 for the other systems, it is necessary to compare this parameter with that found for the commercial photocatalyst (P25). In this sense, only the system A2TiRhB did not show F_{P25} higher than the unity. NHTiRhB and A1TiRhB had similar CF values that were approximately 17% higher than that of P25. The systems A3TiRhB, AP25 and AWP25 showed the highest F_{P25} values, representing 24, 42 and 142% in an increase of competitiveness towards the degradation of the target molecule (RhB). This result is also reinforced if one consider that UV light action (photolysis) favors the decomposition of Rh6G approximately 2.3 times more than that of RhB.

The results in **Table 5** demonstrate that a low heating rate during calcination with the acid route (A3TiRhB) does not guarantee an appreciable gain in the CF value. Moreover, the absence of HCl during catalyst synthesis of sol-gel (A2) results in both a lower removal compared with that of P25 and a CF value that is three times lower than the system with HCl as the catalyst (A1).

A correlation was found between CF and S_{BET} (r_{sp} = 0.714), suggesting that high values of degradation toward target molecule is facilitated due the high values of surface area. In addition, the degradation of RhB was found to be correlated with both CF (r_{sp} = 0.976) and S_{BET} (r_{sp} = 0.700). Considering that no similar correlation regarding the degradation of MB has been found, these findings indicate that the presence of imprinted sites together with high values of surface area represents important aspects to the degradation of the target molecule.

Competitive Photocatalysis of MB and RhB

Competition between RhB and MB was evaluated for the acid route systems, with the results shown in **Table 6**. Considering the adsorption values, all MI systems had higher CF_{ads} values than the NI system (A1Ti), reaching 3.6-fold higher for A3TiRhB. Although the CF_{ads} was lower than that of P25 for the AP25 and AWP25 systems, the A3TiRhB system achieved a CF_{ads} value almost 1.57-fold higher than that of the commercial catalyst.

Table 6: Competitive photocatalysis of RhB and MB.

System	RhB		MB		CF_{ads}	CF_{degr}	F_{P25ads}	$F_{P25degr}$
	Adsorption (%)	Degradation (%)	Adsorption (%)	Degradation (%)				
A3TiRhB	20.9	36.5	18.8	26.5	1.1	1.4	1.57	1.56
AP25	37.5	58.6	59.4	16.6	0.6	3.5	0.86	3.90
AWP25	5.3	11.1	15	34.3	0.4	0.3	0.57	0.33
A1Ti	21.1	8.2	72	1.8	0.3	4.5	0.43	5.00
P25	11.2	79	15.1	85.6	0.7	0.9	1.00	1.00
PHOTO	n.d.	9	n.d.	3.4	n.d.	2.6	n.d.	2.89

All imprinted systems, with the exception of AWP25, had CF_{degr} values above the unity and above that of P25 during the degradation tests. For this system (AP25), the $F_{P25degr}$ was equal

3.9. This result suggests that although no competitiveness in favor of RhB was evident during the dark stage, the quantity of adsorbed RhB molecules (which is almost 4-fold higher than that of P25) must be retained within the pores for a sufficiently long time so that, together with the action of the photocatalyst, a large number of RhB molecules can be preferentially degraded.

It is worth noting that the NI system (A1Ti) demonstrated the lowest CF_{ads} and the highest CF_{degr} and $F_{P25degr}$values. The absence of molecular imprinting explains the former result, but the latter results was unexpected. Once RhB becomes positively charged, it is possible that the highest negative zeta potential showed by this system (**Table 1**) increases the charge affinity and favorable degradation of RhB. Nevertheless, the absolute value of photodegradation of the target molecule is the* lowest among all the systems (8.15), including photolysis. This result suggests that although the CF_{degr} is high, the presence of sites for MI is necessary for a larger number of target molecules to be retained in the silica pores and then degraded.

CF`s values here reported are comparable or even higher than those recent reported in the literature, namely: the MI systems prepared on fly-ash cenosphere via organic polymerization for degradation of tetracycline (CF ranging from 1.25 to 1.67) [29], and that reported by Luo et al (CF ranging from 2.5 to 3.95) in which MI TiO_2/WO_3 nanocomposites were prepared via sol-gel using nitrophenol as the target molecule [30].

In general, the phenomenon of photocatalysis in the systems presented here can be summarized as: The systems that did not go through a calcination process favored the initial adsorption (dark stage) of RhB, because removal of RhB molecules by non-heated extraction is sufficient to generate imprinting sites; otherwise, both adsorption and photodegradation may be compromised and no preference towards the target molecule is achieved. The calcination process can act positively or negatively, i.e., although this process rends complete extraction of RhB

molecules from the silica network, the MI sites can be compromised during the heating process. Therefore, the values of adsorption and photodegradation are the result of these two phenomena occurring simultaneously.

Considering that the contribution of the semiconductor surface other than that regarding the imprinted sites may contribute to the photocatalytic reactions, we have previously studied the potential adsorption behavior of our systems [16, 17, 18]. Through our analysis, we have shown that, although the structural characteristics of the encapsulated and extracted systems are affected by the processing route taken, the structure of the molecule is conserved during and after the encapsulation process. Also, we have shown that acid-catalyzed route yielded an adsorption capacity of 998.3 $mg.g^{-1}$ (Langmuir model), which is comparable or even higher than the recent reports. In the present work, we used as control of the imprinted photocatalyst three different approaches, namely: (i) photolysis, (ii) silica prepared without imprinted and (iii) commercial catalyst (P25). It is also worth mentioning that all experiments with P25 were carried with a concentration that was similar to the estimated TiO_2 content in our prepared samples. Such approach may help a fair comparison. Thus, the effect of our imprinted sites on the photocatalytic performance can be better understood by the average values of the parameters (IF, SF, CF and F_{P25}) herein studied. As shown in **Table 7**, with exception to the CF_{degr} (Rh6G), all MI systems presented values higher than unity. Importantly, the average SF_{degr} (MB) is similar to the average CF_{degr} (MB) – which is a behavior predicted for contaminants that strongly adsorb on the surface of materials [31]. Although the average values of SF and CF can be considered relatively low, one cannot neglect that we have used similar structural molecules (Rh6G and MB) compared to our target molecule (RhB). In addition, considering the average value of IF (2.1), it is reasonable to

expect that SF and CF values will not be at great extend higher than we have showed for the studied molecules.

Importantly, the average values of F_{P25} (both selectivity and competitiveness) suggest a gain in selectivity toward the target molecule if compared to the commercial photocatalyst. In other words, one of the important finding is that, excepting a few cases, our imprinted systems have shown better photocatalytic activities if compared with commercial catalyst.

Table 7: Arithmetic mean of the studied parameters (MI systems)

Parameter	Value
IF_{degr}	2.1
SF_{degr} (Rh6G)	1.7
SF_{degr} (MB)	1.4
CF_{degr} (Rh6G)	0.8
CF_{degr} (MB)	1.7
$F_{P25}^{(*)}$ (selectivity)	1.7
$F_{P25}^{(*)}$ (competitiveness)	1.5

*Estimated from both Rh6G and MB tests.

Taking into account all the above considerations, it is reasonable to suggest that presence of imprinted sites may improve photocatalytic behavior. However, future studies concerning selectivity and competitiveness toward different molecules -- as well as different protocols of synthesis --, could be carried out in order to improve photocatalytic selectivity.

AP25 Reusability

The photocatalyst efficiency in the recycling tests is of great importance for its application in environmental technology. **Figure 2** shows the influence of the recycling on the AP25 system. It can be seen that there is little difference in degradation for the first two cycles compared to that of the initial test. During the cycles, the decrease in degradation is primarily due to material loss during to the washing process (approximately 5% in each cycle).

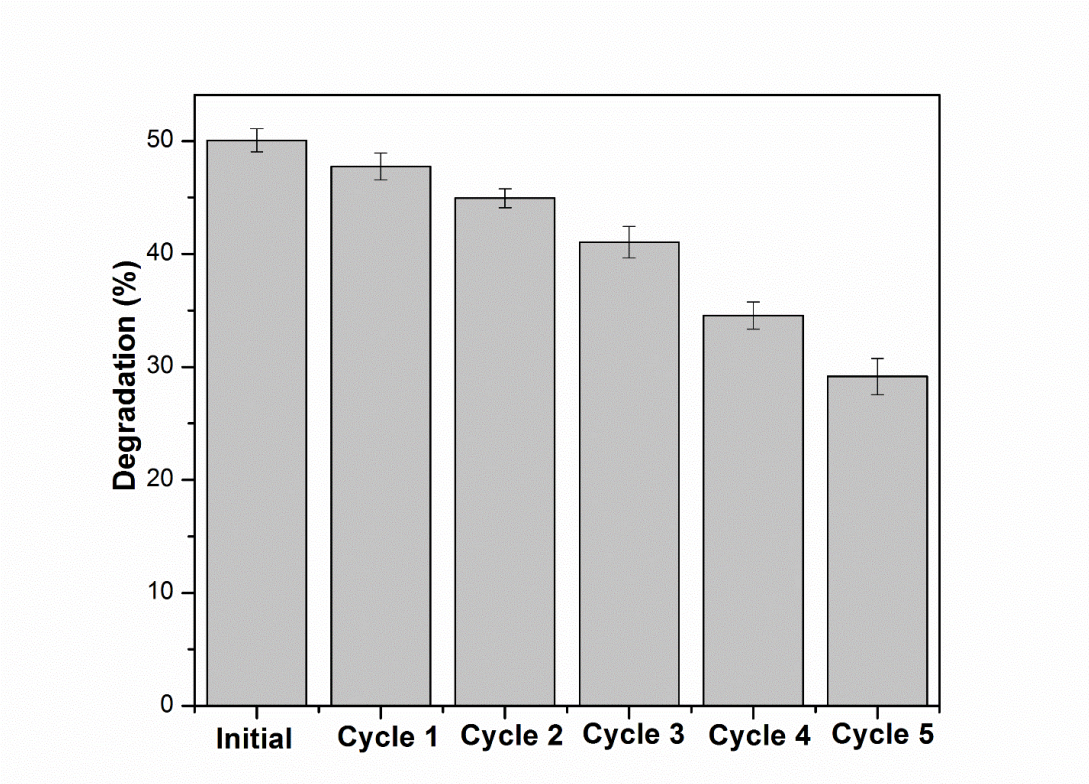

Figure 2: Stability and regeneration of AP25.

Table 8 summarizes the values of adsorption and degradation and provides a comparison of the cycles with P25. It can be seen that until the third cycle, the adsorption and degradation values remained at 75 and 80 %, respectively, of those of the initial test. The decrease is more significant in the last two cycles, reaching approximately 60% of the initial degradation in the last

cycle. In a recent study, Lu et al. [32] reported an efficiency decrease of approximately 50% in the first cycle reuse for a selective magnetic photocatalyst for removal of methyl-imidazole. In another recent study, Deng et al. [33] synthesized a selective photocatalyst prepared by a hydrothermal method and showed that the material was stable (no loss or degradation) for four cycles in the degradation of 4-nitrophenol. Therefore, the photocatalyst developed in the present work is able to maintain stability (in terms of numbers of viable cycles) that is comparable recently reported photocatalysts.

Table 8: Regeneration test for AP25.

Teste	Adsorption (%)	Degradation (%)	F_{P25}
Initial	41.4	50.0	1.1
Cycle 1	38.8	47.7	1.1
Cycle 2	35.3	44.9	1.0
Cycle 3	31.8	41.0	0.93
Cycle 4	29.3	34.5	0.8
Cycle 5	25.4	29.1	0.6

The degradation value is lower than that exhibited by the commercial photocatalyst in the third cycle ($F_{P25} < 1.0$). However, the possibility of recycling, irrespective of the degradation efficiency, is an advantage when comparing to the P25, because P25 is difficult to recover [4].

CONCLUSIONS

Photocatalyst with molecularly imprinted sites were prepared by different sol-gel routes. The correlations between variables (initial adsorption, final degradation, IF_{ads} and IF_{degr}) suggest that dye adsorption occurs on the domains of imprinted silica in the vicinity of the photocatalyst, thereby facilitating photocatalytic degradation. Selectivity tests showed that MI systems based on the sol-gel acid-route were able to achieved selectivity toward target molecule. Compared to the

commercial sample, an increase of selectivity up to 180% was obtained. The addition of P25 during the synthesis (AP25) ensures a higher value of final degradation, although the selectivity is reduced relative to that of the calcined system (A3TiRhB). Competitiveness was also achieved, up to 290% higher than the P25. Regarding the acid route, the absence of HCl during catalyst synthesis resulted in a loss of degradation relative to that of P25 and a 3-fold loss in competitiveness compared to the system with HCl. Furthermore, reusability tests have shown that 60% of the initial degradation is maintained after five cycles.

Acknowledgements

This project was partially financed by the CNPq. C. Escobar is grateful for the grant provided by the CAPES. The authors also thank the LNLS (Project D11A-SAXS1-8691) for SAXS beamline measurements.

REFERENCES

1. Y. Luo, W. Guo, H.H. Ngo, L.D. Nghiem, F.I. Hai, J. Zhang, S. Liang, X.C. Wang, A review on the occurrence of micropollutants in the aquatic environment and their fate and removal during wastewater treatment, Sci. Tot. Environ. 473–474 (2014) 619-641.
2. M.P. Shah, K.A. Patel, S.S. Nair, A.M. Darji, Microbial Decolorization of Methyl Orange Dye by *Pseudomonas spp*, Int. J. Env. Biodivers. 1 (2013) 54-59.
3. K. Nakata, A. Fujishima, TiO_2 photocatalysis: Design and applications, J. Photochem. Photobiol. C: Photochem. Reviews 13 (2012) 169-189.
4. D. Sharabi, Y. Paz, Preferential photodegradation of contaminants by molecular imprinting on titanium dioxide, Appl. Catal. B: Environ. 95 (2010) 169-178.

5. N. Shaham-Waldmann, Y. Paz, Modified Photocatalysts, in Photocatalysis and water purification: From fundamentals to recent reports, ed. Pierre Pichat, Wiley-VCH, Wheinheim, Germany, 2013, pp. 103-128.
6. A.Y. Shan, T.I.M. Ghazi, S.A. Rashid, Immobilisation of titanium dioxide onto supporting materials in heterogeneous photocatalysis: A review, Appl. Catal. A: General 389 (2010) 1-8.
7. A. Ibhadon, P. Fitzpatrick, Heterogeneous Photocatalysis: Recent Advances and Applications, Catalysts, 3 (2013) 189-218.
8. J. Gamage McEvoy, W. Cui, Z. Zhang, Synthesis and characterization of Ag/AgCl–activated carbon composites for enhanced visible light photocatalysis, Appl. Catal. B: Environ. 144 (2014) 702-712.
9. D. Chen, Q. Zhu, F. Zhou, X. Deng, F. Li, Synthesis and photocatalytic performances of the TiO_2 pillared montmorillonite, J.Hazard. Mat. 235–236 (2012) 186-193.
10. R.T. Thomas, P. Abdul Rasheed, N. Sandhyarani, Synthesis of nanotitania decorated few-layer graphene for enhanced visible light driven photocatalysis, J. Coll. Int. Sci. 428 (2014) 214-221.
11. Z. Pan, E.A. Stemmler, H.J. Cho, W. Fan, L.A. LeBlanc, H.H. Patterson, A. Amirbahman, Photocatalytic degradation of 17α-ethinylestradiol (EE2) in the presence of TiO_2-doped zeolite, J. Hazard. Mat. 279 (2014) 17-25.
12. G. Vasapollo, R.D. Sole, L. Mergola, M.R. Lazzoi, A. Scardino, S. Scorrano, G. Mele, Molecularly Imprinted Polymers: Present and Future Prospective, Int. J. Mol. Sci. 12 (2011) 5908-5945.

13. M.J. Whitcombe, N. Kirsch, I.A. Nicholls, Molecular imprinting science and technology: a survey of the literature for the years 2004–2011, J. Mol. Recog. 27 (2014) 297-401.
14. J.E. Lofgreen, G.A. Ozin, Controlling morphology and porosity to improve performance of molecularly imprinted sol-gel silica, Chem. Soc. Reviews 43 (2014) 911-933.
15. E.C. Morais, G.G. Correa, R. Brambilla, J.H.Z. dos Santos, A.G. Fisch, Selective silica-based sorbent materials synthesized by molecular imprinting for adsorption of pharmaceuticals in aqueous matrices, J. Sep. Sci. 36 (2013) 636-643.
16. C. Escobar, J.H.Z. dos Santos, Effect of the Sol-Gel Route on the Textural Characteristics of Silica Imprinted With Rhodamine B, J. Sep. Sci. 37 (2014) 868-875.
17. C. de Escobar, M. Dartora, L. Campo, C. Radtke, J. Bayne, I. Butler, R. Lattuada, J.H. Z. dos Santos, The role of the sol–gel route on the interaction between rhodamine B and a silica matrix, J. Sol-Gel Sci. Tech. 72 (2014) 260-272.
18. C. C. de Escobar, A. Fisch, J. H. Z.dos Santos, Effect of a sol-gel route on the preparation of silica-based sorbent materials synthesized by molecular imprinting for the adsorption of dyes, Ind. Eng. Chem. Res. 54 (2015) 254-262.
19. K.A. Connors, C.J. Eboka, Alternative graphical methods for the spectrophotometric analysis of mixtures, Anal. Chem. 51 (1979) 1262-1266.
20. J. Ilavsky, P.R. Jemian, Irena: tool suite for modeling and analysis of small-angle scattering, J. Appl. Cryst. 42 (2009) 347-353.
21. S. Kline, Reduction and analysis of SANS and USANS data using IGOR Pro, J. Appl. Cryst. 39 (2006) 895-900.
22. G. Beaucage, Approximations Leading to a Unified Exponential/Power-Law Approach to Small-Angle Scattering, J. Appl. Cryst. 28 (1995) 717-728.

23. G. Beaucage, Small-Angle Scattering from Polymeric Mass Fractals of Arbitrary Mass-Fractal Dimension, J. Appl. Cryst. 29 (1996) 134-146.
24. C. J. Brinker, G. W. Scherer, Sol Gel Science: The Physics and Chemistry of Sol-Gel Processing, Academic Press: San Diego, 1990.
25. P. Munusamy, M. N. Seleem, H. Alqublan, R. T. Jr., N. Sriranganathan, G. Pickrell. Targeted drug delivery using silica xerogel system to treat diseases due to intracellular pathogens. Mat. Sci. Eng. C 29(2009) 2313-2318.
26. Xu W-Z, W. Zhou, J-M Pan, X-Y Wu, Y-S Yan, A molecularly imprinted polymer based on TiO_2 as a sacrificial support for selective recognition of dibenzothiophene. Chem. Eng. J. 179 (2011), 191-198.
27. P.W. Schmidt, The Fractal Approach To Heterogeneous chemistry: Surface, Colloids, Polymers, Wiley, London 1989.
28. C. Huang, Z. Tu, X. Shen, J. Hazard Mater. 248 (2013) 379-386.
29. Z. Lu, P. Huo, Y. Luo, X. Liu, D. Wu, Z. Gao, C. Li, Y. Yan, Performance of molecularly imprinted photocatalyst based on fly-ash cenospheres for selective photodegradation of single and ternary antibiotics solution, J. Mol. Catal. A: Chem. 378 (2013) 91-98.
30. X. Luo, F. Deng, L. Min, S. Luo, B. Guo, G. Zeng, C. Au Facile One-Step Synthesis of Inorganic-Framework Molecularly Imprinted TiO_2/WO_3 Nanocomposite and Its Molecular, Recognitive Photocatalytic Degradation of Target Contamiannt. Environ. Sci. Technol. 47 (2013**)** 7404-7412.
31. Y. Paz, Preferential photodegradation- why and how? Comptes Rendus Chimie, 9 (2006) 774-787.

32. Z. Lu, F. Chen, M. He, M. Song, Z. Ma, W. Shi, Y. Yan, J. Lan, F. Li, P. Xiao, Microwave synthesis of a novel magnetic imprinted TiO_2 photocatalyst with excellent transparency for selective photodegradation of enrofloxacin hydrochloride residues solution. Chem. Eng. J. 249 (2014), 15-26.
33. F. Deng, Y. Liu, X. Luo, S. Wu, S. Luo, C. Au, R. Qi, Sol-hydrothermal synthesis of inorganic-framework molecularly imprinted TiO_2/SiO_2 nanocomposite and its preferential photocatalytic degradation towards target contaminant, J. Hazard. Mat. 278 (2014) 108-115.

Supporting Information

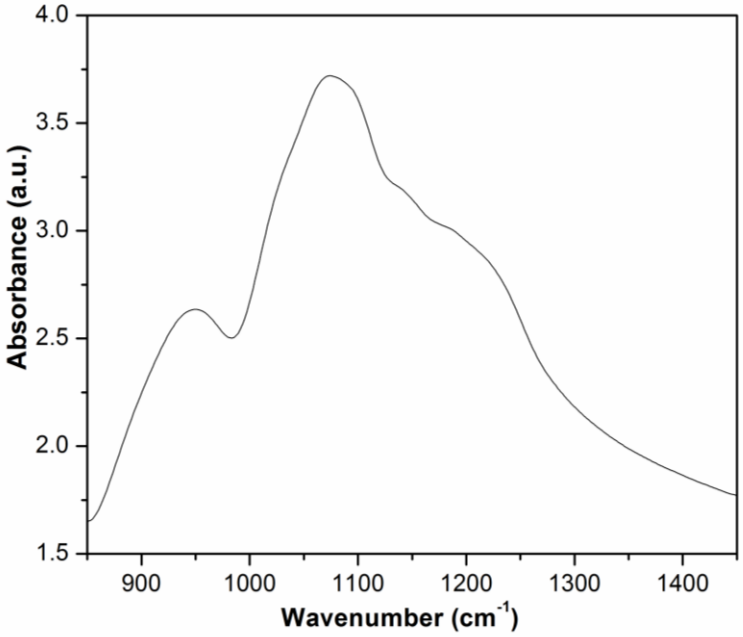

Sup. Figure 1: Typical FT-IR for MI systems (A3TiRhB).

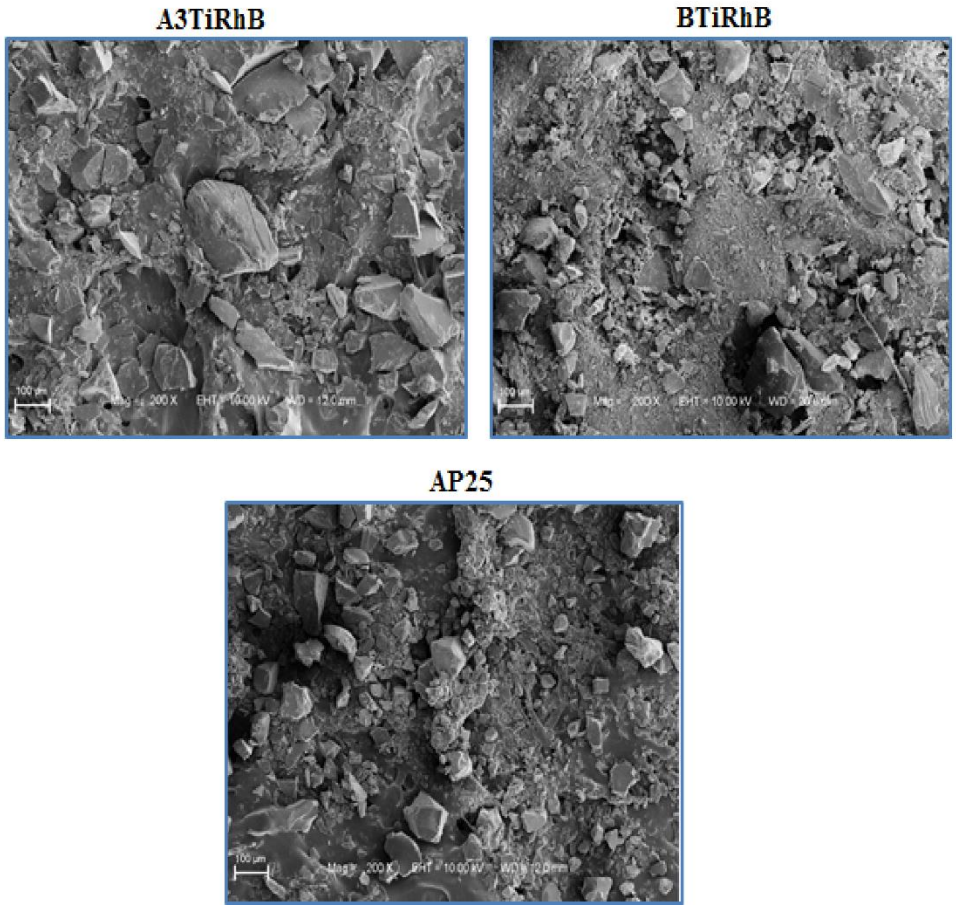

Sup. Figure 2: Scanning electron microscopy for A3RiRhB, BTiRhB and AP25.

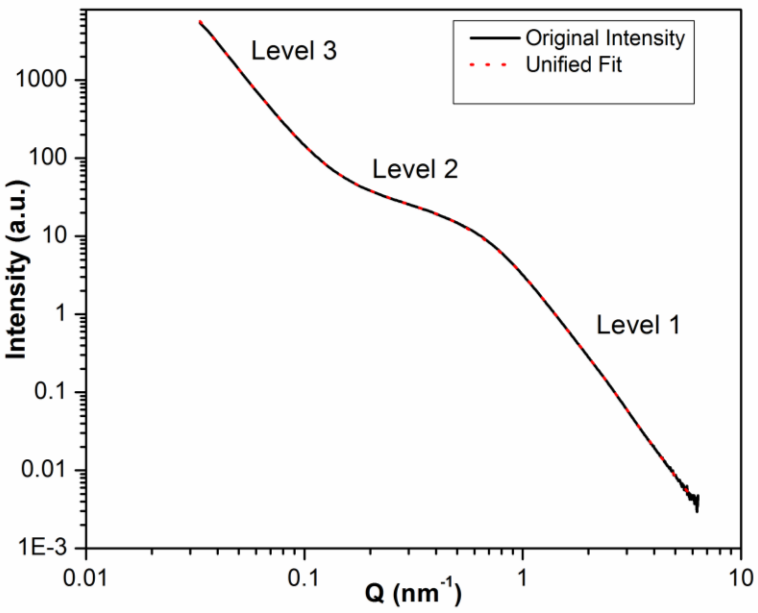

Sup. Figure 3: SAXS curve for A1TiRhB system.

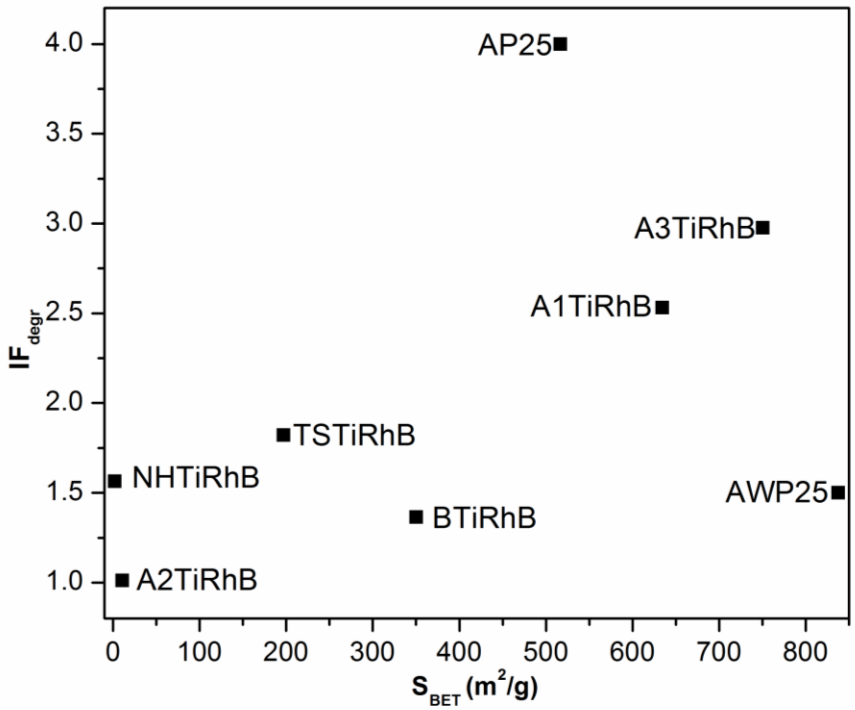

Sup. Figure 4: Effect of route on S_{BET} versus IFdeg

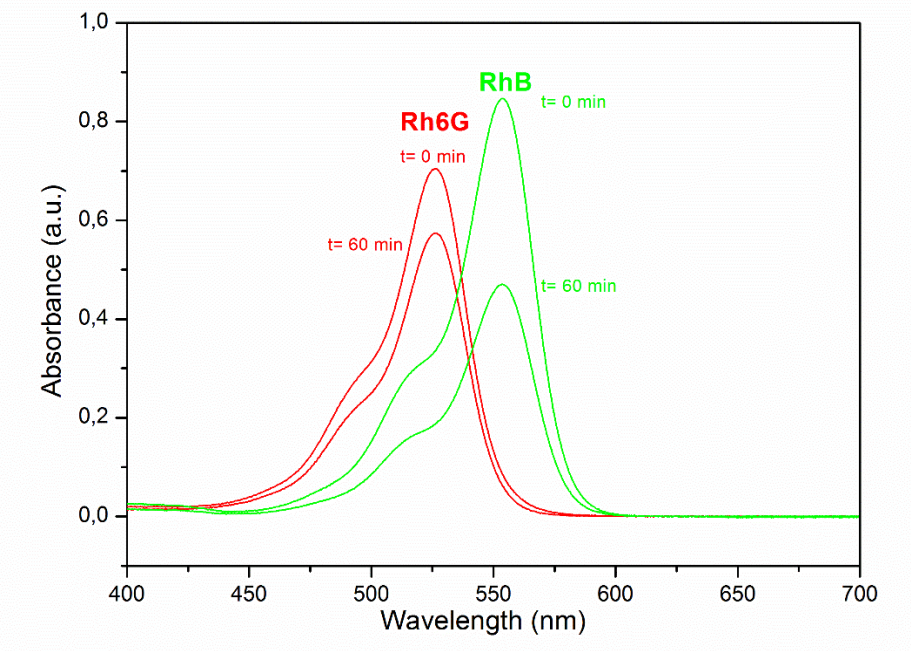

Sup. Figure 5: UV-Vis at different time reaction (photocatalysis) for RhB and Rh6G.

4.5 Artigo 5

Publicado no *Journal of Hazardous Materials*, v. 5, p. 359-366.

Contents lists available at ScienceDirect

Journal of Hazardous Materials

journal homepage: www.elsevier.com/locate/jhazmat

Synthesis of molecularly imprinted photocatalysts containing low TiO_2 loading: Evaluation for the degradation of pharmaceuticals

Cícero Coelho de Escobar[a], Marla Azário Lansarin[a], João Henrique Zimnoch dos Santos[b,*]

[a] Departamento de Engenharia Química – Universidade Federal do Rio Grande do Sul, Rua Eng. Luis Englert s/n, 90040-040 Porto Alegre, RS, Brazil
[b] Instituto de Química, Universidade Federal do Rio Grande do Sul, Av. Bento Gonçalves, 9500, Porto Alegre CEP 91500-000, Brazil

HIGHLIGHTS

- Molecularly imprinted photocatalyst (MIP) containing low TiO_2 loading were prepared by acid-catalyzed sol–gel process.
- Seven pharmaceutical compounds were evaluated as a template.
- Comparing to the P25, MIP has shown an increase of adsorption up to 752%.
- Comparing to the P25, MIP has shown an increase of degradation up to 427%.
- The presence of specific cavities on the silica domain could explain the better results for MIP.

ARTICLE INFO

Article history:
Received 27 August 2015
Received in revised form
11 November 2015
Accepted 18 November 2015
Available online 23 November 2015

ABSTRACT

A molecularly imprinted (MI) photocatalyst containing a low TiO_2 loading (7.00–16.60 mg L^{-1} of TiO_2) was prepared via an acid-catalyzed sol–gel route using different classes of pharmaceutical compounds (i.e., Atorvastatin, Diclofenac, Ibuprofen, Tioconazole, Valsartan, Ketoconazole and Gentamicine) as the template. Herein, our main goal was to test the hypothesis that photocatalysts based on molecular imprinting may improve the degradation performance of pharmaceutical compounds compared to that of a commercial sample (Degussa P25) due to presence of specific cavities in the silica domain. To elucidate certain trends between the performance of photocatalysts and their structural and textural properties, as well the effect of the structure of the drugs on molecular imprinting, the data were analyzed in terms of pore diameter, pore volume, surface area, zeta potential and six-membered ring percentage of silica. In comparison to the commercial sample (P25), we have shown that adsorption and degradation were enhanced from 48 to 752% and from 5 to 427%, respectively. A comparison with the control system (non-imprinted) indicates that the increased performance of the MI systems was due to the presence of specific cavities on the silica domain, and the textural and structural aspects also support this conclusion. The MI photocatalyst was reusable for seven cycles of reuse in which approximately 60% of its photocatalytic efficiency was preserved for the system containing Diclofenac as the template.

INTRODUCTION

Due to the growth of industrial activities, legislation has become increasingly restrictive, especially with respect to the preservation of surface and groundwater [1]. Although many countries have employed advanced treatments (i.e., membrane technologies, activated carbon and ultraviolet radiation) to treat water, there has been comparatively little study of the potential use of these substances [2]. Among the compounds of concern are the so-called emerging contaminants, which encompass pharmaceuticals and personal care products, steroids, surfactants, pesticides and dyes [3, 4]. Pharmaceutical compounds have provoked increasing concern. However, no legal requirements have been set for discharge into surface bodies. Recent reviews have indicated the ubiquitous presence of several classes of pharmaceutical compounds, such analgesics, anti-inflammatories, hormones, preservatives and endocrine disruptors. For example, recent studies have measured the concentrations of 56 active pharmaceutical ingredients and reported a concentration as high as 5,300 ng L^{-1} for Valsartan from wastewater treatment plants across the US [5]. Similarly, nearly 6 kg of 56 compounds are discharged daily into the rivers of South Wales [6].

Advanced oxidation processes (AOPs) are known methods of pollutant degradation that involve the mineralization of a wide variety of organic contaminants. In these cases, mineralization, which is the conversion of the molecules to their highest possible oxidation state and finally to water, carbon dioxide, oxidized inorganic anions and/or other molecules that can be removed by biological processes, is required for complete removal.

Among the AOPs, heterogeneous photocatalysis using TiO_2 is one of the most promising strategies for use with emerging contaminants. This method exhibits several advantages, such as low toxicity, low cost, and chemical stability [7]. However, a serious shortcoming in

heterogeneous photocatalytic oxidation is its low selectivity to target contaminants, which is controlled by photogenerated holes and hydroxyl radicals with strong oxidation potentials [8]. Therefore, heterogeneous photocatalysis lacks selectivity to most of the hazardous contaminants [9, 10]. This characteristic is a disadvantage because mixtures derived from effluent streams may contain nonbiodegradable, highly toxic organic pollutants that coexist with less toxic and biodegradable material. In many cases, the former is present in lower concentrations, and the latter is a major component [9, 10]. However, the preferential degradation of the most toxic materials is desirable.

The commercial use of TiO_2 is also challenging due the cost of separating the treated effluent from the photoactive microparticles. One possible method for overcoming this challenge involves the use of supports [11], which provide additional advantages, such as improved thermal and chemical stability, as well as an increased catalytic material surface area, that can result in higher activity [12]. Therefore, several studies have explored different uses of supports, such as graphene [13], activated carbon [14], clay [15] and zeolites [16].

Although extensively studied, the use of supports in heterogeneous photocatalysis does not necessarily address the problem of selectivity. Therefore, our approach combines the technique of molecular imprinting with heterogeneous photocatalysis. MI is a promising technique for creating a template with a specific molecular recognition [17]. This technique can be carried out in an organic or inorganic matrix due to the presence of a template molecule during the formation of the three-dimensional polymer [18, 19]. The majority of MI applications in inorganic matrix materials are based on a silica network that is synthesized by the sol-gel method. Recent studies have demonstrated the feasibility of this approach for selective adsorption and pre-concentration of various compounds, such as drugs and dyes [20, 21].

The imprinting approach combined with photocatalysis is very promising due to its simplicity. However, few studies have been conducted using this approach [10], and some studies have utilized an organic matrix or films [22-26]. Inorganic-framework molecularly imprinted photocatalysts is an emergent field, with a few works recently published [27, 28]. Therefore, the effect of MI in inorganic matrices on selective photocatalysis is not well understood. We previously investigated the effect of the sol-gel route on molecularly imprinted materials in terms of their textural and structural properties. We demonstrated the potential of silica-imprinted materials for use in selective adsorption and that Ti moieties (using $TiCl_4$ as a source of TiO_2) can be incorporated into a silica network [29, 30]. We also conducted selective and competitive photocatalysis to evaluate the sol-gel route effect on the preparation of molecularly imprinted silica-based materials using Rhodamine B as template [31]. We have shown that the adsorption of the target molecule occurs on the domains of the imprinted silica in the vicinity of the photocatalyst, which facilitate photocatalytic degradation. Among the investigated sol-gel routes, the acid-catalyzed hydrolytic route afforded the best results.

Therefore, the aim of this study was to evaluate the degradation of a series of different classes of pharmaceutical compounds using heterogeneous photocatalysis with MI materials prepared via an acid route. Although many studies have investigated the degradation of pharmaceutical compounds [30-39], to the best of our knowledge, none of the studies involved the use of molecular imprinting based on a sol-gel route for heterogeneous photocatalytic applications. In addition, a majority of these studies used a TiO_2 concentration between 10 to 1000 mg/L. Herein, we report a simple protocol for the production of MI materials containing low concentrations of TiO_2 for heterogeneous photocatalytic applications. We have designed experiments comprising a concentration between 7.00 and 16.6 mg/L of TiO_2 in each catalytic test.

Our main goal was to test the hypothesis that photocatalysts based on MI may improve the degradation performance compared to that of a commercial sample (Degussa P25) due the presence of specific cavities in the silica domain.

EXPERIMENTAL SECTION

Materials and methods

Tetraethoxysilane ($Si(OCH_2CH_3)_4$, TEOS, Merck, >98%) and titanium dioxide (TiO_2, P25-Degussa) were used as received. Hydrochloric acid (HCl, Nuclear) was employed as the catalysts. Atorvastatin calcium (ATO) (Lipton), diclofenac sodium (DIC) (Multilab), ibuprofen (IBU) (Multilab), tioconazole (TIO) (Multilab), valsartan (VAL) (Multilab), ketoconazole (KET) (Multilab and gentamicin (GEN) (IQ Soluções & Química SA) were used as received.

Preparation of the imprinted supported photocatalysts

The photocatalysts were prepared using the sol-gel process via an acid-catalyzed route, and TEOS was used as the raw material. For each sample, pharmaceutical weight was fixed at 150 mg and followed by addition of HCl (0.2 M) and TEOS (45 mmol) at a 1:2 (HCl:TEOS) volume ratio. Then, 100 mg of P25 was added 2 ½ hours after the synthesis reaction was initiated. During this process, the solution was continuously stirred at room temperature until gelation occurred. Then, the solids were dried at room temperature and milled.

For template removal, the samples were submitted to a slow heating process. This process was carried out in a muffle furnace starting at room temperature by maintaining a constant temperature for 50 min at each plateau of 100 °C and a heating rate of 1 °C min^{-1}. This procedure was continued until the temperature reached 400 °C, and then, the material was held at this

temperature for 4 h. Then, the sample was washed with deionized water to remove any residue and finally dried at 80°C.

For comparison, an equivalent synthesized sample (containing P25) was prepared without the addition of pharmaceuticals (i.e., non-imprinted (NI) system).

The resulting photocatalysts were labeled according to the first three letters of the employed pharmaceutical. For example, the MI system containing Diclofenac is referred to as DICMI. For the NI systems, the NI label is used.

Photocatalyst tests

In a typical degradation experiment, 50 mL of a pharmaceutical (20 ppm) was added to 33 mg of the photocatalyst in a bath reactor under flowing air (6.5 mL s^{-1}). The results of the photocatalytic tests were assessed at two stages under magnetic agitation (ca. 400 rpm) as follows: (i) one hour with the lamp off (initial adsorption) and (ii) one hour with the lamp on (degradation). An ultraviolet lamp was used (125 W Hg vapor lamp) (General Electric), and the radiation was adjusted to 45 $W \cdot m^{-2}$ (Radiometer Series 9811, Cole-Parmer Instruments). A circulating water jacket was utilized to maintain the temperature reaction vessel at 30 ºC. The tests were carried out at the natural pH of the drugs.

The samples were collected with a syringe (2 mL for each collect), stored in Eppendorf tubes and protected from light. After the reaction, the final volume of the suspension was 46 mL. For the catalyst separation, the samples were centrifuged for 20 min. at 5,000 rpm (Cientec CT-5000R). The final concentration was determined by UV-Vis molecular absorption spectroscopy using a Varian Cary 100 spectrophotometer at 232, 222, 250, 276, 230, 241 and 190 nm for TIO, IBU, VAL, DIC, KET, ATOR, and GEN, respectively. The adsorption and the degradation were

estimated from the calibration curves for each drug. All of the experiments were performed in duplicate, and the reported results are the mean values.

Photolysis tests were also performed to determine the percentage of drug degradation due to UV light exposure in the absence of the photocatalys. To assess the relative effect of the sample pairs with (MI) and non-imprinting (NI), the imprinting factor (IF), which is defined as the ratio between the final concentrations of these two systems was used. The IF parameter was calculated for the adsorption (IF_{ads}) and degradation steps (IF_{degr}).

For comparison, each system was compared to the commercial photocatalyst (Degussa P25) considering the final mass of the photocatalyst. Therefore, the P25 concentration ranged from 0.02 to 0.0412 g/L.

Considering the mass of photocatalyst obtained for each system, we can estimate the theoretical maximum amount of P25 for each 33 mg of photocatalyst used in each photocatalytic test. Thus, the P25 concentration ranged from 7 to 16.6 mg/L. To assess the relative effect of the sample containing MI and the commercial sample, the P25 factor (F_{P25}) was used. All the equations are shown at Supporting Information S 1.

Scheme 1 illustrates de process for the preparation and testing of the MI photocatalysts.

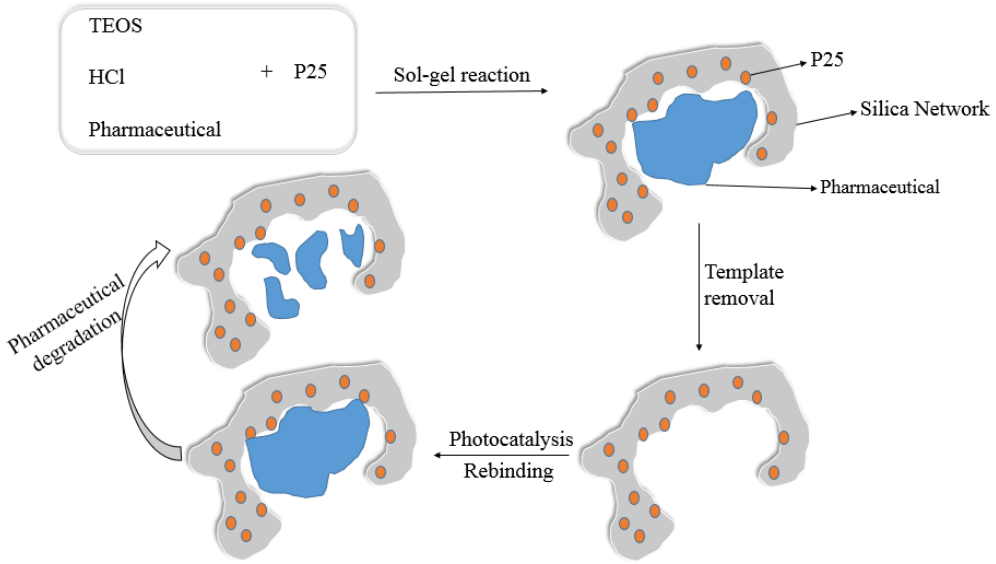

Scheme 1: Preparation and evaluation of MI photocatalysts.

Recycling Tests

The DICMI system was evaluated for recycling using an initial photocatalyst concentration of 2 g L^{-1}. At the end of each cycle, the samples were centrifuged for 10 minutes at 3,500 rpm to remove the supernatant. Then, the photocatalyst was placed in contact with a fresh solution of DIC (20 ppm). During the multiple cycles, no regeneration or desorption processes were employed.

Catalyst Characterization

Transmittance tests were conducted using a Varian Cary 100 spectrophotometer at maximum absorbance wavelengths of the studied drugs, and deionized water as used to set 100% transmittance. All of the samples were prepared at a concentration that was the same as that used in the photocatalytic tests.

The Fourier transform infrared spectroscopy (FTIR) was performed at room temperature on a Bomem MB-102 spectrometer by co-adding 36 scans at a resolution of 4 cm^{-1}. For detailed structural analysis, the υ_{as}(Si-O)-Si and the υ_{s}(Si-O)-Si spectral regions (900-1300 cm^{-1}) were independently deconvoluted into Gaussian components using a previously reported nonlinear least squares fitting method [40]. The percentage of six-member rings (%$(SiO)_6$) was estimated based on the following ratio of fitted areas:

$$\%(SiO)_6 = 100 \times [A(LO_6) + A(TO_6)/A(LO_6) + A(LO_4) + A(TO_4) + A(TO_6)] \quad (1)$$

The specific surface area was determined by the Brunauer-Emmett-Teller (BET) method at -196 °C in the partial pressure range of $0.2 < P/P_0 < 0.9$. Prior to each measurement, the samples were preheated to 110°C for 14 h under vacuum. The total pore volume (Vp) was obtained from a single-point desorption at $P/P_0 = 0.967$. The pore diameter (Dp) was determined using the Barrett-Joyner-Halenda (BJH) method.

X-ray diffraction (XRD) analyses were performed on a Rigaku DMAX 2200 diffractometer equipped with a Cu tube and secondary monochromator, as well as a theta-theta Ultima goniometer and scintillation [NaI(Tl)] detector.

The zeta potential (ZP) measurements were carried out on a Zeta PALS Analyzer (Brookhaven Instruments). Zeta Potential Analyser software version 3.18 (Brookhaven Instruments) was utilized to collect the data. For these studies, 50 mg of the sample was diluted in 20 mL of MilliQ water and filtered through a VertiPure NYLON syringe filter (13 mm, 0.45 μm, 100/pk). Then, 1.5 mL of the filtrate was introduced into polystyrene cuvettes (square, 10 mm, 4.5 mL, four sided clear). The instrument automatically calculated the zeta potential from the electrophoretic mobility using the Smoluchowski equation.

The SAXS experiments were performed on the D11A beamline at the Brazilian Synchrotron Light Laboratory (LNLS, Campinas, Brazil) using a wavelength of 1.488 nm. The incident beam was detected at two different sample-to-detector distances (1549.8 mm and 2245.7 mm) to increase the range of the scattering vector (q, where $q = (4\pi/\lambda) \cdot \sin\theta$; 2θ = scattering angle). The dried samples were placed between two Kapton® foils, and the collimated X-ray beam was passed through a chamber containing the stainless steel sample holder. All of the measurements were performed at room temperature. Silver behenate powder was employed as a standard for calibrating the sample-to-detector distance, detector tilt and direct beam position. Transmission, dark current and Kapton® foil corrections were performed on the 2D image prior to additional data processing.

The isotropic scattering patterns were radially averaged. The SAXS data analysis was performed using the Irena evaluation routine [41], which was implemented using Igor Pro Software [42] (WaveMetrics, Portland, USA). A multilevel unified fit was utilized to describe the two levels of structural organization in the scattering data. In this method, the scattering provided by each structural level is the sum of a Guinier exponential form and a structurally limited power-law tail. A generalized equation that represents the various levels can be expressed as

$$I(q) = \sum_{i=1}^{n} G_i \exp\left(\frac{-q^2 R_{gi}^2}{3}\right) + B_i \exp\left(\frac{-q^2 R_{g(i+1)}^2}{3}\right)\left[\frac{(\mathrm{erf}(qR_{gi}/\sqrt{6}))^3}{q}\right]^{Pi} \qquad (2)$$

where n is the number of observed structural levels, G is the Guinier prefactor, R_g is the radius of gyration and B is a prefactor specific to the power-law scattering, which is specified as the decay of the exponent P [43; 44].

Statistical Analysis

The SPSS Statistical System (SPSS for Windows, version 19, IBM®) was utilized to analyze the relationships (Spearman) between the data. All of statistical tests were performed at a $P < 0.05$ level of significance.

RESULTS AND DISCUSSION

Fig. 1 shows the photocatalytic performance of all of the studied drugs (comparing the MI and NI systems), photolysis and the performance of commercial TiO_2 (P25). According to **Fig. 1**, the average efficiency of pharmaceutical degradation by photolysis was 5.6%. All of the MI systems exhibited superior activity (i.e., values ranging from 80 (ATO) to 711% (DIC) higher) to that of photolysis.

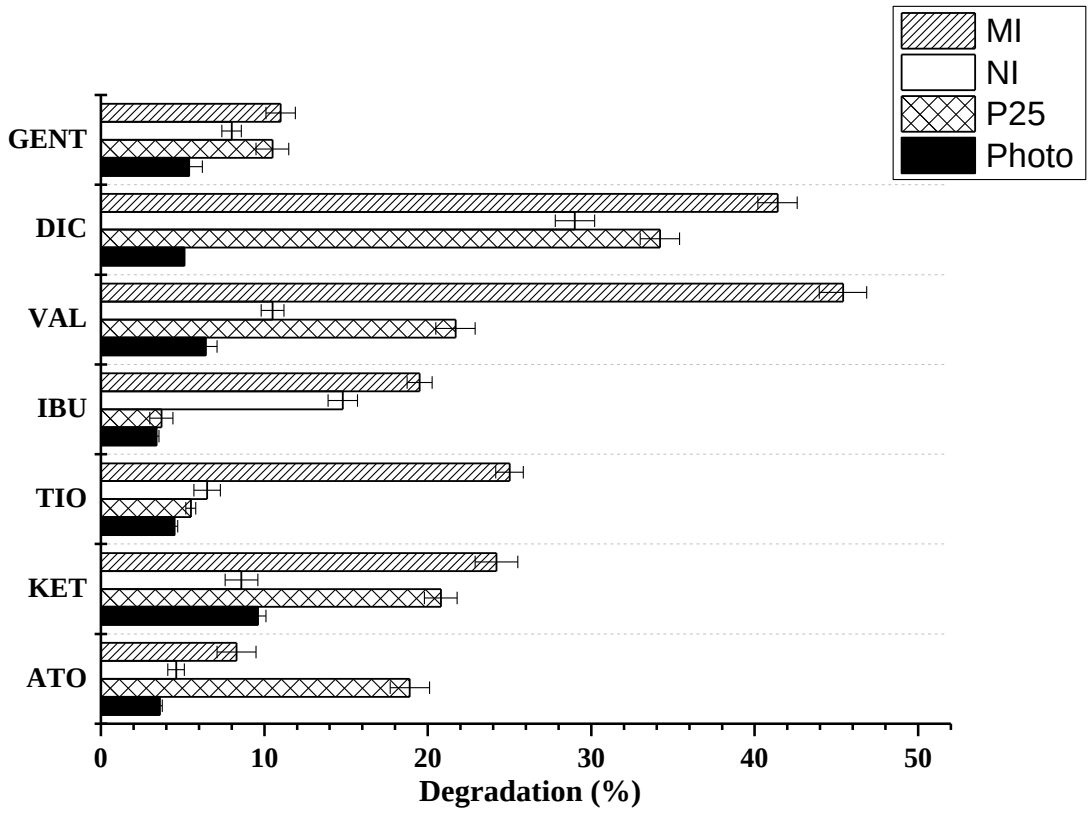

Figure 1: Photocatalytic performance of studied drugs.

By comparing the MI and NI systems, the results presented in **Fig. 1** indicate that the MI systems exhibited better photocatalytic performance for all of the studied drugs. To better elucidate the role of the MI systems in the photocatalytic tests, the imprinting factor (IF) was estimated for the two stages of the reaction (i.e., initial adsorption (IF_{ads}) (lamp off) and degradation (IF_{degr}) (lamp on)). As shown in **Table 1**, all of the MI systems exhibited an IF that was greater than unity due to the presence of imprinted sites on the silica network. This result is also supported by the strong correlation between the initial adsorption and degradation (r_{Sp} = 0.75), suggesting that the degradation performance increased due the adsorption of molecules. Interestingly, a similar correlation was not observed for the NI systems. This result, along with the IF values being higher than unity, confirmed the presence of sites for the specific removal of drugs in the domains of the specific cavities. The highest IF_{ads} (6.76) and IF_{degr} (12.75) values were achieved for TIOMI and KETMI, respectively, which may be due to these systems possessing more suitable sites for molecular recognition that facilitates the enrichment of TIO and KET molecules on the silica network.

Table 1: Imprinted and P25 factors (IF and F_{P25}) for MI and NI systems.

	Imprinted systems (MI)				**Non-imprinted systems (NI)**	
	IF_{ads}	IF_{degr}	F_{P25ads}	$F_{P25degr}$	F_{P25ads}	$F_{P25degr}$
ATO	2.66	3.13	1.48	0.44	0.56	0.24
KET	1.90	12.75	1.85	1.16	0.98	0.41
TIO	6.76	3.85	8.52	4.55	1.26	1.18
IBU	5.38	1.32	5.83	5.27	1.08	4.00
VAL	1.27	4.32	2.45	2.09	1.93	0.48
DIC	2.58	1.43	3.44	1.21	1.33	0.85
GEN	1.12	1.38	3.20	1.05	2.86	0.76

The photocatalyst mass employed by each MI system is shown in **Table 2**, and this mass ranged from 4 to 9.4 g. Therefore, the TiO_2 loading for each 33 mg of photocatalyst used can be estimated in our photocatalytic tests. For comparison, all of the photodegradation tests using the commercial sample were conducted based on the TiO_2 content in each MI system. Therefore, the concentration of commercial TiO_2 ranged from 7.00 to 16.60 mg L^{-1}.

Table 2: Estimated TiO_2 concentration for each MI system.

System	Photocatalyst mass (g)	TiO_2 load for each 33 mg of photocatalyst (mg)	Concentration of TiO_2 (mg/L)
ATOMI	5.14	0.64	12.84
KETMI	8.00	0.41	8.26
TIOMI	8.30	0.39	7.94
IBUMI	8.00	0.41	8.26
VALMI	8.00	0.41	8.26
DICMI	4.00	0.83	16.60
GENMI	9.40	0.35	7.00

As shown in **Fig. 1**, with the exception of ATOMI, all of the MI systems exhibited degradation performances that were higher than that promoted by the commercial catalyst. To evaluate the extension of initial adsorption and degradation, the P25 factor (F_{P25}) may be useful (**Table 1**). For the adsorption, all of the MI systems exhibited F_{P25ads} values that were higher than unity, and these values ranged from 1.45 to 8.52, which represents a 48-752% increase in the performance compared to that of P25. As a general trend, the values of $F_{P25degr}$ were smaller than those of F_{P25ads}. However, the values of $F_{P25degr}$ also indicate an increase in the performance

compared to that of the commercial sample, and these values range are 1.05 (5%) to 5.27 (427%) higher.

The systems used as the control (i.e., NI system) can provide additional insight into the role of imprinted sites in the MI systems. As shown in **Fig. 1**, the performance degradation of the NI system for the majority of the studied drugs was comparable or even lower than that of P25. The F_{P25} value was also estimated for the NI system and is shown in **Table 1**. For adsorption, it is important to note that all of the F_{P25ads} values for the NI systems exhibited lower values than those exhibited by the MI systems (i.e., the TIOMI system had a F_{P25ads} value that was 576% higher than that of the NI system). Similarly, all of the $F_{P25degr}$ values for the NI systems were lower than those of the MI systems. In addition, as previously discussed, the $F_{P25degr}$ obtained for ATOMI was less than unity. However, its value was 1.83-fold higher than that obtained for the NI system. For the IBU drug, a relatively high $F_{P25degr}$ value was obtained for the NI system (4.0). However, its equivalent MI system exhibited a value that was 31.7% higher (5.27). Based on these results, the increase in the performance of our MI systems was due to the presence of specific cavities on the silica domain.

The main goal of our study was to prepare MI systems with improved degradation performances compared to that of the commercial sample containing a low content of TiO_2. Therefore, a comparison with previous results in which photocatalysis was employed for drug degradation is shown in **Table 3**.

Table 3: Comparison of degradation performance among different supported photocatalyts.

Reference Drug	TiO_2 source/Preparation method	TiO_2 concentration[1] (mg/L)	Drug concentration (mg/L)	Degradation (%)/time of reaction/pH	Reference
IBU	Degussa-P25	1000	18.5	61.0/15min/5.6	[34]
	Degussa-P25	20	5.0	55.0/15min/7.8	[32]
	IBUMI	**8.26**	**20.0**	**19.5/1h/4.3**	**Present work**
DIC	Degussa-P25	250	20.0	46.0/1h/6.0	[35]
	Degussa-P25	200	20.0	55.0/2h/4.0	[36]
	TiO_2 (from $TiCl_4$) supported on Nb_2O_5	n.d.[2]	5.0	47.0/2h/n.d.	[39]
	DICMI	**16.60**	**20.0**	**41.4/1h/6.0**	**Present work**
VAL	Degussa-P25	700	20.0	23.0/1h/n.d.	[47]
	VALMI	**8.26**	**20.0**	**45.4/1h/8.7**	**Present work**
ATO	Degussa-P25	700	20.0	20.5/1h/n.d.	[47]
	ATOMI	**12.84**	**20.0**	**8.3/1h/8.4**	**Present work**
TIO	Degussa-P25	700	20.0	31.5/1h/n.d.	[47]
	TIOMI	**7.94**	**20.0**	**25/1h/6.9**	**Present work**
KET	Degussa-P25	700	20.0	22.3/1h/n.d.	[47]
	KETMI	**8.26**	**20.0**	**24.2%/1h/7.4**	**Present work**

1) All MI photocatalyst were used at 660 $mg.L^{-1}$
2) Catalyst concentration used was 600 $mg.L^{-1}$
n.d. = not defined

For IBU drugs, recent studies have reported performances ranging from 55 to 61 % of degradation using P25 as catalyst [32, 34]. Although these values are at least 2.82-fold higher than that exhibited by IBUMI, these reported studies used a TiO_2 concentration that was 2.4-121 higher than that present in the MI system. In addition, low concentrations have been used, which typically improve the degradation. In DIC degradation, the DICMI system exhibited a degradation performance that was comparable to the most recent results [35, 47, 39]. This result is interesting

because the current reaction time is typically lower than those previously employed, and the TiO_2 concentration used in the current MI system is at least 12-fold lower than those reported in the literature. For VAL, the VALMI exhibited nearly twice the degradation performance compared to that in recently report [47], which employed a TiO_2 concentration that was 84.7-fold higher. The ATO and TIO drugs exhibited better degradation performance in a recent study [47]. However, the TiO_2 concentration was 54- and 88-fold higher that in the ATOMI and TIOMI systems, respectively. The same study reported the degradation of KET, which was similar to our KETMI system. However, this study employed a TiO_2 concentration that was 84.7-fold higher than that employed in our study. Therefore, the degradation performance of the MI systems was primarily enhanced by the presence of cavities for the specific recognition of the studied drugs.

Influence of the structural and textural properties on the photocatalytic performance

The results from the transmittance tests indicated that the commercial TiO_2 (P25) solution had a transmittance of 65%. All of the MI systems exhibited transmittances between 87 and 94%, suggesting that the light absorption of TiO_2 may be slightly influenced by the silica network. Although the resulting systems were predominantly amorphous, as shown in **Figure 2**, some characteristics peaks, such as at 2θ of 25 and 48° (anatase), were preserved in the prepared photocatalyst (All of the other MI systems exhibited patterns that were similar to that shown in **Fig. 2a**).

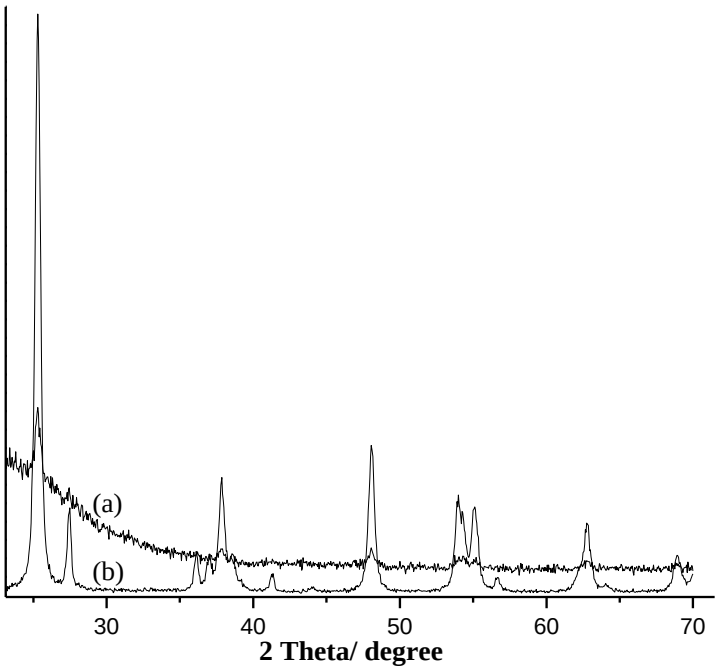

Figure 2: XRD patterns of a) DICMI and b) P25.

To elucidate the trends between the photocatalyst and their structural and textural properties, as well the effect of the structure of the drugs on the molecular imprinting, data were analyzed in terms of Dp, Vp, S_{BET}, ZP and $(SiO)_6$ percentage. All of the investigated characteristics are shown in Table 4. As shown in Table 4, the measured ZP of the photocatalysts were negative, and these values are in agreement with the range of values typically observed for silica-based materials [30, 48].

Table 4: Estimated parameters of the molecular imprinted supported photocatalysts.

System	S_{BET} ($m^2.g^{-1}$)	Vp ($mL.g^{-1}$)	Dp (Å)	Zeta (mV)[a)]	%$(SiO)_6$	Molecular volume[b)] ($Å^3$)	n (Level 1)	Rg (Level 1)	Rg (Level 2)	n (Level 3)
ATOMI	8.3	0.0035	64.5	-7.8	50.3	406.3	3.9	0.47	13.3	3.6
KETMI	2.6	0.0045	55.0	-10.5	52.8	353.2	2.4	0.87	11.6	3.4
TIOMI	6.0	0.055	50.0	-13.3	48.7	266.4	1.8	1.10	11.7	3.5
IBUMI	5.2	0.018	87.7	-25	53.5	169.7	3.9	0.37	15.4	3.6
VALMI	635.0	0,55	52.0	-13.3	61.5	333.3	1.7	0.51	12.2	3.0
DICMI	29.0	0,095	269.0	-16.7	65.4	218.5	2.6	2.70	13.3	3.2
GENMI	7.0	0.018	293.0	-4.6	63.4	n.d.	3.5	1.20	13.2	3.1
NI	90	0.011	23	-15.3	51.2	n.d.	4.0	0.36	13.2	3.9
P25	56	0.07	48	-3.6	n.d.	n.d.	n.d.	n.d.	n.d.	n.d.

a) Measurements were carried out at the same pH of photocatalytic tests (see Table 3).

b) Estimated for drugs. Details can be found elsewhere (da Silva et al, 2015).

n.d – not defined.

The percentage of $(SiO)_6$ estimated for the photocatalyst was higher than 50%. This result indicates that the prepared silica is prone to be more relaxed and is thus more hydrophilic. This state could be advantageous for application in photocatalytic processes because the majority of hazardous materials are typically present in aqueous matrices.

According to **Table 4**, Vp and Dp ranged from 0.0035 to 0.55 $mL.g^{-1}$ and 23 to 293 Å, respectively. In general, the MI systems exhibited the highest pore volume and diameter compared to those of the NI system and P25. The pore size was enhanced compared to the commercial sample and to NI systems that have been reported elsewhere [49, 50], which may be due to the presence of cavities in the MI systems. In addition, it is important to note that a correlation between the degradation and Vp was found (r_{Sp} = 0.883), which reinforces the role of the pores generated via the imprinting process on the silica network.

The S_{BET} values of MI systems ranged from 2.6 to 635 m^2g^{-1}. Possibly, this variation is due to coagulation of some drugs during the synthesis. Further textural and structural investigations are necessary to better understand the interactions between silica network with the templates.

As shown in Figure 1, different photocatalytic performance is achieved depending on the drug. In this sense, the surface area is one parameter that can improve the performance of photocatalysts [49]. Therefore, although no correlation could be observed between S_{BET} and adsorption or degradation, the systems with low S_{BET} values (i.e., ATOMI, KETMI, TIOMI, IBUMI and GENMI) exhibited an estimated average adsorption of 10.4%, which is ca. 1.5 and 2.72 times lower than that obtained for DICMI and VALMI, respectively (see Supporting Information Table 2). Similarly, the average degradation for these drugs is 17.6%, which is 2.35 and 2.55 times lower than the DICMI and VALMI, respectively. These results indicate that higher surface area could indeed enhance both adsorption and degradation of the drugs.

Despite the low surface areas of the systems ATOMI, KETMI, TIOMI, IBUMI and GENMI, an increase in adsorption was observed compared to that of the commercial samples (reaching a F_{P25ads} that was nearly 8.6-fold higher), and an increase in degradation compared to the NI system (where $F_{P25degr}$ was 38 (GENTMI) to 83**%** (ATORMI) higher). In addition, the average S_{BET} of these systems (ATOMI, KETMI, TIOMI, IBUMI and GENMI) was 5.82 $m^2.g^{-1}$, and the S_{BET} of the NI was system was 15.4-fold higher. As previously mentioned, these systems exhibited better degradation performance. Therefore, the primary reason for these improved results may be related to the cavities formed within the silica network. A correlation between S_{BET} and F_{P25ads} was observed ($r_{Sp} = 0.714$), suggesting that despite the low S_{BET} of the samples, the higher surface areas may indeed enhance the adsorption performance compared to that of the commercial sample.

The samples were further analyzed by SAXS, which provides information about the fractal nature of the sample by utilizing the structure formed by the organizational levels composed of a Guinier region and a Potency Law. The former provides an estimation of the Guinier radius of gyration (Rg), and the latter provides details about the system organization. The formation of pores in the silica-based materials is related to the aggregation of primary particles. A typical SAXS curve of these systems is shown in **Figure 3**. Three distinct structural regions were observed for these systems. Each region was composed of one or two contributions as follows: (1) a shoulder-type Guinier region that allows for the estimation of the Rg and/or (2) a linear power-law decay (q^{-n}) that provides details about the organization of the system.

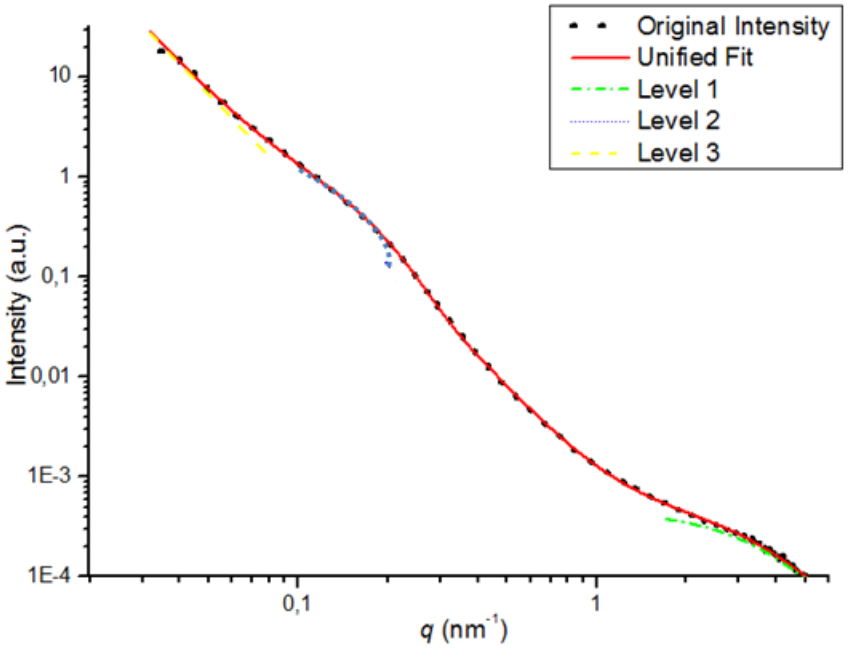

Figure 3: A typical SAXS profile (VALMI).

Table 4 lists the values of n for low (Level 3) and high (Level 1) *q*. At low *q* (dashed yellow line in **Figure 3**), which represents the largest dimension of the system in the SAXS experimental window, no Guinier region was observed. For both low and high q (Level 1 and Level 3), the NI

system exhibits a power law that is higher (q^{-4}) than that of the MI systems. Therefore, along the extraction step, the roughness on the composite surface is reduced because the exponential decay is closer to $q^{-4.0}$, which is the expected value for a perfectly smooth surface. These results may be due to the formation of pores within the silica network in the MI systems. In addition, the power law at high q was negatively correlated with the adsorption and degradation (r_{Sp} = -0.721 and -.829, respectively), which indicates that a higher degree of roughness (i.e., lower P values) may enhance the degradation due the presence of rough silica domains in which pores are generated. The influence of the drug on the Rg was also observed. Although no trend was observed in the low q range, at high q (Level 1), all of the MI systems exhibited Rg values that were higher than those of the NI systems. This structural level is due to the silica–drug clusters that are formed in the composite reaction process, and the high Rg values of the MI systems indicate the formation of pores.

Among the investigated drugs, ATOMI exhibited the lowest initial adsorption and degradation. However, DICMI exhibited one of the best degradation performances. One possible influence of these results is the molecular volume of the drugs, which can make the formation of molecular imprinting difficult if the volume is too high (i.e., for ATO molecules). In this sense, a strong negative correlation was observed between F_{P25ads} and $F_{P25degr}$ (both r_{Sp} = -0.83), suggesting that a higher drug volume could decrease the photocatalytic performance.

Taking into account the discussion above, we have shown that the difference of degradation of pharmaceuticals may be due to several factors, such as molecular volume of the drug, surface area, drug structure and charge on the surface of the photocatalyst. All these factors could also affect the homogeneity of the imprinted sites. Thus, there is an open venue in which other reactions

conditions have to be explored (pH, time of addition of drugs, mass of drugs, mass of P25, calcination time, solvent matrice, etc).

Recycling Tests

To evaluate the potential reuse of DICMI, seven experimental cycles were conducted, and the results are shown in Figure 4. The adsorption values are 5-fold lower at cycle 7, which is consistent with the performance obtained from photolysis of DIC (Figure 1). During the cycles, the decrease in degradation was primarily due to the loss of material during the reusability process (ca. 3% in each cycle). The DICMI system underwent 7 cycles of reuse while preserving approximately 60% of its photocatalytic efficiency. This result is comparable to that in a recent report [51], where a novel methyl orange imprinted chitosan-TiO_2 core-shell composite was employed. Because the reusability process was performed without desorption and regeneration processes, this process would be beneficial from an operational and economic point of view for application in wastewater treatment.

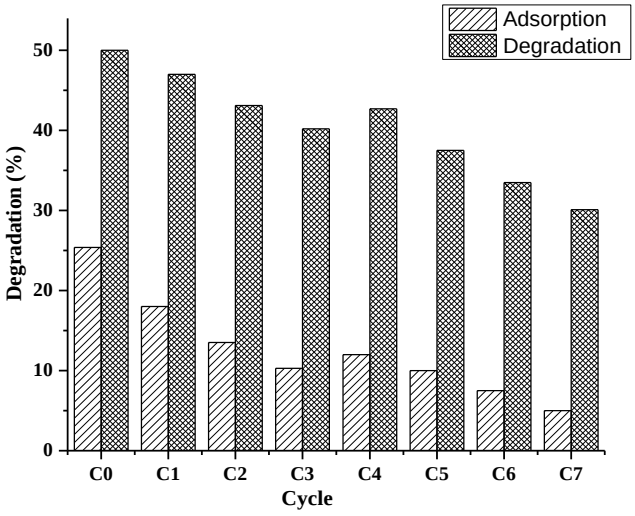

Figure 4: Recycling tests

CONCLUSIONS

Molecularly imprinted (MI) photocatalysts containing a low TiO_2 loading were prepared via an acid-catalyzed sol-gel route using different classes of pharmaceutical compounds as the template. Compared to the commercial sample (P25), the adsorption and degradation were enhanced by 751 and 427%, respectively. Compared to the control system (non-imprinted), the increase in the performance of the MI systems was due to the presence of specific cavities in the silica domain, and the textural and structural properties also support this conclusion. Due to the nature of the inorganic framework, the reusability is compatible with our MI photocatalysts, which underwent 7 cycles of reuse in which the photocatalytic efficiency was maintained at approximately 60% for the DICMI system.

Acknowledgements

This project was partially funded by the CNPq. C. Escobar is grateful for the grant provided by the CAPES. The authors wish to thank the LNLS (Project D11A-SAXS1-8691) for SAXS beamline measurements.

References

[1] V.V. Ranade, V.M. Bhandari, Industrial wastewater treatment, recycling, and reuse—past, present and future, in: V.V. Ranade, V.M. Bhandari (Eds.), Industrial Wastewater Treatment, Recycling and Reuse, Butterworth-Heinemann, Oxford, 2014, pp. 521–535.

[2] O.A. Jones, J.N. Lester, N. Voulvoulis, Pharmaceuticals: a threat to drinking water, Trends Biotechnol. 23 (2005) 163–167.

[3] S.O. de García, G.P. Pinto, P.G.R. Mata, Consumption and occurrence of pharmaceutical and personal care products in the aquatic environment in Spain, Sci. Total Environ. 444 (2013) 451–465.

[4] R.U. Halden, Epistemology of contaminants of emerging concern and literature meta-analysis, J. Hazard. Mater. 282 (2015) 2–9.

[5] M.S. Kostich, A.L. Batt, J.M. Lazorchak, Concentrations of prioritized pharmaceuticals in effluents from 50 large wastewater treatment plants in the US and implications for risk estimation, Environ. Pollut. 184 (2014) 354–359.

[6] B. Kasprzyk-Hordern, R.M. Dinsdale, A.J. Guwy, The occurrence of pharmaceuticals, personal care products, endocrine disruptors and illicit drugs in surface water in South Wales, UK, Water Res. 42 (2008) 3498–3518.

[7] K. Nakata, A. Fujishima, TiO_2 photocatalysis: Design and applications, J. Photochem. Photobiol. C Photochem. Rev. 13 (2012) 169–189.

[8] S. Chai, G. Zhao, Y.-n. Zhang, Y. Wang, F. Nong, M. Li, D. Li, Selective photoelectrocatalytic degradation of recalcitrant contaminant driven by a n-P heterojunction nanoelectrode with molecular recognition ability, Environ. Sci. Technol. 46 (2012) 10182–10190.

[9] D. Sharabi, Y. Paz, Preferential photodegradation of contaminants by molecular imprinting on titanium dioxide, Appl. Catal. B Environ. 95 (2010) 169–178.

[10] N. Shaham-Waldmannm, Y. Paz, Modified Photocatalysts in Photocatalysis and Water Purification: From Fundamentals to Recent Reports, Wiley, Germany, 2013.

[11] A.Y. Shan, T.I.M. Ghazi, S.A. Rashid, Immobilisation of titanium dioxide onto supporting materials in heterogeneous photocatalysis: a review, Appl. Catal. A Gen. 389 (2010) 1–8.

[12] A. Ibhadon, P. Fitzpatrick, Heterogeneous photocatalysis: recent advances and applications, Catalysts 3 (2013) 189–218.

[13] R.T. Thomas, P.A. Rasheed, N. Sandhyarani, Synthesis of nanotitania decorated few-layer graphene for enhanced visible light driven photocatalysis, J. Colloids Interface Sci. 428 (2014) 214–221.

[14] J.G. McEvoy, W. Cui, Z. Zhang, Synthesis and characterization of Ag/AgCl—activated carbon composites for enhanced visible light photocatalysis, Appl. Catal. B Environ. 144 (2014) 702–712.

[15] D. Chen, Q. Zhu, F. Zhou, X. Deng, F. Li, Synthesis and photocatalytic performances of the TiO_2 pillared montmorillonite, J. Hazard. Mater. 235–236 (2012) 186–193.

[16] Z. Pan, E.A. Stemmler, H.J. Cho, W. Fan, L.A. LeBlanc, H.H. Patterson, A. Amirbahman, Photocatalytic degradation of 17 -ethinylestradiol (EE2) in the presence of TiO_2 -doped zeolite, J. Hazard. Mater. 279 (2014) 17–25.

[17] G. Vasapollo, R.D. Sole, L. Mergola, M.R. Lazzoi, A. Scardino, S. Scorrano, G. Mele, Molecularly imprinted polymers: present and future prospective, Int. J. Mol. Sci. 12 (2011) 5908–5945.

[18] M.J. Whitcombe, N. Kirsch, I.A. Nicholls, Molecular imprinting science and technology: a survey of the literature for the years 2004–2011, J. Mol. Recognit. 27 (2014) 297–401.

[19] J.E. Lofgreen, G.A. Ozin, Controlling morphology and porosity to improve performance of molecularly imprinted sol–gel silica, Chem. Soc. Rev. 43 (2014) 911–933.

[20] E.C. Morais, G.G. Correa, R. Brambilla, J.H.Z. dos Santos, A.G. Fisch, Selective silica-based sorbent materials synthesized by molecular imprinting for adsorption of pharmaceuticals in aqueous matrices, J. Sep. Sci. 36 (2013) 636–643.

[21] C. Escobar, J.H.Z. dos Santos, Effect of the sol–gel route on the textural characteristics of silica imprinted with rhodamine B, J. Sep. Sci. 37 (2014) 868–875.

[22] C.H. Chuixiu, Z. Tu, X. Shen, Molecularly imprinted photocatalyst with a structural analogue of template and its application, J. Hazard. Mat. 248 (2013) 379–386.

[23] Z. Lu, F. Chen, M. He, M. Song, Z. Ma, W. Shi, Y. Yan, J. Lan, F. Li, P. Xiao, Microwave synthesis of a novel magnetic imprinted TiO_2 photocatalyst with excellent transparency for selective photodegradation of enrofloxacin hydrochloride residues solution, Chem. Eng. J. 249 (2014) 15–26.

[24] X. Shen, L. Zhu, J. Li, H. Tang, Synthesis of molecular imprinted polymer coated photocatalysts with high selectivity, Chem. Commun. (2007) 1163–1165.

[25] W.H. Tao, X. Xuan, Z. HuiMin, Q. Xie, Enhanced photocatalytic degradation of tetracycline hydrochloride by molecular imprinted film modified TiO_2 nanotubes, Environ. Chem. 57 (2012) 601–605.

[26] X. Shen, L. Zhu, H. Yu, S. Liu, W. Li, Selective photocatalysis on molecular imprinted TiO_2 thin films prepared via an improved liquid phase deposition method, New J. Chem. 33 (2009) 1673–1679.

[27] X. Shen, L. Zhu, C. Huang, H. Tang, Z. Yu, F. Deng, Inorganic molecular imprinted titanium dioxide photocatalyst: synthesis, characterization and its application for efficient and selective degradation of phthalate esters, J. Mat. Chem. 19 (2009) 4843–4851.

[28] X. Luo, F. Deng, L. Min, S. Luo, B. Guo, G. Zeng, C. Au, Facile one-step synthesis of inorganic-framework molecularly imprinted TiO_2 /WO_3 nanocomposite and its molecular recognitive photocatalytic degradation of target contaminant, Environ. Sci. Technol. 47 (2013) 7404–7412.

[29] C. de Escobar, M. Dartora, L. Campo, C. Radtke, J. Bayne, I. Butler, R. Lattuada, J. dos Santos, The role of the sol–gel route on the interaction between rhodamine B and a silica matrix, J. Sol–Gel Sci.Technol. 72 (2014) 260–272.

[30] C.C. de Escobar, A. Fisch, J.H.Z. dos Santos, Effect of a sol–gel route on the preparation of silica-based sorbent materials synthesized by molecular imprinting for the adsorption of dyes, Ind. Eng. Chem. Res. 54 (2015) 254–262.

[31] C.C. de Escobar, A. Dellegrave, M.A. Lasarin, J.H.Z. dos Santos, The sol–gel route effect on the preparation of molecularly imprinted silica-based materials for selective and competitive photocatalysis, Colloids Surf. A Physicochem. Eng. Aspects 486 (2015) 96–105.

[32] F. Braz, M. Silva, F. Silva, S. Andrade, A. Fonseca, M. Kondo, Photocatalytic degradation of ibuprofen using TiO_2 and ecotoxicological assessment of degradation intermediates against Daphnia similis, J. Environ. Protein 5 (2014) 620–626.

[33] J. Choina, H. Kosslick, C. Fischer, G.U. Flechsig, L. Frunza, A. Schulz, Photocatalytic decomposition of pharmaceutical ibuprofen pollutions in water over titania catalyst, Appl. Catal. B Environ. 129 (2013) 589–598.

[34] J. Madhavan, F. Grieser, M. Ashokkumar, Combined advanced oxidation processes for the synergistic degradation of ibuprofen in aqueous environments, J. Hazard. Mater. 178 (2010) 202–208.

[35] A. Achilleos, E. Hapeshi, N.P. Xekoukoulotakis, D. Mantzavinos, D. Fatta-Kassinos, Factors affecting diclofenac decomposition in water by UV-A/TiO_2 photocatalysis, Chem. Eng. J. 161 (2010) 53–59.

[36] L. Rizzo, S. Meric, D. Kassinos, M. Guida, F. Russo, V. Belgiorno, Degradation of diclofenac by TiO_2 photocatalysis: UV absorbance kinetics and process evaluation through a set of toxicity bioassays, Water Res. 43 (2009) 979–988.

[37] M.V. Bagal, P.R. Gogate, Degradation of diclofenac sodium using combined processes based on hydrodynamic cavitation and heterogeneous photocatalysis, Ultrasonics Sonoch 21 (2014) 1035–1043.

[38] S. Murgolo, F. Petronella, R. Ciannarella, R. Comparelli, A. Agostiano, M.L. Curri, G. Mascolo, UV and solar-based photocatalytic degradation of organic pollutants by nano-sized TiO_2 grown on carbon nanotubes, Catal. Today 240 (2015) 114–124.

[39] F.V. de Andrade, G.M. de Lima, R. Augusti, M.G. Coelho, Y.P.Q. Assis, I.R.M. Machado, A new material consisting of TiO_2 supported on Nb_2O_5 as photocatalyst for the degradation of organic contaminants in aqueous medium, J. Environ. Chem. Eng. 2 (2014) 2352–2358.

[40] A. Hu, X. Zhang, K.D. Oakes, P. Peng, Y.N. Zhou, M.R. Servos, Hydrothermal growth of free standing TiO_2 nanowire membranes for photocatalytic degradation of pharmaceuticals, J. Hazard. Mater. 189 (2011) 278–285.

[41] J.C.C. da Silva, J.A.R. Teodoro, R.F.C.F. Afonso, S.F. Aquino, R. Augustini, Photolysis and photocatalysis of ibuprofen in aqueous medium: characterization of by-products via liquid chromatography coupled to high-resolution mass spectrometry and assessment of their toxicities against Artemia salina, J. Mass Spectrom. 49 (2014) 145–153.

[42] A. Fidalgo, L.M. Ilharco, The defect structure of sol–gel-derived silica/polytetrahydrofuran hybrid films by FTIR, J. Non-Cryst. Solids 283 (2001) 144–154.

[43] J. Ilavsky, P.R. Jemian, Irena: tool suite for modeling and analysis of small-angle scattering, J. Appl. Cryst. 42 (2009) 347–353.

[44] S. Kline, Reduction and analysis of SANS and USANS data using IGOR Pro, J. Appl. Cryst. 39 (2006) 895–900.

[45] G. Beaucage, Approximations leading to a unified exponential/power-law approach to small-angle acattering, J. Appl. Cryst. 28 (1995) 717–728.

[47] W.L. da Silva, M.A. Lansarin, P.R. Livotto, J.H.Z. dos Santos, Photocatalytic degradation of drugs by supported titania-based catalysts produced from petrochemical plant residue, Powder Technol. 279 (2015) 166–172.

[48] L. Avadiar, Y.K. Leong, A. Fourie, Physcochemical behaviors of kaolin slurries with and without cations—contributions of alumina and silica sheets, Colloids Surf. A Physicochem. Eng. Aspects 468 (2015) 103–113.

[49] W.Z. Xu, W. Zhou, P.P. Xu, J.M. Pan, X.Y. Wu, Y.S. Yan, A molecularly imprinted polymer based on TiO_2 as a sacrificial support for selective recognition of dibenzothiophene, Chem. Eng. J. 172 (2011) 191–198.

[50] X. Shen, L. Zhu, C. Huang, H. Tang, Z. Yu, F. Deng, Inorganic molecular imprinted titanium dioxide photocatalyst: synthesis, characterization and its application for efficient and selective degradation of phthalate esters, J. Mater. Chem. 19 (2009) 4843–4851.

[51] G. Xiao, H. Su, T. Tan, Synthesis of core–shell bioaffinity chitosan TiO_2 composite and its environmental applications, J. Hazard. Mater. 283 (2015) 888–896.

Supporting Information

Supporting Information S 1: Calibration curves and other equations.

Calibration curves of each drug are shown at Equations 1-7.

$$A_{TIO} = 0.0765.C,\ R^2 = 0.999 \quad (1)$$

$$A_{IBU} = 0.0288.C,\ R^2 = 0.999 \quad (2)$$

$$A_{VAL} = 0.0876,\ R^2 = 0.996 \quad (3)$$

$$A_{DIC} = 0.02892,\ R^2 = 0.998 \quad (4)$$

$$A_{KET} = 0.0226,\ R^2 = 0.999 \quad (5)$$

$$A_{ATO} = 0.033,\ R^2 = 0.999 \quad (6)$$

$$A_{GEN} = 0.023,\ R^2 = 0.998 \quad (7)$$

A is the absorbance value and C is the concentration, mg/L, of each species; N= 7

Final degradation (or adsorption), imprinted factor and P25 factor are shown at equations 8, 9 and 10.

$$\text{Adsorption or Concentration (\%)} = \frac{C_0 - C}{C_0} \times 100\% \quad (8)$$

$$IF = \frac{\text{Concentration}^{IM}}{\text{Concentration}^{NI}} \quad (9)$$

$$F_{P25} = \frac{\text{Concentration}^{MI/NI}}{\text{Concentration}^{P25}} \quad (10)$$

Supporting Information Table 1: Adsorption values obtained at dark-stage (1h)

System	MI	P25
ATO	7.7 ± 0.35	5.2 ± 0.78
KET	7.4 ± 0.28	4 ± 1.2
TIO	23 ± 1.21	2.7 ± 0,21
IBU	7 ± 0.24	1.2 ± 0.09
VAL	28.3 ± 1.3	11.5 ± 0.21
DIC	15.5 ± 0.83	4.5 ± 0.25
GEN	6.7 ± 0.55	2.1 ± 0.085

4.6 Artigo 6

A ser submetido ao *Journal of Sol-Gel Science and Technology*.

Effect of the amount and the time of addition of a dye template on the adsorption and photocatalytic performance of molecularly-imprinted silica prepared via acid-catalyzed sol-gel route

Cícero Coelho de Escobar[1], Francisco Paulo dos Santos[2] and João Henrique Z. dos Santos[2]

[1]Departamento de Engenharia Química—Universidade Federal do Rio Grande do Sul

Rua Eng. Luis Englert s/n, 90040-040–Porto Alegre–RS–BRASIL

[2]Instituto de Química, Universidade Federal do Rio Grande do Sul, Av. Bento Gonçalves, 9500, Porto Alegre, CEP 91500-000, Brazil.

Corresponding author. Phone: +55 51 3308 7238; fax: +55 51 3308 7304; e-mail address: jhzds@iq.ufrgs.br (J.H.Z. dos Santos).

Abstract

A molecularly imprinted (MI) photocatalyst was prepared via an acid-catalyzed sol-gel route using Rhodamine B (RhB) as the template. The aim of this study was to evaluate the effect of the amount and the time of addition of RhB on the photocatalytic degradation. The study also evaluated the MI silica xerogels in terms of adsorption kinetics. Several methods of extraction

were employed and the use of ultrasound (in methanol) has shown the best results in terms of increasing in surface area, nitrogen removal and volume of solvent. The samples were characterized in terms of the pore diameter, surface area and aggregation of primary particles (by small-angle scattering). Regarding the systems containing the mass of template fixed (150 mg), textural evidences suggest that large pores and large surface areas could explain the better results achieved by the sytems with template added at t =0. In addition, the effect of template amount added at a given fixed time clearly shows that there is a threshold at which degradation is improved. Results suggest that higher content of template employed in the synthesis of the photocatalysts may be more difficult to be removed from the silica network and it could increase the aggregation of molecules, and thus affecting the photocatalytic performance.

Introduction

Synthetic dyes are extensively used in the textile, plastic, paper, printing, cosmetic and pharmaceutical industries [1]. It has been estimated that in the last 150 hundred years over 105 different dyes have been produced worldwide with an annual production of ca. 7×10^5 metric tons [2]. In addition, the traditional textile finishing industry consumes approximately 100 L of water to process approximately 1 kg of textile materials [3]. Recent surveys estimated that 280,000 tons of textile dyes are discharged in industrial textile effluent every year worldwide [4]. Discharged dyes color the water systems they enter, hindering sunlight penetration to the lower layers of the water body and hence affecting aquatic life [1].

Different methods are available for the remediation of dye wastewaters, including sedimentation, filtration, chemical treatment, oxidation, advanced oxidation processing, biological

treatment, ion exchange and adsorption [2]. Regarding the latter, research on molecularly imprinted (MI) materials has received considerable attention in recent years. Since such materials represent a valid alternative to molecular recognition system, they demonstrate high affinity and selectivity for the molecules employed as templates for their synthesis [5, 6]. The ability for molecular recognition facilitates use of such materials in processes such as drug delivery [7], catalysis [8], adsorption [9, 10, 11], chemical sensing [12], preconcentration [13], biological antibodies, and receptor systems [14].

In developing such molecular-imprinted materials as sorbents for removal processes, most studies have reported the use of organic polymeric phases. Certain drawbacks are associated with polymeric materials, such as functional chemical groups outside the printing sites, which produce non-specific and weak interactions between the template and polymer functional units. In addition, such materials may yield low-to-moderate template recovery and heterogeneity of the generated receptor sites [15]. A promising approach for overcoming such inconveniences is to use inorganic matrices, such as silica-based materials.

One potential approach for producing silica-based imprinted materials is the sol-gel process. In this strategy, the template reacts with the precursor (e.g., tetraethylorthosilicate–TEOS), which produces a silica network with the encapsulated molecule. Specific adsorptive sites are created after removing the template from the silica network, which produces materials with imprinted sites. As shown in the literature [16, 17], matrices prepared by the sol-gel method offer certain advantages compared with conventional organic polymerization methods, such as rigidity, thermal stability and tailored porosity. In addition, the sol-gel prepared silica shows low reactivity in all but extreme conditions, which include exposure to very strong acid, very strong base, and oxidizers species, which makes it a robust matrix for a variety of chemical environments [18].

Most studies discuss silica materials as adsorbents in solid-phase drug extraction [9], such as for ibuprofen [19], methylxanthines [20] and diethylstilbestrol [21].

In the case of pollutant degradation, Advanced Oxidation Processes (AOPs) are known methods capable of treating a wide variety of organic contaminants. In these cases, mineralization, which is the conversion of the molecules to their highest possible oxidation state and finally to water, carbon dioxide, oxidized inorganic anions and/or other molecules that can be removed by biological processes, is required for complete removal.

Among the AOPs, heterogeneous photocatalysis using TiO_2 is one of the most promising strategies for the use with emerging contaminants. This method exhibits several advantages, such as low cost, low toxicity and chemical stability [22]. However, a serious drawback in heterogeneous photocatalytic oxidation is its low selectivity to target contaminants, which is controlled by photogenerated holes and hydroxyl radicals with strong oxidation potentials [22]. In this sense, heterogeneous photocatalysis lacks selectivity to most of the hazardous contaminants [23, 24]. This characteristic is a disadvantage because mixtures derived from effluent streams may contain nonbiodegradable, highly toxic organic pollutants that coexist with less toxic and biodegradable material. In many cases, the former is present in lower concentrations, and the latter is a major component [23, 24]. However, the preferential degradation of the most toxic materials is desirable.

Inorganic-framework molecularly imprinted photocatalysts is an emergent field, with a few works recently published [25, 26, 27, 28]. We have previously investigated the effect of the sol-gel route on molecularly imprinted materials in terms of their textural and structural properties. We have demonstrated the potential of silica-imprinted materials for use in selective adsorption and that Ti moieties (using $TiCl_4$ as a source of TiO_2) can be incorporated into a silica network

[10, 29]. We also conducted selective and competitive photocatalysis to evaluate the sol-gel route effect on the preparation of molecularly imprinted silica-based materials using Rhodamine B as the template [27]. We have shown that the adsorption of the target molecule occurs on the domains of the imprinted silica in the vicinity of the photocatalyst, which promotes photocatalytic degradation. Among the investigated sol-gel routes, the acid-catalyzed hydrolytic route afforded the best results. However, the effects of the amount and the time of addition of template on photocatalytic performance are poorly understood. This information could help future works for better design of MI materials for specific applications.

Thus, the aim of the present study is to evaluate the effect of the amount and the time of addition of a template (RhB) on the characteristics and catalyst activity of a photocatalyst prepared via an acid-catalyzed sol-gel route. For a better understanding of the behavior of the materials, different extraction methods were studied together with an evaluation of adsorption kinetics of the MI xerogels.

EXPERIMENTAL SECTION

Materials and methods

Rhodamine B (Vetec), tetraethoxisilane ($Si(OCH_2CH_3)_4$, TEOS, Merck, >98 %), titanium tetrachloride (Merck, >99 %) and silicon tetrachloride ($SiCl_4$, Sigma–Aldrich, 99 %) were used as received. Hydrocloric acid (HCl, Nuclear, 38%) was employed as the catalyst.

Preparation of sol-gel materials

The photocatalysts were prepared using the sol-gel process using HCl (0.2 M) as the catalyst, and TEOS (45 mmol) was used as the raw material at a 1:2 (HCl:TEOS) volume ratio and following addition of $TiCl_4$ (10.4 mmol). The effect of the amount of template was investigated

by adding 150, 300 and 500 mg of RhB at starting reaction time. The effect of time of template addition was evaluated by fixing the amount of RhB at 150 mg at t = 0, 60, 90 and 120 min after starting the sol-gel reaction.

The following four extraction methods were evaluated for template removal: Thermal, Soxhlet, solvent washing and ultrasound. Thermal extraction was performed under Ar flow starting at room temperature up to 190 °C at a heating rate of 5 °C/min. Soxhlet extraction was employed in a suitable device for 24 h using methanol as the solvent. Methanol and water were employed as the solvents for ultrasound-assisted extraction. The process was conducted by altering modes of pulse-on (20 s) and pulse-off (5 s) during five min. Extraction with deionized water was employed as the solvent for washing.

Before photocatalytic process, the samples needed to be heated for the formation of photo-active phases (anatase and rutile). The samples extracted using ultrasound (methanol) were submitted to two different heating process. The first one was carried out in a muffle furnace at 450 °C for 4 hours at a rate of 5 °C/min (labeled as 15C0*). The second approach was done at slower heating rate in which calcination occurred keeping the temperature constant for 1 hour at each increment of 100 °C and by using a heating rate of 1 °C/min. This procedure was continued until the temperature reached 450 °C, and then the material was held at this temperature for 4 h. Then, the sample was washed with deionized water to remove any residue and finally dried at 80°C.

Samples were labeled according to the amount and time in which template was added and depending on the stage of preparation. Thus, **A** stands for systems extracted but non-calcined, and **C** stands for systems extracted and calcined. For instance, 15C120 stands for 150 mg of template added at t= 120 min after sol-gel reaction initiated, and 50C0 stands for an addition of template at t= 0 min and 50 mg of RhB.

Xerogel Characterization

The specific surface area was determined by the Brunauer-Emmett-Teller (BET) method at -196 °C within the partial pressure range $0.2 < P/P_0 < 0.9$. Prior to each measurement, the samples were preheated at 110°C for 14 h under a vacuum. The pore diameter was determined using the Barrett-Joyner-Halenda (BJH) method.

Carbon and nitrogen content was determined in a Perkin- Elmer (Wellesley, MA, USA) M-CHNSO/2400 analyzer.

SAXS experiments were performed on the D11A beamline at the Brazilian Synchrotron Light Laboratory (LNLS, Brazil) at 1.488 nm. The incident beam was detected at two different sample-to-detector distances (1549.8 mm and 2245.7 mm) to increase the scattering vector q range ($q = (4\pi/\lambda) \sin\theta$; 2θ = scattering angle). The dried samples were placed between two Kapton® foils, and the collimated X-ray beam passed through a chamber with the stainless steel sample holder. Silver behenate powder was employed as the standard to calibrate the sample-to-detector distance, detector tilt and direct beam position. The isotropic scattering patterns were radially averaged. SAXS data analysis was performed using the Irena evaluation routine [30](30), which was implemented using Igor Pro Software (WaveMetrics, Portland, USA) [31] More details can be found elsewhere [10].

The SPSS Statistical System (SPSS for Windows, version 19, IBM®) was employed to analyze the correlations (Spearman) between the data. All of statistical tests were performed at a $P < 0.05$ level of significance.

Adsorption and photocatalytic evaluation

For adsorption experiments, 10 mg of RhB-imprinted silica were introduced into a cartridge at 25°C, through which 5 mL of RhB solution (20 ppm) was percolated over 360 min. Samples were collected at regular intervals for further centrifugation (4,000 rpm, Cientec CT-5000R) and evaluation of concentration using UV-visible spectrometry at 553 nm.

For photocatalytic experiments, 50 mL of RhB (20 ppm) was added to 33 mg of the photocatalyst in a bath reactor under flowing air (6.5 mL s^{-1}). The results of the photocatalytic tests were assessed at two stages under magnetic agitation (ca. 400 rpm) as follows: (i) one hour with the lamp off (initial adsorption) and (ii) one hour with the lamp on (degradation). An ultraviolet lamp was used (125 W Hg vapor lamp) (General Electric), and the radiation was adjusted to 45 $W \cdot m^{-2}$ (Radiometer Series 9811, Cole-Parmer Instruments). A circulating water jacket was employed to maintain the temperature reaction vessel at 30 ºC. The tests were carried out at the natural pH 4.7

The samples were collected with a syringe (2 mL for each collect), stored in Eppendorf tubes and protected from light. For the catalyst separation, the samples were centrifuged for 20 min at 4000 rpm (Cientec CT-5000R). The final concentration was determined by UV-Vis molecular absorption spectroscopy using a Varian Cary 100 spectrophotometer at 553 nm. All of the experiments were performed in triplicate, and the reported results are the mean values.

Results and Discussion

Xerogel and Photocatalysts Characterization

Table 1 shows the C and N content, the S_{BET} values and the solvent volume used for several different extraction methods for the system 15A0 (non-calcined). Although one can see a decrease of C content compared to the encapsulated silica, carbon content can be misleading due to the potential presence of residual ethoxide groups in silica produced by the sol–gel method [30].

Table 1: Elemental content and textural parameters for encapsulated and extracted silica for the system 15A0.

	C (%)	N (%)	N removal (%)	S_{BET} (m^2/g)	Solvent volume (mL)	Solvent volume/increase of S_{BET} after extraction ($mL.g/m^2$) [a)]
Encapsulated	2.2	0.2	n.d.	639	n.d.	n.d
Thermal	0.12	0.002	99	649	n.d.	n.d
Soxhelt	0.31	0.006	97	854	500	374.1
Washing	0.73	0.008	96	794	700	563.5
Ultrasound - water	1.83	0.17	15	786	80	65.0
Ultrasound - methanol	0.24	0.04	80	831	80	61.5

n.d. – not defined**;** [a)] Calculated considering an increase in area from encapsulated system.

According to **Table 1**, it is possible to identify that the highest removal of N was obtained by thermal extraction. However, no increase in area was achieved, suggesting that silica could have collapsed. Comparing the extractions using solvents, the extraction by ultrasound required an amount of solvent almost 9 times lower if compared with the washing and 6 times lower compared with Soxhlet. In addition, ultrasonic extraction with methanol showed the lowest solvent

consumption and the lowest ratio solvent volume/increase of S_{BET}. Compared with the extraction made by ultrasound with water and with methanol, the latter resulted in higher percentage of nitrogen removal (ca. 5×). Although the performance of extraction can be tuned by different conditions (solvent volume, time of extraction, etc.), the methods herein studied suggest that the best removal of RhB is made by ultrasound with methanol. Therefore, all the further studies were made using this method.

Collapse of silica networks was also suggested in the case of paracetamol extraction from silica network by Morais and collaborators [32]. The same authors reported low efficiency achieved by Soxhelt and intermediary efficiency for ultrassound-assisted extraction without significantly compromise of the surface area.

Table 2 shows the S_{BET} and SAXS measurements results for different systems of photocatalyts studied. Among the systems with fixed mass (150 mg), it is possible to note that slower calcination time (15C0) enhanced both surface area and pore diameter. However, the addition of template at latter stage of sol-gel reaction caused a decrease of area and of pore diameter, reaching almost the half value of the system 15C0 in the case of the systems 15C90 and 15C120. These findings suggest that the efficiency of encapsulated molecules may be compromised if the templated is added after the first stages of sol-gel reaction. In addition, higher content of template added at t= 0 does neither icreases the value of area nor the pore diameter. One can suggest two possible reasons for this behavior with higher content of template: (i) it is more difficult to remove it from the silica network and (ii) it could increase the aggregation of molecules and thus affecting at some extent the textural properties.

For the later reason, it is interesting to note that the system 50C0 showed the lowest value of radius of gyration (Rg) (For both L1 and L2). The formation of pores is related to the

aggregation of primary particles (Rg Level 1 (L1), located in the *q* region greater than 0.03 $Å^{-1}$), while the structure of fractal clusters (Rg Level 2 (L2), located in the *q* region below 0.01 $Å^{-1}$) results from the aggregation of primary particles. In sol-gel reactions, the primary particles have nanometric sizes and act as nucleation sites for the formation of the gel. In this sense, comparing to the system 15C0, the result of Rg is in concordance to the lower value of pore diameter for the systems 30C0 and 50C0.

The structure of the clusters of primary particles that constitute Level 2 can be obtained by analyzing the power law exponent of the scattering curve. If the exponent of the power law ($I \alpha q^{-p}$) is between 1.0 and 3.0, the secondary particles have a mass fractal structure. When the exponent is between 3.0 and 4.0, the secondary particles have a fractal surface. In the case of an exponent equal to 4.0, the secondary particles have a dense core and a uniform surface [33, 34]. According to the results shown in **Table 2**, all systems showed characteristic of fractal surface. These findings are in agreement to the others recent reported in which imprinted photocatalysts have been investigated [28, 29]**.**

Table 2: Textural characteristics of the photocatalysts.

	System	S_{BET} (m^2/g)	Pore diameter (Å)	Rg L1	Rg L2	P
m= 150 mg	15C0*	634.5	30.9	2.2	9.8	3.4
	15C0	750.6	42.3	1.6	9.8	3.6
	15C60	550.4	37.3	3.4	n.d.	3.7
	15C90	387.3	32.4	1.2	n.d.	3.8
	15C120	390.8	33.4	3.2	n.d.	3.9
t= 0h	15C0	750.6	42.3	1.6	9.8	3.6
	30C0	338.4	34.8	1.7	7	3.8
	50C0	347.5	34.6	0.6	3.2	3.9

*) calcined with higher heating rate (5 °C/min).

Adsorption Evaluation

Fig. 1 shows the effect of stirring time and initial Rhodamine B concentration (1000, 400 and 100 ppm) on the adsorbed amount of the Rhodamine B dye per gram of the adsorbent (q). From Fig. 1 it was observed that the amount of dye uptake (q) is increased with increasing the contact time at all initial dye concentrations. Furthermore, the amount of adsorbed dye is increased with the increase in initial dye concentration. Progress of the adsorption of dye shows that the rate of adsorption of the dye molecules was initially very fast and then gradually slows down to reach equilibrium within 240 min for both initial concentrations of 400 and 100 ppm, whereas a longer time (300 min.) for equilibrium was necessary for initial concentration of 1000 ppm. This behavior may be explained by two distinct mechanisms: (i) an initial rapid binding of dye molecules on the adsorbent surface followed by (ii) relatively slow intra-particle diffusion.

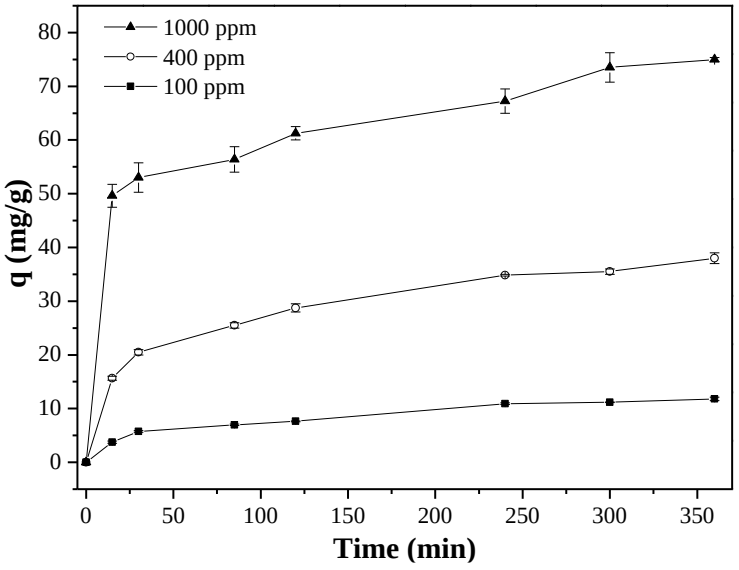

Figure 1: Effect of contact time and dye concentration on the adsorption amount of Rhodamine B dye onto (20 ppm) of adsorbent at 25°C for the system 15A0.

In order to investigate the adsorption of Rhodamine B on the surface of the adsorbate, different kinetic models are used to examine the controlling mechanism of the adsorption process. In this study, pseudo-first-order and pseudo-second-order kinetic models were investigated to find the best fit model for the experimental data. In addition, intra-particle diffusion was also investigated. The linear form of Lagergren´s first order rate follows **equation 1** [34]:

$$\log(q_e - q_t) = logq_e - \frac{k_1 t}{2.303} \quad (1)$$

Where q_e is the amount of Rhodamine B adsorbed onto the adsorbate at equilibrium (mg/g), q_t is the amount of Rhodamine B adsorbed onto the adsorbate at any time t (mg/g), and k_1 (min^{-1}) is the rate constant of the pseudo-first-order adsorption which can be calculated from the slope of the linear plot of ln ($q_e - q_t$) vs. t.

Ho [36] proposed a second order kinetic, according to **equation 2**:

$$\frac{t}{q_t} = \frac{1}{k_2 q_e^2} + \frac{t}{q_e} \quad (2)$$

where k_2 ($g.mg^{-1}.min^{-1}$) is the rate constant of the pseudo-second-order adsorption, q_e is the amount of dye adsorbed on the adsorbent at equilibrium (mg/g), and q_t (mg/g) is the amount of dye adsorbed on the adsorbent at any time. The constant k_2 can be calculated from the slope and intercept of the plot of t/q_t against t.

The most commonly used technique for identifying the mechanism involved in the adsorption process is by using the intraparticle diffusion model as follows by Webber–Morris model (**equation 3**) [37]

$$q_t = k_d t^{0.5} + C_1 \quad (3)$$

where q_t (mg/g) is the amount of dye adsorbed onto the adsorbent at time t, and k_d ($mg.g^{-1}.min^{-0.5}$) is the intraparticle diffusion rate constant and C_1 is a constant related to the thickness of the boundary layer.

The straight line plots of $\log(q_e - q_t)$ against time t for the pseudo-first-order reaction, and t/q_t against time t for the pseudo-second-order reaction of the adsorption of Rhodamine B onto adsorbate were used to calculate pseudo-first-order and pseudo-second-order rate constants (**Fig. 2** and **3**).

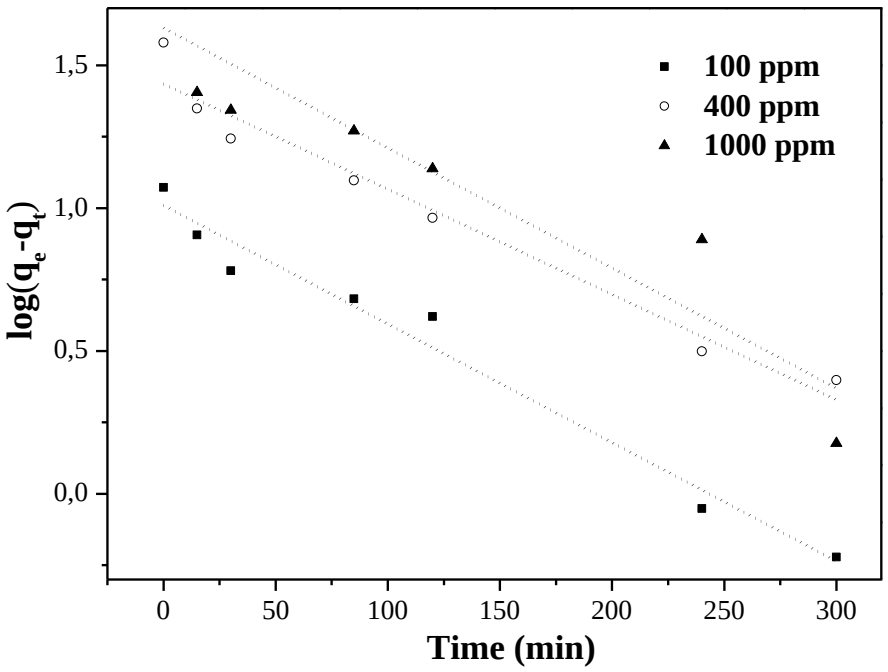

Figure 2: First-order plot of adsorption for the system 15A0.

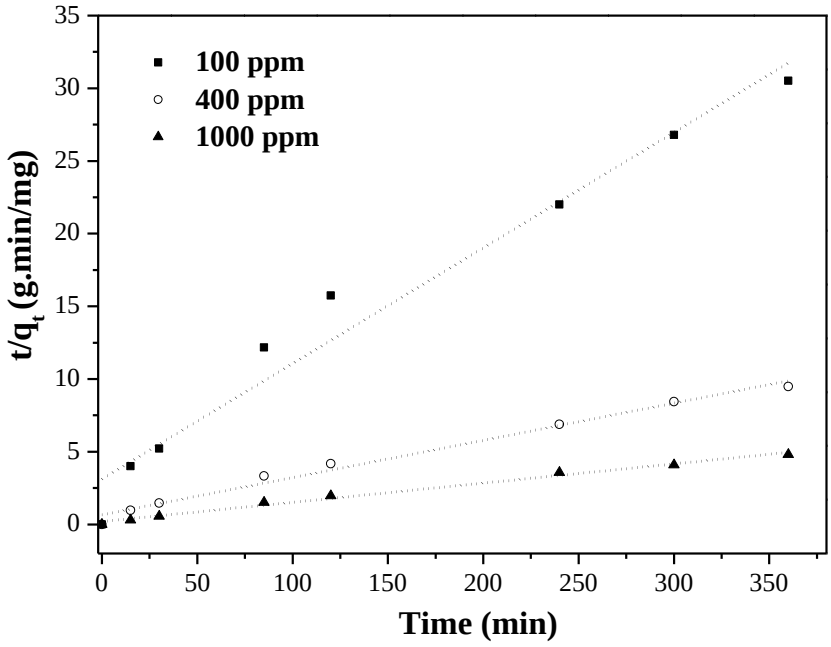

Figure 3: Second-order plot of adsorption for the system 15A0.

Calculated correlation coefficients and rate constants are presented in **Table 4**. It was observed that, at all solution concentrations, the kinetic data had relatively higher determination coefficient (r^2) values for the second-order model. Moreover, comparing the experimental values of q_e, to the calculated ones, they were not reasonable. On the other hand, the calculated q_e values of the pseudo-second-order model were found to be closer to the experimentally determined q_e values, also suggesting its suitability. Taking into account the above discussion, one can consider that pseudo-second-order kinetics was the more appropriate kinetic model to represent data from the adsorption of Rhodamine B onto the adsorbate. This finding is in agreement with recent works exploring adsorption kinetics for MIP materials [38, 39, 40].

Table 4: Rate constants and correlation coefficients of the kinetic models for the system 15A0 (Adsorbent dosage: 20 mg /5 mL; Temperature: 25°C; pH = 4.7).

Dye (mg/L)	Experimental q_e ($mg.g^{-1}$)	Pseudo-first-order			Pseudo-second-order		
		k_1 (min^{-1})	q_e ($mg.g^{-1}$)	r^2	k_2 ($g.min^{-1}.mg^{-1}$)	q_e ($mg.g^{-1}$)	r^2
100	10.7	0.0095	10.0	0.97	0.002	12.57	0.986
400	35.0	0.0085	36.91	0.96	0.001	30.06	0.991
1000	73.5	0.0097	42.65	0.839	0.0008	75.58	0.97

Comparison with different adsorbents could be difficult depending on the conditions in each adsorption test. However, it is possible to see (**Table 5**) that the k_1 obtained from our systems is comparable [41] or even higher [42] than those values reported in recent studies using adsorbents containing silica - but lower than that of the montmorillonite clay [44]. Similarly, the k_2 (Ci = 400 ppm) herein obtained is comparable to the value found for fumed silica, but lower than those for A1MCM-41 and montmorillonite clay.

Table 5: Comparison of kinetic constants with materials containing silica.

Adsorbent	C_i (ppm)	k_1 (min^{-1})	k_2 (g/mg.min)	pH	T (°C)	Reference
Mesoporous silica–titania	67	0.0095	n.d.	n.d.	25	[41]
AlMCM-41	3.83	0.0035	0.0845	n.d.	25	[42]
Silica-fumed	9.58	n.d	0.002	4.73	20	[43]
Na montmorillonite clay	100	0.0454	0.028	7.0	30	[44]

Transportation of the dyes from the solution phase into the pores of the adsorbent may also be considered as the rate controlling stage in batch experiments. Regression coefficient values

obtained from Webber–Morris model (**Figure 4**) indicate a process controlled only by intraparticle diffusion. Since the plot did not pass through the origin, intraparticle diffusion was not the only rate-limiting step. The values of the intra-particle diffusion model constants are shown in **Table 6**, in which the system with initial concentration of 1000 mg/L showed a constant of diffusion 3-fold higher than the system with initial concentration of 100 mg/L of RhB. Moreover, the boundary layer effect is more pronounced (ca. 19-fold higher) for the former system. This suggests that for the later one (100 ppm), the surface diffusion plays a minor role as the rate-limiting step in the overall sorption process.

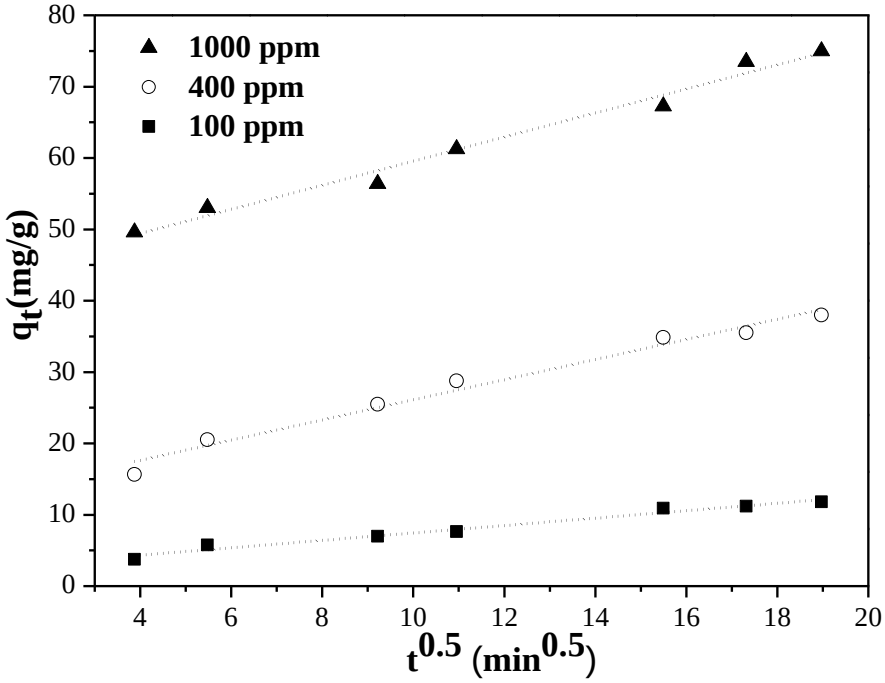

Figure 4: Test of intra-particle diffusion model for 100 (r^2= 0.98), 400 (r^2= 0.97) and 1000 (r^2= 0.98) ppm of RhB for the system 15A0.

Table 6: Estimated values for intra particle diffusion (k_d), constant C_1 and equilibrium adsorption constant (k_{ed}) for the system 15A0.

Dye (mg/L)	100	400	1000
kd (mg/g)	0.51	1.41	1.68
C_1 ($mg.g^{-1}.min^{-0.5}$)	2.25	11.9	46.6

Photocatalysis Evaluation

The photocatalytic performances of the studied systems are shown in **Table 7**. Regarding the systems with fixed mass (150 mg), it is possible to note that slower calcination time improved both adsorption and degradation when the template was added at t= 0 min (system 15C0). Thus, all other systems were investigated under slow heating rate during the calcination.

Table 7: Photocatalytic performance of the studied systems

	System	Adsorption (%)	Degradation (%)
m= 150 mg	15C0*	19.61 ± 0.98	32.21 ± 1.51
	15C0	25.72 ± 1.23	37.82 ± 1.48
	15C60	20.10 ± 1.20	19.80 ± 0.96
	15C90	23.80 ± 1.41	21.61 ± 0.85
	15C120	28.81 ± 1.22	21.93 ± 0.75
t= 0h	15C0	25.72 ± 1.23	37.82 ± 1.48
	30C0	25.22 ± 1.20	50.72 ± 1.89
	50C0	8.10 ± 0.05	6.25 ± 0.18

*calcined at higher heating rate (5 °C/min).

The addition of template at t= 0 min showed the best results for degradation. Comparing other systems with different time of template addition (15C60, 15C90 and 15C120) the

degradation performance is not affected, showing an average of 21.1%, which is ca. 1.8 times lower than the system 15C0. On the other hand, the adsorption value is decreased when the template is added 60 min later of initial sol-gel reaction (15C60), and then an increase in adsorption can be noted for longer addition time, reaching higher value than the system 15C0.

In our previous work [29], we have shown that the encapsulation of RhB prepared at equivalent conditions of 15C0 occurs preferentially inside the silica network instead of on the outermost external surface of silica. It may be reasonable to assume that addition of RhB at latter time to the sol-gel reaction might induce the prevalence of the dye on the surface. Thus, after extraction, an increase in number of sites may be formed. Consequently, this should explain the better adsorption performance for the systems 15C90 and 15C120. However, the degradation seems to be affected by this procedure, once it is not possible to notice difference of performance by these systems.

The higher photocatalytic activity of the system 15C0 can be explained by a combination of some textural aspects, such as presence of large pores and relatively large surface areas (see **Table 3**). The large pores and surface areas of this system may reduce the diffusion problems of the molecules through the cavities, improving both adsorption and the catalyst activity. In this sense, although no correlation could be observed between diameter of pores or degradation, it was found a correlation between area and degradation (r_{Sp} = 0.700). In addition, a strong indirect correlation between P and surface area (r_{Sp} = -0.800) suggests that higher S_{BET} values induce a higher degree of roughness (i.e., lower P values), and thus may enhance the degradation due the presence of rough silica domains in which pores are generated.

The effect of template amount added at a fixed time clearly shows that there is a threshold at which degradation is improved. The addition of 500 mg of template (50C0) greatly decreased

the degradation performance, while in the addition of 300 mg of template (30C0) the degradation was ca. of 34% higher if compared to the system 15C0. As above discussed, high amount of template could produce higher amount of encapsulated molecules within the silica network, and thus being difficult to efficiently remove the dye from the silica network, therefore affecting the aggregation of primary particles that, at some extent, negatively affects the photocatalytic activity.

Conclusions

The present study shows that the effect of the amount and the time of addition of a template (RhB) on the characteristics and catalyst activity of a photocatalyst prepared via an acid-catalyzed sol-gel route as well as an evaluation of adsorption kinetics. The kinetic data was well represented by pseudo-second-order kinetics and the values of kinetic constants are comparable to those of typical silica-based adsorbents. Regarding the systems with fixed mass, textural evidences suggest that large pores and large surface areas could explain the better results achieved by the system 15C0. In addition, the effect of template amount added at fixed time clearly shows that there is a threshold at which degradation is improved. As a general finding, we have shown that higher content of template may be more difficult to remove from the silica network and it could increase the aggregation of molecules, and thus affecting the photocatalytic performance.

Acknowledgements

This project was partially funded by the CNPq. C. Escobar is grateful for the grant provided by the CAPES. The authors wish to thank the LNLS (Project D11A-SAXS1-8691) for SAXS beamline measurements.

References

1. Bharathi KS, Ramesh ST (2013) Removal of dyes using agricultural waste as low-cost adsorbents: a review. Appl Water Sci 3 (4):773-790.

2. Gupta VK, Suhas (2009) Application of low-cost adsorbents for dye removal – A review. Journal of Environmental Management 90 (8):2313-2342.

3. Saratale RG, Saratale GD, Chang JS, Govindwar SP (2011) Bacterial decolorization and degradation of azo dyes: A review. Journal of the Taiwan Institute of Chemical Engineers 42 (1):138-157.

4. Shah MP, Patel KA, Nair SS, Darji AM (2013) Microbial Decolorization of Methyl Orange Dye by *Pseudomonas spp*. International Journal of Environmental Bioremediation & Biodegradation 1 (2):54-59.

5. Chen L, Xu S, Li J (2011) Recent advances in molecular imprinting technology: current status, challenges and highlighted applications. Chemical Society Reviews 40 (5):2922-2942.

6. Cheong WJ, Yang SH, Ali F (2013) Molecular imprinted polymers for separation science: A review of reviews. Journal of Separation Science 36 (3):609-628.

7. Cunliffe D, Kirby A, Alexander C (2005) Molecularly imprinted drug delivery systems. Advanced Drug Delivery Reviews 57 (12):1836-1853.

8. Liu X, Lv P, Yao G, Ma C, Huo P, Yan Y (2013) Microwave-assisted synthesis of selective degradation photocatalyst by surface molecular imprinting method for the degradation of tetracycline onto $ClTiO_2$. Chemical Engineering Journal 217 (0):398-406.

9. Morais EC, Correa GG, Brambilla R, dos Santos JHZ, Fisch AG (2013) Selective silica-based sorbent materials synthesized by molecular imprinting for adsorption of pharmaceuticals in aqueous matrices. Journal of Separation Science 36 (3):636-643.

10. Escobar C, dos Santos JHZ (2014) Effect of the Sol-Gel Route on the Textural Characteristics of Silica Imprinted With Rhodamine B. Journal of Separation Science 37 868-75.

11. de Escobar CC, Fisch A, dos Santos JHZ (2015) Effect of a Sol–Gel Route on the Preparation of Silica-Based Sorbent Materials Synthesized by Molecular Imprinting for the Adsorption of Dyes. Industrial & Engineering Chemistry Research 54 (1):254-262.

12. Santos WdJR, Santhiago M, Yoshida IVP, Kubota LT (2012) Electrochemical sensor based on imprinted sol–gel and nanomaterial for determination of caffeine. Sensors and Actuators B: Chemical 166–167 (0):739-745.

13. Dai C-m, Geissen S-U, Zhang Y-l, Zhang Y-j, Zhou X-f (2011) Selective removal of diclofenac from contaminated water using molecularly imprinted polymer microspheres. Environmental Pollution 159 (6):1660-1666.

14. Longo L, Scorrano S, Vasapollo G (2010) RNA nucleoside recognition by phthalocyanine-based molecularly imprinted polymers. J Polym Res 17 (5):683-687.

15. Mayes AG, Whitcombe MJ (2005) Synthetic strategies for the generation of molecularly imprinted organic polymers. Advanced Drug Delivery Reviews 57 (12):1742-1778.

16. Díaz-García ME, Laínño RB (2005) Molecular Imprinting in Sol-Gel Materials: Recent Developments and Applications. Microchim Acta 149 (1-2):19-36.

17. Walcarius A, Collinson MM (2009) Analytical chemistry with silica sol-gels: traditional routes to new materials for chemical analysis. Annu Rev Anal Chem (Palo Alto Calif) 2:121-143.

18. Lofgreen JE, Ozin GA (2014) Controlling morphology and porosity to improve performance of molecularly imprinted sol-gel silica. Chemical Society Reviews 43 (3):911-933.

19. Farrington K, Regan F (2009) Molecularly imprinted sol gel for ibuprofen: An analytical study of the factors influencing selectivity. Talanta 78 (3):653-659.

20. da Costa Silva RG, Augusto F (2006) Sol–gel molecular imprinted ormosil for solid-phase extraction of methylxanthines. Journal of Chromatography A 1114 (2):216-223. doi:http://dx.doi.org/10.1016/j.chroma.2006.03.073

21. Jiang X, Zhao C, Jiang N, Zhang H, Liu M (2008) Selective solid-phase extraction using molecular imprinted polymer for the analysis of diethylstilbestrol. Food Chemistry 108 (3):1061-1067.

22. Nakata K, Fujishima A (2012) TiO_2 photocatalysis: Design and applications. Journal of Photochemistry and Photobiology C: Photochemistry Reviews 13 (3):169-189.

23. Sharabi D, Paz Y (2010) Preferential photodegradation of contaminants by molecular imprinting on titanium dioxide. Applied Catalysis B: Environmental 95 (1–2):169-178.

24. Shaham-Waldmann N, Paz Y (2013) Modified Photocatalysts. In: Photocatalysis and Water Purification. Wiley-VCH Verlag GmbH & Co. KGaA, pp 103-143.

25. Shen X, Zhu L, Huang C, Tang H, Yu Z, Deng F (2009) Inorganic molecular imprinted titanium dioxide photocatalyst: synthesis, characterization and its application for efficient and selective degradation of phthalate esters. Journal of Materials Chemistry 19 (27):4843-4851.

26. Luo X, Deng F, Min L, Luo S, Guo B, Zeng G, Au C (2013) Facile One-Step Synthesis of Inorganic-Framework Molecularly Imprinted TiO_2/WO_3 Nanocomposite and Its Molecular Recognitive Photocatalytic Degradation of Target Contaminant. Environmental Science & Technology 47 (13):7404-7412.

27. de Escobar CC, Dallegrave A, Lasarin MA, Zimnoch dos Santos JH (2015) The sol–gel route effect on the preparation of molecularly imprinted silica-based materials for selective and competitive photocatalysis. Colloids and Surfaces A: Physicochemical and Engineering Aspects 486:96-105.

28. de Escobar CC, Lansarin MA, Zimnoch dos Santos JH (2016) Synthesis of molecularly imprinted photocatalysts containing low TiO_2 loading: Evaluation for the degradation of pharmaceuticals. Journal of Hazardous Materials 306:359-366.

29. de Escobar C, Dartora M, Campo L, Radtke C, Bayne J, Butler I, Lattuada R, dos Santos J (2014) The role of the sol–gel route on the interaction between rhodamine B and a silica matrix. Journal of Sol-Gel Science and Technology:1-13.

30. Ilavsky J, Jemian PR (2009) Irena: tool suite for modeling and analysis of small-angle scattering. Journal of Applied Crystallography 42 (2):347-353.

31. Kline S (2006) Reduction and analysis of SANS and USANS data using IGOR Pro. Journal of Applied Crystallography 39 (6):895-900.

32. Morais E, Correa G, Brambilla R, Livotto P, dos Santos J, Cardoso M (2012) Silica imprinted materials containing pharmaceuticals as a template: textural aspects. Journal of Sol-Gel Science and Technology 64 (2):324-334.

33. Brinker CJ, Scherer GW (1990) Sol–gel science: the physics and chemistry of sol–gel processing. Academic Press, New York

34. Beaucage G (1996) Small-Angle Scattering from Polymeric Mass Fractals of Arbitrary Mass-Fractal Dimension. Journal of Applied Crystallography 29 (2):134-146.

35. Lagergren, About the Theory of So-called Adsorption of Soluble Substances, Kungliga Svenska Vetenskapsakademiens Handlingar 1898, 24, 1 – 39.

36. Y. S. Ho, Adsorption of Heavy Metals from Waste Streams by Peat, Ph.D. Thesis, University of Birmingham, Birmingham, UK 1995.

37. W. J. Weber, J. C. Morris, Kinetics of Adsorption on Carbon from Solution, J. Sanit. Eng. Div. Am. Soc. Civ. Eng. 1963, 89 (SA2), 31 – 40.

38. Yu Q, Deng S, Yu G (2008) Selective removal of perfluorooctane sulfonate from aqueous solution using chitosan-based molecularly imprinted polymer adsorbents. Water Research 42 (12):3089-3097.

39. Guo W, Hu W, Pan J, Zhou H, Guan W, Wang X, Dai J, Xu L (2011) Selective adsorption and separation of BPA from aqueous solution using novel molecularly imprinted polymers based on kaolinite/Fe_3O_4 composites. Chemical Engineering Journal 171 (2):603-611.

40. Hajizadeh S, Xu C, Kirsebom H, Ye L, Mattiasson B (2013) Cryogelation of molecularly imprinted nanoparticles: a macroporous structure as affinity chromatography column for removal of β-blockers from complex samples. J Chromatogr A 1274:6-12.

41. Messina PV, Schulz PC (2006) Adsorption of reactive dyes on titania–silica mesoporous materials. Journal of Colloid and Interface Science 299 (1):305-320.

42. Eftekhari S, Habibi-Yangjeh A, Sohrabnezhad S (2010) Application of AlMCM-41 for competitive adsorption of methylene blue and rhodamine B: Thermodynamic and kinetic studies. Journal of Hazardous Materials 178 (1–3):349-355.

43. Wang Y, Chu W (2011) Adsorption and Removal of a Xanthene Dye from Aqueous Solution Using Two Solid Wastes as Adsorbents. Industrial & Engineering Chemistry Research 50 (14):8734-8741.

44. Selvam PP, Preethi S, Basakaralingam P, N.Thinakaran, Sivasamy A, Sivanesan S (2008) Removal of rhodamine B from aqueous solution by adsorption onto sodium montmorillonite. Journal of Hazardous Materials 155 (1–2):39-44.

4.7 Artigo 7

A ser submetido ao *Catalysis Science & Technology*.

Molecularly-imprinted photocatalysts containing low loading of Cu-doped and non-doped TiO_2 for selective photocatalysis of diclofenac

Cícero Coelho de Escobar[1], Yolice Patricia Moreno Ruiz[1], Lei Ye[2] and João Henrique Zimnoch dos Santos[3*]

[1]Departamento de Engenharia Química—Universidade Federal do Rio Grande do Sul

Rua Eng. Luis Englert s/n, 90040-040–Porto Alegre–RS–BRASIL

[2]Division of Pure and Applied Biochemistry, Lund University, Box 124, 221 00 Lund, Sweden

[3]Instituto de Química, Universidade Federal do Rio Grande do Sul, Av. Bento Gonçalves, 9500, Porto Alegre, CEP 91500-000, Brazil

Abstract

[*]Corresponding author. *Phone*: +55 51 3316 7238; fax: +55 51 3316 7304; and e-mail address: jhzds@iq.ufrgs.br (J.H.Z. dos Santos).

In order to improve the selectivity in the photocatalytic process, TiO_2 molecularly-imprinted photocatalysts were prepared containing low loadings (20 mg) of non-doped and Cu-doped P25, via organic precipitation method using diclofenac (DIC) as the template. The MIPs (MIP25 and MICuP25) exhibits a superior specific oriented recognition capability for selectivity degrading of DIC by comparing with fluoxetine (FLU) and paracetamol (PARA). Compared to the commercial sample of TiO_2, the average value of the coefficient of selectivity for photocatalysis degradation is estimated of ca. 2.8, which suggest that the presence of three-dimensional cavities designed by molecularly imprinted is the major reason to this higher efficiency. After 06 cycles under UV-light, the system MIP25 showed an imprinting factor ca. 2.5. In addition, the morphology and structure of the organic MIP are preserved after several cycles. The reported findings suggest that MIPs such herein studied can be a good candidate for selective photocatalysis degradation according to practical requirements.

Keywords: Molecularly imprinting / Selective photocatalysis / doped-P25 / Diclofenac

Introduction

During recent years, legislation has become increasingly restrictive, especially with respect to the preservation of surface and groundwater [Ranade et al, 2014]. Among the compounds of concern there are the so-called emerging contaminants, which encompass pharmaceuticals and personal steroids, care products, pesticides, surfactants, and dyes [García et al, 2013; Halden, 2015]. These coumpounds possess high persistence and low biodegradability [Mompelat et al. 2009]. As consequence, pharmaceuticals and their metabolites have increasingly been found in the various water bodies, including surface water and wastewater treatment plants effluents.

Recent reviews have indicated the ubiquitous presence of several classes of pharmaceutical compounds, such analgesics, anti-inflammatories, hormones, preservatives and endocrine disruptors [Kasprzyk-Hodern et al, 2008; Kostich et al, 2014; Halden, 2015]. These compounds are of great concern because of their potential impact even at low concentration levels on human health and the environment [Letzel et al., 2009]. Diclofenac (DIC) is one of the most widely available non-steroidal anti-inflammatory drugs, and widely used to reduce inflammation and as an analgesic in conditions such as in arthritis or acute injury. Estimations have shown that 15% of DIC is excreted unchanged after consumption [Landsdorp, 1990]. It still is one of the most frequently detected pharmaceuticals in the water environment [Andreozzi et al, 2003; Andrade et al, 2014], and has been detected in influents and effluents from water treatment plants at concentrations up to mg/L level [Mompelat et al., 2009; Scheurell et al., 2009]. Conventional wastewater treatment systems do not efficiently remove DIC [Yu et al, 2013], and thus it is necessary to develop methods to effectively remove DIC in the aquatic environment.

Advanced oxidation processes (AOPs) are known methods for pollutant degradation that involve the mineralization of a wide variety of organic contaminants. In these cases, the conversion of the molecules to their highest possible oxidation state and finally to water, carbon dioxide, oxidized inorganic anions and/or other molecules is required for complete removal.

Among the AOPs, heterogeneous photocatalysis using TiO_2 is one of the most promising strategies for use with emerging contaminants. This method exhibits several advantages, such as low cost, low toxicity and chemical stability [Nakata, 2012]. Recently, several works have explore the viability to employ photocatalytic degradation of DIC [Alchilleos et al, 2010; Rizzo et al, 2009; Andrade et al, 2014; Escobar et al, 2015]. However, a serious shortcoming in heterogeneous photocatalytic oxidation is its low selectivity to target contaminants, which cannot differentiate

high toxic target pollutant from other low toxic organic pollutants [Sharabi & Paz, 2010; Lu et al, 2014]. This characteristic is a disadvantage because mixtures derived from effluent streams may contain highly toxic organic pollutants (normally nonbiodegradable) that coexist with less toxic and biodegradable material. In many cases, the former is present in lower concentrations, and the latter is a major component [Sharabi & Paz, 2010; Shaham-Waldmannm & Paz, 2013]. Notwithstanding, the preferential degradation of the most toxic materials is desirable.

In order to overcome these drawbacks, molecularly imprinting (MI) technique can be introduced. MI is a promising technique for creating a template with a specific molecular recognition [Vasapollo et al, 2011]. This technique can be carried out in an organic or inorganic matrix due to the presence of a template molecule during the formation of the three-dimensional polymer [Whitcombe, et al 2014; Lofgreen et al, 2014]. Although there are some reports showing the feasibility of imprinting compounds like DIC [Noee et al, 2012; Dai et al, 2011; Duan et al, 2013; Sun et al, 2008], the combination of photocatalyts containing MI sites for pharmaceuticals molecules is an emerging field [Lu et al, 2014; Escobar et al, 2015].

There are others intrinsic drawbacks of pure TiO_2 that limits its applications, such as the difficulty to recycle [Shan et al, 2010] and its limitation for absorbing only in the UV light spectrum due to its large bandgap of approximately 3.2 eV [Banerjee et al, 2014] which limits its use for solar light harvesting. In order to improve the visible-light-active photocatalytic efficiency and inhibit charge recombination, several research groups have doped the TiO_2 with compounds capable to decrease band gap energy and thus effectively activate by visible light. In this sense, doping with non-noble metals has been increasingly studied [Akpan, 2010; Wang et al, 2014; Kerkez-Kuyumcu et al, 2015]. Among these metals, Cu-doped TiO_2 has been found to be a good modifier for both UV and visible-light responsive [Lalitha et al, 2010; Chu and Zheng et al, 2011;

López et al, 2009; Kerkez-Kuyumcu, 2015; Xu and Liang, 2008; Sorolla et al, 2012; Khalid et al, 2013; Huang et al, 2009]. In a recent comparative study with different metals (Cu, Ni, Co, Fe, Mn and Cr) [Kerkez-Kuyumcu, 2015], the authors reported that Cu/TiO_2 sample exhibited the highest photocatalytic activity under visible light owing to the low band gap energy and delayed electron-hole recombination.

Some papers have reported degradation of DIC using a large range of TiO_2 concentration, typically ranging from 200 to 1000 mg/L [Achilleos et al, 2010; Rizzo et al, 2009; Calza et al, 2006; Hartmann et al, 2008; Madhavan et al, 2010]. However, the presence of specific cavities can be explored to concentrate the desired molecule before the photodegradation, and thus lower concentration of TiO_2 might be used (Escobar et al, 2016). For these reasons, and the above drawbacks mentioned, in this paper, a composite of TiO_2 and MI organic polymer was prepared via precipitation method containing a low loading of TiO_2 (fixed at 20 mg and a typical concentration estimated of 44 mg/L in each catalytic essay). Our main goal is to investigate the enhancement of selectivity of the photocatalyst compared to that of a commercial sample (Degussa P25) due the presence of specific cavities. In addition, a composite containing Cu-doped TiO_2 was investigated. To our knowledge, Cu-doped TiO_2 combined with organic MI has not yet been reported.

EXPERIMENTAL SECTION

Materials and methods

Methacrylic acid (MAA, 98.5%) and azobisisobutyronitrile (AIBN, 98%) were purchased from Merck (Darmstadt, Germany). AIBN was recrystallized from methanol before use.

Fluoxetine (FLU) (Multilab) and paracetamol (PARA) (Multilab), glucose (Merck), hydrated copper (II) acetate (Janssen Chimica) and titanium dioxide (TiO_2, P25-Degussa) were used as received. Diclofenac sodium (DIC) (Multilab) and DFC were extracted into chloroform from an acidic solution in order to obtain its acid form. All the aqueous solutions were prepared in deionized water.

Preparation of doped-TiO_2

A Cu_2O doped-TiO_2 was prepared by an alcohol-aqueous based chemical precipitation method as described elsewhere [Huang et al., 2009]. A calculated amount of copper acetate was dissolved in 100 mL of ethanol to form a deep green solution and stirred for 30 min. To this solution sufficient TiO_2 (P25-Degussa) amount was added such that the weight percentage was 50/50 CuO_2:TiO_2 and the solution was sonicated (Branson 3200) to achieve a uniform suspension. Then, 100 mL glucose aqueous solution (0.2 M) as a reducing agent was dropwisely added to the solution heated at 60°C. Whereafter, 120 mL NaOH solution (0.3 M) dissolved in 70 mL ethanol and 50 mL water added dropwise, producing some yellow precipitates. The precipitates were then separated from the suspension by centrifugation (3500 rpm) (Awel MF 48R) for 20 min, and then washed for three times with ethanol and water to remove residual acetate, glucose and NaOH. The final product was then dried in vacuum overnight.

Preparation of the imprinted photocatalysts

Molecularly imprinted polymer photocatalyst (MIP25) was synthesized as follows. The template molecule, diclofenac (0.53 mmol), was dissolved in 40 mL of acetonitrile in a 150 mm × 25 mm borosilicate glass tube equipped with a screw cap. Methacrylic acid (1.31 mmol), trimethylolpropane trimethacrylate (2.02 mmol), azobisisobutyronitrile (28 mg) and titanium dioxide (20 mg) were then added. To get a good dispersion of P25, the solution was put in ultrassond bath for 10 min. Then, the solution was purged with a gentle flow of nitrogen for 5 min and sealed. Polymerization was carried out by rotating the borosilicate glass tube horizontally in a Stovall HO-10 Hybridization Oven (Greensboro, NC, USA) at a speed of 20 rpm, at 60 °C for 24 h. After polymerization, the polymer particles were collected by centrifugation. The template was removed by washing with methanol containing 10% acetic acid (v/v), until no template could be detected from the washing solvent using UV spectrometric measurement. The polymer particles were finally washed with acetone and dried in a vacuum chamber.

For the preparation of molecularly imprinted polymer photocatalyst consist of doped-TiO_2 (MIPCuP25), the same procedure was used. In this case, the doped-TiO_2 was added instead of non-doped TiO_2. As control systems, two non-imprinted polymers were synthesized under the same condition except that no template was added in the reaction: One adding P25 (NIP25) and other without P25 (NIP). Similarly, a control system containing doped-TiO_2 (NICuP25) was also synthesized.

Adsorption experiments

For adsorption capacity measurement, 33 mg of photocatalyst was added into 50 mL of a solution of DIC (0.062 mmol/L) under room temperature. Aliquots were collected with a syringe at regular interval. Then, the samples were sedimented by centrifugation at 12,000 rpm (Biofuge) for 15 min. The concentration was determined by UV-Vis molecular absorption spectroscopy using a DU 800 spectrophotometer (Beckman Coulter) at 274 nm. The experiments lasted for 2h and were performed in triplicates.

Photocatalyst tests

In a typical degradation experiment, 50 mL of DIC (0.062 mmol/L) was added to 33 mg of the photocatalyst in a bath reactor under flowing air (3 mL/min) under room temperature. The results of the photocatalytic tests were assessed at two stages under magnetic agitation (ca. 400 rpm) as follows: (i) dark stage, which consist of one hour with the lamp off (initial adsorption) and (ii) one hour with the lamp on (degradation). An ultraviolet lamp was used (366 nm, Sylvania 8W Blacklight Blue Fluorescent). The tests were carried out at the natural pH of the drugs.

The samples were collected with a syringe and stored in Eppendorf tubes and protected from light. For the catalyst separation, the samples were centrifuged for 20 min at 12,000 rpm. The final concentration was determined by UV-Vis molecular absorption spectroscopy using a DU 800 spectrophotometer (Beckman Coulter) at 274 for DIC. Photolysis tests were also performed to determine the percentage of drug degradation due to UV light exposure in the absence of the photocatalyst. The adsorption and the degradation were estimated from the calibration curve. All of the experiments were performed in triplicate. The adsorption and degradation were calculated by using the following equation:

$$Ads/Degr = \left(\frac{Ci - C_f}{C_i}\right) \times 100\% \quad (1)$$

(C_i: initial concentration; C_f: final concentration after adsorption/degradation; For degradation, C_i is the normalized initial concentration after 1h of dark-stage).

Selective experiment

To assess the selectivity, separated experiments of photodegradation of FLU and PARA were carried in accordance with above photochatalysis activity experiment (drug concentration of 0.062 mmol/L and mass of photocatalyst of 33 mg). The final concentration was determined by UV-Vis molecular absorption spectroscopy at 242 and 225 nm for PARA and FLU, respectively. The adsorption and the degradation were estimated from the calibration curves for each drug. The coefficient of selectivity ($k_{selectivity}$) was calculated using the following equations.

For the imprinted systems (MIP25 and MIPCuP25):

$$k_{imprinted} = \frac{Ads/Degr_{DIC}}{Ads/Degr_{FLU/PARA}} \quad (2)$$

For other photocatalysts (NIP25, NIPCuP25, P25 and CuP25):

$$k_{comparison} = \frac{Ads/Degr_{DIC}}{Ads/Degr_{FLU/PARA}} \quad (3)$$

$$k_{selectivity} = \frac{k_{imprinted}}{k_{comparison}} \quad (4)$$

Photochemical stability of MIP25

To further evaluate the stability of the system MIP25, several cycles were conducted. The experiments were done in accordance to the above photocatalyst activity experiments. At the end of each cycle, the samples were centrifuged for 15 minutes at 3,500 rpm to remove the supernatant. During the multiple cycles, regeneration was carried out to remove the template (similar to the above described) from the imprinted sites. For comparison reasons, similar experiments were done with the system NIP25. Then, the relative effect of the sample pairs with (MI) and non-imprinting (NI) could be assessed. For each cycle, the imprinting factor (IF) was estimated by using the following equation:

$$IF = \frac{C^{MIP25}}{C^{NIP25}} \quad (5)$$

The IF parameter was calculated for the adsorption (IF_{ads}) and degradation steps (IF_{degr}). Thus, C is the final concentration after dark-stage or UV-light stage. The value of IF was calculated considering the mean of the triplicates for each cycle.

Catalyst Characterization

FTIR analysis was carried out on a Nicolet iS5 FT-IR Spectrophotometer (Thermo Scientific). The dry particles were transferred onto the sample plate of the FTIR instrument and directly analysed. All spectra were collected at room temperature in the 4000 cm^{-1} to 500 cm^{-1} region using 16 scan.

Scanning electron microscopy (SEM) analysis was carried out using SEM LEO 1560 microscope (Zeiss, Oberkochen) operated at a voltage of 10 kV. The samples were previously deposited on a carbon tape and then sputtered with a thin layer of conductive gold.

The specific surface area was determined by the Brunauer-Emmett-Teller (BET) method at -196 °C, in the partial pressure range of $0.2 < P/P_0 < 0.9$. Prior to each measurement, samples were preheated at 110°C for 14 h under vacuum. The total pore volume was obtained from single-point desorption at $P/P_0 = 0.967$. The pore diameter was determined by the Barret-Joyner-Halenda (BJH) method.

Thermogravimetric analysis (TGA) was performed on a SDT Q600 thermal analyzer Q20 (TA Instruments) at a scanning rate of 20 C/min from 25 to 800 °C.

RESULTS AND DISCUSSION

Characterization

The specific surface area and pore characteristics of the studied photocatalyst are shown in **Table 1**. For the sake of clarity, a brief description of each system is also shown. The system containing non-extracted template molecules (NEP) showed a value of surface area of 19.2 and 4-

fold higher than that of NIP25 or NIP, respectively, thus indicating that the presence of the template perturbs the system and occludes the pores.

Comparing the system NEP with MIP25, it can be seen an increasing in surface area of 61% for the latter. This result indicates that DIC molecules were removed from the polymer matrix. The surface area increased after extraction because the pores, which were previously occupied by template molecules, became free and facilitated nitrogen adsorption. In this sense, increased surface area after the extraction process can be attributed to cavity formation, forming an imprinted material. Similar results are found in the literature for MIPs based on silica matrices [Morais et al 2012; Escobar et al 2014]. In addition, the higher surface area in the imprinted polymers (MIP25 and MICuP25) compared to the NIP and NIP25 indicates formation of more binding sites created during the imprinting process. As reported in the recent works, this finding is consistent with the reported results showing that MIPs tend to have higher surface area than that of corresponding NIPs [Kareuhanon et al, 2009; Lu et al, 2015].

Table 1: Textural properties of the studied systems.

System	Specific surface area (m^2/g)	Pore volume (cm^3/g)	Pore diameter (Å)	Description
NEP	57.7	27.50	235.7	(DIC + monomer + P25)
MIP25	92.9	0.16	114.4	(extracted DIC+ monomer + P25)
MICuP25	21.0	0.05	119.0	(extracted DIC+ monomer + doped-P25)
NIP25	3.0	0.01	315.6	(monomer + P25)
NIP	14.4	0.03	125.5	(monomer)
P25	54.0	0.07	48.0	---

NEP: Non Extracted Polymer; MIP25: Molecularly Imprinted Polymer with P25;MICuP25: Molecularly Imprinted Polymer with doped-P25; NIP25: Non-Imprinted Polymer with P25; NIP: Non-Imprinted Polymer

According to the IUPAC classification, all studied polymers showed macropores size [Rouquerol et al, 1994]. Both imprinted systems showed larger pore volume and smaller pore diameter than that of NI systems (NIP and NIP25). According to similar results in the literature, this finding indicates the presence of dimensional imprinted cavities in the MI systems [Xu et al 2011; Escobar et al 2016; Lu et al, 2016].

Fig. 1 shows a comparison of SEM images of systems NIP, NIP25 and MIP25. Comparing NI and NIP25, both showed spherical particles and the former showed a much more homogeneous distribution and lower diameter. The system containing imprinted cavities (MIP25) showed a rougher structure and agglomerated particles. Similar morphologies of MIP is found in polymer

based on MAA [Noee et al, 2012; Hassanzadeh-Khyyat 2011] and acrylamide [Arabzadeh et al 2015] as functional monomers (both synthetized by precipitation method). As discussed elsewhere [Beltran et al 2009], the particle diameter of the final product can be influenced by the nucleation stage of the reaction and the duration of the polymerization. The template addition could also influence the nucleation stage of a precipitation polymerization. In this sense, the presence of P25 and the extraction process can impinge the differences of morphologies observed among the samples.

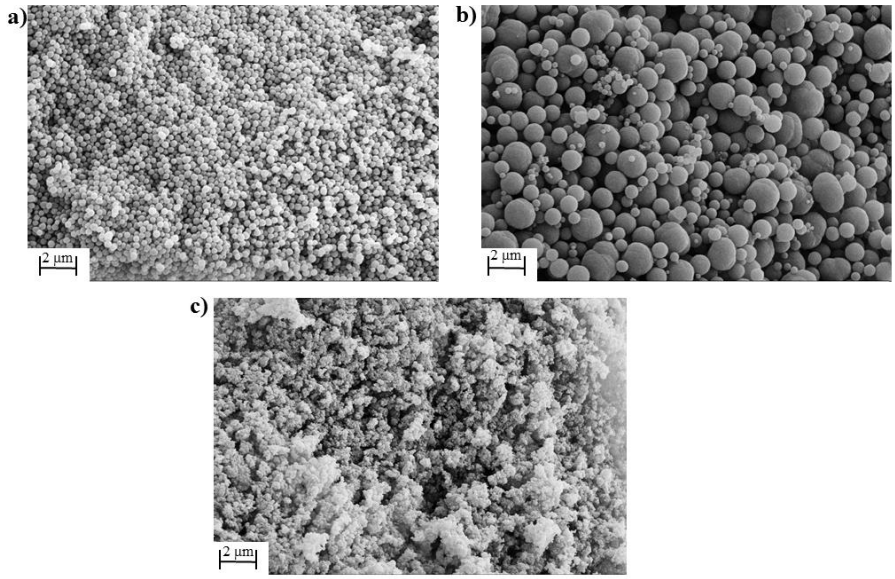

Figure 1: SEM images of systems NI (a), NIP25 (b) and MIP25 (c).

Fig. 2 showed the TGA patterns of MIP25 and MIPCuP25. For the system MIP25 the weight loss reached 93.4% at 755°C. This was attributed to the decomposition of the polymer layer, and thus the remaining mass was assigned to residual TiO_2. For the system MIPCuP25, it is noticeable a pronounceable weight loss at 90 and 275°C, probably due to the evaporation of water molecules. The remaining mass after 430°C was assigned to the thermal resistance of TiO_2 and

Cu_2O. The values of remaining mass obtained from MIP25 and MIPCuP25 (6.6% and 16.55%, respectively), were used to estimate the mass used in the experiments aimed to test the selectivity of the P25 and the doped-P25, which were 2.2 and 5.5 mg, respectively.

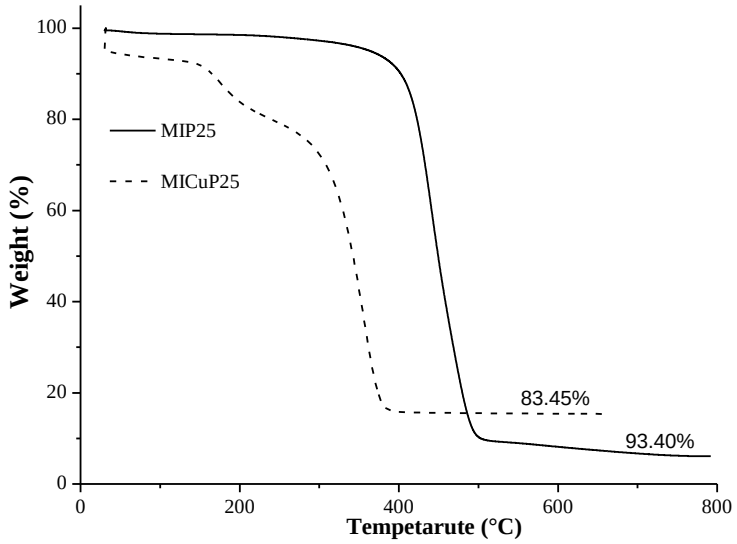

Figure 2: Thermogramms of MIP25 and MICuP25.

Adsorption experiment

In order to investigate the desired time for adsorption of DIC, the adsorption experiment was carried out. As shown in **Fig. 3**, it could be clearly seen that, before 30 min, the adsorption capacity (Q) significantly increased. After 60 min, there was no appreciable increasing in the value of Q for the MIP25, which is ca. of 8.6 mg/g (59% higher than the Q for NIP25). This result is consistent to the presence of three-dimensional imprinted cavities that possesses ability to recognize DIC. Thus, the following experiments of photocatalysis, 60 min was chosen as the time for dark-stage.

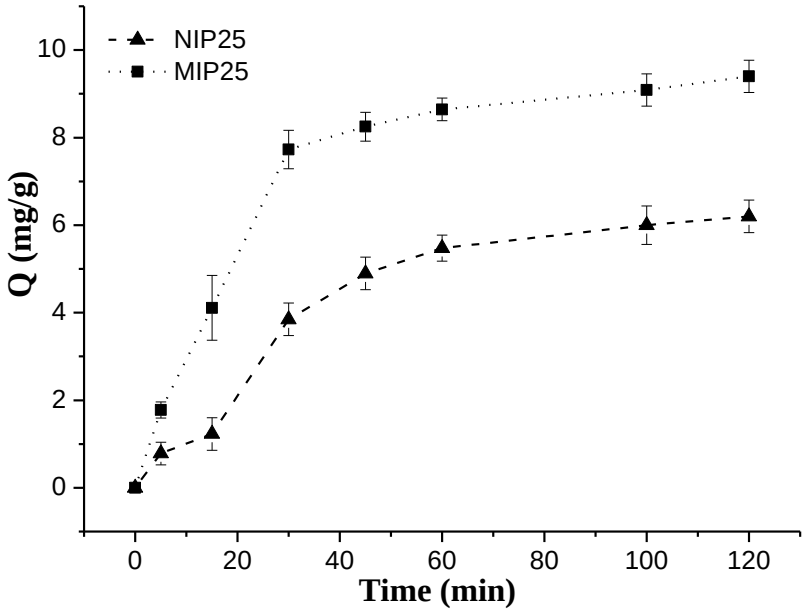

Figure 3: Adsorption isotherms of DIC on NIP25 and MIP25.

Comparison of different photocatalysts

The photocatalytic activities for degradation of DIC of the studied photocatalyst and the photolysis are shown in **Fig. 4**. After the UV light irradiation for 300 min, the degradation rate of MIP25 reached 62.5%, which was much higher than that of NIP25 (1.45-fold higher) and NIP (2.96-fold higher). In addition, MIP25 showed a degradation rate 7-fold higher than the photolysis. There were no imprinted cavities designed for the systems NIP25 and NIP. Therefore, this result suggests that the presence of three-dimensional imprinted cavities for the MIP25 may improve the degradation.

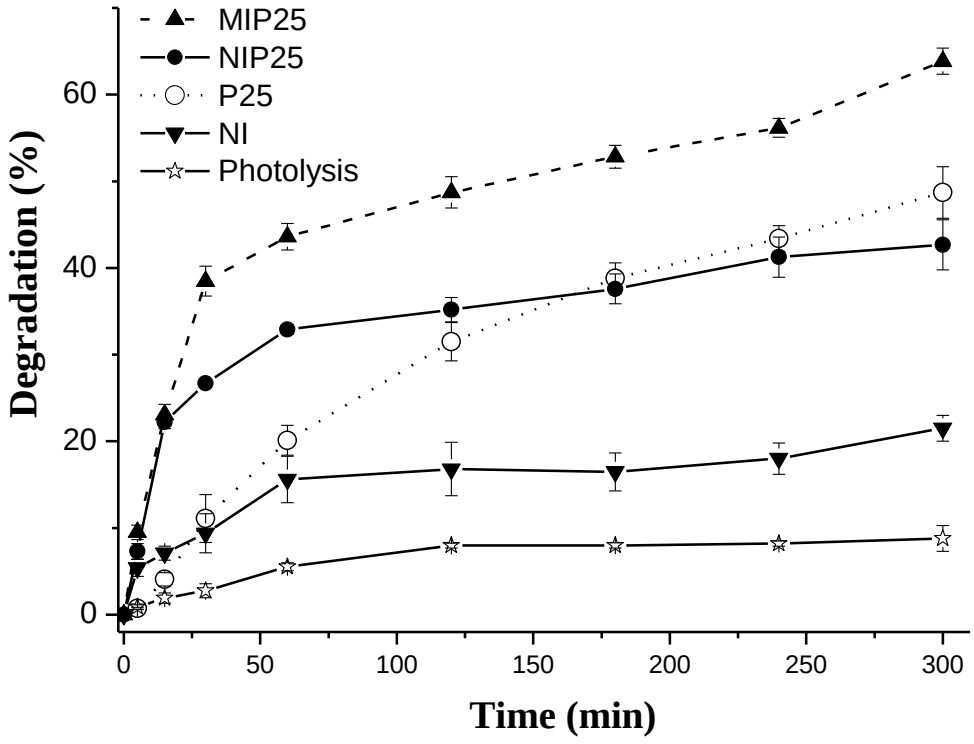

Figure 4: Degradation curves of DIC over different systems.

Selective experiments for non-doped systems

Fig. 5 shows the photocatalytic activity of MIP25, NIP25 and P25 for degradation of DIC, FLU and PARA. As shown in **Fig. 5a** (MIP25), after 120 min of reaction under UV irradiation, the degradation of DIC was higher than that of PARA and FLU. Comparing to the FLU, one can see that better results of degradation were achieved for this molecule for the first 5 min. However, it can be seen that more molecules of DIC were degraded for the longest reaction time. These results suggest that using DIC as a template molecule it is possible to create three-dimensional imprinted cavities of selective recognition. Once the structure of FLU at some degree is much similar to the DIC than the PARA (both FLU and DIC possess two aromatic rings) it is reasonable

to expect that the imprinted cavities could accommodate molecules of FLU, and thus increase the photocatalytic activity for this molecule. On the other hand, the structure of PARA is quite different compared to the template, which could not be recognized by the imprinted cavities.

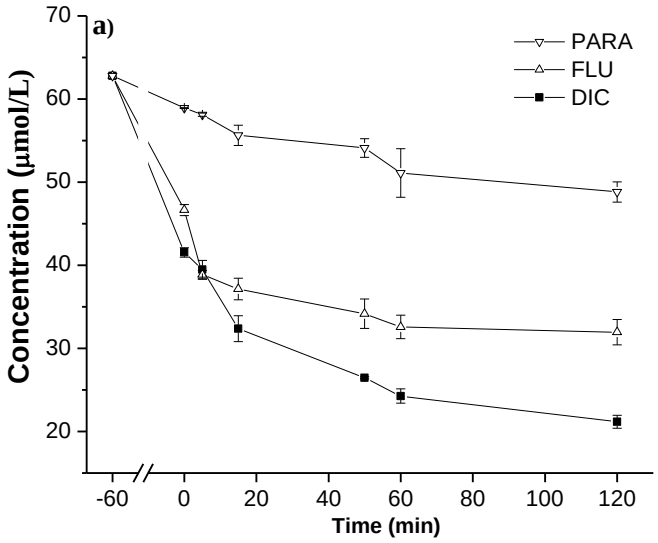

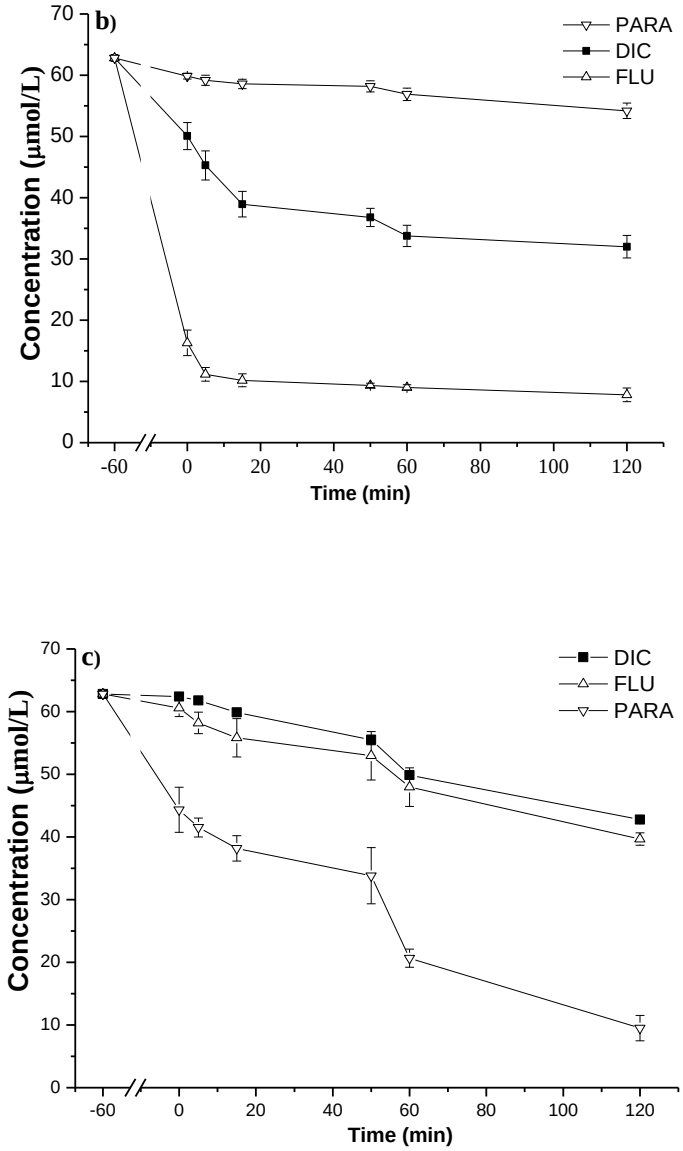

Figure 5: Photocatalytic activity of MIP25 (a), NIP25 (b) and P25 (c) for degradation of DIC, FLU and PARA.

It is interesting to compare the ratio of degradation obtained from photodegradation with that obtained from photolysis after 2h of reaction (herein as R_{photo}). Lower values suggest that the

photodegradation is comparable to the efficiency obtained from the photolysis. In this sense, control experiments have shown that R_{photo} was 2.62, 3.95 and 6.1 for PARA, FLU and DIC, respectively. This finding indicates a much better result obtained for the degradation of the target molecule, which was due the presence of imprinted sites.

The photocatalytic activities of NIP25 and P25 for degradation of DIC, FLU and PARA are shown in **Fig. 5 b and c**, respectively. It can be seen that the target molecule (DIC) had an intermediate performance of degradation in the case of system NIP25 and the worst performance in the case of P25. Actually, the degradation of FLU obtained by P25 is quite similar to that of DIC, while PARA was the most degradable molecule. This result may be attributed to the fact that PARA is rather a simple molecule if comparable to the other two, which may be easier to remove in the case of the system containing only TiO_2. Interestingly, the degradation of PARA was the worst obtained for the system NIP25. In this system, FLU was the molecule that had higher adsorption and degradation performance. Possibly, some charge interaction with surface of the polymer may be the reason of change of degradation performance for this system compared to the P25.

In addition, in order to further evaluate the selectivity of the MIP25, the coefficient of selectivity ($K_{selectivity}$) was calculated for adsorption and degradation step, and it is shown in **Table 2** and **3**. During the adsorption step (**Table 2**), the $K_{selectivity}$ of MIP25 relative to NIP25 and P25 was higher than the unity for both FLU and PARA. One exception is that there was no appreciable selectivity comparing to the adsorption of PARA for the system NIP25. As it can be seen, although there is an imprinting factor relative high against PARA ($K_{imprinted}$= 6.59) it turns out that the system NIP25 did show low value of adsorption (3.46 %). Thus, it has an impact on the $K_{comparison}$

that cause the noticed low selectivity effect. Despite this result, all other values of $\kappa_{selectivity}$ ranged from 4.03 to 329.5.

Table 2: Selectivity parameters for adsorption step (dark-stage) for different non-doped systems after 1h of mixture.

System	Adsorption (%)	$K_{imprinted}$	$K_{comparasion}$	$K_{selectivity}$
MIP25 (DIC)	32.58	-	-	-
MIP25 (FLU)	27.82	1.17	-	-
MIP25 (PARA)	4.94	6.59	-	-
NIP25 (DIC)	22.20	-	-	-
NIP25 (FLU)	74.8	-	0.29	4.03
NIP25 (PARA)	3.46	-	6.41	1.02
P25 (DIC)	0.73	-	-	-
P25 (FLU)	6.3	-	0.11	10.63
P25 (PARA)	28.4	-	0.02	329.5

The results of selectivity for the photodegradation step are shown in **Table 3**. As it can be seen, the $K_{selectivity}$ of MIP25 relative to NIP25 and P25 was higher than the unity for both FLU and PARA. Similar to the adsorption step, the exception was for the degradation of PARA with the system NIP25. On the other hand, the selectivity against PARA relative to the P25 also showed the better value. Although the values of coefficient are lower for degradation step compared to the adsorption step, the ability to recognize the template molecule persist, which is evident for the values of $K_{selectivity}$ ranging from 2.12 to 7.10.

The values obtained for the $K_{imprinted}$ suggest that the imprinted system (MIP25) possesses better ability to recognize FLU molecules, while does not easily recognize PARA molecules. This agrees to the previous discussion, in which one possible cause is that FLU is at some degree much similar to the template molecule (DIC). The results of selectivity obtained relative to the P25 seem to reflect the ability to better recognize FLU molecules, once the $K_{selectivity}$ is always lower than that of the PARA molecules.

Comparing with some recent studies [Achilleos et al, 2010; Rizzo et al, 2009. Bagal et al, 2014], the degradation of DIC was reported varying from 46 to 55% using concentration of TiO_2 from 200 to 250 mg/L (for a similar drug concentration herein investigated) and typically 2h of reaction under UV light. Thus, the system MIP25 system exhibited a degradation performance that was comparable to the typically reported concentration of photocatalyst.

Table 3: Selectivity parameters for photodegradation step (UV-light) for different non-doped systems after 2h of reaction.

System	Degradation (%)	$\square K_{imprinted}$	$\square K_{comparasion}$	$\square K_{selectivity}$
MIP25 (DIC)	48.72	-	-	-
MIP25 (FLU)	31.40	1.55	-	-
MIP25 (PARA)	17.13	2.84	-	-
NIP25 (DIC)	35.20	-	-	-
NIP25 (FLU)	48.0	-	0.73	2.12
NIP25 (PARA)	9.45	-	3.72	0.76
P25 (DIC)	31.49	-	-	-
P25 (FLU)	34.51	-	0.91	1.70
P25 (PARA)	78.3	-	0.40	7.10

Studies have shown (Calza et al, 2006; Achilleos et al, 2010; Kanakaraju et al, 2013) that, although the photocatalytic efficiency increased with the amount of TiO_2, high loadings (800 - 900 mg/L) showed no positive effect on the degradation probably due to scattering of light. In this sense, the imprinting technique could be designed to enhance not only selectivity but also the degradation performance of photocatalysts by using low concentration of TiO_2. From TGA results it is possible to estimate that the current MIP25 contains ca. of 44 mg/L of TiO_2 in each photocatalytic test, which represents at least 4.5-fold lower than that reported in the literature.

Therefore, this result indicates that the degradation performance of the MIP25 was primarily enhanced by the presence of cavities for the specific recognition of the studied molecule.

Taking together, all above results demonstrated that MIP25 possessed strong ability to selectively adsorb and photodegradate the template molecule. One important result is that -- for which pair of molecules--, the greater values of $K_{imprinted}$ compared to the $\square_{comparison}$ obtained from commercial sample of TiO_2 suggest that imprinted modifications can increase the selectivity of P25.

Selective experiments for doped systems

The selectivity of the system MICuP25, for both for adsorption and degradation step, is shown in **Tables 4** and **5**.

During the adsorption step (**Table 4**), the $K_{selectivity}$ of MICuP25 relative to NICuP25 and CuP25 was higher than unity for both FLU and PARA, ranging from 1.48 to 159.20. As a general trend (exception to the $K_{selectivity}$ of the system NICuP25 for PARA), the selectivity found to the doped-TiO_2 was lower (ca. 2.8-fold, considering the average of the systems) comparing to the non-doped systems.

Table 4: Selectivity parameters for adsorption step (dark-stage) for different doped systems after 1h of mixture.

System	Adsorption (%)	$\square K_{imprinted}$	$\square K_{comparasion}$	$\square K_{selectivity}$
MICuP25 (DIC)	70.07	-	-	-
MICuP25 (FLU)	56.72	1.23	-	-
MICu25 (PARA)	8.88	7.96	-	-
NICuP25 (DIC)	31.10	-	-	-
NICuP25 (FLU)	37.94	-	0.83	1.48
NICuP25 (PARA)	32.11	-	0.96	8.29
CuP25 (DIC)	0.33	-	-	-
CuP25 (FLU)	0.80	-	0.41	3.00
CuP25 (PARA)	6.60	-	0.05	159.20

The results of selectivity for the photodegradation step are shown in **Table 5**. Comparing the $K_{imprinted}$ between the doped and non-doped systems (**Tables 3** and **5**), it is possible to note that there is no difference in the case of FLU and a decrease is observed in the case of PARA, but the both are higher than unity. This indicates that the ability of recognize the target molecule is not compromised under the presence of copper. The coefficients of selectivity relative to NICuP25 for FLU and PARA were 3.97 and 2.95, respectively. These data indicated that $K_{selectivity}$ is mainly depended on the structure of MICuP25 that possessed three-dimensional imprinted cavities.

Table 5: Selectivity parameters for photodegradation step (UV-light) for different doped systems after 2h of reaction.

System	Degradation (%)	$K_{imprinted}$	$K_{comparasion}$	$K_{selectivity}$
MICuP25 (DIC)	45.72	-	-	-
MICuP25 (FLU)	29.38	1.55	-	-
MICuP25 (PARA)	23.04	1.98	-	-
NICuP25 (DIC)	10.92	-	-	-
NICuP25 (FLU)	27.97	-	0.39	3.97
NICuP25 (PARA)	16.1	-	0.67	2.95
CuP25 (DIC)	17.62	-	-	-
CuP25 (FLU)	5.37	-	3.28	0.47
CuP25 (PARA)	17.60	-	1.00	1.98

Comparing the systems CuP25 and P25, the value of $K_{comparision}$ is higher to the former (3.6 and 2.5-fold, for FLU and PARA, respectively). This suggests that the addition of copper could influence preferential degradation of DIC. In the case of FLU, due to the more similarity with the template molecule, it may cause the low value of the observed $K_{selectivity}$ (0.47). On the other hand, the molecules of PARA are not very suitable for imprinted sites, and thus the selectivity is preserved. As consequence, the $K_{selectivity}$ achieved for the doped-TiO_2 is lower than the non-doped one (3.6 and 3.5-fold, for FLU and PARA, respectively).

Photochemical stability of MIP25

The following experiments were carried out to evaluate the photochemical stability of MIP25. As shown in **Fig. 6**, although the system MIP25 undergone 6 cycles with a noticeable loss of adsorption, a little loss of photocatalytic efficiency was observed, indicating an excellent photochemical stability.

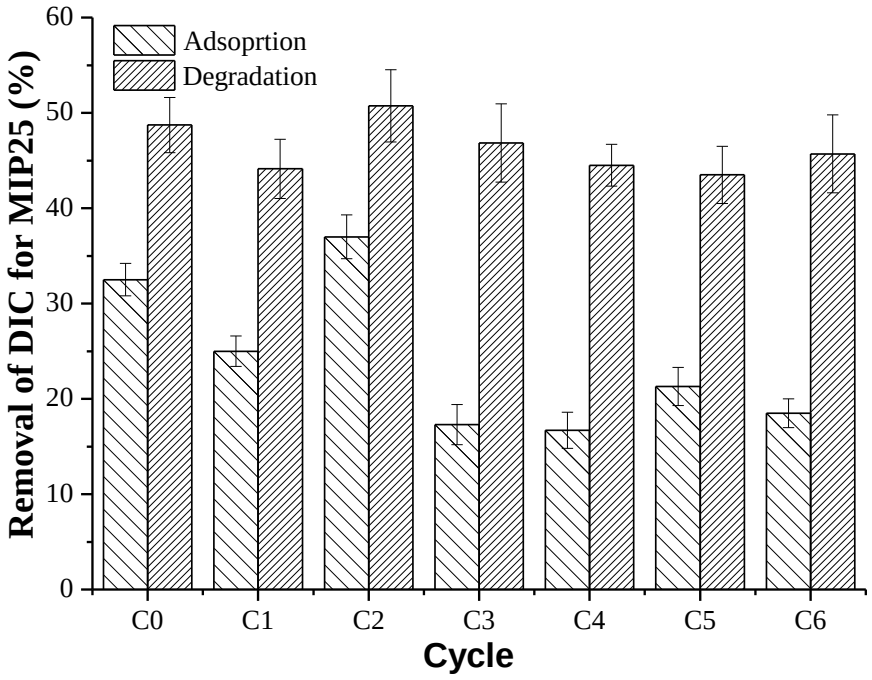

Figure 6: Several cycles of photocatalysis (DIC) for MIP25.

A comparison with the system NIP25 is shown in **Fig. 7**, and the results are presented in terms of imprinted factor (IF). As a general trend, if the IF for adsorption increased, the IF for degradation also increased (and vice-versa). The increase in IF up to cycle 4 is because the non-imprinted system (NIP25) showed a decrease of value for both adsorption and degradation over

the cycles. More importantly, the IF is higher than unity for all the cycles, indicating that the imprinted sites for the system MIP25 possess more suitable sites for molecular recognition.

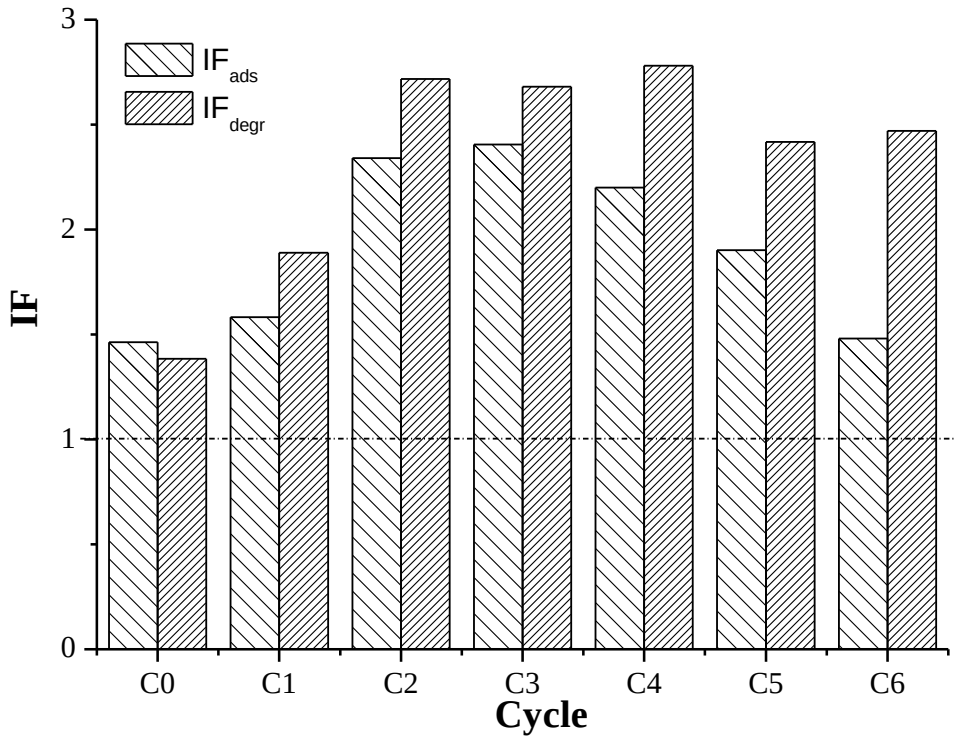

Figure 7: Imprinting factor under several cycles of photocatalysis (DIC) of system MIP25.

Considering that the samples consisted of polymer network, one question arises about the degradation of the polymer itself after several cycles of 2h of irradiation under UV light. **Fig. 8** showed that the FT-IR spectrum of the sample after 6 cycles was nearly identical to that of initial sample. Both spectra have shown some typical peaks found in the polymers based on the MAA and/or TRIM monomers [Lu et al, 2014; Liu et al, 2014] such as those at 1257, 1389 and 1725 cm^{-}

[1] attributed to stretching vibration of C-O, -O- and C=O, respectively. In addition, from **Fig. 9** it is possible to notice that the morphologies of the sample have no considerable change after 6 cycles. These results suggest that the morphology and the structure of the polymer, and possible the imprinted sites, are not damaged over several cycles of reaction under action of UV light.

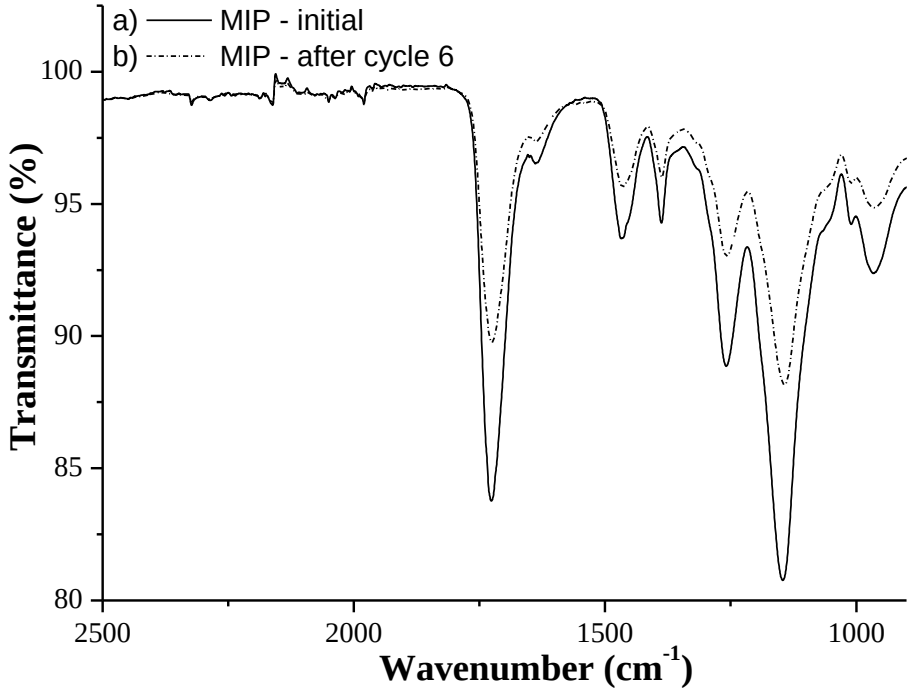

Figure 8: FT-IR spectra of system the MIP25 (a) before photocatalysis and (b) after 6 cycles of photocatalysis under UV-light.

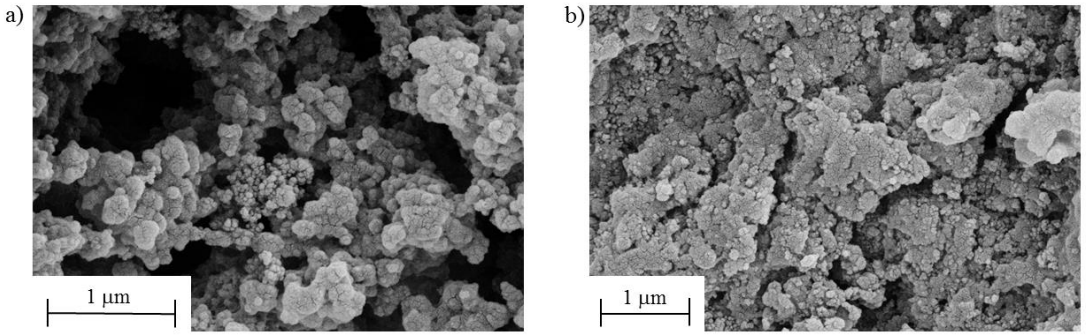

Figure 9: SEM images of system the MIP25 (a) before photocatalysis and (b) after 6 cycles of photocatalysis under UV-light.

Conclusions

In this work, TiO_2 imprinted photocatalysts were prepared, containing low loading of non-doped and Cu-doped P25, via organic precipitation method. The MIPs (MIP25 and MIPCuP25) exhibit a superior specific oriented recognition capability for selectivity degrading of DIC by comparing with FLU and PARA. As a general trend, molecules of PARA showed better results of removal, which reflects the better ability of MIPs to recognize molecules akin with the template. Compared to the commercial sample of TiO_2, the average value of coefficient of selectivity for photocatalysis degradation (both doped and non-doped one) is estimated of ca. 2.8, which suggest the presence of three-dimensional cavities designed by molecularly imprinted is the major reason to this higher efficiency. After 6 cycles under UV-light, the system MIP25 showed an imprinting factor of ca. 2.5. In addition, the morphology and structure of the organic MIP are preserved after several cycles. The reported findings suggest that MIPs such herein studied can be a good candidate for selective photocatalysis degradation according to practical requirements.

References

H. Yu, E. Nie, J. Xu, S. Yan, W. J. Cooper and W. Song, *Water Research*, 2013, **47**, 1909-1918.

Y.-h. Xu, D.-h. Liang, M.-l. Liu and D.-z. Liu, *Materials Research Bulletin*, 2008, **43**, 3474-3482.

W.-z. Xu, W. Zhou, P.-p. Xu, J.-m. Pan, X.-y. Wu and Y.-s. Yan, *Chemical Engineering Journal*, 2011, **172**, 191-198.

M. J. Whitcombe, N. Kirsch and I. A. Nicholls, *Journal of Molecular Recognition*, 2014, **27**, 297-401.

Y. Wang, R. Zhang, J. Li, L. Li and S. Lin, *Nanoscale Research Letters*, 2014, **9**, 46-46.

G. Vasapollo, R. D. Sole, L. Mergola, M. R. Lazzoi, A. Scardino, S. Scorrano and G. Mele, *International Journal of Molecular Sciences*, 2011, **12**, 5908-5945.

Z. Sun, W. Schüssler, M. Sengl, R. Niessner and D. Knopp, *Analytica Chimica Acta*, 2008, **620**, 73-81.

M. G. Sorolla Ii, M. L. Dalida, P. Khemthong and N. Grisdanurak, *Journal of Environmental Sciences*, 2012, **24**, 1125-1132.

D. Sharabi and Y. Paz, *Applied Catalysis B: Environmental*, 2010, **95**, 169-178.

A. Y. Shan, T. I. M. Ghazi and S. A. Rashid, *Applied Catalysis A: General*, 2010, **389**, 1-8.

B.

N. Shaham-Waldmann and Y. Paz, in *Photocatalysis and Water Purification*, Wiley-VCH Verlag

GmbH & Co. KGaA, 2013, DOI: 10.1002/9783527645404.ch5, pp. 103-143.

M. Scheurell, S. Franke, R. M. Shah and H. Hühnerfuss, *Chemosphere*, 2009, **77**, 870-876.

L. Rizzo, S. Meric, D. Kassinos, M. Guida, F. Russo and V. Belgiorno, *Water Research*, 2009, **43**, 979-988.

V. V. Ranade and V. M. Bhandari, in *Industrial Wastewater Treatment, Recycling and Reuse*, eds. V. V. Ranade and V. M. Bhandari, Butterworth-Heinemann, Oxford, 2014, DOI: http://dx.doi.org/10.1016/B978-0-08-099968-5.00014-3, pp. 521-535.

S. Ortiz de García, G. Pinto Pinto, P. García Encina and R. Irusta Mata, *Science of The Total Environment*, 2013, **444**, 451-465.

S. Noee, N. Salimraftar, M. Abdouss and G. Riazi, *Polymer International*, 2013, **62**, 1711-1716.

K. Nakata and A. Fujishima, *Journal of Photochemistry and Photobiology C: Photochemistry Reviews*, 2012, **13**, 169-189.

E. Morais, G. Correa, R. Brambilla, P. Livotto, J. dos Santos and M. Cardoso, *Journal of Sol-Gel Science and Technology*, 2012, **64**, 324-334.

S. Mompelat, B. Le Bot and O. Thomas, *Environment International*, 2009, **35**, 803-814.

J. Madhavan, P. S. S. Kumar, S. Anandan, M. Zhou, F. Grieser and M. Ashokkumar, *Chemosphere*, 2010, **80**, 747-752.

Z. Lu, M. He, L. Yang, Z. Ma, L. Yang, D. Wang, Y. Yan, W. Shi, Y. Liu and Z. Hua, *RSC Advances*, 2015, **5**, 47820-47829.

Z. Lu, F. Chen, M. He, M. Song, Z. Ma, W. Shi, Y. Yan, J. Lan, F. Li and P. Xiao, *Chemical Engineering Journal*, 2014, **249**, 15-26.

R. López, R. Gómez and M. E. Llanos, *Catalysis Today*, 2009, **148**, 103-108.

J. E. Lofgreen and G. A. Ozin, *Chemical Society Reviews*, 2014, **43**, 911-933.

X. Liu, D. Yu, Y. Yu and S. Ji, *Applied Surface Science*, 2014, **320**, 138-145.

M. Letzel, G. Metzner and T. Letzel, *Environment International*, 2009, **35**, 363-368.

K. Lalitha, G. Sadanandam, V. D. Kumari, M. Subrahmanyam, B. Sreedhar and N. Y. Hebalkar, *The Journal of Physical Chemistry C*, 2010, **114**, 22181-22189.

M. S. Kostich, A. L. Batt and J. M. Lazorchak, *Environmental Pollution*, 2014, **184**, 354-359.

N. R. Khalid, E. Ahmed, Z. Hong, M. Ahmad, Y. Zhang and S. Khalid, *Ceramics International*, 2013, **39**, 7107-7113.

Ö. Kerkez-Kuyumcu, E. Kibar, K. Dayıoğlu, F. Gedik, A. N. Akın and Ş. Özkara-Aydınoğlu, *Journal of Photochemistry and Photobiology A: Chemistry*, 2015, **311**, 176-185.

B. Kasprzyk-Hordern, R. M. Dinsdale and A. J. Guwy, *Water Research*, 2008, **42**, 3498-3518.

W. Kareuhanon, V. S. Lee, P. Nimmanpipug, C. Tayapiwatana and M. Pattarawarapan, *Chromatographia*, 2009, **70**, 1531-1537.

D. Kanakaraju, B. D. Glass and M. Oelgemöller, in *Green Materials for Energy, Products and Depollution*, eds. E. Lichtfouse, J. Schwarzbauer and D. Robert, Springer Netherlands, Dordrecht, 2013, DOI: 10.1007/978-94-007-6836-9_3, pp. 69-133.

L. Huang, F. Peng, H. Wang, H. Yu and Z. Li, *Catalysis Communications*, 2009, **10**, 1839-1843.

J. Hartmann, P. Bartels, U. Mau, M. Witter, W. v. Tümpling, J. Hofmann and E. Nietzschmann, *Chemosphere*, 2008, **70**, 453-461.

R. U. Halden, *Journal of Hazardous Materials*, 2015, **282**, 2-9.

Y.-P. Duan, C.-M. Dai, Y.-L. Zhang and C. Ling, *Analytica Chimica Acta*, 2013, **758**, 93-100.

C. C. de Escobar, M. A. Lansarin and J. H. Zimnoch dos Santos, *Journal of Hazardous Materials*, 2016, **306**, 359-366.

C. C. de Escobar, A. Dallegrave, M. A. Lasarin and J. H. Zimnoch dos Santos, *Colloids and Surfaces A: Physicochemical and Engineering Aspects*, 2015, **486**, 96-105.

C. de Coelho Escobar and J. H. Z. dos Santos, *Journal of Separation Science*, 2014, **37**, 868-875.

F. V. de Andrade, G. M. de Lima, R. Augusti, M. G. Coelho, Y. P. Q. Assis and I. R. M. Machado, *Journal of Environmental Chemical Engineering*, 2014, **2**, 2352-2358.

C.-m. Dai, S.-U. Geissen, Y.-l. Zhang, Y.-j. Zhang and X.-f. Zhou, *Environmental Pollution*, 2011, **159**, 1660-1666.

S. Chu, X. Zheng, F. Kong, G. Wu, L. Luo, Y. Guo, H. Liu, Y. Wang, H. Yu and Z. Zou, *Materials Chemistry and Physics*, 2011, **129**, 1184-1188.

P. Calza, V. A. Sakkas, C. Medana, C. Baiocchi, A. Dimou, E. Pelizzetti and T. Albanis, *Applied Catalysis B: Environmental*, 2006, **67**, 197-205.

A. Beltran, R. M. Marcé, P. A. G. Cormack and F. Borrull, *Journal of Chromatography A*, 2009,

1216, 2248-2253.

S. Banerjee, S. C. Pillai, P. Falaras, K. E. O'Shea, J. A. Byrne and D. D. Dionysiou, *The Journal of Physical Chemistry Letters*, 2014, **5**, 2543-2554.

M. V. Bagal and P. R. Gogate, *Ultrasonics Sonochemistry*, 2014, **21**, 1035-1043.

N. Arabzadeh, A. Khosravi, A. Mohammadi and N. M. Mahmoodi, *Desalination and Water Treatment*, 2016, **57**, 3142-3151.

R. Andreozzi, M. Raffaele and P. Nicklas, *Chemosphere*, 2003, **50**, 1319-1330.

U. G. Akpan and B. H. Hameed, *Applied Catalysis A: General*, 2010, **375**, 1-11.

A. Achilleos, E. Hapeshi, N. P. Xekoukoulotakis, D. Mantzavinos and D. Fatta-Kassinos, *Chemical Engineering Journal*, 2010, **161**, 53-59.

5. CONCLUSÕES E SUGESTÕES PARA TRABALHOS FUTUROS

Conforme apresentado nos capítulos precedentes, a proposta da tese consistiu em explorar estratégias de síntese de fotocatalisadores dotados com impressão molecular com aplicação em degradação seletiva de poluentes.

Os resultados apresentados na presente tese apontam para a viabilidade de síntese de materiais dotados de impressão molecular para contornar a baixa seletividade no processo de fotocatálise. Os resultados obtidos por análises texturais, estruturais e morfológicas sugerem que os fotocatalisadores seletivos são capazes de manter a eficiência fotocatalítica em pelo menos 50% acima da atividade inicial após vários ciclos de reação sob ação de luz ultravioleta. De maneira geral, considerando a matriz inorgância, a rota ácida (HCl como catalisador) apresentou os melhores resultados. O uso de $TiCl_4$ durante a síntese mostrou-se promissor, e os melhores resultados são alcançados com uma taxa de calcinação lenta (1°C/min). Tanto a matriz inorgânica como a orgânica são sensíveis ao tipo de molécula presente na solução; ou seja, moléculas estruturalmente mais parecidas com a molécula *template* devem ser mais privilegiadas para a interação com sítios de adsorção do que moléculas menos parecidas.

Na primeira parte da tese (**Artigo 1-2**), concluiu-se que os sistemas com maiores valores de área específica foram observados pela rota ácida (com uso de HCl como catalisador). Embora a rota não-hidrolítca tenha mostrado o maior aumento de área após a extração do solvente (933%, por ultrassom com metanol), o melhor desempenho quanto à seletividade na adsorção foi alcançado pela rota ácida, apresentando um fator de seletividade 47% maior que a rota não-hidrolítica (**Artigo 1**). Do ponto de vista estrutural, as evidências sugerem que a estrutura molecular do *template* rodamina B é conservada durante e após o processo de encapsulamento

independente da rota sol-gel (**Artigo 2**). O encapsulamento ocorreu preferencialmente no interior da rede de sílica nas rotas ácidas (com HCl), básica e *two-steps*; e o Ti (advindo do $TiCl_4$) é preferencialmente presente na superfície da sílica nas rotas ácida (ausente de HCl), básica e *two-steps* (**Artigo 2**).

A rota ácida (com HCl) resultou em um material que combinou a melhor distribuição do *template* no interior da rede de sílica com elevada área específica após o processo de extração -- resultando, dessa forma, em melhores resultados de adsorção seletiva (**Artigo 1-2**). Os resultados obtidos por análise de isotermas também convergem no sentido de revelarem que a rota ácida (com HCl) apresentou a maior capacidade de adsorção (997,9 mg/g para o modelo de isoterma de BET-modificada) dentre as diferentes rotas de síntese pelo método sol-gel (**Artigo 3**).

Comparado com a amostra comercial de TiO_2 (P25), conseguiu-se um aumento de seletividade e competitividade na fotodegradação da rodamina B de até 187% ($TiCl_4$ como precursor de TiO_2) e 290% (P25 como precursor de TiO_2), respectivamente. Testes de reuso do fotocatalisador (com etapa de regeneração) também foram conduzidos, mostrando que 60% da degradação inicial é mantida após cinco ciclos (**Artigo 4**).

O conjunto de resultados apontou a rota ácida (sol-gel) como a mais eficiente para o aumento da seletividade nos fotocatalisadores. Dessa forma, uma série de fármacos foram usados como *template* na síntese de fotocatalisadores contendo baixa massa de TiO_2 (P25) (entre 7,00 a 16,60 $mg.L^{-1}$ em cada teste fotocatalítico) via rota ácida por método sol-gel. Comparado com o P25, os fotocatalisadores com impressão molecular obtiveram um aumento na adsorção e degradação de até 751 e 427%, respectivamente. Após 7 ciclos de reuso, o fotocatalisador dotado de impressão molecular de diclofenaco manteve a eficiência fotocatalítica em aproximadamente 60% do valor original (**Artigo 5**).

O efeito da massa e do tempo de adição do *template* (rodamina B) na eficiência do fotocatalisador também foi estudado. Os resultados apontam que uma quantidade fixa de 150 mg adicionada no início da reação apresenta os melhores resultados em termos de fotodegradação, provavelmente devido às melhores propriedades texturais (maiores poros e área específica) que garantem a eficiência de adsorção advinda das cavidades de impressão molecular (**Artigo 6**).

Os fotocatalisadores em matriz orgânica mostraram capacidade de reconhecimento molecular superior em comparação a outros sistemas ausentes de impressão quando testados com outros fármacos (fluoxetina e paracetamol). Comparado com o material comercial de TiO_2 ausente de impressão (P25), o valor médio do coeficiente de seletividade dos sistemas dotados de impressão foi estimado em 2,8 – portanto sugerindo que a presença de cavidades tridimensionais é um dos principais fatores da seletividade observada. Após 6 ciclos de reações sob ação de luz ultravioleta, o fotocatalisador seletivo manteve sua estrutura e morfologia preservada (**Artigo 7**).

A combinação de técnicas de impressão molecular com fotocatalisadores visando aumentar a seletividade ainda é uma linha de pesquisa relativamente pouco explorada na literatura. Algumas das limitações que impedem o uso de processos fotocatalíticos aplicados em casos reais são a dificuldade do reuso e a baixa seletividade, e a presente tese teve como objetivo explorar soluções a eles. Dessa forma, algumas lacunas ainda persistem. Por exemplo, são escassos na literatura os trabalhos explorando a viabilidade de fotocatálise seletiva sob luz visível. Nesse sentido, os resultados da tese também abrem um caminho de potencialidade, já que os materiais dopados com cobre apresentaram resultados satisfatórios (não comprometem a seletividade) para futuras aplicação sob ação do espectro visível. Nesse contexto, uma possibilidade para futuros trabalhos é a comparação de alguns dos melhores dopantes reportados combinados com fotocatalisadores

seletivos. É possível que um fotocatalisador que contivesse um dopante não tão eficiente na luz visível, porém mais barato, possa ser beneficiado pela presença dos sítios de adsorção seletiva.

Outra limitação é a escassez de dados comparando a competitividade, ou seja, a interação dos sítios de impressão com a molécula alvo sob a presença de vários poluentes na mesma matriz aquosa. Outrossim, a síntese de materiais com múltiplos *templates* para aplicação em fotocatálise ainda não foram reportados na literatura. Além disso, o efeito de outras variáveis como o pH podem influenciar a remoção seletiva, e um controle sob este parâmetro pode resultar em melhores eficiências de degradação. Por fim, outras combinações podem ser exploradas, como o efeito da adição de aceptores de elétrons (por exemplo, H_2O_2), que embora já bem conhecidas na fotocatálise convencional ainda foi pouco estudada no contexto de fotocatálise seletiva.

Em suma, a presente tese alega que é possível delinear fotocatalisadores dotados de impressão molecular em matriz inorgânica ou orgânica visando à degradação seletiva de contaminantes emergentes contendo baixa concentração de TiO_2. Do ponto de vista prático, a tese mostrou resultados promissores para aplicação dos fotocatalisadores em vários ciclos sem perda apreciável da atividade e sem comprometer as cavidades de impressão molecular.

6. REFERÊNCIAS BIBLIOGRÁFICAS

ALEXANDER, C. *et al*. Molecular imprinting science and technology: a survey of the literature for the years up to and including 2003. **Journal of Molecular Recognition,** v. 19, n. 2, p. 106-180, 2006. ISSN 1099-1352. Disponível em: < http://dx.doi.org/10.1002/jmr.760 >.

ALIZADEH, T. Development of a molecularly imprinted polymer for pyridoxine using an ion-pair as template. **Analytica Chimica Acta,** v. 623, n. 1, p. 101-108, 2008. ISSN 0003-2670. Disponível em: < http://www.sciencedirect.com/science/article/pii/S0003267008010842 >.

AVNIR, D. Organic Chemistry within Ceramic Matrixes: Doped Sol-Gel Materials. **Accounts of Chemical Research,** v. 28, n. 8, p. 328-334, 1995/08/01 1995. ISSN 0001-4842. Disponível em: < http://dx.doi.org/10.1021/ar00056a002 >.

BALE, H. D.; SCHMIDT, P. W. Small-Angle X-Ray-Scattering Investigation of Submicroscopic Porosity with Fractal Properties. **Physical Review Letters,** v. 53, n. 6, p. 596-599, 1984. Disponível em: < http://link.aps.org/doi/10.1103/PhysRevLett.53.596 >.

BEAUCAGE, G. Approximations Leading to a Unified Exponential/Power-Law Approach to Small-Angle Scattering. **Journal of Applied Crystallography,** v. 28, n. 6, p. 717-728, 1995. ISSN 0021-8898. Disponível em: < http://dx.doi.org/10.1107/S0021889895005292 >.

BEAUCAGE, G. Small-Angle Scattering from Polymeric Mass Fractals of Arbitrary Mass-Fractal Dimension. **Journal of Applied Crystallography,** v. 29, n. 2, p. 134-146, 1996. ISSN 0021-8898. Disponível em: < http://dx.doi.org/10.1107/S0021889895011605 >.

BELTRAN, A. *et al*. Molecularly-imprinted polymers: useful sorbents for selective extractions. **TrAC Trends in Analytical Chemistry,** v. 29, n. 11, p. 1363-1375, 2010. ISSN 0165-9936. Disponível em: < http://www.sciencedirect.com/science/article/pii/S0165993610002529 >.

BRINKER, C. J.; SCHERER, G. W. **Sol-gel science - the physics chemistry of sol-gel processing**. San Diego: Academic Press Inc, 1990

BURLEIGH, M. C. *et al*. Enhanced ionic recognition by a functionalized mesoporous sol-gel. **Science and Technology,** v. 36, n. 15, p. 3395-3409, 2001/11/30 2001. ISSN 0149-6395. Disponível em: < http://www.tandfonline.com/doi/abs/10.1081/SS-100107910 >.

CARP, O.; HUISMAN, C. L.; RELLER, A. Photoinduced reactivity of titanium dioxide. **Progress in Solid State Chemistry,** v. 32, n. 1–2, p. 33-177, 2004. ISSN 0079-6786. Disponível em: < http://www.sciencedirect.com/science/article/pii/S0079678604000123 >.

CHATTERJEE, D.; DASGUPTA, S. Visible light induced photocatalytic degradation of organic pollutants. **Journal of Photochemistry and Photobiology C: Photochemistry Reviews,** v. 6, n. 2–3, p. 186-205, 2005. ISSN 1389-5567. Disponível em: < http://www.sciencedirect.com/science/article/pii/S1389556705000316 >.

CHEN, D. *et al*. Synthesis and photocatalytic performances of the TiO_2 pillared montmorillonite. **Journal of Hazardous Materials,** v. 235–236, n. 0, p. 186-193, 2012. ISSN 0304-3894. Disponível em: < http://www.sciencedirect.com/science/article/pii/S0304389412007698 >.

CHEN, L.; XU, S.; LI, J. Recent advances in molecular imprinting technology: current status, challenges and highlighted applications. **Chemical Society Reviews,** v. 40, n. 5, p. 2922-2942, 2011. ISSN 0306-0012. Disponível em: < http://dx.doi.org/10.1039/C0CS00084A >.

CHEONG, W. J.; YANG, S. H.; ALI, F. Molecular imprinted polymers for separation science: A review of reviews. **Journal of Separation Science,** v. 36, n. 3, p. 609-628, 2013. ISSN 1615-9314. Disponível em: < http://dx.doi.org/10.1002/jssc.201200784 >.

CHU, S. *et al.* Architecture of Cu_2O@TiO_2 core–shell heterojunction and photodegradation for 4-nitrophenol under simulated sunlight irradiation. **Materials Chemistry and Physics,** v. 129, n. 3, p. 1184-1188, 2011. ISSN 0254-0584. Disponível em: < http://www.sciencedirect.com/science/article/pii/S0254058411005153 >.

COLÓN, G. *et al*. Cu-doped TiO_2 systems with improved photocatalytic activity. **Applied Catalysis B: Environmental,** v. 67, n. 1–2, p. 41-51, 2006. ISSN 0926-3373. Disponível em: < http://www.sciencedirect.com/science/article/pii/S0926337306001081 >.

COLLINSON, M. M. Imprinted Functionalized Silica, **The supramolecular chemistry of organic-inorganic hybrid materials**, ed. K. Rurack and R. Martínez-Máñez, John Wiley & Sons, Hoboken. p. 581-598, 2010.

COWAN, A. J. *et al*. Water Splitting by Nanocrystalline TiO_2 in a Complete Photoelectrochemical Cell Exhibits Efficiencies Limited by Charge Recombination. **The Journal of Physical Chemistry C,** v. 114, n. 9, p. 4208-4214, 2010/03/11 2010. ISSN 1932-7447. Disponível em: < http://dx.doi.org/10.1021/jp909993w >.

DENG, F. *et al*. Sol-hydrothermal synthesis of inorganic-framework molecularly imprinted TiO_2/SiO_2 nanocomposite and its preferential photocatalytic degradation towards target contaminant. **Journal of Hazardous Materials,** v. 278, p. 108-115, 2014. ISSN 0304-3894. Disponível em: < http://www.sciencedirect.com/science/article/pii/S0304389414004439 >.

DÍAZ-GARCÍA, M. E.; LAÍNÑO, R. B. Molecular Imprinting in Sol-Gel Materials: Recent Developments and Applications. **Microchimica Acta,** v. 149, n. 1-2, p. 19-36, 2005/02/01 2005. ISSN 0026-3672. Disponível em: < http://dx.doi.org/10.1007/s00604-004-0274-7 >.

DONG, L. *et al*. Enhanced photocatalytic degradation properties of nitrogen-doped titania nanotube arrays. **Transactions of Nonferrous Metals Society of China,** v. 19, n. 6, p. 1583-1587, 2009. ISSN 1003-6326. Disponível em: < http://www.sciencedirect.com/science/article/pii/S1003632609600741 >.

DOODY, M. A. *et al*. Affinity and Mobility of Polyclonal Anti-Dansyl Antibodies Sequestered within Sol−Gel-Derived Biogels. **Chemistry of Materials,** v. 12, n. 4, p. 1142-1147, 2000/04/01 2000. ISSN 0897-4756. Disponível em: < http://dx.doi.org/10.1021/cm990782z >.

FALAH, M.; MACKENZIE, K. J. D. Synthesis and properties of novel photoactive composites of P25 titanium dioxide and copper (I) oxide with inorganic polymers. **Ceramics International,** v. 41, n. 10, Part A, p. 13702-13708, 2015. ISSN 0272-8842. Disponível em: < http://www.sciencedirect.com/science/article/pii/S0272884215015102 >.

FELTRIN, J. et al. Superfícies fotocatalíticas de titânia em substratos cerâmicos: Parte I: Síntese, estrutura e fotoatividade. **Cerâmica**, v. 59, p. 620-632, 2013. ISSN 0366-6913. Disponível em: < http://www.scielo.br/scielo.php?script=sci_arttext&pid=S0366-69132013000400020&nrm=iso >.

FUJII, Y.; MATSUTANI, K.; KIKUCHI, K. Formation of a specific co-ordination cavity for a chiral amino acid by template synthesis of a polymer Schiff base cobalt(III) complex. **Journal of the Chemical Society, Chemical Communications**, n. 7, p. 415-417, 1985. ISSN 0022-4936. Disponível em: < http://dx.doi.org/10.1039/C39850000415 >.

GAFFNEY, V. J. *et al.*, Análise de fármacos em águas por SPE-UPLC-ESI-MS/MS, **Química Nova**, v. 37, p. 138-149, 2014. Disponível em: < http://www.scielo.br/scielo.php?script=sci_arttext&pid=S0100-40422014000100023 >.

GLAZE, W. H.; KANG, J.-W.; CHAPIN, D. H. Chemistry of water treatment processes involving ozone, hydrogen peroxide and ultraviolet radiation. Ozone: Science and Engineering, 1987, 4. p.335-352.

GOGATE, P. R.; PANDIT, A. B. A review of imperative technologies for wastewater treatment I: oxidation technologies at ambient conditions. **Advances in Environmental Research,** v. 8, n.

3–4, p. 501-551, 2004. ISSN 1093-0191. Disponível em: < http://www.sciencedirect.com/science/article/pii/S1093019103000327 >.

GREEN, D. L. *et al*. Size, volume fraction, and nucleation of Stober silica nanoparticles. **Journal of Colloid and Interface Science,** v. 266, n. 2, p. 346-358, 2003. ISSN 0021-9797. Disponível em: < http://www.sciencedirect.com/science/article/pii/S0021979703006106 >.

HAJIZADEH, S. *et al*. Cryogelation of molecularly imprinted nanoparticles: a macroporous structure as affinity chromatography column for removal of β-blockers from complex samples. **Journal of chromatography. A,** v. 1274, p. 6-12, 2013/01// 2013. ISSN 0021-9673. Disponível em: < http://dx.doi.org/10.1016/j.chroma.2012.10.073 >.

HERRMANN, J.-M. Photocatalysis fundamentals revisited to avoid several misconceptions. **Applied Catalysis B: Environmental,** v. 99, n. 3–4, p. 461-468, 2010. ISSN 0926-3373. Disponível em: < http://www.sciencedirect.com/science/article/pii/S0926337310002110 >.

HUANG, C.; TU, Z.; SHEN, X. Molecularly imprinted photocatalyst with a structural analogue of template and its application. **Journal of Hazardous Materials,** v. 248–249, n. 0, p. 379-386, 2013. ISSN 0304-3894. Disponível em: < http://www.sciencedirect.com/science/article/pii/S0304389413000551 >.

HUANG, L. *et al*. Preparation and characterization of Cu_2O/TiO_2 nano–nano heterostructure photocatalysts. **Catalysis Communications,** v. 10, n. 14, p. 1839-1843, 2009. ISSN 1566-7367. Disponível em: < http://www.sciencedirect.com/science/article/pii/S1566736709002428 >.

IBHADON, A.; FITZPATRICK, P. Heterogeneous Photocatalysis: Recent Advances and Applications. **Catalysts,** v. 3, n. 1, p. 189-218, 2013. ISSN 2073-4344. Disponível em: < http://www.mdpi.com/2073-4344/3/1/189 >.

ILAVSKY, J.; JEMIAN, P. R. Irena: tool suite for modeling and analysis of small-angle scattering. **Journal of Applied Crystallography,** v. 42, n. 2, p. 347-353, 2009. ISSN 0021-8898. Disponível em: < http://dx.doi.org/10.1107/S0021889809002222 >.

JARDIM, W. F. *et al*. An integrated approach to evaluate emerging contaminants in drinking water. **Separation and Purification Technology,** v. 84, n. 0, p. 3-8, 2012. ISSN 1383-5866. Disponível em: < http://www.sciencedirect.com/science/article/pii/S1383586611003583 >.

KABIR, E. R.; RAHMAN, M. S.; RAHMAN, I. A review on endocrine disruptors and their possible impacts on human health. Environmental Toxicology and Pharmacology, v. 40, n. 1, p. 241-258, 2015. ISSN 1382-6689. Disponível em: <

http://www.sciencedirect.com/science/article/pii/S1382668915300120 >.

KAMRA, T. *et al*. Covalent immobilization of molecularly imprinted polymer nanoparticles using an epoxy silane. **Journal of Colloid and Interface Science,** v. 445, p. 277-284, 2015. ISSN 0021-9797. Disponível em: < http://www.sciencedirect.com/science/article/pii/S002197971401056X >.

KAMRA, T. *et al*. Covalent immobilization of molecularly imprinted polymer nanoparticles on a gold surface using carbodiimide coupling for chemical sensing. **Journal of Colloid and Interface Science,** v. 461, p. 1-8, 2016. ISSN 0021-9797. Disponível em: < http://www.sciencedirect.com/science/article/pii/S0021979715301806 >.

KERKEZ-KUYUMCU, Ö. *et al*. A comparative study for removal of different dyes over M/ TiO_2 (M = Cu, Ni, Co, Fe, Mn and Cr) photocatalysts under visible light irradiation. **Journal of Photochemistry and Photobiology A: Chemistry,** v. 311, p. 176-185, 2015. ISSN 1010-6030. Disponível em: < http://www.sciencedirect.com/science/article/pii/S1010603015002567 >.

KISCH, H.; MITORAJ, D. Preparative and Mechanistic Semiconductos Photocatalysis, in CRC **Handbook of Organic Photochemistry and Photobiology**, v. 1., 3° ed. W. Horspool, F. Lenci. Boca Raton, Florida, 2012.

KLINE, S. Reduction and analysis of SANS and USANS data using IGOR Pro. **Journal of Applied Crystallography,** v. 39, n. 6, p. 895-900, 2006. ISSN 0021-8898. Disponível em: < http://dx.doi.org/10.1107/S0021889806035059 >.

KONDRAKOV, A. O. *et al*. Roles of water and dissolved oxygen in photocatalytic generation of free OH radicals in aqueous TiO_2 suspensions: An isotope labeling study. **Applied Catalysis B: Environmental,** v. 182, p. 424-430, 2016. ISSN 0926-3373. Disponível em: < http://www.sciencedirect.com/science/article/pii/S092633731530165X >.

LAZAR, M. A.; DAOUD, W. A. Achieving selectivity in TiO_2-based photocatalysis. **RSC Advances,** v. 3, n. 13, p. 4130-4140, 2013. Disponível em: < http://dx.doi.org/10.1039/C2RA22665K >.

LEVI, G. Imprinting Chirality in Mesoporous Silica Structures, Advanced Topics in Crystallization, Prof. Yitzhak Mastai (Ed.), InTech, 2015. DOI: 10.5772/59620. Available from: http://www.intechopen.com/books/advanced-topics-in-crystallization/imprinting-chirality-in-mesoporous-silica-structures

LI, L.; LEI, J.; JI, T. Facile fabrication of p–n heterojunctions for Cu_2O submicroparticles deposited on anatase TiO_2 nanobelts. **Materials Research Bulletin,** v. 46, n. 11, p. 2084-2089, 2011. ISSN 0025-5408. Disponível em: < http://www.sciencedirect.com/science/article/pii/S0025540811002911 >.

LI, Z.-D. *et al*. Preparation and photocatalytic performance of magnetic Fe_3O_4@TiO_2 core–shell microspheres supported by silica aerogels from industrial fly ash. **Journal of Alloys and Compounds,** v. 659, p. 240-247, 2016. ISSN 0925-8388. Disponível em: < http://www.sciencedirect.com/science/article/pii/S092583881531553X >.

LIU, X. *et al*. Selective degradation of ciprofloxacin with modified NaCl/TiO_2 photocatalyst by surface molecular imprinted technology. **Colloids and Surfaces A: Physicochemical and Engineering Aspects,** v. 441, p. 420-426, 2014. ISSN 0927-7757. Disponível em: < http://www.sciencedirect.com/science/article/pii/S0927775713007590 >.

LIU, X. *et al*. Preparation of a magnetic molecularly imprinted polymer for selective recognition of rhodamine B. **Applied Surface Science,** v. 320, p. 138-145, 2014. ISSN 0169-4332. Disponível em: < http://www.sciencedirect.com/science/article/pii/S016943321401900X >.

LOFGREEN, J. E.; OZIN, G. A. Controlling morphology and porosity to improve performance of molecularly imprinted sol-gel silica. **Chemical Society Reviews,** v. 43, n. 3, p. 911-933, 2014. ISSN 0306-0012. Disponível em: < http://dx.doi.org/10.1039/C3CS60276A >.

LU, Z. *et al*. Microwave synthesis of a novel magnetic imprinted TiO_2 photocatalyst with excellent transparency for selective photodegradation of enrofloxacin hydrochloride residues solution. **Chemical Engineering Journal,** v. 249, p. 15-26, 2014. ISSN 1385-8947. Disponível em: < http://www.sciencedirect.com/science/article/pii/S1385894714003660 >.

LU, Z. *et al*. Performance of molecularly imprinted photocatalysts based on fly-ash cenospheres for selective photodegradation of single and ternary antibiotics solution. **Journal of Molecular Catalysis A: Chemical,** v. 378, p. 91-98, 2013. ISSN 1381-1169. Disponível em: < http://www.sciencedirect.com/science/article/pii/S1381116913002306 >.

LU, Z. *et al*. Specific oriented recognition of a new stable ICTX@Mfa with retrievability for selective photocatalytic degrading of ciprofloxacin. **Catalysis Science & Technology**, 2015. ISSN 2044-4753. Disponível em: < http://dx.doi.org/10.1039/C5CY01324K >.

LUO, Y. *et al*. A review on the occurrence of micropollutants in the aquatic environment and their fate and removal during wastewater treatment. **Science of the Total Environment,** v. 473–474, p. 619-641, 2014. ISSN 0048-9697. Disponível em: <

http://www.sciencedirect.com/science/article/pii/S0048969713015465 >.

LUO, Y. *et al*. Selective photodegradation of 1-methylimidazole-2-thiol by the magnetic and dual conductive imprinted photocatalysts based on TiO_2/Fe_3O_4/MWCNTs. **Chemical Engineering Journal,** v. 240, n. 0, p. 244-252, 2014. ISSN 1385-8947. Disponível em: < http://www.sciencedirect.com/science/article/pii/S1385894713015660 >.

MACHADO, T. C. Degradação fotocatalítica da rosuvastatina em solução aquosoa empregando ZnO em suspensão: cinética, produtos e toxicidade. Dissertação de Mestrado, Universidade Federal do Rio Grande do Sul, Porto Alegre, 2011.

METCALF, L.; EDDY, H. P. Tratamento de efluentes e recuperação de recursos. 5°ed. Porto Alegre: AMGH, 2016.

MAYES, A. G.; WHITCOMBE, M. J. Synthetic strategies for the generation of molecularly imprinted organic polymers. **Advanced Drug Delivery Reviews,** v. 57, n. 12, p. 1742-1778, 2005. ISSN 0169-409X. Disponível em: < http://www.sciencedirect.com/science/article/pii/S0169409X0500150X >.

McNIVEN, S. *et al*. Enhancing the Selectivity of Molecularly Imprinted Polymers. **Chemistry Letters,** v. 26, n. 12, p. 1297-1298, 1997.

MURRAY, A.; ÖRMECI, B. Application of molecularly imprinted and non-imprinted polymers for removal of emerging contaminants in water and wastewater treatment: a review. **Environmental Science and Pollution Research,** v. 19, n. 9, p. 3820-3830, 2012. ISSN 1614-7499. Disponível em: < http://dx.doi.org/10.1007/s11356-012-1119-2 >.

NITOI, I.; ONCESCU, T.; OANCEA, P. Mechanism and kinetic study for the degradation of lindane by photo-Fenton process. **Journal of Industrial and Engineering Chemistry,** v. 19, n. 1, p. 305-309, 2013. ISSN 1226-086X. Disponível em: < http://www.sciencedirect.com/science/article/pii/S1226086X12002778 >.

NOGUEIRA, R. F. P.; JARDIM, W. F. A fotocatálise heterogênea e sua aplicação ambiental. **Química Nova**, v. 21, p. 69-72, 1998. Disponível em: < www.scielo.br/pdf/qn/v21n1/3471.pdf >.

OLIVEIRA, M. A. M.; NELE, M.; PINTO, J. C. Polimerização RAFT em miniemulsão. **Polímeros,** v. 23, p. 784-797, 2013. ISSN 0104-1428. Disponível em: < http://www.scielo.br/scielo.php?script=sci_arttext&pid=S0104-14282013000600015&nrm=iso

>.

PARK, H. *et al*. Surface modification of TiO_2 photocatalyst for environmental applications. **Journal of Photochemistry and Photobiology C: Photochemistry Reviews,** v. 15, p. 1-20, 2013. ISSN 1389-5567. Disponível em: < http://www.sciencedirect.com/science/article/pii/S1389556712000676 >.

PAZ, Y. Preferential photodegradation – why and how? **Comptes Rendus Chimie,** v. 9, n. 5–6, p. 774-787, 2006. ISSN 1631-0748. Disponível em: < http://www.sciencedirect.com/science/article/pii/S1631074805002857 >.

PELAEZ, M. *et al*. A review on the visible light active titanium dioxide photocatalysts for environmental applications. **Applied Catalysis B: Environmental,** v. 125, p. 331-349, 2012. ISSN 0926-3373. Disponível em: < http://www.sciencedirect.com/science/article/pii/S0926337312002391 >.

PESSOA, G. P. *et al*. Occurrence and removal of estrogens in Brazilian wastewater treatment plants. **Science of the Total Environment,** v. 490, n. 0, p. 288-295, 2014. ISSN 0048-9697. Disponível em: < http://www.sciencedirect.com/science/article/pii/S0048969714006664 >.

POMA, A.; TURNER, A. P. F.; PILETSKY, S. A. Advances in the manufacture of MIP nanoparticles. **Trends in Biotechnology,** v. 28, n. 12, p. 629-637, ISSN 0167-7799. Disponível em: < http://dx.doi.org/10.1016/j.tibtech.2010.08.006 >.

RAHIM POURAN, S.; ABDUL AZIZ, A. R.; WAN DAUD, W. M. A. Review on the main advances in photo-Fenton oxidation system for recalcitrant wastewaters. **Journal of Industrial and Engineering Chemistry**, n. 0, ISSN 1226-086X. Disponível em: < http://www.sciencedirect.com/science/article/pii/S1226086X14002548 >.

RAHIM POURAN, S.; ABDUL RAMAN, A. A.; WAN DAUD, W. M. A. Review on the application of modified iron oxides as heterogeneous catalysts in Fenton reactions. **Journal of Cleaner Production,** v. 64, p. 24-35, 2014. ISSN 0959-6526. Disponível em: < http://www.sciencedirect.com/science/article/pii/S0959652613006161 >.

RAMSTRÖM, O.; NICHOLLS, I. A.; MOSBACH, K. Synthetic peptide receptor mimics: highly stereoselective recognition in non-covalent molecularly imprinted polymers. **Tetrahedron: Asymmetry,** v. 5, n. 4, p. 649-656, 1994. ISSN 0957-4166. Disponível em: < http://www.sciencedirect.com/science/article/pii/0957416694800278 >.

RAMSTRÖM, O., 1996, Molecular Imprinting Technology - Design and Recognition Properties

of Antibody/Receptor Mimics, Lund Thesis, 1996

RANADE, V. V.; BHANDARI, V. M. Chapter 14 - Industrial Wastewater Treatment, Recycling, and Reuse—Past, Present and Future. In: RANADE, V. V. e BHANDARI, V. M. (Ed.). **Industrial Wastewater Treatment, Recycling and Reuse**. Oxford: Butterworth-Heinemann, 2014. p.521-535. ISBN 978-0-08-099968-5.

RICCARDO, C.; MARIANA, O.; MANUEL, A. Molecularly Imprinted Sol-Gel Materials for Medical Applications. Current Topics in Medicinal Chemistry, v. 15, n. 3, p. 199-222, 2015. ISSN 1568-0266/1873-5294. Disponível em: < http://www.eurekaselect.com/node/127189/article >.

SAHEL, K. *et al*. Photocatalytic degradation of anionic and cationic dyes over TiO_2 P25, and Ti-pillared clays and Ag-doped Ti-pillared clays. **Applied Clay Science,** v. 95, n. 0, p. 205-210, 2014. ISSN 0169-1317. Disponível em: < http://www.sciencedirect.com/science/article/pii/S016913171400129X >.

SCHAEFER, D. W.; KEEFER, K. D. Fractal Geometry of Silica Condensation Polymers. **Physical Review Letters,** v. 53, n. 14, p. 1383-1386, 1984. Disponível em: < http://link.aps.org/doi/10.1103/PhysRevLett.53.1383 >.

SCHMIDT, P. W. Small-angle scattering studies of disordered, porous and fractal systems. **Journal of Applied Crystallography,** v. 24, n. 5, p. 414-435, 1991. ISSN 1600-5767. Disponível em: < http://dx.doi.org/10.1107/S0021889891003400 >.

SELLERGREN, B. Chapter 5 - The non-covalent approach to molecular imprinting. In: BÖRJE, S. (Ed.). **Techniques and Instrumentation in Analytical Chemistry**: Elsevier, v.Volume 23, 2001. p.113-184. ISBN 0167-9244.

SERPONE, N.; EMELINE, A. V. Suggested terms and definitions in photocatalysis and radiocatalysis. **International Journal of Photoenergy,** v. 4, n. 3, p. 91-131, 2002. Disponível em: < http://dx.doi.org/10.1155/S1110662X02000144 >.

SHAH, M. P. *et al*. Microbial Decolorization of Methyl Orange Dye by *Pseudomona ssp.*. ETL-M. **International Journal of Environmental Bioremediation & Biodegradation,** v. 1, n. 2, p. 54-59, 2013. Disponível em: < http://pubs.sciepub.com/ijebb/1/2/4 >.

SHAHAM-WALDMANN, N.; PAZ, Y. Modified Photocatalysts. In: (Ed.). **Photocatalysis and Water Purification**: Wiley-VCH Verlag GmbH & Co. KGaA, 2013. p.103-143. ISBN 9783527645404.

SHARABI, D.; PAZ, Y. Preferential photodegradation of contaminants by molecular imprinting on titanium dioxide. **Applied Catalysis B: Environmental,** v. 95, n. 1–2, p. 169-178, 2010. ISSN 0926-3373. Disponível em: < http://www.sciencedirect.com/science/article/pii/S0926337309004925 >.

SHEA, K. J.; DOUGHERTY, T. K. Molecular recognition on synthetic amorphous surfaces. The influence of functional group positioning on the effectiveness of molecular recognition. **Journal of the American Chemical Society,** v. 108, n. 5, p. 1091-1093, 1986/03/01 1986. ISSN 0002-7863. Disponível em: < http://dx.doi.org/10.1021/ja00265a046 >.

SILVA, Da, W. L. Síntese, caracterização e atividade fotocatalítica de catalisadores nanoestruturados de TiO_2 dopados com metais. Dissertação de mestrado, UFRGS, 2012.

SILVA, Da, W. L *et al*. Industrial and agroindustrial wastes: an echotechnological approach to the production of supported photocatalysts. **Water Science & Technology**, v. 73, p. 28-38, 2016. Disponível em: < http://www.ncbi.nlm.nih.gov/pubmed/26744932>.

SHEN, X. *et al*. Inorganic molecular imprinted titanium dioxide photocatalyst: synthesis, characterization and its application for efficient and selective degradation of phthalate esters. **Journal of Materials Chemistry**, v. 19, n. 27, p. 4843-4851, 2009. ISSN 0959-9428. Disponível em: < http://dx.doi.org/10.1039/B900196D >.

SHEN, X. *et al*. Selective photocatalytic degradation of nitrobenzene facilitated by molecular imprinting with a transition state analog. **Catalysis Today,** v. 225, n. 0, p. 164-170, 2014. ISSN 0920-5861. Disponível em: < http://www.sciencedirect.com/science/article/pii/S0920586113003453 >.

SCHUBERT, U.; HÜSING, N. **Synthesis of Inorganic Materials, 2nd edition**. New York: Wiley, 2005.

SODRÉ, F.; LOCATELLI, M.; JARDIM, W. Occurrence of Emerging Contaminants in Brazilian Drinking Waters: A Sewage-To-Tap Issue. **Water, Air, and Soil Pollution,** v. 206, n. 1-4, p. 57-67, 2010/02/01 2010. ISSN 0049-6979. Disponível em: < http://dx.doi.org/10.1007/s11270-009-0086-9 >.

SOROLLA II, M. G. *et al*. Photocatalytic degradation of paraquat using nano-sized Cu-TiO_2/SBA-15 under UV and visible light. **Journal of Environmental Sciences,** v. 24, n. 6, p. 1125-1132, 2012. ISSN 1001-0742. Disponível em: < http://www.sciencedirect.com/science/article/pii/S1001074211608747 >.

SUN, Z. *et al*. A comparative study of different porous amorphous silica minerals supported TiO2 catalysts. **Applied Catalysis A: General,** v. 458, n. 0, p. 103-110, 2013. ISSN 0926-860X. Disponível em: < http://www.sciencedirect.com/science/article/pii/S0926860X1300166X >.

SUN, Z. *et al*. Effect of preparation conditions on the characteristics and photocatalytic activity of TiO_2/purified diatomite composite photocatalysts. **Applied Surface Science,** v. 314, n. 0, p. 251-259, 2014. ISSN 0169-4332. Disponível em: < http://www.sciencedirect.com/science/article/pii/S0169433214014895 >.

TANAKA, K. *et al*. Effect of Crystal Form of TiO_2, on the Photocatalytic Degradation of Pollutants. Photocatalytic Treatment of Water and Air, OLLIS, D.F.; ALEKABI, H.; Elsevier Science Publishers B. V., Amsterdam, 1993.

TEIXEIRA, C. P. A. B.; JARDIM, W. F. **Processos Oxidativos Avançados. Conceitos teóricos. Caderno temático**, v. 3, Instituto de Química UNICAMP, Campinas/SP, 2004.

TOMINAGA, Y. *et al*. Effective Recognition on the Surface of a Polymer Prepared by Molecular Imprinting Using Ionic Complex. **Macromolecules,** v. 42, n. 8, p. 2911-2915, 2009/04/28 2009. ISSN 0024-9297. Disponível em: < http://dx.doi.org/10.1021/ma802880z >.

US EPA, Guidelines for water reuse. US Agency for International Development, Washington DC, 2012. Disponível em*:* < pdf.**usaid**.gov/pdf_docs/PNABM586.pdf >.

VASAPOLLO, G. *et al*. Molecularly Imprinted Polymers: Present and Future Prospective. **International Journal of Molecular Sciences,** v. 12, n. 9, p. 5908, 2011. ISSN 1422-0067. Disponível em: < http://www.mdpi.com/1422-0067/12/9/5908 >.

WALCARIUS, A.; COLLINSON, M. M. Analytical chemistry with silica sol-gels: traditional routes to new materials for chemical analysis. **Annu Rev Anal Chem (Palo Alto Calif),** v. 2, p. 121-43, 2009. ISSN 1936-1335 (Electronic). Disponível em: < http://www.ncbi.nlm.nih.gov/pubmed/20636056 >.

WANG, H. *et al*. Enhanced photocatalytic degradation of tetracycline hydrochloride by molecular imprinted film modified TiO_2 nanotubes. **Chinese Science Bulletin,** v. 57, n. 6, p. 601-605, 2012/02/01 2012. ISSN 1001-6538. Disponível em: < http://dx.doi.org/10.1007/s11434-011-4897-x >.

WANG, X. *et al*. Hierarchically pores carbon-covered alumina/ TiO_2 catalysts from particle stabilized foams. **Colloids and Surfaces A: Physicochemical and Engineering Aspects**, n. 0, ISSN 0927-7757. Disponível em: <

http://www.sciencedirect.com/science/article/pii/S092777571400658X >.

WANG, Y. *et al*. Design of a Novel Cu_2O/TiO_2/Carbon Aerogel Electrode and Its Efficient Electrosorption-Assisted Visible Light Photocatalytic Degradation of 2,4,6-Trichlorophenol. **ACS Applied Materials & Interfaces,** v. 4, n. 8, p. 3965-3972, 2012/08/22 2012. ISSN 1944-8244. Disponível em: < http://dx.doi.org/10.1021/am300795w >.

WANG, Z. *et al*. Enhancing the photocatalytic degradation of salicylic acid by using molecular imprinted S-doped TiO_2 under simulated solar light. **Ceramics International,** v. 40, n. 6, p. 8863-8867, 2014. ISSN 0272-8842. Disponível em: < http://www.sciencedirect.com/science/article/pii/S0272884214001370 >.

WANG, Z. *et al*. Enhancing the photocatalytic degradation of salicylic acid by using molecular imprinted S-doped TiO_2 under simulated solar light. **Ceramics International,** v. 40, n. 6, p. 8863-8867, 2014. ISSN 0272-8842. Disponível em: < http://www.sciencedirect.com/science/article/pii/S0272884214001370 >.

WHITCOMBE, M. J. *et al*. A New Method for the Introduction of Recognition Site Functionality into Polymers Prepared by Molecular Imprinting: Synthesis and Characterization of Polymeric Receptors for Cholesterol. **Journal of the American Chemical Society,** v. 117, n. 27, p. 7105-7111, 1995/07/01 1995. ISSN 0002-7863. Disponível em: < http://dx.doi.org/10.1021/ja00132a010 >.

WULFF, G.; BEST, W.; AKELAH, A. Enzyme-analogue built polymers, 17 Investigations on the racemic resolution of amino acids. **Reactive Polymers, Ion Exchangers, Sorbents,** v. 2, n. 3, p. 167-174, 1984. ISSN 0167-6989. Disponível em: < http://www.sciencedirect.com/science/article/pii/0167698984901326 >.

WULFF, G. *et al*. Enzyme-analogue built polymers, 4. On the synthesis of polymers containing chiral cavities and their use for the resolution of racemates. **Die Makromolekulare Chemie,** v. 178, n. 10, p. 2799-2816, 1977. ISSN 0025-116X. Disponível em: < http://dx.doi.org/10.1002/macp.1977.021781004 >.

XIAO, G.; SU, H.; TAN, T. Synthesis of core–shell bioaffinity chitosan–TiO_2 composite and its environmental applications. **Journal of Hazardous Materials,** v. 283, p. 888-896, 2015. ISSN 0304-3894. Disponível em: < http://www.sciencedirect.com/science/article/pii/S0304389414008905 >.

YANG, M.; PARK, M. S.; LEE, H. S. Endocrine Disrupting Chemicals: Human Exposure and

Health Risks. **Journal of Environmental Science and Health, Part C,** v. 24, n. 2, p. 183-224, 2006/12/01 2006. ISSN 1059-0501. Disponível em: < http://dx.doi.org/10.1080/10590500600936474 >.

YE, L.; A. G. CORMACK, P.; MOSBACH, K. Molecularly imprinted monodisperse microspheres for competitive radioassay. **Analytical Communications,** v. 36, n. 2, p. 35-38, 1999. ISSN 1359-7337. Disponível em: < http://dx.doi.org/10.1039/A809014I >.

YAO, *et al*. Synthesis and characterization of novel Ti-containing mesoporous silicas support. **Journal of Ceramics Processing Research**, v. 12, n. 3, p, 289-293, 2011. Disponível em: < http://ir.lzu.edu.cn/handle/262010/105306>.

YE, L.; WEISS, R.; MOSBACH, K. Synthesis and Characterization of Molecularly Imprinted Microspheres. **Macromolecules,** v. 33, n. 22, p. 8239-8245, 2000/10/01 2000. ISSN 0024-9297. Disponível em: < http://dx.doi.org/10.1021/ma000825t >.

ZALESKA, A. Doped-TiO_2: A Review. **Recent Patents on Engineering 2008**, v. 2, p. 157-164157, 2008. Disponível em: < https://www.researchgate.net/publication/230718297_Doped-TiO2_a_review>.

ZETTERLUND, P. B.; KAGAWA, Y.; OKUBO, M. Controlled/Living Radical Polymerization in Dispersed Systems. **Chemical Reviews,** v. 108, n. 9, p. 3747-3794, 2008/09/10 2008. ISSN 0009-2665. Disponível em: < http://dx.doi.org/10.1021/cr800242x >.

ZHANG, J. *et al*. Enhanced decoloration activity by Cu_2O@TiO_2 nanobelts heterostructures via a strong adsorption-weak photodegradation process. **Applied Surface Science,** v. 282, p. 84-91, 2013. ISSN 0169-4332. Disponível em: < http://www.sciencedirect.com/science/article/pii/S0169433213009811 >.

ZHANG, J. *et al*. TiO_2 Film/Cu_2O Microgrid Heterojunction with Photocatalytic Activity under Solar Light Irradiation. **ACS Applied Materials & Interfaces,** v. 1, n. 10, p. 2111-2114, 2009/10/28 2009. ISSN 1944-8244. Disponível em: < http://dx.doi.org/10.1021/am900463g >.

ZHANG, Y. *et al*. Graphene TiO_2 nanocomposites with high photocatalytic activity for the degradation of sodium pentachlorophenol. **Journal of Environmental Sciences,** v. 26, n. 10, p. 2114-2122, 2014. ISSN 1001-0742. Disponível em: < http://www.sciencedirect.com/science/article/pii/S1001074214001338 >.

ZHANG, Z. *et al*. Microwave degradation of methyl orange dye in aqueous solution in the presence of nano-TiO_2-supported activated carbon. **Journal of Hazardous Materials,** v. 209–210, n. 0, p. 271-277, 2012. ISSN 0304-3894. Disponível em: < http://www.sciencedirect.com/science/article/pii/S0304389412000374 >.

ZHAO, C. *et al*. Photodegradation of oxytetracycline in aqueous by 5A and 13X loaded with TiO_2 under UV irradiation. **Journal of Hazardous Materials,** v. 176, n. 1–3, p. 884-892, 2010. ISSN 0304-3894. Disponível em: < http://www.sciencedirect.com/science/article/pii/S0304389409019190 >.

ZHAO, K. *et al*. Adsorption and photocatalytic degradation of methyl orange imprinted composite membranes using TiO_2/calcium alginate hydrogel as matrix. **Catalysis Today,** v. 236, Part A, p. 127-134, 2014. ISSN 0920-5861. Disponível em: < http://www.sciencedirect.com/science/article/pii/S0920586114002715 >.

ZONGYAN, Z.; QINGJU, L. Mechanism of higher photocatalytic activity of anatase TiO_2 doped with nitrogen under visible-light irradiation from density functional theory calculation. **Journal of Physics D: Applied Physics,** v. 41, n. 2, p. 025105, 2008. ISSN 0022-3727. Disponível em: < http://stacks.iop.org/0022-3727/41/i=2/a=025105 >.